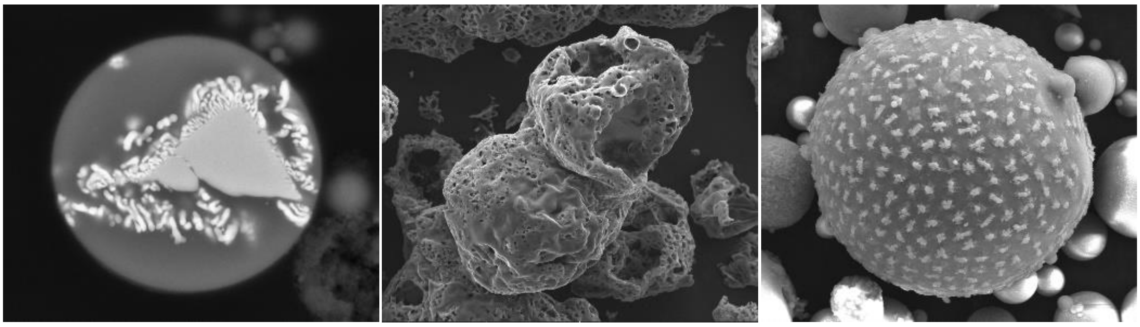

Assessing the rare earth elements and carbon potential of coal ashes from a Portuguese Power Plant and its temporal and lateral variation

Ana Cláudia Alves Santos

Programa Doutoral em Geociências
Especialidade em Recursos Geológicos e Geomateriais

Departamento de Geociências, Ambiente e Ordenamento do Território
2022

Orientador
Bruno Renato Valério Valentim, Investigador Principal, FCUP

Coorientador
Maria Alexandra de Mascarenhas Guedes, Professor Auxiliar, FCUP

universidade
de aveiro

U.PORTO

FACULDADE DE CIÊNCIAS
UNIVERSIDADE DO PORTO

PhD

To my beloved granny

Declaração de Honra

Eu, Ana Cláudia Alves Santos, inscrito(a) no Programa Doutoral em Geociências da Faculdade de Ciências da Universidade do Porto declaro, nos termos do disposto na alínea a) do artigo 14.º do Código Ético de Conduta Académica da U.Porto, que o conteúdo da presente tese reflete as perspetivas, o trabalho de investigação e as minhas interpretações no momento da sua entrega.

Ao entregar esta tese, declaro, ainda, que a mesma é resultado do meu próprio trabalho de investigação e contém contributos que não foram utilizados previamente noutros trabalhos apresentados a esta ou outra instituição.

Mais declaro que todas as referências a outros autores respeitam escrupulosamente as regras da atribuição, encontrando-se devidamente citadas no corpo do texto e identificadas na secção de referências bibliográficas. Não são divulgados na presente tese quaisquer conteúdos cuja reprodução esteja vedada por direitos de autor.

Tenho consciência de que a prática de plágio e auto-plágio constitui um ilícito académico.

Ana Cláudia Santos

Porto, 4 de novembro de 2022

Assessing the rare earth elements and carbon potential of coal ashes from a Portuguese Power Plant and its temporal and lateral variation

Ana Cláudia Alves Santos

Dissertation submitted to Faculty of Sciences at University of Porto for the degree of Doctor of Philosophy in Earth Sciences

This research was funded by the Fundação para a Ciência e Tecnologia (FCT), Grants Number SFRH/BD/131713/2017 and COVID/BD/151941/2021. This work was supported by the Portuguese Foundation for Science and Technology (FCT) project UIDB/04683/2020-ICT (Institute of Earth Sciences). The author thanks to the CHARPHITE project (ERA-MIN/0005/2015) – “Coal char as a substituting material of natural graphite in green energy technologies” for technical and financial support.

Ana Cláudia Alves Santos

Assessing the rare earth elements and carbon potential of coal ashes from a Portuguese Power Plant and its temporal and lateral variation

Keywords: Commercial Coal, Fly Ash, Bottom Ash, Critical Raw Materials, Rare Earth Elements, Graphite, Char, Graphitization, Magnetic Concentrates

PhD Thesis, Geological Resources and Geomaterials specialization, Porto University, Portugal (2022)

Dissertation written in English

Acknowledgements

I would like to express my thanks to everyone that helped and supported me in this amazing journey:

My supervisors, Professor Bruno Valentim, and Professor Alexandra Guedes, for your guidance, support, and trust during this journey. I am extremely greatfull for all the opportunities that you provided me that helped me growth as researcher and as a person.

Institute of Earth Sciences and Department of Geosciences, Environment and Spatial Plannings of Faculty of Sciences of the University of Porto for the facilities and conditions granted to me.

Pego power plant for providing me the samples to develop my research and allowing me to do an internship at the power plant. It was a unique experience that provided me with essential know-how for the development of my thesis. I want to thank to Eng. Felicissimo Matos, Eng. Jorge Henriques, Eng. Carla Sousa, Dr. Maria João Ribeiro, and Dr. Vera Oliveira. A special thanks to Dr. Maria João Cordeiro for being a mentor during my internship at power plant and for all the support that gave me through this journey.

Partners from Charphite project for making me feel as part of the team since day one and for all the knowledge that shared with me. I would like to make a special thanks to the Requimte team, Marta Nunes, Iwona Kuźniarska-Biernacka, Andreia Peixoto e Diana Fernandes, with whom I worked most closely and were always available to help me and clarify my queries.

Dr. David French from School of Biological, Earth and Environmental Sciences, University of New South Wales (New South Wales, Australia) for X-ray diffraction analysis.

Eng. Aurora Futuro from Faculty of Engineering, University of Porto (Porto, Portugal) for the laser diffractions analysis.

Dr. João Waerenborgh and Dr. Bruno Vieira from Centro de Ciências e Tecnologias Nucleares, DECN, Instituto Superior Técnico, Universidade de Lisboa (Lisboa, Portugal) for the aquisition of Mössbauer spectra, data treatment and interpretation.

Dr. Helena Sant`Ovaia and Dr. Cláudia Cruz for helping me with the magnetic susceptibility analysis and further interpretation.

Dr. Eric Font from Department of Earth Sciences, University of Coimbra (Coimbra, Portugal) for the guidance in the IRM experiments and the interpretation of the results.

Dr. Rui Rocha from Materials Centre of the University of Porto (CEMUP, Porto Portugal) for the assistance with SEM/EDS analysis.

Dr. Marta Ferro and Dr. Suzana Peripolli from the Department of Engineering and ceramics from University of Aveiro (Aveiro, Portugal) for carrying out the TEM analysis.

Dr. Helena Ribeiro for helping with the demineralization stage and for clarifying my queries about statistic.

Colleagues Karen Moreira, Alina Vyacheslavovna and Renato Guimarães for their collaboration in some laboratorial tasks.

Dr. Sofia Santos who was always available to clarify my questions regarding the bureaucratic processes involved in this journey.

The staff from Department of Geosciences, Environment, and Spatial Plannings, Paulo Ferreira, Cristina Vilas Boas, Cândida Neto, Irene Costa, Mónica Alves, Joana Damásio for all the help that provided me.

My geologist collegues and friends Alyna Vyacheslavovna, Andreia Pereira, Ana Marta Gonçalves, António Oliveira, Carolina Marques, Charlotte Badenhorst, Cláudia Cruz, Guilherme Insua, Helena Moura, Joana Ribeiro, Karen Moreira, Luis Lima, Marcela Rodrigues, Miguel Maia, Patrícia Santos, Rita Lamas, Sara leal and Vanessa Laranjeira.

My friends Bebiana Silva, Bruno Ferreira, Cátia Silva, Ilda Henriques, Fernanda Torrié, João Sousa, Juvenal Campos, Márcia Santos, Margarida Seixas, Patricia Barros, Rose Silva and Sabina Cunha.

To my family that even being far physically always supported me to get through this journey. My mom for being always so positive and my sister to be as stressed as me but always trying to rationalize.

To Pedro who followed this journey closely and always supported me to achieve my goals, thank you.

Abstract

The increasing demand for rare earth elements (REE), noble elements and graphite, associated with their economic importance and supply risk, motivated the research for secondary sources for these elements/minerals or materials that could replace them. Coal combustion ashes have been pointed out as potential raw material for REE and are a proven source of carbonaceous solid residue (char) and magnetic materials. The REE potential depends on the feed coal being used, which in turn changes among power plants, so it is necessary numerous research to assess ashes being produced worldwide. In the case of char and magnetics their availability in the ashes is known, but few research explored the possibility of using them to replace natural graphite and noble metals, respectively.

The main objective of this thesis is to assess the feasibility to use coal combustion ashes as secondary raw material for REE, and to recover, characterize and test char as a graphitic precursor, to be used as substitute of natural graphite, and Fe-rich morphotypes to be applied in wastewater treatment instead of noble metals.

For this purpose, four sampling campaigns were carried out at Pego power plant (Abrantes, Portugal) over a year to collect samples of feed coals and ashes from different collection points. The samples were characterized regarding chemical (proximate and ultimate analysis, X-ray fluorescence - XRF, carbon forms, and inductively coupled plasma mass spectrometry - ICP-MS), mineralogical (X-ray diffraction - XRD and scanning electron microscopy with energy dispersive X-ray spectroscopy - SEM/EDS) and petrographic composition (optical microscopy). Some of the ash samples studied were selected to be fractionated based on particle size and magnetic properties and then were further characterized to assess potential trends on targeted elements/morphotypes.

The investigated feed coals being burned at Pego power plant consisted of commercial coal imported from Colombia mostly within medium rank D, vitrinite-rich, very low to medium ash, and low REE concentrations (<25 ppm). All ashes studied were classified as Class F, sialic with medium acidity, and were mainly composed by an amorphous phase (mostly aluminosilicate glass), quartz and mullite.

The highest contents of carbon and REE were consistently found in fly ashes (FA) from the electrostatic precipitator (ESP) making them more promising for char and REE recovery. The REE contents increased towards ESP back rows along with the LREE/HREE ratio which was attributed to changes in fly ash petrology since no fractionation of these elements was observed. Furthermore, REE were mainly observed in <10 µm discrete particles having P and Al-Si as the major components and it was confirmed they are mostly enriched in nonmagnetic <25 µm fraction from fly ashes. Nevertheless, sequential sieving and magnet separation was proved to be insufficient to reach the economical cut-off (1000 ppm).

After a set of physical concentration trials using a selected FA sample, i.e., combining sieving, sink-float, vibration-induced segregation and elutriation, a char concentrate (CC) was obtained to be transformed in high temperature treatments (HTT). Before HTT the CC was demineralized to avoid clogging of the graphitization chamber. The CC obtained was characterized along with three other CC from different provenances that also underwent through HTT. In addition to chemical characterization, microstructural changes were assessed using optical microscopy (Reflectance Indicating Surface characterization), XRD, transmission electron microscopy (TEM) and Raman microspectroscopy.

It was concluded that the CC obtained in this research had the lowest ability to graphitize despite having initial characteristics similar to the CC that graphitized better, namely random reflectance, interlaying spacing – d_{002} and the spatial arrangement of basic structural units - BSU. This was mainly attributed to low contents of mineral matter, namely Al_2O_3 which was found to be correlated with d_{002}, and hydrogen that is known to promote BSU mobilization, both removed during demineralization. Char morphotypes are another factor seemingly to have influenced the graphitization attained by the different CC studied since analogous char morphotypes had different responses to graphitization.

It was demonstrated that all CC studied are promising electrocatalysts in oxygen reduction reaction (essential for energy conversion) not needing to be graphitized. This is very interesting since FA commonly contains 2-12 wt.% of carbon (mostly as char), relatively easy to recover, its removal improves FA quality, and may substitute natural graphite.

During the collection of magnetic concentrates (MC), it was found that the Fe magnet is more selective than the Nd magnet in the collection of Fe-rich particles since the latter recovers high amounts of Fe-bearing aluminosilicate glass. Nevertheless, the Fe-MC still contain >45 wt.% of amorphous phase (mainly aluminosilicate glass), where some Fe is incorporated, and other nonmagnetic minerals such as quartz and mullite. Magnetite, hematite, magnesioferrite, and maghemite were the predominant iron-bearing minerals. Ferrospheres, i.e., discrete spherical Fe-rich morphotypes exhibiting skeletal-dendritic microtextures and crystals of Fe-minerals predominate in Fe-MC from ESP FA. Some elements known for its ability to substitute Fe in the spinel structure, such as Mn, Co and Ni, were found enriched in Fe-MC, but are depleted compared to world coal ashes.

The Fe-MC from the FA were tested as electrocatalysts in the reduction reaction of 4-nitrophenol (toxic compound found in wastewaters) and catalytic activity was verified, which is very promising regarding their use as substitutes for noble metals (e.g., Au, Pd, Pt and Ag). Furthermore, the MC are abundant and very easy to recover from FA, and after being used can be easily recovered via magnetic separation to be reapplied.

The results obtained in this thesis contribute with relevant know-how for coal combustion ashes recycling and prevention of its landfilling. It was proved that simple separation methods are enough to recover char and Fe-rich morphotypes from fly ash. Consequently, these materials will pass from the status of detrimental materials in FA uses in civil construction materials to value added products as substitutes of natural graphite and noble metals.

Resumo

A crescente procura por elementos terras raras (REE), elementos nobres e grafite, associada à sua importância económica e risco de fornecimento, tem motivado a investigação sobre fontes secundárias para esses elementos/minerais e sobre a sua substituição por outros materiais. As cinzas de combustão de carvão têm sido apontadas como potencial matéria-prima para os REE e são uma fonte comprovada de resíduos carbonosos sólidos (char) e materiais magnéticos. O potencial em REE depende em grande parte do carvão usado em cada central e, por isso, a sua avaliação requer um elevado número de estudos que incluam cinzas produzidas em todo o mundo. Relativamente ao char e os materiais magnéticos a disponibilidade nas cinzas é conhecida, mas poucos estudos exploraram a possibilidade de usar o char como substituto da grafite e os materiais magnéticos para substituir metais nobres.

O principal objetivo desta tese é avaliar a viabilidade de usar cinzas de combustão de carvão como matéria-prima secundária para REE, e recuperar, caracterizar e testar o char como precursor de grafite, para ser usado como substituto do grafite natural, e os morfotipos ricos em ferro para aplicação no tratamento catalítico de efluentes em substituição aos metais nobres.

Ao longo de um ano, foram realizadas quatro campanhas de amostragem na central termoelétrica do Pego (Abrantes, Portugal), para recolha de amostras de carvões e de cinzas de diferentes locais. As amostras foram caracterizadas quanto à sua química (análise aproximada e final, fluorescência de raios X, formas de carbono e espectrometria de massa com plasma indutivamente acoplado), mineralogia (difração de raios X - XRD e microscopia eletrónica de varrimento com microanálise por raios-X) e composição petrográfica (microscopia ótica). Algumas amostras de cinzas estudadas foram selecionadas para fracionamento de acordo com a dimensão das partículas e propriedades magnéticas e, em seguida, as diferentes frações foram caracterizadas para avaliar potenciais tendências relativamente aos elementos/morfotipos de interesse.

Os carvões da central termoelétrica do Pego, importados da Colômbia, caracterizam-se por ser de grau médio D, rico em vitrinite, e por apresentar um rendimento em cinzas muito baixo a médio e baixas concentrações de REE (<25 ppm). As cinzas estudadas são classificadas como Classe F, siálicas e com acidez média, e eram compostas principalmente por uma fase amorfa (sobretudo vidro aluminossilicato), quartzo e mulite.

Os teores de carbono e REE mais elevados foram consistentemente determinados em cinzas volantes do precipitador eletrostático (ESP), sendo por esta razão as mais promissoras para recuperação de char e REE. A concentração de REE e a razão entre REE leves e pesadas aumentam em direção às linhas do fundo do ESP, tendências estas que foram atribuídas a mudanças na petrologia das cinzas volantes, uma vez que não foi observado fracionamento desses elementos. Além disso, os REE foram observados principalmente em partículas discretas com dimensão <10 µm apresentando P e Al-Si como principais componentes e foi confirmado que estes se encontravam enriquecidos na fração não magnética <25 µm das cinzas volantes do ESP. A aplicação sequencial de peneiração e separação magnética mostrou-se insuficiente para atingir o teor de corte que possibilita uma extração economicamente viável (1000 ppm).

Após um conjunto de ensaios de concentração usando uma amostra de cinza volante, combinando peneiração, flutuação, segregação induzida por vibração e elutriação, obteve-se um concentrado de char (CC) para os tratamentos térmicos de alta temperatura (HTT). Antes destes, desmineralizou-se o concentrado de char para evitar o entupimento da câmara de grafitização. O CC foi caracterizado conjuntamente com outros três concentrados de diferentes proveniências que também foram submetidos a HTT. Além da caracterização química, as alterações microestruturais foram avaliadas através de microscopia ótica (caracterização da *Reflectance Indicating Surface*), XRD, microscopia eletrónica de transmissão e microespectroscopia Raman.

Concluiu-se que o CC obtido nesta apresenta baixa capacidade de grafitização, embora apresentasse características semelhantes ao CC que melhor grafitizou, nomeadamente refletância aleatória, espaçamento interplanar – d_{002} e arranjo espacial das unidades básicas estruturais. A baixa capacidade de grafitização poderá estar relacionada com teores mais baixos de matéria mineral, particularmente Al_2O_3, que atua como catalisador, e hidrogénio, conhecido por promover a mobilização das unidades básicas estruturais, ambos removidos durante a desmineralização. Os morfotipos de char também parecem ter influenciado a habilidade de grafitização dos diferentes CC estudados, uma vez que morfotipos de char análogos tiveram respostas diferentes à grafitização.

No entanto, foi demonstrado que todos os concentrados de char estudados são eletrocatalisadores promissores na reação de redução de oxigénio (reação essencial para conversão de energia) não necessitando para isso ser grafitizados. Este resultado é muito interessante, pois a cinza volante geralmente contém 2-12% em massa de carbono (principalmente char), relativamente fácil de recuperar que pode substituir a grafite natural na reação mencionada.

Relativamente aos concentrados magnéticos (MC), verificou-se que o íman de ferrite é mais seletivo que o íman de neodímio na recolha de partículas ricas em Fe, uma vez que este último recupera grandes quantidades de vidro aluminossilicato contendo ferro. Contudo, os concentrados magnéticos recolhidos com o íman de Fe ainda contém >45 % em peso de fase amorfa (sobretudo vidro aluminossilicato), onde algum Fe é incorporado, e outros minerais não magnéticos, como quartzo e mulite. Os minerais portadores de ferro predominantes nesses concentrados foram a magnetite, a hematite, a magnesioferrite e a maghemite. As ferroesferas, morfotipos esféricos ricos em Fe exibindo microtexturas esquelético-dendríticas e cristais de minerais de Fe predominam nos concentrados recolhidos das cinzas volantes. Alguns elementos conhecidos pela sua capacidade de substituir o Fe na estrutura das espinelas, como Mn, Co e Ni, encontravam-se enriquecidos nos concentrados relativamente aos rejeitados, no entanto, comparativamente aos teores das cinzas globais encontravam-se empobrecidos.

Os concentrados magnéticos recolhidos da cinza volante foram testados como eletrocatalisadores na redução do 4-nitrofenol (composto tóxico encontrado em efluentes) e foi verificada atividade catalítica, o que é bastante promissor quanto ao uso destes morfortipos como substitutos de metais nobres. Os concentrados magnéticos são fáceis de obter e muito abundantes e apresentam a vantagem de depois de utilizados poderem ser facilmente recuperados com um íman e reaplicados.

Os resultados obtidos nesta tese representam um contributo relevante para o conhecimento sobre a reciclagem das cinzas derivadas da combustão de carvão comercial e minimização da deposição em aterro. Foi comprovado que a separação do char e dos morfortipos de ferro pode ser feita de forma relativamente simples e os testes de aplicação confirmam o potencial de utilização como substitutos de materiais críticos. Desta forma, ao serem removidos o char e o ferro deixam de ser materiais prejudiciais no uso das cinzas volantes na indústria do cimento e passam a ser produtos de valor acrescentado.

Index

List of Figures

Part II

Part III

List of Tables

Part II

Part III

Abbreviations and Acronyms

ad	Air dry basis
a.u.	Arbitrary units
ASTM	American Society for Testing and Materials
B	Bireflectance
$B_{1/2}$	Field at which half of the SIRM is reached
BA	Bottom ash
bdl	Below detection limit
B_{hf}	Magnetic hyperfine field
BSE	Backscattered electron mode
BSU	Basic Structural Units
CC	Concentration coefficient
CC	Char concentrate
CCD	Charge-coupled device
C_{CO2}	Inorganic carbon
CD	Char demineralized
C_{gra}	Graphite carbon
Char	Carbonaceous solid residue
CLG	Cumulative log-Gaussian
C_{org}	Organic carbon
C_{outl}	Outlook coefficient
C_{tot}	Total carbon
CV	Coefficient of variation
db	Dry basis
d_{002}	Average value of interlayer spacing
daf	dry ash free basis
DP	Dispersion parameter
DS	Dry sieving
e.g.	Exempli gratia, for example
ECO	Economizer
EF	Enrichment factor
ESP	Electrostatic precipitator
FA	Fly ash
FC	Fixed carbon
FCUP	Faculty of Sciences of University of Porto
Fe-MC	Magnetic concentrate collected with ferrite magnet
FGD	Flue gas desulphurization
FWHM	Full width at half maximum
GCV	Gross calorific value
H	External magnetic field

HCl	Hydrochloric acid
HF	Hydrofluoric acid
hkl	Miller indices
HREE	Heavy rare earth elements
HTT	High Temperature Treatment
i.e.	Id est, that is
ICCP	International Committee for Coal and Organic Petrology
ICP-MS	Inductively coupled plasma mass spectrometry
IRM	Isothermal remanent magnetization
IS	Isomer shifts
ISO	International Organization for Standardization
J	Material magnetization
L/H	Ratio between LREE and HREE
L_a	Average value of the crystallite width
L_c	Average value of the crystallite height
LOI	Loss on ignition
LREE	Light rare earth elements
MC	Magnetic concentrate
MREE	Medium rare earth elements
n.a.	Not attributed
n.d.	Not determined
NA	Numerical aperture
Nd-MC	Magnetic concentrate collected with neodymium magnet
NPh	Nitrophenol
ORR	Oxygen reduction reaction
PSD	Particle size distribution
QS	Quadrupole splitting
R'_{max}	Apparent maximum reflectance value
R'_{min}	Apparent minimum reflectance value
R_{am}	RIS anisotropy magnitude
RE	Relative enrichment
REE	Rare earth elements
R_{ev}	Reflectance of equivalent volume isotropic RIS (parameter of RIS)
REO	REE as oxides
RHA	regenerative air heaters
R_{INT}	Intermediate reflectance axis of RIS
RIS	Reflectance Indicating Surface
R_{MAX}	Maximum reflectance axis of RIS
R_{MIN}	Minimum reflectance axis of RIS
rpm	Revolutions per minute
R_r	Mean value of random vitrinite reflectance

R_{st}	RIS style
SCR	Selective catalytic reduction
SE	Secondary electrons mode
SEM/EDS	Scanning electron microscopy with energy dispersive spectroscopy
SIRM	Saturation of isothermal remanent magnetization
S_t	Total sulfur
TEM	Transmitted electronic microscopy
TGA	Thermogravimetric analyzer
TL	Tailings
UCC	Upper continental crust
VM	Volatile matter
WS	Wet sieving
XRD	X-ray Diffraction
XRF	X-ray fluorescence

Symbols and Units

<N>	Number of aromatic layers
°C	Celsius
χ	Magnetic susceptibility
cm^{-1}	Reciprocal centimeter (or wavenumber)
g	Grams
KeV	Kiloelectronvolt
Kg	Kilogram
kV	Kilovolt
m^3/Kg	Meter cubed per kilogram
mA	Milliampere
min	Minutes
mL	Milliliter
mm	Millimeter
mT	MiliTesla
nm	Nanometers
ppb	Part per billion
ppm	Part per million
r	Pearson's correlation coefficient
s	Seconds
vol.%	Volume percentage
wt.%	Weight percentage
ε	Quadrupole shift estimated for quadrupole doublets and magnetic sextets (mm/s)
µm	Microns
ρ	Level of marginal significance within a statistical hypothesis test
ω	frequency, cm^{-1}

Part I | Introduction

1. Subject

The demand for raw materials has been increasing along with population growth and the improvements in the living conditions (Schulz et al., 2017). Meanwhile, the policies to achieve carbon neutrality and energy transition are pushing even more the demand of raw materials, especially for elements related with energy conversion and storage (Graedel and Reck, 2016). In European Union (EU), concerns about getting secure sources for raw materials, particularly the critical ones, arose and the search for alternative materials and secondary sources has increased (European Commission, 2020).

Coal represents a large share of energy production and is estimated that by 2030 still represents 46% of the world electricity supply (Yao et al., 2015). Every year, approx. 750 million tons of fly ash are produced of which in average 25 % is used mainly in concrete and cement (Bhatt et al., 2019; Blissett and Rowson, 2012; Wang, 2008). The remaining ashes are usually landfilled or ponded, mostly because they are produced far consumption locations, which can lead to environmental problems, such water, and soils contamination (Gollakota et al., 2019). Nevertheless, this trend is progressively shifting since coal ashes are now becoming a scarce resource in EU and have been pointed out as potential raw materials for critical elements such as Rare Earth Elements (REE) (Dai and Finkelman, 2018). Meanwhile, the potential utilization of the carbonaceous solid residue (char) and the Fe-rich morphotypes, commonly occurring in these ashes in concentrations up to 15 wt.% and 25 wt.%, respectively (Ahmaruzzaman, 2010; Blissett and Rowson, 2012), is far from being exploited despite having characteristics not far from graphite and other metals, respectively.

In this thesis, the fundamental subjects are related with specific characteristics of coal combustion ashes, such as the ones derived from international commercial coals (e.g., the ones burned at Pego power plant, Portugal), which are relevant for EU autonomy regarding REE, graphite and noble metals. These specific characteristics are related to scientific subjects regarding the genesis and distribution of REE, char and Fe-rich morphotypes in coal ashes, which needed to be linked with assessment of economic potential in the case of the REE, materials concentration and catalysis in the case of char and Fe-rich morphotypes, and thermal transformations also in the case of the char.

2. Objectives

The main objective of this thesis is to assess the feasibility to utilize coal combustion ashes as secondary raw material for REE, char as a graphitic precursor material, and Fe-concentrates to replace noble metals.

Taking into consideration that coal combustion products are heterogeneous materials, a detailed characterization is needed to accomplish these goals. Therefore, specific objectives were defined as follows:

i) Characterize feed coals and respective ashes considering variations within space (sampling sites) and time (sampling campaigns) with focus on the target elements/morphotypes stablished for this research.

ii) Fractionate selected ash samples by particle size and magnetic proprieties and characterize them to assess potential trends on targeted elements/morphotypes that can be used in further concentration processes.

iii) Identify REE-bearing phases, for the optimization of further concentration processes and assessment of ashes REE-potential using the method described by Seredin and Dai (2012) and updated by Dai et al. (2017).

iv) Identification of the most promising sample for char recovery and develop a process to obtain a char concentrate without resorting to techniques that use dense liquids that may preclude its use in the targeted chemical reactions. Concurrently, optimizing the recovery of iron-rich morphotypes.

v) Characterize the char concentrate and assess the transformations induced by high temperature treatments (HTT).

vi) Undertake multidisciplinary preliminary trials with char and graphitized char as catalysts in electro-assisted reactions for green energy products (oxygen reduction reaction, ORR).

vii) Obtain magnetic concentrates (Fe-rich fraction), fractionate by particle-size, and carry detailed characterization.

viii) Carry out multidisciplinary preliminary trials to assess the feasibility to use magnetic concentrates as catalysts, instead of noble metals, in wastewater treatment (4-nitrophenol reduction reaction).

3. Overview of the thesis structure

The present thesis is structured in four main parts.

Part I includes a general approach to the subject, the main objectives, and the literature review.

Part II is divided in two main chapters; the first one includes the samples provenance with a brief description of Pego power plant and its operation, sampling methodology and nomenclature. The second chapter presents the analytical procedures used for characterization of coals and respective ashes, the char concentration process, the method used for demineralization and the procedure used for the heat treatment experiments (carbonization and graphitization).

Part III includes the results and discussion obtained during the research and discussion and it is divided in three main chapters. The first chapter includes the characterization of feed coals and respective combustion ashes and the detailed characterization carried out to evaluate the potential of the coal combustion ashes as a REE raw material. Both subjects are comprised in the following article in which the chapter was based on:

Santos, A.C.; Guedes, A.; French, D.; Futuro, A.; Valentim, B. Integrative Study Assessing Space and Time Variations with Emphasis on Rare Earth Element (REE) Distribution and Their Potential on Ashes from Commercial (Colombian) Coal. Minerals 2022, 12, 194. https://doi.org/10.3390/min12020194.

The second chapter includes results relative to the char concentration process, detailed char characterization and their potential use as graphitic precursor material. A manuscript with these results is being prepared. Additionally, an overview of the results of char application in the oxidation reduction reaction (ORR) is also included. The research was mainly carried out under the scope of Charphite project (ERA-MIN/0005/2015) - “Coal char as a substituting material of natural graphite in green energy technologies” and most of the results were included in collaborative articles listed below. Thus, in the subchapter regarding char characterization, samples from Charphite partners (Poland, Romania and South Africa) were included. Further information concerning the project can be consulted in the web site https://www.fc.up.pt/charphite/

Badenhorst, C. J., Wagner, N. J., Valentim, B. R. V., **Santos, A. C**., Guedes, A., Bialecka, B., Calus-Moszko, J., Popescu, L., Cruceru, M., Predeanu, G., Viljoen, K., S., Lázaro-Martínez, J. M., Abagiu, T. A., 2019. Char from coal ash as a possible precursor for synthetic graphite – Recent developments of the Charphite project. World of Coal Ash (WOCA) Conference, St. Louis (Missouri), 13th-16th May. In: http://www.flyash.info/2019/077-paper.pdf

Badenhorst, C.; **Santos, C.;** Lázaro-Martínez, J.; Białecka, B.; Cruceru, M.; Guedes, A.; Guimarães, R.; Moreira, K.; Predeanu, G.; Suárez-Ruíz, I.; Cameán, I.; Valentim, B.; Wagner, N. Assessment of Graphitized Coal Ash Char Concentrates as a Potential Synthetic Graphite Source. Minerals 2020, 10, 986. https://doi.org/10.3390/min10110986

Fernandes, D.M., Abdelkader-Fernández, V.K., Badenhorst, C.J., Białecka, B., Guedes, A., Predeanu, G., **Santos, A.C**., Valentim, B., Wagner, N., & Freire, C. (2021). Coal chars recovered from fly ash as promising electrocatalysts for oxygen reduction reaction. International Journal of Hydrogen Energy. https://doi.org/10.1016/j.ijhydene.2021.08.009

Nunes, M., Pereira, C., Guedes, A., **Santos, A.C**., Valentim, B., Freire, C., 2022. Assessment of coal fly ash char as a substituting material of graphite with electrocatalytic activity for the oxygen reduction reaction. Sustainable Chemistry and Pharmacy, 27, 100705. https://doi.org/10.1016/j.scp.2022.100705

The third chapter comprises the characterization of the Fe-bearing morphotypes collected by magnetic separation and respective size-fractions. A manuscript with these results is being prepared. Furthermore, it is made a resume of the results obtained regarding magnetic concentrates utilization as catalyst in 4-nitrophenol reduction reaction, some included in the following paper:

Kuźniarska-Biernacka, I., **Santos, A.C.,** Jarrais, B., Valentim, B., Guedes, A., Freire, C., Peixoto, A.F., 2022. Application of Fe-rich coal fly ashes to enhanced reduction of 4-nitrophenol. Cleaner Chemical Engineering, 2, 100019. https://doi.org/10.1016/j.clce.2022.100019

It should be noted that in cases where the data are already incorporated in articles that have already been published, the text presented is an adaptation of these. Furthermore, the description of the samples and analytical methodologies were relocated to the Part II.

Part IV encompasses a summary of the main conclusions of this research and outlines for further research.

4. Literature review

4.1. Rare earth elements (REE)

4.1.1. Nature, applications, and classification

The International Union of Pure and Applied Chemistry (IUPAC) defines the rare earth elements (REE) as a group of 17 chemical elements, which includes 15 lanthanoids (La, Ce, Pr, Nd, Pm, Sm, Eu, Gd, Tb, Dy, Ho, Er, Tm, Yb, Lu) plus Yttrium (Y) and Scandium (Sc) (Connelly, 2005). Promethium (Pm) has no stable isotopes, and it is only found in trace amounts in natural materials, and for this reason is mainly obtained synthetically (Castor and Hedrick, 2006). The 17 elements exhibit similarities in the valence electron that give them similar physicochemical properties (Fu et al., 2022). Nevertheless, Sc is frequently excluded from discussions about REE due to its ionic radius and electronic configuration (Samson and Chassé, 2018).

Despite the name, and apart from Pm, the REE are relatively abundant on the upper continental crust (UCC). Even the rarest element, Thulium (Tm), is more abundant than gold (0.0015 ppm) (Rudnick and Gao, 2014). Nevertheless, REE extraction can often be hindered by the concentrations found and the processes needed to extract elements with such similar ionic radii (Zhou et al., 2017).

The REE are strategic materials that play a key role in numerous economic segments such as defense, green energies, electronic and chemical industries (Haque et al., 2014). In particular to the European Union (EU), REE are fundamental for changing energy paradigm and to achieve carbon neutrality by 2050 given their requirement to the production of electric vehicles, wind turbines, solar panels and batteries (European Commission, 2019; European Commission et al., 2020) Due to their unique proprieties (electronic, optic, catalytic, and magnetic) the REE replacement in many industries applications is possible but difficult, and recycling is practically null, usually < 1% (European Commission et al., 2020; Huang et al., 2018; Klyucharev et al., 2013).

A wide range of classifications for REE have been developed and used, but the geochemical classification of REE in groups by (Seredin and Dai, 2012) has been considered more suitable to study the REE distribution in coals and ores: light (LREE — La, Ce, Pr, Nd, and Sm), medium (MREE — Eu, Gd, Tb, Dy, and Y), and heavy (HREE — Ho, Er, Tm, Yb, and Lu). Nevertheless, in some studies is given preference to the two-folded system which divides REE in LREE (La to Sm) and HREE (Eu to Lu) and Y is sometimes included in HREE (Eskenazy, 1999; Hower and Groppo, 2021; Wang et al., 2019).

4.1.2. REE in coal and combustion ashes

Coal, and especially coal combustion ashes, have been pointed out as promising sources of REE, and numerous studies were conducted concerning REE contents, modes of occurrence, and the extraction potential (e.g.,Blissett and Rowson, 2012; Dai et al., 2014c; Eskenazy, 1999; Franus et al., 2015; Hower et al., 2017c, 2017b; Lin et al., 2018, 2017; Liu et al., 2017; Mutlu et al., 2018; Rosita et al., 2020; Seredin and Dai, 2012; Taggart et al., 2016)

According to (Ketris and Yudovich, 2009), the average REE content (lanthanide plus Y and Sc) in world hard coals is 72.1 ppm, approximately 2.5 times lower than in upper continental crust (UCC: 183.14 ppm; (Rudnick and Gao, 2014), but several coal beds with concentrations above 0.1% have been identified and extensively studied (e.g., Dai et al., 2016b; Hower et al., 2016, 1999b; Seredin, 1996). Little attention has been given to commercial thermal coals (usually highly beneficiated). However, 76% of the coal traded in 2019 (1445 Mt) corresponded to thermal coal, and 10% (approx. 110 Mt) was imported by Europe (International Energy Agency (IEA), 2020). Indeed, the coals ash from commercial coals are potential source of REE and other elements since they already exist in a powder form without need to be mined.

The accumulation of REE in coals may occur at peat bog stage with the input of REE via surface waters and by incorporation and leaching of volcanic ashes but also via interactions with meteoric waters, commonly epigenetic, and hydrothermal fluids, at any stage (Seredin and Dai, 2012). The REE can be associated inorganically (REE-bearing minerals, substitution in crystal lattice, adsorbed in clays and dissolved in water pores) or organically (linked to carbon functional groups and organometallics) (Arbuzov et al., 2019; Dai et al., 2016a, 2016b; Eskenazy, 1999, 1987a, 1987b, 1987c; Finkelman, 1993; Finkelman et al., 2018; Hower et al., 2018, 1999b; Seredin, 1996; Zhao et al., 2015). In general, low rank coals with low ash have higher proportions of organically associated REE, specially HREE, while minerals are primary REE hosts in high-rank coals (Eskenazy, 1999, 1987a, 1987b, 1987c; Finkelman et al., 2018; Seredin and Dai, 2012). The mode of occurrence is important to understand the behavior and partitioning of REE during combustion, but the quantification of the REE organic/inorganically associated is not straightforward being often indirectly inferred from sequential leaching (Fu et al., 2022).

Due to the low size and amounts (often residual for determination by X-ray diffraction - XRD) of REE-bearing minerals in coals, the identification of these is often done via Scanning Electron Microscopy with Energy Dispersive Spectroscopy (SEM/EDS) (e.g., (Dai et al., 2017b; J. Liu et al., 2019), which include: monazite ((Ce,La,Nd,Th) PO_4), xenotime (YPO_4), zircon ($ZrSiO_4$), florencite $CeAl_3(PO_4)_2(OH)_6$), allanite ($(Ca,Ce,La,Y)_2(Al, Fe)_3(SiO4)_3(OH)$), apatite ($Ca_5F(PO_4)_3$), alunite supergroup minerals ($AD_3(XO_4)_2(OH)_6$), water-bearing REY phosphates (rabdophane group - $(REE,Ca,Th)(PO_4)\cdot H_2O$ and cherchite - $Y(PO_4)\cdot 2H_2O$), oxides (rarely), and carbonates (kimuraite - $Ca(Y,Nd)_2(CO_3)_4\cdot 6H_2O$, lanthanite - $(REE)_2(CO_3)_3\cdot 8(H_2O)$) or fluorocarbonates (bastnaesite - $(REE)CO_3F$) (Dai et al., 2016a; Seredin and Dai, 2012).

Since REE have low volatility, and in many cases occur in resilient minerals such as monazite, during coal combustion these are retained in the solid residue, i.e., fly ash, bottom ash, and slag (Clarke and Sloss, 1992; Meij, 1995; Ratafia-Brown, 1994). For this reason, the REE tend to be concentrated in coal ash, and the average concentration in world coal combustion ashes estimated by (Fu et al., 2022) is 435.45 ppm (Sc not included), which is about 2.4 times higher than the concentration in UCC (Rudnick and Gao, 2014).

Most of the research already made indicates that REE in coal combustion ash are mainly associated with the aluminosilicate glass (e.g., Bartoňová et al., 2018; Izquierdo and Querol, 2012; Kolker et al., 2017; Lin et al., 2018; P. Liu et al., 2019; Stuckman et al., 2018; Tang et al., 2019) This association can result from the incorporation of the REE-bearing phases or REE diffusion into the glass phase, but the distinction is highly dependent on the scale of the equipment being used (Fu et al., 2022). The REE also appear in discrete minerals (e.g., monazite) and the quantification of these phases is important to further extraction processes (Fu et al., 2022; Thompson et al., 2018). Less commonly REE occurs in nanosized particles within a carbonaceous material surrounding glass and Fe-rich particles (Hower et al., 2020b, 2017b)

The distribution patterns of REE in combustion ashes are comparable to the ashes obtained in laboratory, supporting non-partitioning during combustion (Dai et al., 2014c). However, it has been observed that REE can be unevenly distributed among the combustion products and their respective fractions, and numerous studies have reported lower REE contents in bottom ashes relatively to fly ashes (Dai et al., 2010; Ma et al., 2019; Wang et al., 2019; Wei and Song, 2020). Moreover, the LREE/HREE ratio tends to decrease towards the ESP back rows and with decreasing particle sizes, while the REE content increases (Blissett et al., 2014; Campbell et al., 1978; Hower et al., 2020a, 2017c, 2013; Lanzerstorfer, 2018a; Lin et al., 2017; Liu et al., 2017; Mardon and Hower, 2004; Rosita et al., 2020). The mechanisms behind the increase in HREE contents towards electrostatic precipitator back rows are fully understood but may comprise (Fu et al., 2022; Hower et al., 2020a): (1) capture of the REE-bearing phase by glass of variable grain size, chemistry, and structure and (2) the higher affinity of HREE with organic matter in coal may lead to HREE enrichment in finer fly ash particles through vaporization-condensation process during combustion.

4.1.3. Evaluation of coal combustion byproducts as raw material for REE

Although the economic assessment of coal combustion ash as secondary raw materials for REE should include the weighting of several factors such as modes of occurrence, extraction methods, environmental issues, and the relation between demand and supply, a preliminary assessment can be made considering the REE (lanthanoids+Y; Sc not considered) concentration and their individual composition (Seredin and Dai, 2012).

A cut-off of 1000 ppm of REO grade (REE oxides; Sc not included) valuable for recovery of REE was stablished based in extraction experiences carried out on combustion wastes from some Russian Far East coals (Seredin, 2004 in Dai et al., 2017a). The average REO in coal ashes is 485 ppm (Seredin and Dai, 2012) considering the mean values calculated by Ketris & Yudovich (2009). Therefore, coal ash whose REO concentration is about two times the average concentration has potential to be considered secondary raw materials for REE.

However, individual REE do not have the same importance and value for the industry. Based on the forecasts for demand and supply of each REE, Seredin, (2010) developed a new classification for a primarily evaluation of REE ores where REE elements are divided into critical (Nd, Eu, Tb, Dy, Y, and Er), uncritical (La, Pr, Sm, and Gd) and excessive (Ce, Ho, Tm, Yb, and Lu). In the same work the outlook coefficient index (C_{outl}) was also proposed for the assessment of the REE ore quality, and to suggest the method for determining how promising is the ore.

The C_{outl} is defined as the ratio between the relative amount of critical REY in total REY and the relative amount of excessive REY in total REY. The higher is the C_{outl} value, better the ore quality. The evaluation of an ore as a REY raw material is made through a plot of $REY_{def,rel}$ (percentage of critical elements in the total REY) vs. C_{outl} Seredin, (2010). Meanwhile, this method was updated by (Dai et al., 2017a) by applying the cut off of 1000 ppm of REE as oxides which is plotted against C_{outl}. Several studies already used those methods to a primarily evaluation of coal ash as raw material for REE (e.g., (Franus et al., 2015; Hower et al., 2018; Valentim et al., 2019; Wagner and Matiane, 2018).

4.2. Carbonaceous solid residue (char)

4.2.1. Nature

During the first stage of coal combustion, termed devolatilization, organic particles undergo through thermal decomposition (pyrolysis) in which depolymerization and decomposition of functional groups of the macromolecular network takes place. This process yields tar and light gases (responsible for a rich-fuel / oxygen-poor pyrolytic atmosphere), and a solid carbonaceous residue (char) is formed (Solomon et al., 1993, 1988).

The evolution of char structure during devolatilization is conditioned by several factors such as pyrolysis conditions, coal rank, and maceral composition (Alonso et al., 1999; Bend et al., 1992; Jones et al., 1985; Tsai and Scaroni, 1987; Yu et al., 2003). Bituminous coals upon heating usually undergo through a plastic stage (softening) and organic particles may experience an increase in porosity and volume (swelling), due to the pressure exerted by volatiles, and formation of vesicles (Dakič et al., 1989; Valentim, 2020; Yu et al., 2003). Nevertheless, thermoplasticity can be hindered in the presence of oxygen (Annamalai and Ryan, 1993; Tsai and Scaroni, 1987).

Depending on the coal rank, the maceral groups exhibit different behaviors during combustion, but the impact of coal maceral composition decreases as coal rank increases (Barranco et al., 2003; Crelling et al., 1992; Valentim, 2020). Low rank coals and anthracites generally do not undergo through softening and swelling as vitrinite macerals and reactive semifusinite of bituminous (medium rank) coals (Gray and Devanney, 1986; Hower et al., 2010).

The research work of Bend (1989) and Bend et al., (1992) using vitrinite-rich coals within different ranks have proved that char characteristics were related to attributes of vitrinite molecular structure which were associated to the coal rank. In these studies, it was also concluded that: (1) low rank coals (subbituminous to high volatile C bituminous) produce isotropic tenuinetworks, (2) up to semi-anthracite anisotropic cenospheres predominate with differences regarding wall thickness and porosity and (3) anthracites generate isotropic solid char. However, the combustion conditions, e.g., heating rate and pressure impacts the morphology of vitrinite-derived chars, as those parameters increase the wall thickness, porosity, and particle size follows (Alonso et al., 2001; Benfell et al., 2000; Gadiou, 2002).

Inertinite macerals were considered non-reactive for decades regarding coke manufacture, but when Gondwana coals were studied it was found that low to mediumreflective semifusinite may also undergo through a plastic deformation (as vitrinite) producing different char morphotypes during combustion, such as thin-walled and mixed morphotypes (Barranco et al., 2003; Bend, 1989; Bend et al., 1992; Borrego et al., 1997; Thomas et al., 1993a; Vleeskens et al., 1993). Liptinite is the most reactive maceral group since its lipidic compounds rapidly devolatilize during the early stages of combustion contributing to flame stability but leaving no liptinite-derived char (Suárez-Ruiz and Ward, 2008; Valentim, 2020).

4.2.2. Contents, distribution, and recovery

The term unburned carbon (UC) is frequently used in literature to designate the residual carbon found in the ash, which includes char and all organic materials containing carbon, such as soot and unreacted coal. Thus, the amount of char in coal combustion ash can only be properly addressed using optical microscopy since this technique is very effective not only for quantifying particles (in vol.%) but specially to identify and categorize them regarding its structure and optical proprieties (Lester et al., 2010; Suárez-Ruiz et al., 2017; Valentim, 2020). Other methods, such as loss on ignition (LOI), fixed carbon and elemental analysis (carbon forms), can be used to determine the amount of carbon in ash and estimate the char contents. The LOI is widely applied to estimate the UC and used as reference in the standard regarding fly ash application in concrete (ASTM C618, 2005), but it is known that can provide overestimated results due to breakdown of mineral phases, e.g., carbonates, and water physically absorbed (Brown, 1995; Fan and Brown, 2001; Hower et al., 2017a).

The amount of carbon remaining in the ash depends on the combustion system design and operating conditions (e.g., pulverization, combustion temperature and pressure) and coal characteristics (e.g., rank, macerals, volatile matter) (Bartoňová, 2015). According to Ahmaruzzaman, (2010), the LOI in fly ashes is usually in the range of 2-12 wt.% and ash generated from bituminous coal in general present higher LOI (0-15 wt.%) than the ones generated from sub-bituminous or lignite (0-3 wt.% and 0-5 wt.%, respectively). However, very high values were reported in the literature as is the case of Wulantuga fly ash presenting a LOI of 57 wt.%, which was attributed to the high inertinite content in feed coal (Dai et al., 2014b). The major implication of UC in fly ash is that a LOI greater than 6 wt.% classifies the fly ash unsuitable for being applied in concrete (ASTM C618, 2005). In this sense, the removal of carbon from ashes would be beneficial for their further application in concrete.

In general, fly ash present higher carbon contents than bottom ash (Bartoňová et al., 2007; Liu et al., 2017; Wilczyńska-Michalik et al., 2014), and fly ash collected in the back rows of ESP contains more carbon than the one from the first rows (Ahn and Lee, 2006; Mardon and Hower, 2004; Senneca, 2008; Suárez-Ruiz et al., 2007). Associations of unburned carbon with particle-size have been established in several studies: in pulverized-coal combustion (PFC) systems, the carbon content in fly ash tends to increase with increasing particle size (Hower et al., 1999c; Hurt and Gibbins, 1995; Kızgut et al., 2016; Lu et al., 2007; Querol et al., 1995; Senneca, 2008; Suárez-Ruiz et al., 2007) while in bottom ash the reverse is observed (Demir et al., 2008). In opposition, the fly ash derived from fluidized bed combustion exhibit a carbon distribution similar to PFC bottom ash (Bartoňová et al., 2007).

The recovery of char from coal combustion ash has been carried out employing methods that are usually applied for mineral processing (Bartoňová, 2015; Wills and Finch, 2016), which can be divided into two main types: dry and wet methods. The dry methods include size classification, incipient fluidization and triboelectrostatic separation. The advantage of these methods is that they do not leach of elements neither contaminate the char (Bartoňová, 2015). The wet methods include sink-float, froth flotation, oil agglomeration and acid digestion (Bartoňová, 2015).

According to Hower et al. (2017) only three of the referred techniques are suitable for industrial purposes: size classification, triboelectrostatic separation, and froth flotation. However, the method(s) selection must accomplish with the char utilization objectives, namely the final application that is intended to be given to the product obtained (Baltrus et al., 2002; Ban et al., 1997; Hurt and Gibbins, 1995; Rubio et al., 2008). In the current research char pores cannot be occluded since char will be used as electrocatalyst. Therefore, any method involving dense liquids, oil or frothing agents are excluded from char concentration tasks. However, to obtain nearly pure char, acid digestion is effective and the only method for removing the inherent or infilling mineral matter, but the strong acids used to dissolve silicates may change char characteristics (Bartoňová, 2015; Li et al., 2021).

Size classification (separation based in particle size) is widely used and can be very efficient to separate carbon if this is unevenly distributed among the size-fractions, especially when it is concentrated in the coarser fractions (Bartoňová, 2015; Hower et al., 2017a). For example, Wang and Li, (2005) obtained a concentrate with 85 wt.% of carbon from a fly ash with initial 5 wt.% of UC by using sieving (size-fraction not specified) and water washing. However, in the research of Hwang et al., (2002) the sieving to obtain 150 µm size-fractions from three fly ash samples did not allow to go beyond 41 % LOI.

Although it is less used, incipient fluidization is effective to concentrate char in coarser fractions of fly ash. Hurt and Gibbins, (1995) obtained concentrates with 75 wt.% of carbon from the size-fraction 90-180 µm fly ash with initial LOI in the range 5.4-10.8 wt.%.

Triboelectrostatic separation consists in the separation of the materials based in their electric proprieties and is already applied in industrial scale (Bartoňová, 2015). This technique has been proved to be effective for carbon concentration from ash (Ban et al., 1997; Cangialosi et al., 2009; Gray et al., 2002; Harja et al., 2008), but the charging proprieties can be affected by moisture (Baltrus et al., 2002). When combined with size-separation, triboelectrostatic separation is more effective and can provide higher concentration of carbon (Maroto-Valer et al., 1999).

Overall, the research works regarding char concentration have showed that higher concentrations can only be obtained by combining several methods in sequence (Bartoňová, 2015).

4.2.3. Char as raw material for synthetic graphite

Graphite is a carbon allotrope composed of stacked parallel layers of graphene with sp^2 atomic hybrid configuration, with an interlayer spacing of 0.335 nm for crystalline graphite (Franklin, 1951), and naturally found in metamorphic and igneous rocks (Anthony et al., 1990; Fitzer et al., 1995). Within graphene layers, each carbon is bonded to other three by high strength covalent bonds (524 kJ mol^{-1}) forming hexagons (Pierson, 1994). The hybridized fourth valence electrons pair with electrons from adjacent planes by van der Waals bonds (7 kJ mol^{-1}) (Pierson, 1994).

Graphite has good thermal and electrical conductivity, high sublimation point (3726 °C at 1 atm), low density (2.26 g/cm^3), high thermal resistance and lubricity, is resistant to corrosion, chemical inert and non-toxic (European Commission et al., 2020; Pierson, 1994). These properties place graphite in the forefront of technological applications, such as anode in batteries and fuel cells for electric vehicles and energy storage systems, essential to decarbonize the energy sector.

The EU imports 98% of the graphite that uses, and it is important to reduce the external dependence and ensure reliable supply chains (European Commission et al., 2020). The recycling of graphite is limited and only in few applications the graphite is recovered (Beyssac and Rumble, 2014). However, it is possible to substitute natural graphite by its synthetic alternative, other compounds, or other forms of carbon (Burgess-Clifford et al., 2009; Schobert and Song, 2002). Petroleum coke is one of the most used products to obtain synthetic graphite but given the directives towards the reduction of fossil fuels consumption, it is not the most appropriate option (Inagaki, 2001).

The process to produce synthetic graphite encompasses two steps: carbonization of the organic precursor and graphitization of carbonized residue. The carbonization process comprises slow pyrolysis of the organic precursor under an inert atmosphere at temperatures up to 1300 °C, which may result in devolatilization, dehydrogenation, condensation, and isomerization (Fitzer et al., 1995; Pierson, 1994). The material resulting from carbonization is essentially composed of turbostratic carbon (non-graphitizing carbon), i.e., individual stacks of Basic Structural Units (BSU) randomly orientated (Biscoe and Warren, 1942; Franklin, 1951; Oberlin, 1984; Pierson, 1994). The following thermal treatment at temperatures in the range 2200-3000 ºC (graphitization) transforms all or part of the turbostractic structure into a graphitic structure (Fitzer et al., 1995; Franklin, 1951; Oberlin, 1984; Rouzaud and Oberlin, 1989).

It was found that char concentrates from high-rank coal combustion fly ash present carbon contents >90 %, high degree of structural order, and a lamellar microtexture (Hurt and Gibbins, 1995), which is the most graphitizable form of carbon, mainly where a preferential planar orientation of the polyaromatic basic structural units (BSU) exists (Rouzaud et al., 1991). However, there are several factors that can affect the graphitization process and the quality of the final product such as the treatment temperature, the feed-coal, the mineral matter and the carbonaceous microtexture (Burgess-Clifford et al., 2009; Rodrigues et al., 2012, 2011b; Suárez-Ruiz and García, 2007). Meanwhile, the presence of inorganic components in coal ash, such as metallic species and silicon, can be an asset due to the catalyzing effect on the graphitization process (Rouzaud and Oberlin, 1989).

Limited research has been made concerning the utilization of char from coal combustion products as raw material to produce graphite-like materials (Cabielles et al., 2009, 2008; Cameán and Garcia, 2011). Cabielles et al., (2008, 2009) have graphitized char concentrates from fly ash and compared with commercial oil byproduct derived synthetic graphite used in several industrial applications (e.g., anode material in rechargeable lithium-ion batteries). Using a combination of techniques (XRD, Raman and TEM) these authors have found that crystalline parameters of graphitized char are similar to the ones observed for synthetic graphite. Besides that, confirmed that mineral matter (mainly iron and silicon) can improve the crystalline order of the final product. Later, Cameán and Garcia, (2011) studied the performance of coal fly ash char-based graphite materials as electrodes in lithium-ion batteries. It was verified that graphite-like materials prepared from char have a similar performance to the synthetic graphite being used.

Basically, one may say that char is a potential precursor for graphitized carbon for clean energy conversion technologies. Based on a series of electrochemical reactions, char catalyzed by novel electro-catalysts such transition metals (oxides) as alternatives to precious metals (Pt, Ir and Ru) may be of crucial importance in next decades due to the climate change and depleting of petroleum supplies (Benson et al., 2009; Jiao et al., 2015; Wolfschmidt et al., 2010; Wood et al., 2014).

4.3. Iron-bearing phases

4.3.1. Coals

Iron (Fe) is one of the main inorganic constituents of coal occurring in the percentage range (Finkelman, 1999; Raask, 1985). It may be associated with organic matter, particularly in low rank coals (Francis, 1961; Li et al., 2010, 2007), however it is frequently associated with mineral phases such as:

- Sulfides, namely pyrite (FeS_2), marcasite (FeS_2), pyrrhotite ($Fe_{(1-x)}S$), chalcopyrite ($CuFeS$), ferroselite ($FeSe_2$), eskebornite ($CuFeSe_2$), melnikovite (FeS_2+(As,FeS,H_2O)) and mispickel ($FeS_2 \cdot FeAs_2$) (Raask, 1985; Ward, 2016).
- Sulphates resultant from oxidation of pyrite such as coquimbite ($Fe_2(SO_4)_3 \cdot 9H_2O$), melanterite ($FeSO_4 \cdot 7H_2O$), rozenite ($FeSO_4 \cdot 4H_2O$), szomolnokite ($FeSO_4 \cdot H_2O$), jarosite ($(Na,K)Fe_3(SO_4)_2(OH)_6$), halotrichite ($FeAl_2(SO_4)_4 \cdot 22H_2O$) and roemerite ($FeSO_4 \cdot Fe2(SO_4)_3 \cdot 14H_2O$) (Ehlers and Stiles, 1965; Gluskoter, 1977; Gruner and Hood, 1971; Kossenberg and Cook, 1961; Rao and Gluskoter, 1973).
- Silicates (clays), for instance illite $(K,H_3O)(Al,Mg,Fe)_2(Si,Al)_4O_{10}[(OH)_2,(H_2O)]$ and chlorite ($(MgFeAl)_6(AlSi)_4O_{10}(OH)_8$), namely chamosite (Dai et al., 2014a; Dai and Chou, 2007).
- Carbonates such as ankerite ($CaCO_3 \cdot FeCO_3$), usually epigenetic, and siderite ($FeCO_3$) that is mainly syngenetic (Golab et al., 2013; Permana et al., 2013; Stach et al., 1982).
- Iron oxides like magnetite (Fe_3O_4), hematite (α-Fe_2O_3), limonite ($Fe_2O_3 \cdot H_2O$) and goethite (α-FeOOH) (Raask, 1985).

During coal combustion, the Fe-bearing phases within organic matrix undergo over thermochemical conversions and may coalesce with products derived from aluminosilicates decomposition to form melt droplets of variable composition (FeO–SiO_2–Al_2O_3–CaO–MgO) that later will cool and crystallize (Sokol et al., 2002, 2000; Tomeczek and Palugniok, 2002). The excluded Fe-bearing minerals also undergo through transformations, although the temperatures reached are generally not as high as those of included minerals. However, the contact with other minerals is unlikely (Bryers, 1986; McLennan et al., 2000; Tomeczek and Palugniok, 2002). The transformations experienced by included/excluded minerals may follow similar paths, as verified for pyrite and siderite – the most common Fe-bearing minerals in coals, but oxidation reactions in the included minerals are hindered until the complete burnout of char (McLennan et al., 2000).

The excluded pyrite decomposes at 497-697 ºC into pyrrhotite and gaseous sulfur (S_2), then pyrrhotite melts at approximately 1100 ºC and may oxidize to magnetite or wüstite (FeO). These phases will further melt and form an Fe-oxysulphide. Under oxidizing conditions hematite will be formed, while under reduction conditions the Fe-oxysulphide prevails (McLennan et al., 2000; Srinivasachar and Boni, 1989). Experiments with Upper Freeport bituminous coal containing excluded pyrite showed that it may fragment and originate smaller magnetite particles (Srinivasachar et al., 1990). Excluded siderite decomposes into wüstite at around 1400 ºC that holds in reduction conditions. However, in oxidizing conditions wüstite may oxidize to magnetite or hematite (McLennan et al., 2000).

4.3.2. Ashes

Fisher et al., (1978) recognized opaque spheres under transmitted light microscopy as a morphotype from fly ashes and inferred to be composed of magnetite and other Fe oxides. However, the term “ferrosphere” was proposed by Lauf, (1982) and Lauf et al., (1982) to describe the Fe-rich morphotypes from coal ashes distinguished for their high reflectance when observed in cross-section under reflected light microscopy. Ever since, other classifications were proposed based in parameters such as iron oxidation state, chemical composition, and surface topography (microstructure) (Anshits et al., 2011; Valentim et al., 2018; Vassilev and Vassileva, 1996; Zhao et al., 2006).

Vassilev and Vassileva (1996) classified the Fe-morphotypes into two classes: (a) ferrospheres, mainly composed by dendrites, lamellae, and skeleton magnetite and less often hematite and magnesioferrite ($MgFe_2O_4$) and (b) ferrispheres, spheres with skeletal hematite and limonite.

Zhao et al. (2006) used the Fe content locally determined by field emission SEM equipped with EDS and distinguished four groups: (a) ferriooxides, Fe >75 %, (b) aluminosilicate-bearing ferrooxides, 75% > Fe ≥ 50%, (c) high-ferriferous aluminosilicates, 50 %> Fe ≥25, and (d) ferroaluminosilicates Fe <25 %, More recently, Valentim et al., (2018) systematizing the nomenclature of morphotypes petrographically classified as undifferentiated inorganics and defined ferrospheres as morphotypes with Fe as the distinctive element in the EDS spectra and dendrites as the distinctive patterns. Furthermore, morphotypes presenting euhedral magnesioferrite crystals as the ones observed by Anshits et al. (2011) and Sokol et al. (2002) were classified separately as magnesiaferrospheres (Valentim et al., 2018).

Zhao et al., (2006) have classified the ferrospheres according to their structure into seven groups: sheet, dendritic, granular, smooth, ferroplerospheres, porous, and molten drop. Later, Anshits et al., (2011) verified that as the Fe_2O_3 content increased (36-92 wt. %) the structure of the ferrospheres would change as follows: porous, glass-like, dendritic, skeleton-dendritic, and block-like. The increase in the glass phase from skeletal to dendritic is explained by a decrease in spinel-forming ions (Fe^{2+} and Fe^{3+}) in the melt accompanied by an increase in the oxidation potential and ferrite complexes $[Fe_3{+}O_2]^-$ and $[Fe_2^{3+}O_5]^{4-}$ (Anshits et al., 2019, 2018).

Sokol et al., (2002) attributed dendritic and skeletal morphologies to a crystallization under non-equilibrium conditions, i.e., supercooling, as is usually observed in magmatic rocks (e.g., basalts). Other authors assume that it is due to the combination of several factors related to the formation conditions from coal chemical composition to the cooling conditions (Blaha et al., 2008; Ramsden and Shibaoka, 1982). Nevertheless, several systematic research done in narrow fractions of magnetic concentrates regarding the relationship between major elements and specific morphologies have been made and show that certain minerals may act as precursors (Anshits et al., 2021, 2020, 2019, 2018; Sharonova et al., 2015a, 2013). Nevertheless, the correlation between the content of Fe in coals and the amount of ferrospheres found in fly ashes suggest that all Fe-bearing phases from coals contribute to the formation of those morphotypes (Kizil'shtein et al., 1995 *in* Sharonova et al., 2013).

The presence of Fe in coal combustion ashes can preclude its reutilization and difficult extraction processes of valuable elements (e.g., Nugroho et al., 2019). Furthermore, potential toxic elements, such as Cd, Cr and Mn, are commonly enriched in Fe-rich fractions and its removal might decrease the potential risks of pollution during ash utilization and landfill (Hansen et al., 1981; Hower et al., 1999a; Hulett et al., 1980; Kukier et al., 2003; Lu et al., 2009; Strzałkowska, 2021; Vassilev et al., 2004a; Vassilev and Vassileva, 1996).

Ferrospheres can be recovered as magnetic concentrates (MC) from coal ashes, usually yielding between 0.5 to 18.1 wt.% (Bibby, 1977; Lu et al., 2009). The Fe content may range between 23 - 66 wt.% and particle size can reach up to a few hundred micrometers (up to 300 µm) although greater yields are generally found in fractions <100 µm (Hansen et al., 1981; Hower et al., 1999a; Lauf et al., 1982; Querol et al., 1995; Sokol et al., 2002; Vassilev et al., 2004a).

The chemical composition of bulk MC may vary in a broad range as one may see in the results from (Vassilev et al., 2004a) where MC were collected from four ashes derived from Spanish coals and one from an imported Gondwana coal (not specified): Fe_2O_3 28.7-42.4 wt.%, SiO_2 31.1-39.7 wt.%; Al_2O_3 16.0-20.6 wt.%. Magnetic concentrates may contain several Fe-bearing minerals and phases such as magnetite (Fe_3O_4), hematite (Fe_2O_3), magnesioferrite ($MgFe_2O_4$), maghemite (Fe_2O_3), martite (Fe_2O_3), ferrian spinel, wüstite (FeO) and Ca and Ca–Mg ferrite spinels and Fe-bearing glass (Hower et al., 1999a; Kukier et al., 2003; Querol et al., 1995; Sokol et al., 2002; Strzałkowska, 2021; Valentim et al., 2018; Vassilev et al., 2004a; Zhao et al., 2006). Furthermore, MC contain non-magnetic phases such as aluminosilicate glass, char, quartz and mullite. The lack of purity primarily arises from the ferrospheres glass matrix but can also be related to the occurrence of agglomerates and limitations on the separation technique (Hower et al., 1999a; Valentim et al., 2009b).

The MC with variable composition and proprieties may have limited applications and several research have focused on gathering narrow fractions from ferrospheres with stable compositions and microstructures for further application as a valued added product (Anshits et al., 2016, 2000; Kirik et al., 2019; Vereshchagin et al., 2012; Vereshchagina et al., 2016). The beneficiation techniques commonly used to obtain the narrow fractions are size classification and purification in a pulsating ascending water stream (Anshits et al., 2019, 2020). It was shown that concentrates of ferrospheres with 30-80 wt. % of Fe_2O_3 have high catalytic activity for the deep oxidation of methane (Anshits et al., 2011), and those containing >83 wt.% of Fe_2O_3 are efficient for oxidative coupling of methane (Vereshchagin et al., 2012).

Several research has been carried out regarding the application of coal combustion ashes in wastewater treatment, namely in oxidative degradation of pollutants via photocatalysis or (photo)Fenton process (Mushtaq et al., 2019). However, few research was made regarding ashes application in catalytic reduction of 4-nitrophenol (4-Ph) (Park et al., 2020; Park and Bae, 2019, 2018), one of the most common contaminants found in wastewaters (Nemanashi and Meijboom, 2013). The magnetic fraction of fly ashes have been applied as support for catalysts (Pd) given the ease of retrieval using a magnet (Park and Bae, 2019). Nevertheless, it is known that iron oxides may act as catalysts in the reduction reaction of 4-NPh in the presence of sodium borohydride ($NaBH_4$; Bae et al., 2017; Mandlimath and Gopal, 2011).

Several variables can affect the catalytic behavior of ferrospheres, such as the amount of amorphous phase which can block the active sites and incorporation of elements in spinels, being therefore their characterization extremely important before its application (Anshits et al., 2011).

Part II | Samples and Methodologies

1. Samples

1.1. Provenance

The samples used in the current study were provided by the coal-fired thermoelectric power plant of Pego, located in Abrantes, about 150 Km NE from Lisbon, Portugal. This power plant was closed in 2021 after the Portuguese government decision to reduce CO_2 emissions.

At the time of the sampling, Pego power plant was composed by two identical groups to generate electricity, with a combined electrical power of 628 MW (314MW per unit). Each group was equipped with a pulverized coal-fired boiler, a turbine-alternator, a main transformer with its own supporting infrastructure including cooling tower, water supply and exhaust system. The natural circulation boilers could burn up to 108 ton/h of pulverized coal, generating at maximum continuous rating more than 950 ton/h of superheated steam at 535 °C and 167 bar. All the water used in the power plant came from the Tejo River. The water extraction system and the station for its treatment were shared by both groups.

The atmospheric emissions were minimized by selective catalytic reduction (SCR), electrostatic precipitators (ESP) and wet flue gas desulphurization (FGD), keeping the levels of NO_x, particles and SO_2 under the legal limits (Decreto-Lei n.o 127/2013). The SCR system (1 per boiler) reduced the NOx emissions about 75% through a chemical reaction with ammonia (NH_3) in the presence of a catalyst based on titanium dioxide and vanadium pentoxide. The ESP removed the solid fraction in suspension on flue gas by using electrical forces to move particles from the air stream to the collection plates. Each group has two ESP with an efficiency per unit of 99.8 %. The FGD system (1 per boiler) removes about 90% of the SO_2 from the flue gas by the reaction with a limestone ($CaCO_3$) slurry.

In Figure II - 1 it is shown a simplified scheme of the electricity production process at Pego thermoelectric power plant. The coal was imported from other countries, such as Colombia, and delivered to the power plant by train from the port of Sines, and then stored in stockpiles for prompt use (active) and/or reserve (passive). After, the coal was removed by bucket wheel, stacker/reclaimer and transported through conveyor belts to the boiler bunkers. From those, it was taken to the coal feeders and transported to the mills where it was ground and mixed with primary air (preheated by the boiler exhaust gases) which has a double function of drying the coal at the entrance and transport it as powder to the burners. The coal combustion heated the water pipped inside the boiler, generating superheated steam. The steam was pipped through a turbine that is linked to a generator whose function is to convert the mechanical energy associated with the motion of the shaft into electrical energy. In each group composing the coal-fired power plant there are four turbines (1-high, 1-medium, and 2-low pressure) to maximize the efficiency in the energy production. After crossing the turbines-generator system, the vapor is directed to the condensers where it was cooled and converted to pure water. The condensers were cooled by a close circuit using water from Tejo River.

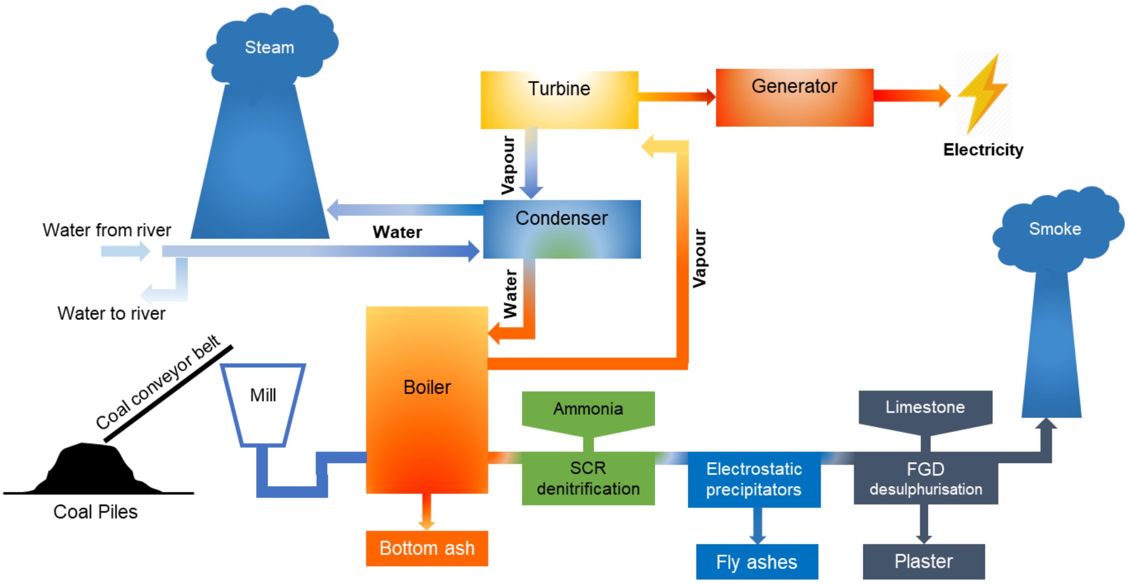

Figure II - 1. Operation Scheme of the Pego thermoelectric power plant.

During the coal combustion process, ashes were generated. The bottom ashes (BA) fall into the bottom of the boiler and were cooled by water. They were then transported to a silo via a conveyor belt and taken directly to landfill by trucks. The remaining ashes (fly ashes) were dragged by the flue gas. Some of them were captured on the economizer (ECO) and the regenerative air heaters (RAH) cyclones but the vast majority were captured on the electrostatic precipitators positioned after the denitrification system (SCR). The FA was then directed to an intermediate silo, designated as production silo, where samples were daily collected to determine the unburned carbon content, through the Loss-on-ignition (LOI) method (ASTM D7348, 2013). When the LOI was below 7 wt.% the ashes were directed to the silo for sale (cement industry) otherwise were landfilled along with BA. Overall, at the time of this study sampling, fly ash represented 92 % of the total ashes produced on Pego power plant (2 % captured on ECO/RHA and 90 % on the ESP) while the bottom ashes represented only 8 % (personal communication, July 2017).

1.2. Sampling

Table II - 1 lists the samples selected for the current study. The sampling was accomplished by the power plant personnel under the supervision of the engineer in charge of the coal-fired power plant, Jorge Henriques. Over a period of a year, samples of feed coal (C), fly ash (FA), and bottom ash (BA) were collected approximately every three months from Group 1 except for the third campaign, which was conducted on Group 2 (Figure II - 2). Fly ash was collected from several locations in each sampling campaign, including from the economizer (ECO), different electrostatic precipitator (ESP) hoppers, and silos. During the first sampling campaign, FA samples from both ESPs of Group 1 were collected in order to assess the possible lateral variations (Figure II - 2).

Table II - 1. General information about the samples used for the current study.

Sample identification	Campaign	Type of material	Description	
S1-C	dez/16	Coal	Cerrejon 254	
S1-BA		Bottom ash	Bottom ash silo	
S1-Eco		Fly ash	Economizer	
S1-ESP12		Fly ash	ESP	Hopper 12
S1-ESP15		Fly ash		Hopper 15
S1-ESP22		Fly ash		Hopper 22
S1-ESP25		Fly ash		Hopper 25
S1-ESP32/42		Fly ash		Hopper 32+42
S1-ESP35/45		Fly ash		Hopper 35+45
S1-Silo		Fly ash	Silo for sale	
S2-C1	mar/17	Coal	Calenturitas 244	
S2-C2		Coal	Drummond 257	
S2-Eco		Fly ash	Economizer	
S2-ESP12		Fly ash	ESP	Hopper 12
S2-ESP22		Fly ash		Hopper 22
S2-ESP32/42		Fly ash		Hopper 32+42
S2-Silo		Fly ash	Silo for sale	
S3-C1	sep/2017	Coal	Cerrejon 263	
S3-C2		Coal	Calenturitas 262	
S3-BA		Bottom ash	Bottom ash silo	
S3-ESP12		Fly ash	ESP	Hopper 12
S3-ESP22		Fly ash		Hopper 22
S3-ESP32/42		Fly ash		Hopper 32
S3-Silo		Fly ash	Production silo	
S4-C1	dez/17	Coal	Calenturitas 265	
S4-C2		Coal	Cerrejon 266	
S4-BA		Bottom ash	Bottom ash silo	
S4-Eco		Fly ash	Economizer	
S4-ESP12		Fly ash	ESP	Hopper 12
S4-ESP22		Fly ash		Hopper 22
S4-ESP32/42		Fly ash		Hopper 32
S4-Silo		Fly ash	Production silo	

C – Coal; BA – Bottom ash; Eco – Economizer; ESP - Electrostatic precipitator

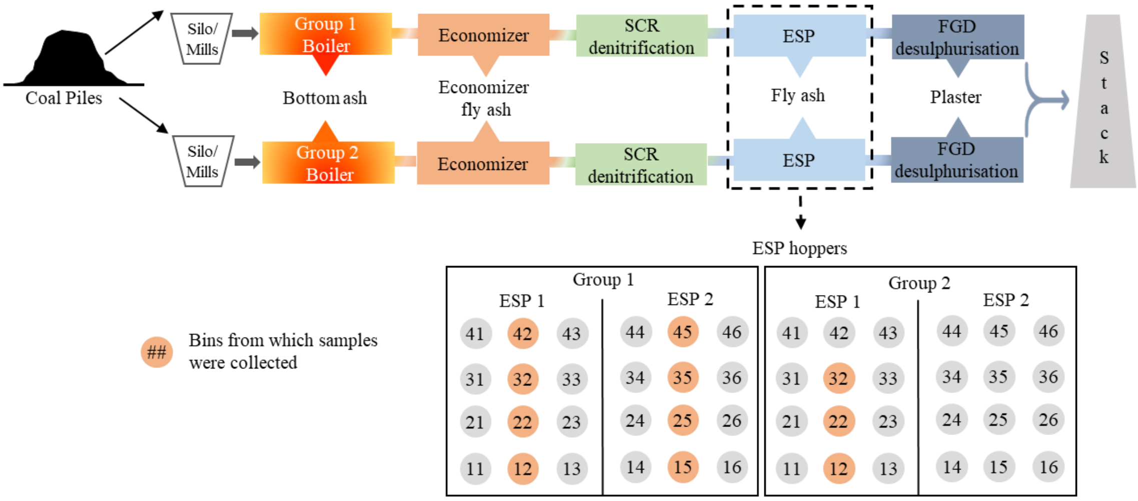

Figure II - 2. Simplified scheme of Pego power plant and ESP arrays, with indications of bins numbers where the samples were collected.

1.3. Nomenclature

The nomenclature of bulk samples was made by merging the sampling campaign ID (SX, where X corresponds to the number of the campaign) and the short form corresponding to the type of material and/or location (C: coal; BA: bottom ash; ECO: economizer; ESP: Electrostatic precipitator). In the case of the FA from the ESP, the number of the ESP bin associated to a hopper from which the sample was collected was added to the sample label.

The size-fractions obtained by sieving were identified by adding the corresponding particle size, e.g., S1-ESP12 <25 μm, plus “ws” in the cases where wet sieving was used. Fractions obtained by magnetic separation were designated as magnetic concentrates and identified as “MC”. Depending on the magnet used Fe or Nd was added, e.g., Fe-MC from ESP FA. The tailings from magnetic separation were identified as “TL”.

The char concentrate was designated as “CC” and the respective demineralized char concentrates as “CD”. The letter “C” and “G” were added to designate samples that were carbonized and carbonized plus graphitized, respectively. Since the char concentrate obtained within this thesis was compared with other three char concentrate samples, acronyms corresponding to the country of provenance were added: Portugal, PT (char obtained within this thesis), PL (Poland), Romania (RO) and South Africa (SA).

2. Analytical methodologies

2.1. Optical microscopy

The reflected light optical microscopy analyzes were carried out at Institute of Earth Sciences – Porto Pole, Faculty of Sciences, University of Porto.

All analyzes were made on polished blocks with randomly oriented particles prepared following the standard procedures of (ISO 7404-2, 2009) using a Microscope Leica DM4500P (Leica Microsystems GmbH, Wetzlar, Germany) equipped with a ×50 oil objective (combined magnification of ×500), controlled by the software Fossil (Hilgers Technisches Büro, Königswinter, Germany).

In the case of the ash samples preparation for petrographic analysis the standard procedures of ISO 7404-2, (2009) were adapted. The polished blocks were cut in two halves perpendicular to the top and bottom of the blocks, and the new surfaces polished for analysis. This adaptation is necessary due to grains density segregation while the resin cure.

The determination of the maceral group composition of the feed coals was performed by point-counting, following the standard (ISO 7404-3, 2009) and nomenclature guidelines from the International Committee for Coal and Organic Petrology (ICCP) (ICCP, 2001, 1998; Pickel et al., 2017). The determination of the mean random reflectance (Rr%) of vitrinite as a parameter for the rank determination, (ICCP, 1998; ISO 7404-5, 2009).

The determination the morphotypes composition via point-count analysis was also conducted on bulk coal combustion ashes and demineralized char concentrates using the fly ash simplified classification and nomenclature in Hower et al., (2005) and Hower, (2012), respectively, and for char the system developed by the ICCP (Suárez-Ruiz et al., 2017).

Moreover, optical microscopy was used to characterize the reflectance indicating surface (RIS) of chars and assess potential changes derived from carbonization, demineralization, and graphitization. Before each reflectance measurement run, calibration was made using a 5.4 % reflectance standard (Klein & Becker GmbH & Co. KG, Obertstein, Germany). To minimize operator bias, the measurement was always made at the particle closest to the intersection of the crosshairs.

Three reflectance measurements were made in each particle by rotating the microscope stage 45º (R1, R2 and R3; (Ting, 1981) and minimum and maximum apparent reflectance (R'max% and R'min%, respectively) were calculated using Ting's equations (Ting, 1981, 1978):

$$R'max = (R1 + R3)/2 + (((R1 - R2)^2 + (R1 - R3)^2)/2)^{1/2}) \quad \text{(Equation 1)}$$

$$R'min = (R1 + R3)/2 - (((R1 - R2)^2 + (R1 - R3)^2)/2)^{1/2}) \quad \text{(Equation 2)}$$

From the values obtained, RIS main axes (R_{MAX}%, R_{INT}%, and R_{MIN}%) were determined according to the procedures established by (Kilby, 1991, 1988) later modified by (Duber et al., 2000) and then used to calculate the parameters R_{am}, R_{ev}, and R_{st} using the equations 3-5.

$$R_{ev} = \sqrt[3]{R_{MAX}\% \times R_{MIN}\% \times R_{INT}\%} \quad \text{(Equation 3)}$$

$$R_{am} = \sqrt{a^2 + b^2} \quad \text{(Equation 4)}$$

$$R_{st} = 30 - arctan\left(\frac{a}{b}\right) \quad \text{(Equation 5)}$$

Where $a = [1/3 - R_{MIN} / (R_{MAX} + R_{INT} + R_{MIN})]/\cos(30) - b\tan(30)$ and

$b = R_{MAX} / (R_{MAX} + R_{INT} + R_{MIN}) - 1/3.$

The R_{ev} characterizes the structure of BSU (Basic structural Units) while R_{st} and R_{am} gives information about the texture (spatial arrangement of BSU) (Duber, 2000). Additionally, anisotropy parameters such as bireflectance (B, R_{MAX} - R_{MIN}) and ((R_{MAX}%-R_{MIN}%)/R_{MAX}%) (González et al., 2004; Suárez-Ruiz and García, 2007) were calculated.

2.2. Scanning electron microscopy with energy dispersive spectroscopy (SEM/EDS)

The SEM/EDS analysis were performed at the Materials Centre of the University of Porto, Portugal (CEMUP) using a FEI Quanta 400 FEGESEM/EDAX Genesis X4M. The SEM was operated at 15 kV in high vacuum mode with a manual aperture and an instrument-specific 4.5 beam spot-size setting. To gather high-quality analysis under vacuum conditions, the samples (polished block and powder) were previously sputter coated with a thin layer of carbon (~10 nm) and fixed to the support with carbon double-sided adhesive tape. The backscattered electron (BSE) mode was mainly used for detailed imaging of the inorganic phases internal structure and its identification since it is highly sensitive to the changes in atomic number and where necessary X-ray microanalysis (EDS) was made for semiquantitative chemical analysis, and the interpretation of the acquired spectra was performed through comparison with a EDS spectra data basis published by (Severin, 2004) regarding the spectrum of known minerals. The secondary electron (SE) mode was mainly used for detailed imaging of particles surface (topography and pores).

Tracking of REE-bearing phases in polished blocks from coal combustion ashes (FA and BA) was performed according to the method proposed by Valentim et al., (2019) since it has been proven effective for the identification of the REE-bearing phases. However, this method was applied only on the ashes from the first sampling campaign (S1) since it is tedious and expensive.

Char particles were described combining the terminology from Vleeskens et al., (1994), 1990), Menéndez et al., (1993) and Valentim et al., (2009b).

2.3. Chemical analysis

Proximate (moisture, ash, and volatile matter) and ultimate (carbon, hydrogen, and nitrogen) analyses and calorific value of the feed coals were carried out in the certified laboratory of the Pego power plant as part of an internship. Moisture (M), ash (A), and volatile matter (VM) of the feed coal samples were determined using a Thermogravimetric Analyzer, model TGA 701, according to the ASTM standard (ASTM D7582, 2015), and fixed carbon (FC) calculated by difference. The C, H, N and S concentration was determined using LECO equipment (Leco Corporation, Michigan, USA) following ASTM standards (ASTM D4239, 2017; ASTM D5373, 2016). Oxygen was calculated by difference. The calorific value was determined using a AC500 Isoperibol Calorimeter (Leco Corporation, Michigan, USA).

The proximate analysis of the coal combustion ashes were performed following ISO standards (ISO, 2013a, 2010a, 2010b). The data was converted to different basis following the standard guidelines on ISO 1170 (2020) and the fixed carbon calculated according to ISO 17246 (2010). The adoption of ISO standards for the ashes was supported by the fact that further analyses performed at Faculty of Sciences of University of Porto (FCUP) by this standard could be comparable. The ultimate analysis from char concentrates were carried out at Chemistry Department from University of Aveiro using a Truspec Micro CHNS 630-200-200 (Leco Corporation, Michigan, USA).

The determination of major and minor oxides, loss-on-ignition (LOI), minor and trace elements, total sulphur (S_t) and carbon forms (organic, inorganic, and graphitic) was carried out at the Bureau Veritas Minerals, Vancouver, Canada (Accredited laboratory by ISO/IEC 17025, 2017, using Inhouse Certified Reference Material or in its absence samples are certified against internationally certified reference materials such as CANMET and USGS standards).

For major and minor oxides, the samples were previously digested via lithium borate fusion (XF702). LOI was determined by roasting a sample split at 1000 °C. Total sulphur (S_t) and carbon (C_{tot}), graphite carbon (C_{gra}) and inorganic carbon (C_{Co2}) were determined using Leco equipment. For the total carbon and sulphur determination an induction flux is added to the sample which is then ignited in an induction furnace. The gas released are read in an infrared spectrometric cell and attributed to carbon and sulphur in all forms (TC001 and TC002). Graphite carbon is determined in the residue after samples being leached with HCl followed by ignition at 500 °C (TC005) while inorganic carbon is determined by directly measuring the CO_2 gas evolved into the LECO analyser in a prepared sample split leached with perchloric acid (TC006). Organic carbon (TC007) content is determined by difference wherein: Organic Carbon (C_{org}) = $C_{tot} – C_{CO2} –C_{gra}$.

Minor and trace elements were determined via Inductively coupled plasma mass spectrometry (ICP-MS). For rare earth and refractory elements determination, it was made a fusion in $LiBO_2/Li_2B_4O_7$ flux followed by dissolution with ACS grade nitric acid (LF100), since it enables the dissolution of the most resistant phases and a better recovery of those elements (Godoy et al., 2001). Nevertheless, high fusion temperatures can lead to the loss of volatile elements, such As, and for this reason, a multi-acid digestion was used for the determination of the remaining elements (MA200) in magnetic concentrates and respective fractions.

The REE contents were normalized to the upper continental crust (UCC) to eliminate the Oddo–Harkins effect (zig-zag shape) and to provide information about the enrichment patterns and anomalies of individual elements that can be used to assess the REE differentiation during coal combustion (Dai et al., 2016a, 2014c; Fu et al., 2022; Liu et al., 2017). Thus, the values were normalized to Upper Continental Crust (UCC), N, and the decoupling of Ce, Eu, and Gd was quantified according to the equations (Bau and Dulski, 1996; Dai et al., 2016a; Rudnick and Gao, 2014):

$$\mathrm{Eu_N/Eu_N^*} = \mathrm{Eu_N}/[(\mathrm{Sm_N} \times 0.67) + (\mathrm{Tb_N} \times 0.33)] \qquad (6)$$

$$\mathrm{Ce_N/Ce_N^*} = \mathrm{Ce_N}/[(\mathrm{La_N} \times 0.5) + (\mathrm{Pr_N} \times 0.5)] \qquad (7)$$

$$\mathrm{Gd_N/Gd_N^*} = \mathrm{Gd_N}/[(\mathrm{Sm_N} \times 0.33) + (\mathrm{Tb_N} \times 0.67)] \qquad (8)$$

2.4. X-ray diffraction (XRD)

The identification of the mineralogical phases and quantification of the amorphous phase in coal low temperature ashes, coal combustion ashes and magnetic concentrates was carried out by XRD in the School of Biological, Earth & Environmental Sciences – University of South Wales (Australia).

Prior to X-ray diffraction analysis, coal samples were ashed in a low temperature radio-frequency oxygen plasma asher. Ashing is done at a low temperature (typically ~120 ˚C) in a stream of activated oxygen under a partial vacuum under an applied radio frequency field. The activated oxygen reacts with the organic matter, leaving a mineral matter residue. The advantage of the technique is that the mineral matter is largely unaffected by the ashing process due to the low temperature of the ashing process. Samples are ground to a nominal particle size of 212 µm and approximately 1 g is weighed out into each of two petri dishes. Samples are weighed during the ashing process until a constant weight is achieved, indicating that all organic matter has been removed. No prior treatment of the ash samples was necessary.

For XRD analysis, each sample was lightly pressed into a sample holder. Samples were run a Panalytical Empyrean X-ray diffractometer (Malvern Panalytical, Worcestershire, UK), using cobalt K-alpha radiation at tube settings of 45kV and 40mA. To minimize the effects of sample inhomogeneity, the sample was spun throughout the data acquisition. The pattern was acquired over an angular range from 3˚ 2ө to 80˚ 2ө at a step interval of 0.013˚ 2ө for a scan time of 45 min.

Prior to quantitative analysis, a qualitative phase identification was carried out using Panalytical HighScore Plus in conjunction with the ICCD pattern diffraction database. Quantitative analysis was performed using Siroquant™ (Sietronics Pty. Ltd., Canberra, Australia), a least squares full pattern matching Rietveld procedure developed by CIRO (Taylor, 1991). This procedure has the advantage that the full XRD pattern is used for analysis, rather than a subset of peaks in non-Rietveld procedures. An added advantage of Siroquant is that it makes use of what are termed “observed HKL files” for analysis of poorly crystalline phases such as clays and determination of amorphous content. For this study a calculated pattern of metakaolinite was used to determine the amorphous content in the ash samples. To check the validity of this procedure, a subset of samples was measured using the procedure described by (Ward and French, 2006) in which a known amount of alumina is weighed into the sample and the calculated weight of the alumina was sued to determine the amorphous content of the sample. The results of this initial study showed that the use of the metakaolinite observed pattern was a valid approach that could be used for analysis of subsequent samples.

To determine carbon structural order and crystalline parameters (Lc, La and d_{002}) in char concentrates and demineralized graphitized chars, XRD analysis were carried out at Instituto de Ciencia y Tecnología del Carbono (Oviedo, Spain). The XRD diffractograms were recorded using a Bruker D8 Advance powder diffractometer (Bruker, Billerica, MA, USA) equipped with a monochromatic Cu KαX-ray source and an internal silicon powder standard. Diffraction data were collected by step scanning using a step size of 0.02° 2θ and a scan step of 2s. For each sample, three diffractograms were obtained, employing a different representative batch of samples for each run. The mean interlayer spacing, d_{002}, was determined from the position of the (002) peak by applying Bragg's equation (Equation 9). The crystallite sizes, Lc and La, were calculated by measuring the full width at half maximum (FWHM) of the (002) and (110) peaks, respectively, and by applying Scherrer's equation (Equation 10). The average number of aromatic layers <N> in the stack was determined following the procedure described by (Laggoun-Défarge et al., 1994) (Equation 11). The broadening of the diffraction peaks due to instrumental factors was corrected by using a silicon standard. The d_{002} values show standard errors lower than 0.1 %.

$$d_{002} = \frac{\lambda}{2sin\theta} \quad \text{(Equation 9)}$$

$$L = \frac{K\lambda}{\beta \ cos\theta} \quad \text{(Equation 10)}$$

$$< N > = \frac{Lc}{d_{002}} \quad \text{(Equation 11)}$$

2.5. Raman microspectroscopy

The characterization of the structural order of char morphotypes and identification of Fe-bearing phases in magnetic concentrates were made via Raman microspectroscopy. The analyzes were carried out at Institute of Earth Sciences – Porto Pole, Faculty of Sciences, University of Porto.

The analyses were carried at room temperature using the polished blocks previously prepared for petrographic analysis. The instruments were calibrated before each run against the Stokes Raman signal of pure Si at 520 cm^{-1} using a silicon wafer ((111) crystal plane surface).

Char morphotypes were analyzed using a XploRA^{TM} (Horiba, Scientific) spectrometer equipped with a CCD camera and a Nd:YAG laser at an excitation wavelength of 532 nm was used to analyze char. An optical microscope from Olympus (Shinjuku, Tokyo, Japan) with a ×100 objective lens (NA = 0.90) was used to focus the laser beam on the sample surface and to collect the scattered radiation. To avoid laser-induced degradation of char and reduce the fluorescence background the power of the laser was reduced using a neutral filter density (minimum 50 %). Additionally, a spike density filter of 50 % was used. Scans from 1000 cm^{-1} to 3500 cm^{-1} were performed using an acquisition time of 20 s and 10 accumulations. Spectral resolution was near 1 cm^{-1}.

Raman spectra were collected in the most abundant morphotypes found in char concentrates (Badenhorst et al., 2020) and in solid/fusinoids. At least five spectra were taken by morphotype and in cases where different reflectance and/or texture coexist in the same particle those were also registered.

Deconvolution of the spectra obtained was carried out to determine band position (ω, frequency, cm^{-1}); full width at half maximum (FWHM, cm^{-1}) and the relative integrated intensities of the bands (area). From the results obtained, the following parameters concerning D1 and G bands were calculated for all samples: (a) area (relative integrated intensity) ratio, (b) FWHM ratio and (c) distance between bands. These parameters, specially D1/G area ratio, have been widely used to assess structural order of carbonaceous materials (e.g., Beyssac et al., 2003, 2002; Guedes et al., 2012; Li et al., 2006; Sadezky et al., 2005; Schito et al., 2017). Additionally, for graphitized samples the relative intensity of D band, ID/It (It = ID1 + ID2 + IG) was also determined (Cabielles et al., 2009, 2008; González et al., 2005, 2004, 2003, 2002).

Adequate fits to the experimental data were obtained using a mixed Gaussian–Lorentzian curve-fitting procedure in a Labspec software (Horiba Scientific) and were conducted according to the deconvolution proposed by Li et al., (2006). Considering that D band position can change with the excitation laser (Mernagh et al., 1984; Vidano et al., 1981; Wang et al., 1990), the peaks were not fixed during the deconvolution.

The Raman microspectroscopy analyzes of Fe-bearing morphotypes were performed using a LabRaman spectrometer (Jobin–Yvon, Horiba Scientific,) equipped with a CCD camera and a He–Ne laser at an excitation wavelength of 632.8 nm. An optical microscope from Olympus (Shinjuku, Tokyo, Japan) with a ×100 objective lens (NA = 0.95) was used to focus the laser beam on the sample surface and to collect the scattered radiation. A neutral density filter was used to reduce the power of the laser in 75 % to avoid laser induced transformation of the Fe-bearing phases. Scans from 100 cm^{-1} to 1000 cm^{-1} were performed on the particles surface. The acquisition time and respective accumulations were individually adjusted to acquire an optimized spectrum at spectral resolutions near 1 cm^{-1}.

2.6. Transmitted electronic microscopy (TEM)

Transmitted electron microscopy analyzes were carried out at Department of Materials and Ceramic Engineering from University of Aveiro (Portugal) to characterize the structure (existence of layers, isolated or stacked) and the texture (orientation of the layers) of carbonaceous material at atomic scale. Before analysis, the samples were dispersed in a mixture of pure water and Isopropanol (50 vol.%) in an ultrasonic bath (FB11201 Fisherband, Thermo Fisher Scientific, New Hampshire, EUA) for 30 min. After, the dispersion was dropped into a porous carbon film supported on a copper grid (Holey, Agar Scientific, Essex, United Kingdom), and dried in air. The TEM analysis was made in a JEOL-2200FS (JEOL Ltd., Tokyo, Japan).

2.7. Magnetic susceptibility and isothermal remanent magnetization (IRM)

To investigate the concentration and type of natural magnetic carriers in the ash samples selected to obtain magnetic concentrates, two magnetic parameters were measured and analyzed, namely magnetic susceptibility and isothermal remanent magnetization (IRM).

The magnetic susceptibility was measured using a KLY-4S Kappabridge instrument in the Institute of Earth Sciences – Porto Pole, FCUP, University of Porto (Portugal). At least three susceptibility measurements of each sample were taken, and the average value was used. The specific or mass susceptibility, c (measured in m^3/kg), is defined as the ratio of the material magnetization, J (per mass unit) to the weak external magnetic field, H, according to the equation $J = cH$.

The IRM was measured using a Minispin fluxgate magnetometer (Molspin Ltd, Oxfordshire, UK) after magnetization in a pulse magnetizer at the Department of Earth Sciences, University of Coimbra (Portugal). The IRM was imparted at fields up to −1000 mT.

The S ratio parameter (S ratio = IRM_{-300} mT/SIRM) was determined to assess the relative contribution of ferromagnetic minerals (Evans and Heller, 2003; Maher and Thompson, 1999; Thompson and Oldfield, 1986). An S ratio close to unity indicates that the remanence is dominated by magnetite-like structures (Bloemendal et al., 1988). Decomposition of the IRM curves to identify distinct magnetic components was performed with cumulative log-Gaussian (CLG) function (Kruiver et al., 2001; Robertson and France, 1994a) and MAX UnMix (Maxbauer et al., 2016).

2.8. Mössbauer spectroscopy

The Mössbauer spectroscopy was used to investigate the Fe-bearing phases present in the magnetic concentrates. The analyzes were carried out at Center of Nuclear Sciences and Technologies from Instituto Superior Técnico (University of Lisbon, Portugal). The spectra were collected in transmission mode using a conventional constant-acceleration spectrometer and a 25 mCi ^{57}Co source in a Rh matrix. The velocity scale was calibrated using α-Fe foil. Isomer shifts, IS, are given relative to this standard. The absorbers were obtained by packing the powdered samples into Perspex holders. The absorber thickness was calculated based on the corresponding electronic mass-absorption coefficients for the 14.4 keV radiation (Long et al., 1983) The spectra were fitted to Lorentzian lines using a non-linear least-squares method (Waerenborgh et al., 2000)

2.9. Laser granulometry

Particle size distribution (PSD) of coal combustion ashes from S1 and S4 (campaigns with all sampling sites represented) was determined via laser granulometry analysis performed at Faculty of Engineering of University of Porto (FEUP, Portugal) using a Mastersizer 2000 (Malvern Panalytical, Malvern, United Kingdom). The equipment is coupled to a Hydro 2000G, which enables measurements to be made in aqueous dispersions. The reagent IGEPAL was employed as a dispersant and the PSD was determined through the Mie theory (de Boer et al., 1987) by comparing with the standard silica 1.0 with a refractive index of 1.544. The BA and the ECO fly ash samples were previously manually sieved bellow 500 µm to prevent damages to the equipment.

3. Physical separations

3.1. Fractionation for chemical analysis

To evaluate the distribution of the elements and find potentially promising fractions for carbon and REE recovery, coal combustion ash samples were fractionated by size and magnetic properties for subsequent chemical analysis.

3.1.1. Sieving

Mechanical sieving trials were carried out at at Institute of Earth Sciences – Porto Pole, Faculty of Sciences, University of Porto. Firstly, the ash samples were dried in an oven at 30°C until constant weight. Sieving was carried out using a Retsch AS200 (Verder Scientific, Hope Valley, UK) sieve shaker and two sets of standard test sieves from Retsch (200 × 50 mm), with the following nominal apertures: (a) 150, 75, 45, and 25 µm (100, 200, 325 and 500 mesh, respectively); and, (b) 4, 2, and 1 mm, and 500, 250, 125, 90, and 63 µm (5, 10, 18, 35, 60, 120, 170, and 230 mesh, respectively). The sieves were chosen based on the ash characteristics (BA is typically coarser than FA) and on previous research using similar materials (Hower et al., 1999c; Valentim et al., 2019, 2008). For each trial, 20 g of sample was sieved during 30 min, using a shaking amplitude of 70 %.

Additionally, fractions <45 µm from selected FA samples were also mechanically wet-sieved using a clamping cover with a nozzle and a collecting pan with an outlet, respectively, at the top and the bottom of a standard sieve with a nominal aperture of 25 µm. The system was kept running until the water flowed out clean. The subsamples obtained were dried in an oven at 30 ˚C until reaching a constant weight.

3.1.2. Magnetic separation

Magnetic concentrates (MC) were obtained via wet magnetic separation using a ferrite magnet (Fe-magnet concentrates) followed by separation using a neodymium magnet (Nd-magnet concentrates). The solid/liquid ratio used was 0.01 (100 g to 10 L). The sample was initially mixed for 5 min at 250 rpm using a laboratory mixer SCILOGEX OS20-S to promote the particles deagglomeration, then the velocity was reduced and kept at 150 rpm to avoid settling during the magnetic separation. The system was kept running until no particles were collected by the magnets, and the recovered materials were dried in an oven at 60 °C until they reach a constant weight.

3.1.3. Char concentration process

The efficiency of the char concentration methods used was primarily assessed via proximate analysis since enables the determination of fixed carbon and estimation of the char yield (Jones et al., 1985) and SEM/EDS. Moreover, sample yield (Equation 12), and the carbon recovery (Equation 13) were determined to assess the overall process efficiency. Later, elemental analysis (C_{tot} and S) and XRF were carried in subsamples collected across the different steps of the process.

$$\text{Yield} = (\text{Product stream (g)})/(\text{Feed stream (g)})\ \text{X}\ 100 \quad \text{(Equation 12)}$$

$$\text{Carbon recovery} = \frac{\text{Carbon product stream (g)}}{\text{Carbon feed stream (g)}}\ \text{X}\ 100 \qquad \text{(Equation 13)}$$

The initial objective was to obtain a 500 g char concentrate, but maintaining as much as possible the char proprieties, i.e., without pores clogging, since this is important for char application in green chemistry technologies. Consequently, liquids susceptible to be retained on char pores, such as dense liquids and froth flotation reagents, were ruled out in order not to prevent its char use as electrocatalyst in oxygen reduction reaction (ORR).

A specific sampling task was made to collect approx. 50 kg of fresh FA from the first row of the ESP at Pego power plant needed for trials and obtaining the char concentrate.

After several trials based on former reported cases (e.g., Cabielles et al., 2008; Külaots et al., 2004; Liu et al., 2017; Lu et al., 2007; Rubio et al., 2008; Sharonova et al., 2008; Wang and Li, 2005) and information gathered during bulk samples characterization and handling, a sequence of separations steps was defined as shown in the flow chart on Figure II - 1. Before and after each separation step involving water, the samples were dried in an oven for 24h at 40 ˚C until constant weight.

The first step in the char concentration process was dry sieving to separate the fraction retained in the 75 µm sieve (Figure II - 3). The equipment and methodology are described section 3.1.1.

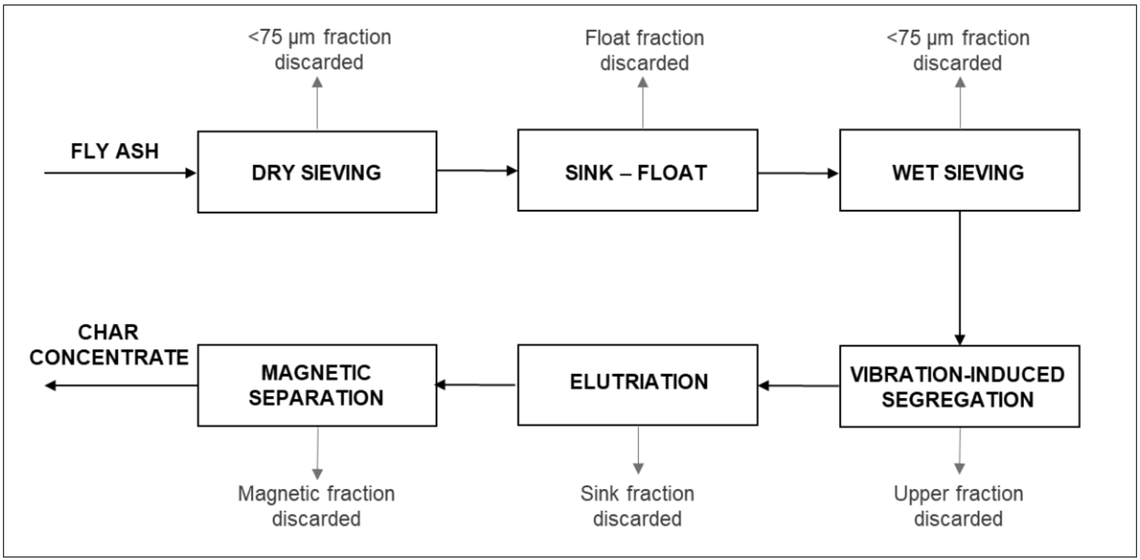

Figure II - 3. Flow diagram of the process used to concentrate char from fly ash.

After, fly ash >75 µm the size-fraction was immersed in water to (1) removing the hollow aluminosilicate spheres that are the main components of fly ash floating fraction; and then (2) was wet sieved to remove fine particles that didn’t pass the 75 µm sieve during the dry sieving trials. In detail, for the gravimetric separation the sample was placed in a glass vessel with tap water (liquid-solid ratio of 1:10) at ambient temperature, stirred with a glass rod for ca. 5 min and let to settle. The floating fraction was removed after decantation of the sink fraction and filtrated using filter paper (FILTER-LAB 1300/8, Anoia Filters S.A., Barcelona, Spain) and dried. The sink fraction was then wet sieved as described in section 3.1.1 but using only the 75 µm sieve to recover the >75 µm size-fraction for further beneficiation.

The next step of the char concentration process consisted of vibration-induced segregation, also named as the “dry impaction” method, using a sieve shaker to cause the vibration and impaction of the particles against each other. Segregation is a process where the particles composing a bulk solid became unevenly distributed (Rosato and Blackmore, 2000). It is a complex process that can result from differences in particles size, density, shape, and/or surface roughness (Schulze, 2007). In the current research, segregation was achieved by placing the wet sieved >75 µm sample in a glass vessel and exposing it to vibration using a sieve shaker (Figure II - 4A). A light-gray char-poor layer formed at the top (Figure II - 4B) was removed by suction using a vacuum cleaner ECOLA EL-BT 13 coupled to a pressure reducing chamber containing a 63 µm sieve to ensure particles retention (Figure II - 4C). The process was repeated until no segregation occurred, i.e., when it no longer formed a char-poor layer thick enough to be collected without recover the dark char-rich fraction.

After vibration-induced segregation, further separation of the char-rich fraction was carried through a wet elutriation-based process. Elutriation enables the separation of the particles based on terminal velocity when subjected to an upward current of fluid, usually air or water, i.e., particles with terminal velocity lower than that from the fluid overflow while the remaining sink (Wills and Finch, 2016). Figure II - 5 shows a representative scheme of the wet elutriation-based method (Figure II - 5A) and an image of the actual scheme used (Figure II - 5B).

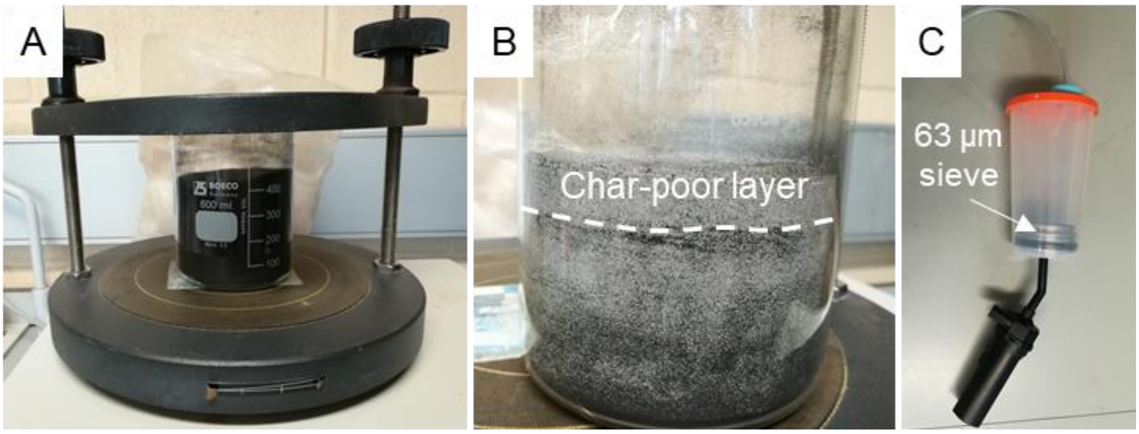

Figure II - 4. Vibration-induced segregation: A) glass vessel with FA sample on a sieve shaker; B) FA in the glass vessel after agitation with an upper greyish layer (char-poor) and C) vacuum cleaner coupled to a pressure reducing chamber with a 63 µm sieve inside.

In detail, a closed water-circuit was assembled between two vessels (the feeder and the collector) and two water pumps (handheld vacuum cleaner from HANDY) (Figure II - 5).

This way, the particles kept in suspension by the water flux (mainly char) could be collected by suction and retained in a 75 µm sieve placed between the vessels to retain the char. The process was stopped once no more particles were retained in the sieve, and all the fractions were collected/filtrated and dried.

Finally, Fe-bearing particles were separated from the char-rich fraction using a ferrite handheld magnet (Magsy, s.r.o., Czech Republic). The sample was placed over a plastic tray and the process repeated until no more particles were collected by the magnet.

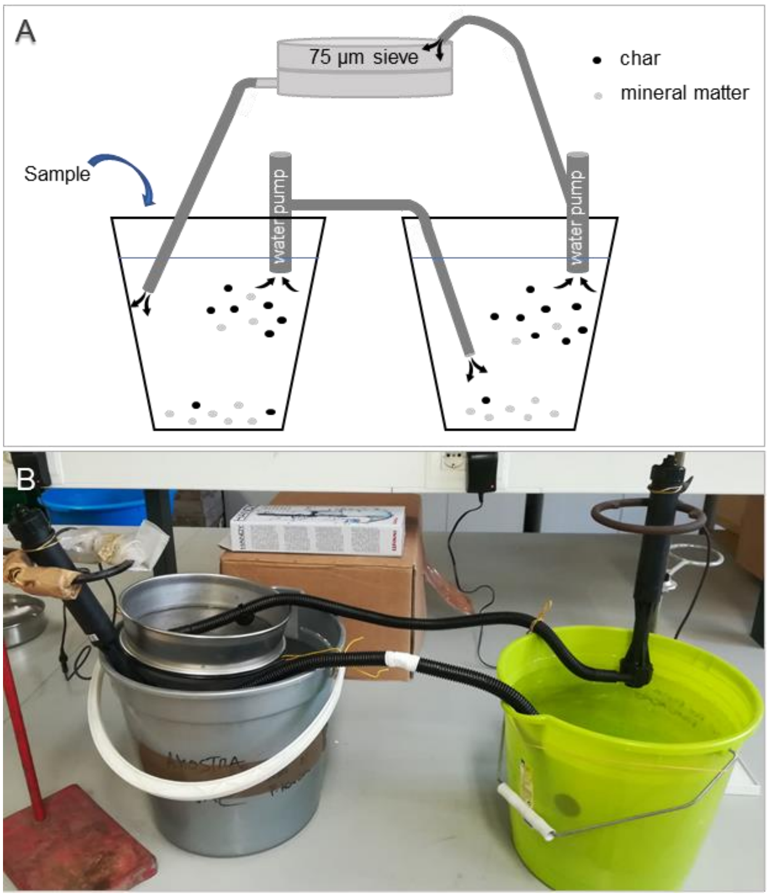

Figure II - 5. (A) Scheme of elutriation-based separation and (B) image showing the system used in this study.

4. Demineralization

To avoid the clogging of the graphitization chamber, char demineralization was carried out in char concentrate to reduce the content of carbonates and silicates before graphitization. For this purpose, char concentrates were sequentially leached with HCL (37 %, EMSURE, Merck, Darmstadt, Germany) and HF (40 %, Sigma Aldrich, Missouri, USA). In detail, ten grams of char concentrates were placed in a 1L Teflon bottle, 250 ml of HCL (diluted to 20 %) was then added and the bottle was agitated in a Sky Line Shaker Dos-20L (Elmi, Riga, Latvia) for approx. 18 hours. After, distilled water (≈750mL) was added, left for rest 6 hours, and finally filtrated using a SEFAR PET 1500 mesh (Sefar AG, Heiden, Switzerland). After, 150 mL of HF (40 %) was added to sample and agitated for 18 hours, and this was followed by rinsing and filtration as early described. Finally, the HCL step was repeated, followed by two-stage of washing with distilled and filtration, and dried at 80 °C until reach constant weight.

5. High temperature treatments (HTT)

Carbonization and graphitization trials were carried out at Instituto de Ciencia y Tecnología del Carbono (INCAR), Oviedo, Spain.

5.1. Carbonization

To remove the volatiles from the chars, the carbonization of the demineralized char concentrates was made at 1000 °C in a Carbolite horizontal tube furnace (CTF model) under argon flow (50 mL/min), at a heating rate of 2 °C and a residence time of 1 h. The samples were cooled to room temperature inside the furnace under argon. The samples were weighed before and after the carbonization process to determine the weight loss during the process.

5.2. Graphitization

The graphitization trials by high-temperature thermal treatments (HTT) were conducted in a Xerion three-phase electric furnace with the software Eurotherm 2704 (KD485, Eurotherm, Worthing, UK). The heating rate, residence time, and the cooling of the furnace were controlled. The furnace is equipped with a graphite heating and insulation system in water-cooled double-wall vessels, with an optical pyrometer (Keller model PZ 30, Keller, Ibbenbüren, Germany) able to measure temperatures up to 3000 °C. The samples were placed in graphite crucibles and heated to a temperature of 2600 °C in the graphite furnace, under argon flow, at heating rates of 50 °C/min, 100 °C/min, 25 °C/min, and 10 °C/min in the temperature intervals of 20–700 °C, 700–1000 °C, 1000–2000 °C, and 2000–2600 °C, respectively. The samples were kept at the maximum temperature (2600 °C) for 1 h. These experimental conditions were selected based on previous work by González et al. (González et al., 2005, 2004, 2003, 2002). Meanwhile, Cabielles et al. (2008, 2009) graphitized coal ash char obtained from a power plant burning anthracite coal and found that graphitization is seemingly completed at 2400 °C. However, in the same study imaging analyses showed that there are still some individual particles that were not graphitized and may continue to graphitize above 2400 °C. Therefore, in our study 2600 °C was chosen to enhance the graphitization process.

Part III | Results and Discussion

1. Bulk samples characterization and REE potential assessment

1.1. Feed coals

Table III - 1 lists the results regarding proximate and ultimate analysis (wt.%), gross calorific value (GCV, MJ/Kg) and carbon forms (wt.%) of the feed coals. The samples present low to medium ash contents, up to 20 wt.%, db (ISO 11760, 2005), low sulphur, <1 wt.% (Chou, 2012) and average gross calorific value of 30.21 MJ/Kg.

The ash yield among the coals analysed ranged from 3.28 to 10.19 wt.%, corresponding to a variation coefficient (CV) of 27 % (Table III - 1). Excluding sample S1-C, which presents a significant lower ash yield the CV would be lowered to 11 %. Elements that are usually associated with mineral matter in coals, such REE (e.g., Finkelman et al., 2018), are expected to be found in lower concentrations in the afore mentioned sample.

Table III - 1. Proximate and ultimate analysis (wt.%), gross calorific value (GCV, MJ/Kg) and forms of carbon (wt.%) of the feed coals.

	S1-C	S2-C_1	S2-C_2	S3-C_1	S3-C_2	S4-C_1	S4-C_2	Average	CV
Proximate analysis									
M_{ad}	6.24	6.04	8.31	6.20	6.88	6.71	5.84	6.60	11.72
A_{db}	3.28	7.39	8.25	10.19	9.12	10.10	9.01	8.19	26.88
VM_{daf}	39.82	41.74	42.37	41.16	41.88	41.70	40.44	41.30	2.00
FC_{daf}	60.18	58.26	57.63	58.84	58.12	58.30	59.56	58.70	1.41
Ultimate analysis									
S_{db}	0.52	0.79	0.79	0.66	0.63	0.73	0.72	0.69	12.92
C_{daf}	80.34	77.21	77.30	79.72	78.62	78.53	80.30	78.86	1.54
H_{daf}	6.20	5.93	6.22	6.18	6.17	6.07	6.08	6.12	1.55
N_{daf}	1.64	1.63	1.56	1.60	1.62	1.60	1.57	1.60	1.72
O_{daf}	11.28	14.37	14.06	11.77	12.90	12.98	11.25	12.66	9.32
Atomic H/C	0.92	0.92	0.96	0.92	0.93	0.92	0.90	0.93	1.78
Atomic O/C	0.11	0.14	0.14	0.11	0.12	0.12	0.11	0.12	10.87
GCV_{db}	29.19	30.21	28.94	29.46	29.68	29.66	29.78	29.56	1.30
Carbon forms									
C_t	72.45	66.48	64.49	65.37	65.09	65.32	67.93	66.73	3.83
C_{org}	72.42	66.43	64.44	65.31	65.02	65.28	67.87	66.68	3.85
C_{CO2}	0.01	0.04	0.03	0.01	0.03	0.03	0.02	0.02	54.67
C_{gra}	0.07	0.02	0.06	0.15	0.15	0.05	0.15	0.09	55.43

CV, coefficient of variation; M, moisture; A, ash yield; VM, volatile matter; S, sulfur; C, carbon; H, hydrogen; N, nitrogen; GCV, gross calorific value; C_t, total carbon; org, organic; gra, graphitic; CO_2, inorganic; ad, air-dry basis; db, dry basis; daf, dry and ash-free basis

The atomic ratios H/C and O/C are compatible with bituminous coal rank (van Krevelen, 1993) and according to the ASTM D388 (1999) all coals can be classified as high volatile A bituminous coal. As expected, the carbon is predominantly organic (> 99 wt.%, Table III - 1). The differences in the carbon content from elemental analysis and fixed carbon

(FC) may originate from the loss of carbon as hydrocarbon in volatile matter during proximate analysis (Speight, 2015).

The results of the petrographic analyses carried out on feed coals is given in Table III - 2. The nomenclature used followed the guidelines of ICCP (ICCP, 2001, 1998; ISO 7404-3, 2009; Pickel et al., 2017). The feed coals have moderate to high vitrinite contents (77 - 83 vol.% mineral-ash free basis, mmf; ISO 11760, 2005) with collodetrinite being dominant, up to 67 vol.% of the total vitrinite content. The inertinite group represents 14-19 vol.% mmf and liptinite was found in minor amounts, 3 to 5 vol.% mmf.

Table III - 2. Petrographic analysis results for the feed coals.

	S1-C	S2-C_1	S2-C_2	S3-C_1	S3-C_2	S4-C_1	S4-C_2
Vitrinite (vol.%)	79.8	76.9	72.6	78.2	74.9	75.5	71.7
Telinite	1.8	2.9	2.6	1.3	2.6	1.3	2.5
Collotelinite	11.0	10.6	20.6	14.4	14.1	19.3	10.0
Vitrodetrinite	4.1	5.8	8.7	5.2	7.0	4.9	7.6
Collodetrinite	53.5	47.0	32.0	47.8	43.0	41.6	44.5
Corpogelenite	9.2	10.0	8.0	9.1	8.2	7.8	6.9
Gelenite	0.2	0.5	0.7	0.4	0.0	0.5	0.2
Inertinite (vol.%)	15.7	15.3	17.2	13.1	12.8	15.6	17.2
Fusinite	1.8	0.9	3.1	2.8	2.6	1.8	1.6
Semifusinite	7.5	3.6	5.2	3.9	2.9	5.3	5.1
Funginite	0.4	0.4	0.7	0.0	0.2	0.2	0.5
Secretinite	0.0	0.2	0.5	0.2	0.2	0.4	0.2
Macrinite	2.5	3.8	2.6	3.2	2.0	2.0	3.4
Micrinite	0.0	0.0	0.0	0.0	0.0	0.0	0.0
Inertodetrinite	3.5	6.4	5.2	3.0	4.9	6.0	6.4
Liptinite (vol.%)	2.9	4.4	4.0	3.0	4.8	2.7	4.0
Cutinite	0.4	0.5	1.2	0.9	0.9	0.5	0.4
Suberinite	0.0	0.0	0.0	0.0	0.0	0.0	0.0
Sporinite	0.6	1.3	0.5	0.9	1.1	0.7	0.9
Resinite	0.6	0.7	1.2	0.4	0.9	0.0	0.0
Exsudatinite	0.0	0.0	0.0	0.0	0.0	0.0	0.0
Chlorophyllinite	0.0	0.0	0.0	0.0	0.0	0.0	0.0
Alginite	0.0	0.0	0.0	0.0	0.0	0.0	0.0
Liptodetrinite	1.4	1.8	1.2	0.7	1.8	1.5	2.7
Bituminite	0.0	0.0	0.0	0.0	0.0	0.0	0.0
Mineral matter (vol.%)	1.6	3.5	5.9	5.8	7.5	6.2	7.1
Total reactive macerals (vol.%)	82.7	81.2	76.6	81.2	79.7	78.2	75.7
Vitrinite Reflectance							
Mean random reflectance (RoV%)	0.53	0.55	0.48	0.58	0.55	0.53	0.57
Standard deviation	0.06	0.05	0.04	0.05	0.05	0.04	0.07
Rank Category	Medium rank D	Medium rank D	Low-rank A	Medium rank D	Medium rank D	Medium rank D	Medium rank D

The feed coal S1-C presents the lowest observable mineral matter content (1.6 vol.%, Table III - 2), which agrees with the ash yield (Table III - 1) and differs from the other coal samples studied by the absence of fines resulting from coal beneficiation (Laskowski, 2001; Valentim et al., 2009b, 2006). Based on vitrinite reflectance, all feed coals analyzed can be classified as medium rank D (bituminous), except of S2-C2 which is a low rank A (sub-bituminous) borderline to medium rank D (ISO 11760, 2005).

Major and minor oxides (whole-coal basis; wt.%), Loss on ignition (LOI; wt.%) and LTA mineralogy (wt.%) of the feed coals are given on Table III - 3. The predominant oxides are SiO_2 and Al_2O_3, average of 4.85 and 1.57 wt.%, respectively (Table III - 3). The average ratio SiO_2/Al_2O_3 of 3.06 is higher than the theoretical ratio of kaolinite of 1.18, indicating the presence of quartz (Yuan et al., 2019).

Table III - 3. Major oxides, LOI, and mineralogical results for feed coals (wt.%).

	S1-C	S2-C$_1$	S2-C$_2$	S3-C$_1$	S3-C$_2$	S4-C$_1$	S4-C$_2$
Major oxides							
SiO_2	1.76	4.78	3.97	6.94	5.72	5.64	5.11
TiO_2	<0.01	0.07	0.05	0.07	0.04	0.06	0.06
Al_2O_3	0.65	1.5	1.56	2.21	1.48	1.83	1.78
Fe_2O_3	0.05	0.53	1.08	0.71	0.84	0.56	0.41
MnO	<0.01	<0.01	<0.01	<0.01	<0.01	<0.01	<0.01
CaO	0.06	0.11	0.19	0.13	0.11	0.14	0.12
MgO	<0.01	<0.01	<0.01	0.01	<0.01	<0.01	<0.01
Na_2O	<0.01	<0.01	0.08	<0.01	<0.01	<0.01	<0.01
K_2O	0.04	0.14	0.14	0.23	0.12	0.18	0.19
P_2O_5	0.01	<0.01	<0.01	0.02	<0.01	<0.01	<0.01
SO_3	0.03	0.41	0.26	0.08	0.28	0.08	0.07
Cr_2O_3	<0.01	<0.01	<0.01	<0.01	<0.01	<0.01	<0.01
SiO_2/Al_2O_3	2.71	3.19	2.54	3.14	3.86	3.08	2.87
LOI	97.0	91.5	91.7	88.2	90.8	90.0	91.0
LTA mineralogy							
Quartz (SiO_2)	31	35.9	37.7	30.6	41.6	38.7	n.d.
Albite ($NaAlSi_3O_8$)	0.6	0.0	0.8	1.5	0.2	0.7	n.d.
Hornblende ($Ca_2(Mg, Fe^{2+})_4Al(Si_7AlO_{22})(OH,F)_2$)	0.8	0.8	0.5	0.8	0.7	0.4	n.d.
Muscovite ($KAl_2(AlSi_3)O_{10}(OH)_2$)	4.0	9.4	6.3	8.9	7.0	8.4	n.d.
Illite ($K_{1.5}Al_4(Si_{6.5}Al_{1.5})O_{20}(OH)_4$)	4.2	6.1	9.8	12	6.5	7.9	n.d.
Kaolinite ($Al_2Si_2O_5(OH)_4$)	45.5	27	22.6	26.9	27.8	25.6	n.d.
Montmorillonite ($(Na,Ca)_{0.33}(Al,Mg)_2(Si_4O_{10})(OH)_2 \cdot nH_2O$)	0.3	0.3	0.3	0.5	0.2	0.0	n.d.
Chlorite ($(MgFeAl)_6(AlSi)_4O_{10}(OH)_8$)	0.3	1.6	2.0	2.3	2.2	0.3	n.d.
Anatase (TiO_2)	0.3	1.0	0.6	0.6	0.2	0.7	n.d.
Boehmite ($Al \cdot O \cdot OH$)	0.2	0.3	0.4	0.1	0.1	0.1	n.d.
Calcite ($CaCO_3$)	0.0	0.0	0.1	0.0	0.0	0.0	n.d.
Siderite ($FeCO_3$)	0.3	0.0	0.3	0.7	0.3	0.0	n.d.
Bassanite ($CaSO_4 \cdot 0.5H_2O$)	0.7	0.5	2.4	0.5	2.1	1.2	n.d.
Gypsum ($CaSO_4 \cdot 2H_2O$)	3.4	2.3	4.4	3.6	4.3	3.5	n.d.
Hexahydrite ($MgSO_4 \cdot 6H_2O$)	2.3	1.2	1.0	1.7	2.2	4.2	n.d.
Jarosite ($(K,Na)Fe_3(SO_4)_2(OH)_6$)	1.1	3.5	1.4	3.0	1.2	2.3	n.d.
Alunogen ($Al_2(SO_4)_3 \cdot 17H_2O$)	3.3	8.5	3.3	4.5	0.6	4.0	n.d.
Tschermigite ($NH_4Al(SO_4)_2 \cdot 12H_2O$	0.0	0.2	0.5	0.0	0.8	0.0	n.d.
Apatite ($Ca_5F(PO_4)_3$)	0.6	0.1	1.2	0.6	1.2	0.5	n.d.
Pyrite (FeS_2)	1.2	1.3	4.5	1.2	0.9	1.7	n.d.

SX, sampling campaign; C, coal; n.d. – not determined

Minor amounts of Fe_2O_3 (0.05 to 1.09 wt.%), SO_3 (0.03 to 0.41 wt.%), K_2O (0.04 to 0.23 wt.%), CaO (0.06 to 0.19 wt.%) and TiO_2 (up to 0.07 wt.%) were detected while the remaining elements were below detection limits (bdl; < 0.01 wt.%). The coal from the first sampling campaign (S1-C) shows lower contents of all oxides comparatively to the other samples studied (Table III - 3).

The feed coals LTA are mainly composed of silicates (≥ 80 wt.%), with quartz and kaolinite being predominant, representing in average 65 wt.% of the total mineral matter (Table III - 3). The kaolinite content is markedly higher in S1-C relatively to the other samples (>17 wt.%). Observations under SEM/EDS showed massive aggregates of kaolinite in this sample (Figure III - 1A,B) which were not detected in the other samples.

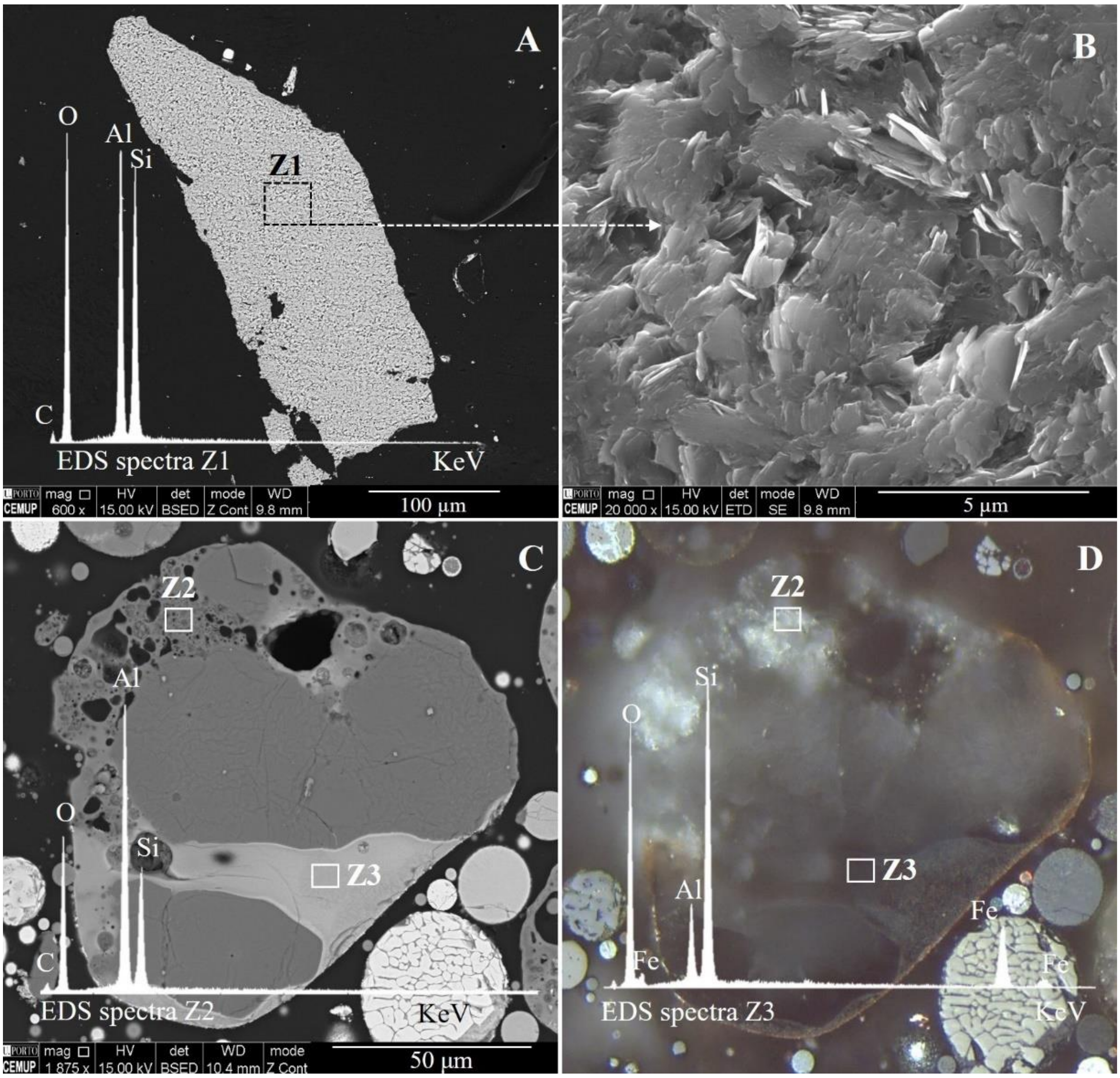

Figure III - 1. Massive kaolinite aggregate observed under SEM/EDS in coal sample from campaign S1: (A) whole-particle view (×600; BSE mode) and respective EDS spectra and (B) magnification of dashed square area in “a” showing the kaolinite lamellae (×20000; SE mode). Particle from fly ash sample of first ESP row observed under SEM/EDS (C) and optical microscopy (D), and EDS spectra relative to Z2 and Z3 noted in the microphotographs.

Sulphates represent between 11 to 16 wt.% of the mineral matter. However, bassanite and other sulphates such as hexahydrite, alunogen and, tschermigite are usually considered an artifact from the ashing process (Ward, 2016). The presence of gypsum (2.3 - 4.4 wt.%) may suggest that some of the bassanite (0.5 - 2.4 wt.%) is due to partial dehydration of pre-existing gypsum and/or reaction of organic sulphur with organically associated calcium. During SEM/EDS analysis no gypsum was detected so it is assumed that is also an artifact from ashing process. Jarosite probably resulted from the sulphide oxidation, such as pyrite, during coal exposure or storage (Oliveira et al., 2012). Pyrite was detected in contents that ranged from 0.9 to 4.5 wt.% (Table III - 3).

Other minerals were detected in low concentrations, such as apatite (0.6 - 1.2 wt.%), anatase (0.3 - 1.0 wt.%) and boehmite (0.1 - 0.4 wt.%) (Table III - 3). Siderite was detected in four samples (S1-C, S1-C2, S3-C1 and S3-C2) in concentrations ranging from 0.3 to 0.7 wt.% while calcite was detected in a single coal (S2-C2) with a content of 0.1 wt.% (Table III - 3).

1.2. Coal combustion ashes

Texturally, BA and ECO FA are easily distinguished from the FA collected on the ESP (Figure III - 2). The first two are coarser with particles predominantly in the silt-size range, avg. 67 vol.% (Table III - 4). In FA from ESP, particles within the sand-size 71 vol.% average dominates but it also contains particles in size-range of sand and clay, 23 and 6 vol.%, respectively. A large range of D90-D10 is verified for BA and ECO FA, avg. 259 µm, however the lower span (avg. 2.5) indicates a better homogeneity in comparison to the ESP FA (average span of 5) (Table III - 4). Nevertheless, it must be considered that those samples were sieved <500 µm before the analysis, excluding in average 60 wt.% of the material. Still, according to (Folk and Ward, 1957) the ashes analysed are poorly (1 < SD < 2) to very poorly sorted (2 < SD < 4).

The mean particle size (volume weighted) decreases as follows: BA (avg. 167 µm) > ECO (avg. 114 µm) > ESP (avg. 48 µm). The D50 follows the same trend (Table III - 4). The decrease of particle size from ECO to the ESP was expected since the first lines of any system of pollution control tends to separate the coarsest particles from the flue gas stream, concentrating the finer particles in ESP (Hood et al., 2017; Hower et al., 1999c; Mardon and Hower, 2004; Valentim et al., 2008). The ashes from silo in S1 present an average particle size similar to ESP FA while in S4 it is closer to the ECO FA (Table III - 4). Both ashes are redirected to silo, and sampling could have been affected by a heterogeneous distribution inside the structure.

Usually, a decrease on particle size towards the back rows of the ESP array is expected but slight variations were observed. In campaign S1, opposite trends were observed towards the ESP back rows (Figure III - 2C): (a) in 12-32/42 row the mean particle size increases 8.3 μm while (b) in 15-35/45 row decreases 3.3 μm. In both, the lowest mean particle size is found in the middle row (Table III - 4). On campaign S4, the mean particle size decreases towards the ESP back rows (8 μm) like 15-35/45 row from S1, and D50 reduces approx. 50 % from the first to the last row (Figure III - 2D).

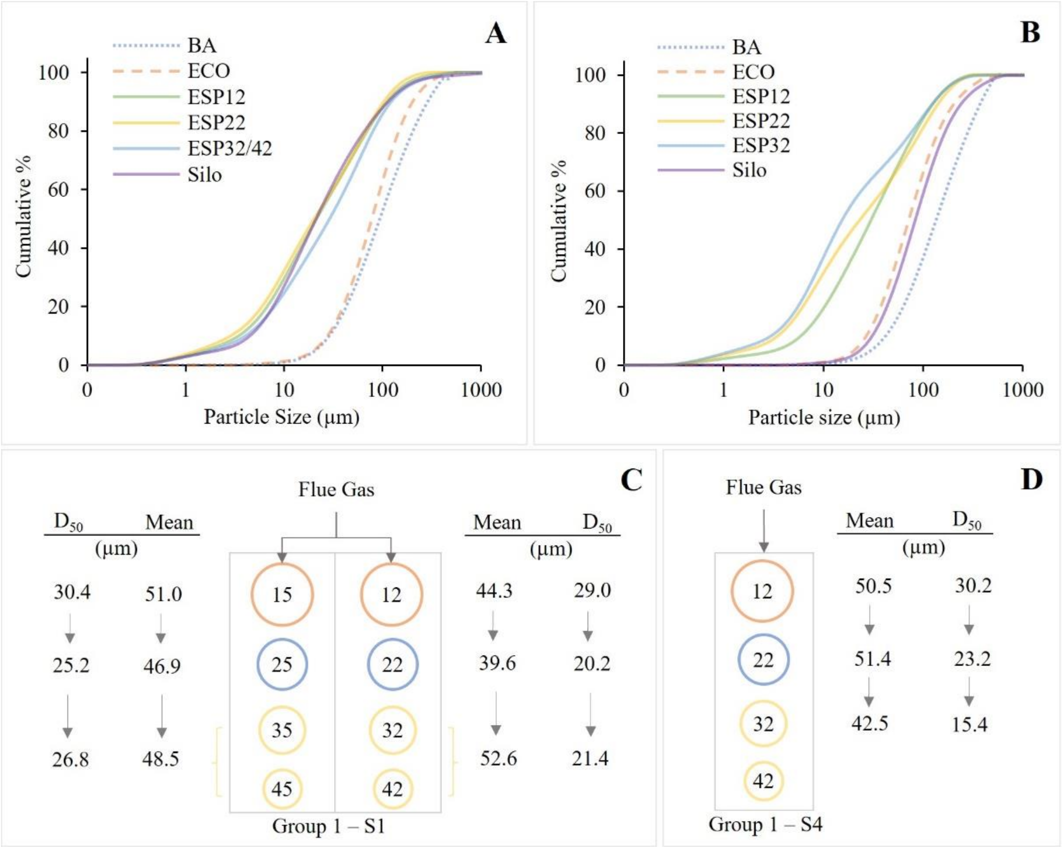

Figure III - 2. Particle size distribution for ashes from campaign S1 (A), only ESP row 12-32/42 included, and S4 (B); Scheme illustrating the variation of mean particle-size and D50 inside ESP on S1 (C) and S4 (D).

The results of proximate analysis, sulfur, carbon forms and major oxides are listed on Table III - 5. The ashes have moisture contents varying from 0.04 to 0.59 wt.%, ash values between 92.27 and 99.89 wt.%, sulfur up to 0.49 wt.% and carbon from 0.22 to 6.32 wt.%. The contents of sulfur and carbon increase as follows: BA < ECO fly ash < ESP fly ash. The carbon distribution is corroborated by char vol.% determined in the ash petrographic analysis (Table III - 7).

Except in S1, the sulfur tends to increase towards the back of the ESP, at an average of 2.7 times. Similar trends were found for SO_3 (Table III - 6). This was expected given the sulfur volatility and the cooler flue gas temperatures in the back end of the ESP (Mardon and Hower, 2004; Meij, 1995). In terms of the carbon distribution inside the ESP, in S1 and S2, there is an increase towards the back hoppers, which agrees with the reported data (Ahn and Lee, 2006; Mardon and Hower, 2004; Senneca, 2008; Suárez-Ruiz et al., 2007), while the reverse is observed in the two remaining campaigns. The variations found can be related to the changes in the combustion conditions. The carbon in FA is predominantly organic and elemental, which together account for 94 - 100 wt.% of the total carbon, while inorganic carbon is residual, accounting for <6 wt.%. In BA, the organic carbon is the dominant form (37 - 64 wt.%) and is up to three times more abundant than elemental carbon (S1-BA and S3-BA) (Table III - 5).

Table III - 4. Particle size characteristics of the FA and BA samples analyzed by laser granulometry.

Campaign	Sample	Mean (µm)	D_{10} (µm)	D_{50} (µm)	D_{90} (µm)	D_{90} - D_{10} (µm)	Span	SD (φ)	Clay % (< 2 µm)	Silt % (2-63µm)	Sand % (63-2000 µm)
S1	BA	147.7	33.05	108.3	331.7	298.7	2.8	1.3	0.0	31.7	68.3
	ECO	115.3	31.55	89.37	232.1	200.6	2.2	1.1	0.0	37.2	62.8
	ESP12	44.3	3.5	21.4	111.2	107.8	5.0	2.0	6.7	73.1	20.3
	ESP15	51.0	4.7	30.4	125.9	121.2	4.0	1.9	4.8	69.8	25.4
	ESP22	39.6	2.9	20.2	103.5	100.6	5.0	2.0	8.0	72.6	19.4
	ESP25	46.9	4.1	25.2	115.0	111.0	4.4	1.9	5.8	72.6	21.6
	ESP32/42	52.6	4.1	29.0	122.5	118.4	4.1	2.0	5.8	69.8	24.4
	ESP35/45	48.5	4.6	26.8	125.6	121.0	4.5	1.9	5.0	70.4	24.5
	Silo	51.4	4.5	21.1	113.6	109.1	5.2	1.9	5.1	76.1	18.9
S4	BA	174.0	42.0	135.5	375.2	333.3	2.5	1.2	0.0	22.9	77.1
	ECO	112.7	30.9	82.7	234.7	203.8	2.5	1.1	0.0	40.9	59.1
	ESP12	50.5	5.9	30.2	126.0	120.0	4.0	1.7	3.8	71.2	25.0
	ESP22	51.4	3.5	23.2	141.8	138.3	6.0	2.1	6.3	66.1	27.6
	ESP32	42.5	3.0	15.4	123.4	120.4	7.8	2.2	7.7	70.6	21.7
	Silo	116.0	31.0	83.7	240.0	209.1	2.5	1.2	0.0	40.5	59.5

BA, bottom ash; ECO, economizer; ESP, electrostatic precipitator; SD, standard deviation

The ashes are mainly composed of SiO_2 and Al_2O_3, which, together, represent up to 84.35 wt.% of all oxides (Table III - 6). Those are followed by Fe_2O_3 (6.29 - 9.01 wt.%), K2O (1.33 - 2.45 wt.%), CaO (1.24 - 2.38 wt.%), MgO (1.13 - 2.04 wt.%), and some minor oxides (≤1 wt.%), such as Na_2O, TiO_2, SO_3, P_2O_5, MnO, and Cr_2O_3 (Table III - 6). The ashes from S1 present similar compositions to the remaining ashes analyzed, even though the feed coal from which they were derived presented the lowest oxide concentrations (Table III - 3). Furthermore, they show slightly higher average concentrations of K_2O and MgO, at 2.27 and 1.88 wt.%, respectively. The CaO and NaO are slightly more concentrated in S2, at 1.96 and 1.29 wt.%, respectively, which is related to the higher concentrations observed in the respective feed coals (Table III - 3). However, this is not verified for Fe_2O_3 and SO_3, which are more concentrated in ashes from S4, at 8.19 and 0.40 wt.%, respectively, while the feed coals from S2 presented higher average concentrations, at 0.81 and 0.33 wt.%, respectively. The bottom ashes and fly ashes from the ECO present similar compositions to the ESP fly ashes, but they are generally richer in SiO_2 and Fe_2O_3, and slightly poor in Al_2O_3, K_2O, MgO, Na_2O, P_2O_5, SO_3, and TiO_2 (Table III - 6).

Table III - 5. Proximate and ultimate analyses and carbon form results for the bulk ashes (wt.%).

Campaign	Sample	M_{ad}	A_d	VM_d	S_t	C_t	C_{org}	C_{gra}	C_{Co2}
S1	BA	0.12	99.63	0.45	<0.02	0.35	0.19	0.09	0.24
	ECO	0.12	98.31	0.46	0.05	1.69	0.81	0.85	0.10
	ESP12	0.27	94.25	1.02	0.13	5.51	2.75	2.74	0.09
	ESP15	0.28	95.33	0.87	0.13	4.38	1.86	2.51	<0.02
	ESP22	0.27	93.67	1.31	0.14	5.92	2.82	3.09	0.07
	ESP25	0.27	94.60	1.45	0.20	4.92	2.28	2.63	0.02
	ESP32/42	0.26	93.45	0.88	0.12	6.17	2.83	3.31	0.10
	ESP35/45	0.31	94.35	1.16	0.15	5.26	2.29	2.95	0.07
	Silo	0.17	95.88	1.08	0.13	3.03	0.97	2.06	<0.02
S2	ECO	0.32	98.42	0.93	0.11	1.37	0.76	0.59	0.05
	ESP12	0.30	97.44	1.22	0.17	2.36	1.44	0.9	0.04
	ESP22	0.37	97.10	2.05	0.29	2.30	1.44	0.85	0.04
	ESP32/42	0.37	95.88	2.22	0.33	2.98	1.55	1.42	0.04
	Silo	0.25	97.36	1.50	0.22	2.66	1.79	0.86	0.06
S3	BA	0.08	99.52	0.54	<0.02	0.35	0.29	0.03	0.10
	ESP12	0.32	96.15	1.22	0.14	3.46	1.98	1.47	0.05
	ESP22	0.37	95.09	1.70	0.21	4.25	2.35	1.89	<0.02
	ESP32	0.59	95.00	2.99	0.49	3.43	1.77	1.66	<0.02
	Silo	0.25	95.13	1.18	0.15	4.17	1.94	2.21	0.04
S4	BA	0.04	99.89	0.25	<0.02	0.22	0.16	0.05	0.04
	ECO	0.11	94.32	0.59	0.04	5.32	1.49	3.79	0.16
	ESP12	0.35	93.26	1.12	0.15	6.32	2.27	4.02	0.09
	ESP22	0.35	92.27	1.72	0.23	6.12	1.92	4.19	0.04
	ESP32	0.48	93.37	2.69	0.4	5.41	1.83	3.57	<0.02
	Silo	0.25	94.32	1.36	0.17	5.32	1.93	3.36	0.09
Minimum		0.04	92.27	0.25	<0.02	0.22	0.16	0.03	<0.02
Average		0.27	95.63	1.28	0.19	3.60	1.61	1.97	0.06
Maximum		0.59	99.89	2.98	0.49	6.32	2.83	4.19	0.24
CV (%)		45.60	2.22	51.44	60.51	52.78	47.10	64.84	81.63

M, moisture; A, ash yield; VM; Volatile matter; S, sulfur; C, carbon; t, total; org, organic; g, graphite or elemental carbon; CO_2, inorganic; ad, air-dried; d, dry basis; BA, bottom ash; ECO, economizer; ESP, electrostatic precipitator; CV, coefficient of variation

The ashes from the ECO present slightly higher SiO_2/Al_2O_3 ratios, which is probably due to the higher contents of quartz, as was verified by XRD and petrography (Table III - 7). Despite some variations, the oxide concentration tends to slightly increase to the back of the ESP, while the SiO_2 and SiO_2/Al_2O_3 ratio behaves in reverse, which can be related to the decreasing quartz content (Table III - 6). Similar to sulfur, P and Na tend to volatilize during combustion, but their condensation on FA is triggered by the decrease in the temperature in the ESP, so lower concentrations in BA and an increase in the ESP are expected (Meij, 1995). The uneven distribution of nonvolatile elements (e.g., Si, Fe, Al, and K) must be related to their modes of occurrence, such as the association to the glass phase (Figure III - 1).

Table III - 6. Major oxide results for the bulk coal ashes (wt.%).

Campaign	Sample	SiO_2	TiO_2	Al_2O_3	Fe_2O_3	MnO	CaO	MgO	Na_2O	K_2O	P_2O_5	SO_3	Cr_2O_3	LOI	SiO_2/Al_2O_3
S1	BA	66.07	0.81	18.28	7.95	0.08	1.50	1.87	1.04	2.11	0.14	0.03	0.02	0.10	3.61
	ECO	67.77	0.66	15.15	8.13	0.08	1.81	1.86	1.10	1.72	0.13	0.07	0.02	1.51	4.47
	ESP12	59.65	0.88	20.22	6.36	0.06	1.34	1.83	1.07	2.37	0.16	0.13	0.02	5.89	2.95
	ESP15	61.27	0.84	18.71	7.30	0.07	1.59	1.97	1.14	2.13	0.18	0.15	0.02	4.63	3.27
	ESP22	58.81	0.89	20.58	6.31	0.06	1.24	1.79	1.06	2.45	0.16	0.12	0.02	6.49	2.86
	ESP25	58.74	0.88	20.31	6.55	0.06	1.61	1.91	1.14	2.26	0.18	0.37	0.02	5.99	2.89
	ESP32/42	59.77	0.85	19.62	6.29	0.06	1.30	1.76	1.04	2.33	0.15	0.13	0.02	6.68	3.05
	ESP35/45	59.23	0.87	19.91	6.65	0.07	1.62	1.93	1.14	2.26	0.17	0.15	0.02	5.96	2.97
	Silo	60.30	0.90	20.81	6.74	0.06	1.35	1.89	1.11	2.44	0.17	0.17	0.02	4.04	2.90
S2	ECO	68.25	0.67	15.40	8.42	0.06	1.49	1.13	0.73	1.33	0.11	0.33	0.27	1.81	4.43
	ESP12	62.52	0.84	19.16	7.89	0.04	2.02	1.25	1.33	1.78	0.13	0.30	0.02	2.72	3.26
	ESP22	57.22	0.95	21.76	8.32	0.05	2.38	1.61	1.62	2.10	0.21	0.43	0.02	3.32	2.63
	ESP32/42	56.65	0.98	22.18	7.62	0.06	1.88	1.86	1.43	2.38	0.23	0.37	0.02	4.33	2.55
	Silo	61.07	0.87	19.65	8.13	0.04	2.05	1.36	1.32	1.88	0.14	0.35	0.02	3.12	3.11
S3	BA	65.89	0.77	18.03	8.85	0.07	1.44	1.57	0.94	1.89	0.14	0.09	0.02	0.30	3.65
	ESP12	61.02	0.86	19.94	7.70	0.06	1.33	1.58	1.06	2.10	0.15	0.25	0.02	3.93	3.06
	ESP22	57.20	0.94	21.63	7.93	0.06	1.38	1.78	1.20	2.31	0.19	0.30	0.02	5.05	2.64
	ESP32	54.78	0.99	22.35	8.71	0.07	1.52	1.97	1.22	2.39	0.28	0.45	0.03	5.24	2.45
	Silo	60.91	0.84	19.66	7.48	0.06	1.36	1.60	1.07	2.08	0.17	0.18	0.02	4.56	3.10
S4	BA	66.56	0.79	17.60	9.01	0.07	1.56	1.65	0.94	1.88	0.10	0.03	0.02	−0.20	3.78
	ECO	63.11	0.70	16.23	8.37	0.07	1.76	1.63	0.87	1.70	0.11	0.05	0.01	5.38	3.89
	ESP12	58.71	0.83	18.97	7.82	0.06	1.57	1.76	1.06	2.08	0.13	0.34	0.02	6.66	3.10
	ESP22	54.79	0.90	20.52	7.92	0.07	1.60	1.95	1.16	2.25	0.17	0.56	0.02	8.09	2.67
	ESP32	53.82	0.94	21.49	8.15	0.07	1.67	2.04	1.23	2.34	0.22	0.98	0.02	7.03	2.50
	Silo	58.94	0.85	19.31	7.84	0.06	1.62	1.83	1.06	2.14	0.14	0.42	0.02	5.76	3.05
Minimum		53.82	0.66	15.15	6.29	0.04	1.24	1.13	0.73	1.33	0.10	0.03	0.01	−0.20	3.55
Average		60.52	0.85	19.50	7.70	0.06	1.60	1.74	1.12	2.11	0.16	0.27	0.03	4.34	3.10
Maximum		68.25	0.99	22.35	9.01	0.08	2.38	2.04	1.62	2.45	0.28	0.98	0.27	8.09	3.05
CV (%)		6.5	9.8	9.7	10.2	15.3	16.4	13.0	15.7	12.9	24.7	76.1	163.3	51.3	0.67

LOI: loss-on-ignition; BA: bottom ash; ECO: economizer; ESP: electrostatic precipitator; CV: coefficient of variation.

Table III - 7. X-ray diffraction (wt.%) and petrographic (vol.%) results for bulk coal combustion ashes.

	S1									S2					S3					S4					
	BA	ECO	ESP						Silo	ECO	ESP			Silo	BA	ESP			Silo	BA	ECO	ESP			Silo
			12	15	22	25	32/42	35/45			12	22	32/42			12	22	32/42				12	22	32/42	
XRD (wt.%)																									
Quartz (SiO_2)	11.5	24.8	12.5	16.1	10.3	12.8	12.5	13.6	12.3	21.4	21.9	11.0	10.1	20.4	19.5	16.1	11.1	6.8	16.7	8.8	18.0	12.0	8.1	7.0	13.5
Cristobalite (SiO_2)	0.3	0.1	0.0	0.1	0.0	0.0	0.1	0.0	0.1	0.0	0.1	0.0	0.1	0.1	0.1	0.1	0.1	0.0	0.1	0.8	0.0	0.0	0.0	0.0	0.1
Mullite ($Al_6Si_2O_{13}$)	6.6	8.3	4.7	5.2	4.4	5.1	4.6	5.3	5.1	6.7	7.5	4.4	5.2	6.9	12.5	5.8	5.2	4.6	6.6	6.6	4.6	4.1	3.1	3.5	5.8
Cordierite ($Mg_2Al4Si_5O_{18}$)	0.2	0.1	0.2	0.1	0.1	0.2	0.0	0.1	0.1	0.1	0.3	0.1	0.1	0.2	0.1	0.2	0.1	0.1	0.1	0.5	0.2	0.1	0.1	0.1	0.1
Albite ($NaAlSi_3O_8$)	0.0	1.4	0.9	0.9	0.9	0.0	1.5	1.4	1.4	0.1	2.2	1.9	1.2	1.8	1.9	1.4	2.0	0.8	1.0	0.5	0.1	1.9	1.6	0.8	1.0
Diopside ($(Ca,Mg,Fe)_2Si_2O_6$))	0.1	0.7	0.8	1.3	0.4	0.0	0.2	1.2	1.4	0.3	0.5	0.8	1.9	1.1	0.5	0.3	0.8	1.3	0.2	0.0	0.4	0.5	0.6	0.7	0.4
Calcium aluminate ($Ca_3Al_2O_6$)	0.1	0.5	0.1	0.0	0.1	0.1	0.1	0.0	0.2	0.0	0.4	0.5	0.3	0.2	0.1	0.3	0.3	0.3	0.2	0.1	0.1	0.2	0.4	0.3	0.3
Rutile (TiO_2)	0.1	0.5	0.3	0.4	0.2	0.1	0.2	0.2	0.0	0.0	0.4	0.1	0.1	0.3	0.3	0.4	0.2	0.0	0.4	0.1	0.2	0.2	0.0	0.1	0.4
Hematite (α-Fe_2O_3)	0.6	0.6	0.7	1.0	0.6	0.7	0.6	0.9	0.5	1.4	0.8	0.5	0.6	1.8	2.3	0.7	0.7	0.5	0.6	1.1	1.1	0.6	0.5	0.4	0.9
Maghemite (γ-Fe_2O_3)	1.0	1.2	0.2	0.5	0.4	1.3	0.4	0.5	0.5	2.3	0.0	0.1	0.3	0.7	0.7	0.5	0.5	0.3	0.3	2.0	3.2	0.4	0.3	0.2	0.5
Magnetite (Fe_3O_4)	0.0	2.0	0.9	1.5	0.9	1.1	1.0	0.0	0.0	0.5	2.0	1.7	0.8	0.2	0.5	0.8	0.5	0.8	1.5	0.1	0.4	0.6	0.8	0.7	1.1
Magnesioferrite ($MgFe_2O_4$)	0.0	0.2	0.4	0.7	0.0	0.0	0.0	1.0	0.5	0.0	0.2	0.2	0.0	0.7	0.0	0.2	0.3	0.0	0.2	0.0	0.0	0.5	0.0	0.2	0.3
Hercynite ($FeAl_2O_4$)	0.0	0.4	0.0	0.2	0.0	0.1	0.0	0.0	0.0	0.0	0.0	0.0	0.1	0.0	0.1	0.0	0.1	0.1	0.0	0.3	0.0	0.0	0.0	0.0	0.1
Calcite ($CaCO_3$)	0.0	0.1	0.1	0.1	0.1	0.1	0.1	0.1	0.1	0.0	0.2	0.2	0.2	0.2	0.1	0.1	0.2	0.2	0.0	0.0	0.0	0.2	0.2	0.2	0.2
Gypsum ($CaSO_4 \cdot 2H_2O$)	1.5	0.4	0.3	0.3	0.2	1.6	0.2	0.6	0.3	2.8	0.5	0.3	0.3	0.5	0.5	0.4	0.3	0.3	0.2	0.2	1.0	0.4	0.4	0.3	0.6
Anhydrite ($CaSO_4$)	0.0	0.1	0.1	0.1	0.1	0.2	0.1	0.1	0.1	0.1	0.2	0.3	0.3	0.2	0.0	0.2	0.2	0.3	0.1	0.2	0.3	0.1	0.2	0.3	0.3
Amorphous	77.9	58.5	78.0	71.4	81.1	76.8	78.4	75.0	77.3	64.2	63.0	78.0	78.6	64.7	60.7	72.7	77.3	83.7	71.7	78.8	70.4	78.3	83.8	85.4	74.7
Petrography (vol.%)																									
Glass	78.9	71.2	76.1	72.0	80.2	77.6	79.8	77.4	79.6	72.2	76.3	83.1	83.6	79.0	80.5	78.8	84.2	77.3	76.8	79.6	71.2	74.3	75.9	79.3	76.9
Quartz	4.8	14.2	4.0	7.4	4.2	4.8	1.5	4.8	5.4	12.4	9.5	4.8	5.7	8.0	6.5	9.0	3.4	1.8	6.0	5.9	9.0	5.6	4.7	4.1	5.5
Mulllite	8.8	1.5	0.8	0.6	1.0	0.8	1.0	0.4	0.4	1.2	0.0	0.2	0.2	0.0	5.9	1.0	0.2	0.0	0.8	6.3	0.8	0.6	0.3	0.5	0.8
Anorthite	0.0	0.0	0.0	0.0	0.0	0.0	0.0	0.0	0.0	0.0	0.0	0.0	0.0	0.0	0.0	0.0	0.0	0.0	0.0	0.4	0.0	0.0	0.0	0.0	0.0
Ferrosphere	2.6	3.7	3.2	2.8	1.6	1.8	2.2	1.6	1.6	3.4	4.4	2.2	2.9	4.0	2.5	2.0	2.2	4.3	2.4	2.9	2.6	3.0	2.1	2.4	2.5
Other	2.4	2.0	3.8	3.2	2.0	1.8	2.0	3.0	2.8	1.0	2.2	1.8	0.7	2.0	1.3	1.2	0.6	3.7	2.4	3.1	1.8	1.4	1.6	2.4	3.7
Partially baked	2.2	5.2	1.3	3.0	1.6	2.4	2.5	1.2	3.2	6.4	3.4	2.4	1.2	4.0	2.1	3.0	1.0	0.7	4.0	1.4	5.6	3.8	0.3	0.5	2.9
Char	0.0	2.0	10.8	11.0	9.0	10.9	10.6	11.0	7.0	2.8	4.2	5.3	5.5	3.0	0.0	4.6	8.0	11.7	7.2	0.4	9.0	11.2	15.3	10.2	7.8
Unburned coal	0.0	0.0	0.0	0.0	0.4	0.0	0.5	0.6	0.0	0.6	0.0	0.2	0.2	0.0	1.1	0.4	0.4	0.5	0.4	0.0	0.0	0.2	0.0	0.5	0.0

BA, bottom ash; ECO, economizer; ESP, electrostatic precipitator.

The oxides, P_2O_5, SO_3 and Cr_2O_3, presented the highest coefficient of variation (CV > 25%). In the case of Cr_2O_3, the value is largely influenced by an anomalous concentration found on the sample, S2-ECO.

According to (Vassilev and Vassileva, 2007), all the ashes analyzed belong to the sialic type, with a medium acid tendency. The authors attribute this type of acidity to coals enriched in clay and mica, quartz, and minor amounts of authigenic sulfates, carbonates, and sulfides, which is corroborated by the respective feed coal mineralogy (Table III - 3). From the perspective of the cement industry, the ashes are classified as F, and where the LOI is greater than 6 %, additional tests would be required to approve its use (ASTM C618, 2005).

The ashes are mainly composed of an amorphous phase (58.2 - 85.4 wt.%), which encompasses aluminosilicate glass (71.2 - 84.2 vol.%), char (up to 15.3 wt.%), and unburned coal (up to 1.1 wt.%), identified via petrographic analysis (Table III - 7). SEM/EDS investigations enabled the discrimination of two main types of glass (Valentim et al., 2009b; Wang et al., 2019): (a) A major class, with chemical compositions similar to illite/smectite, occurring as large masses in BA and as subrounded/rounded particles in FA (Figure III - 1, Z3); and (b) A minor class, essentially composed of Al and Si, generally occurring with irregular shapes and spongy textures, in FA and BA (Figure III - 1, Z2). The latter is similar to the vesicular Al-Si glass, described by (Matjie et al., 2006; Wang et al., 2019), in BA samples from the pulverized-coal Luzhou Chuannan Power Station. Previously, Matjie et al., (2006) had already described an Al-Si glass with a honeycomb structure, but in clinker/coarse ash from a Sasol–Lurgi fixed bed dry bottom, which was attributed to kaolinite dehydration. Kolker et al., (2017), via a SHRIMP-RG ion microprobe analysis on FA from U.S. power plants, describe a glass almost exclusively composed of Al-Si depleted in REE. The Al-Si glass identified under the current research is easily distinguished under petrographic analysis by its bright white color and its spongy/vesicular texture (Figure III - 1D). The remaining glasses exhibit a wide range of colors but, in general, are less porous. The presence of Ca has been associated with yellowish colors (Valentim et al., 2018) while iron seems to be responsible for a dark brown color (Figure III - 1D). In the current work, this brownish glass was more often observed in BA during petrographic analysis, suggesting that the glasses in BA are richer in Fe.

Quartz and mullite are the dominant crystalline phases, corresponding to 6.8 - 24.8 wt.% and 3.1 - 12.5 wt.%, respectively (Table III - 7). Because of its high melting temperature (approximately 1800 °C), quartz is expected to pass through combustion without major alterations (Ward, 2016). Nevertheless, surface reaction rims, which are characterized by the loss of the quartz translucence and the presence of bubbles, were observed in several grains. Mullite is mainly derived from kaolinite and can be incorporated into the matrix of the glass spheres (e.g., Henry et al., 2004; Hulett and Weinberger, 1980; Wang et al., 2019). The small nature of FA particles limits the identification of mullite during petrographic analysis, and they are, therefore, undervalued (Table III - 7). Economizer FA presents the highest contents of quartz and partially baked particles (Table III - 7). The coarser nature of these particles must control their early retention in the particle control system. The content of quartz and mullite tend to decrease towards to the back of the ESP, contrary to the amorphous phase trend (Table III - 7). The increase in the amorphous phase trend corresponds not only to the increase in the glass content, but also to the char (Table III - 7). These trends are consistent with previous works (e.g., (Valentim et al., 2009).

Iron oxides, such as magnetite, hematite, and maghemite, represent approx. 2 wt.%, on average, of the FA. The economizer FA presents higher maghemite contents (1.2 – 3.2 wt.%) than the BA and ESP FA, which may be the result of magnetite oxidation. These phases result from the decomposition of the Fe-bearing phases present in feed coals (Table III - 3), such as pyrite and siderite, and are found embedded in Fe-rich aluminosilicate glass, which are the main components of ferrospheres (Lauf, 1982). Some of them react with MgO originating magnesioferrite (up to 0.2 wt.%), a distinctive mineral of the magnesiaferrosphere morphotypes (Sokol et al., 2002; Valentim et al., 2018), which are counted as “others” in this study’s petrographic analysis (Table III - 7).

1.3. REE and other refractory elements in feed coals and respective ashes

1.3.1. Contents, distribution, and partitioning

The results regarding the trace elements (ppm), enrichment patterns, and anomalies of the individual REE in feed coals, and the respective bulk combustion ashes, are available in the Supplementary Information, Table A1 and Table A2.

The concentrations of REE (∑REE) in the feed coals range from 6.97 to 23.15 ppm, corresponding to an overall coefficient of variation (CV) of 26.9% (Table A1). The average REE concentration (18.70 ppm) is significantly lower than the average concentrations reported for the world hard coals (WHC): 68.41 ppm; U.S. coals: 62.09 ppm; and Chinese coals: 138.47 ppm (Dai et al., 2008; Finkelman, 1993; Ketris and Yudovich, 2009). The feed coal with the smallest ash yield (3.28 wt.%, S1-C) also presents the lowest ∑REE, at 6.97 ppm, suggesting an association of REE with the mineral matter, which is corroborated by the positive correlation between REE and the ash yield (Figure III - 3A). Excluding S1-C, the REE content changed slightly over time, corresponding to an average of 20.65 ppm, and a CV of 7.9 %.

With regard to the REE enrichment patterns after the normalization to UCC: four coals present H-type enrichment ($La_N/Lu_N < 1$), namely, C1 and C2 from S2, and C1 and C2 from S4; two present L-type enrichment ($La_N/Lu_N > 1$), namely, S1-C and S3-C1; and one presents M-type enrichment ($La_N/Sm_N < 1$, $Gd_N/Lu_N > 1$), without Eu anomaly, namely, S3-C2 (Table A1; (Rudnick and Gao, 2014; Seredin and Dai, 2012). All coals present negative Ce anomalies and positive Gd anomalies. The samples, S2-C2 and S1-C, can be differentiated from the others through the negative anomalies in Eu and Y, respectively (Table A1).

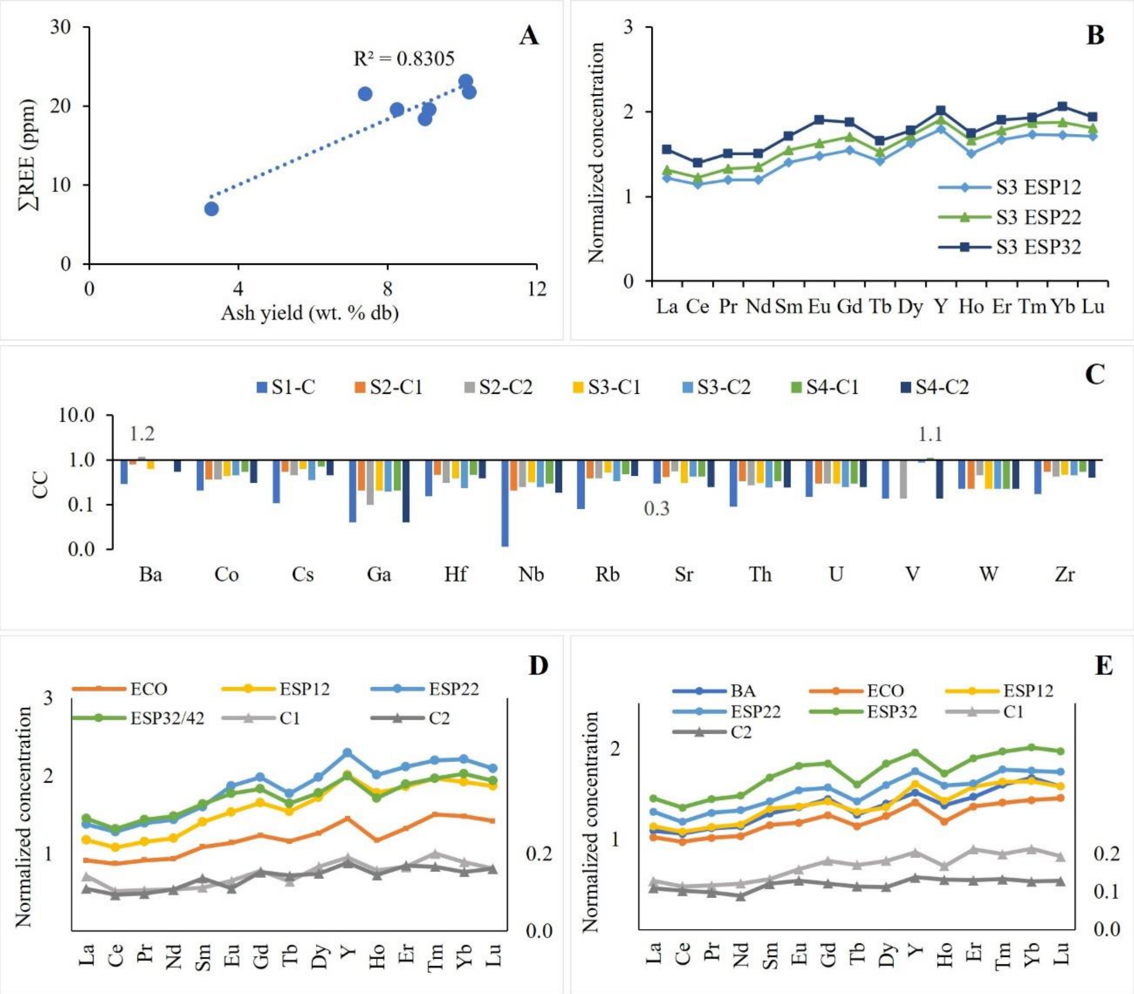

Figure III - 3. Bivariate plot correlating ash yield (wt.%) with ∑REE; (B) REE concentrations from ESP ashes of S3, normalized to UCC (Rudnick and Gao, 2014); (C) concentration coefficients (CC) of trace elements in the feed coals—normalized to average trace-element concentrations in world hard coals (Ketris and Yudovich, 2009); comparison of REE concentrations normalized to UCC from feed coals and the respective ashes from the campaigns: (D) S2, and (E) S4.

The remaining trace elements analyzed occur in the following order of average concentrations: Ba > Sr > V > Zr > Rb > Co > Nb > Ga > Th > U > Cs > Hf > W (Table A1). Be, Sn, and Ta were below the detection limits. Most of these trace elements were depleted, relative to the world hard coals, with low concentration coefficient (CC < 0.5) (Dai et al., 2015; Ketris and Yudovich, 2009) (Figure III - 3C). As was verified for the REE, the feed coal from S1 has the lowest concentrations for all the trace elements analyzed.

The coal combustion ashes present higher concentrations than their respective feed coals, for all the trace elements analyzed (Table A2). The REE contents in the coal ashes are in the range of 159.9 - 266.6 ppm, 8 to 30 times more than the feed coals, with a global CV of 13.10 % (Table A2). Still, the average REE content, 211 ppm, is low compared to the averages reported for coal ashes from China (473 ppm), the United States (460 ppm), Europe (279 ppm), and others (298 ppm) (Fu et al., 2022), as well as the references therein. The ashes present H-type enrichment ($La_N/Lu_N < 1$), positive anomalies of Y, Eu, and Gd, and negative anomalies of Ce (Table A2). The similarities to the feed coal patterns and anomalies suggest that the REE have not been significantly differentiated among the ashes (Figure III - 3D,E).

The predominance of other trace elements in the ashes, considering their average concentrations, is similar to that found in feed coals: Ba > Sr > V > Zr > Rb > Ga > Co > Nb > Th > Cs > Sn > U > Hf > W > Be > Ta (Table A2). The elements, Nb, Cs Ga, Rb, V, and Th, presented the highest enrichments in relation to the respective feed coals, by 21 to 92 times, on average. Compared to the average values defined by Ketris and Yudovich, (2009) for coal ashes, most of the elements were found depleted or in normal concentrations (CC < 2), except for V, which was slightly enriched (2 < CC <5) in the ESP fly ashes, from the last rows from S2 and S4. However, the Ga concentrations in the back ESP rows are near or above the cutoff of 50 ppm for its coproduction with Al (Dai and Finkelman, 2018). Gallium shows relative enrichments (RE), up to 6 in the back rows, and about 1 in BA (Table A3), suggesting its volatilization during combustion and further condensation triggered by the temperature decrease in the ESP. The back rows capture small amounts of fly ash. However, a selective collection could be considered for the extraction of this critical raw material (European Commission, 2020).

The average REE concentrations of the sampling campaigns decrease as follows: S3, 226.76 ppm > S2, 225.19 ppm > S4, 214.81 ppm > S1, 190.65 ppm (Table III - 8). This shows the importance of the REE content in the parent coal, since the coal ashes generated from S1 resulted from the feed coal containing the lowest amount of REE

(Table A1). Campaign S2 presented the greatest variation in the REE content among the ashes (88.67 ppm), corresponding to a CV of 14.25 % (Table III - 8).

Table III - 8. Descriptive statistics regarding REE contents (∑REE) of coal ashes by sampling campaign.

		Minimum	Maximum	Range	Average	Coefficient of Variation (CV)
		ppm				%
S1	Bulk	159.94	207.80	47.86	190.65	7.19
	ESP 12–42	191.14	194.53	3.39	193.00	0.73
	ESP 15–45	178.19	206.85	28.66	193.14	0.86
S2	Bulk	169.79	258.46	88.67	225.19	14.25
	ESP 12–42	220.24	258.46	38.22	244.84	7.12
S3	Bulk	197.48	266.07	68.59	226.76	10.33
	ESP 12–32	219.08	266.07	46.99	240.87	8.03
S4	Bulk	182.33	257.14	74.81	214.81	11.02
	ESP 12–32	205.09	257.14	52.05	230.06	8.10

SX, sampling campaign; ESP, electrostatic precipitator fly ash

The REE concentration is dependent on the sampling site and follows the order, ESP FA > BA > ECO FA (Table A2), which correlates positively with the production ratios of the materials within the power plant: 90 % ESP FA; 8 % BA; and 2 % ECO FA. The smaller concentrations of REE found in the BA, compared to the ESP fly ash, is aligned with what has been reported (Dai et al., 2010; Ma et al., 2019; Wang et al., 2019; Wei and Song, 2020). Except for Zr, which is slightly more concentrated in the BA compared to the ECO and the ESP FA, the remaining trace elements present similar distributions to the REE. Zirconium, as a REE, and Cs, Hf, Sr, and Th are classified as nonvolatile elements, and are expected to have an even distribution among the combustion products (RE ≈ 1) (Meij, 1995). Nevertheless, some variations are observed (Table A3) and may be related to aspects other than volatility, such as the mode of occurrence (Clarke, 1993; Hower et al., 2020a; Mardon and Hower, 2004; Meij, 1995).

Despite some variations, the REE concentrations and the respective relative enrichments, tend to increase towards the last row of ESP hoppers (Table A3). The highest variation of ∑REE among the ESP fly ashes was found in S4, corresponding to 52.02 ppm, and a CV of 8.10 % (Table III - 8). Except in the referred campaign, the LREE/HREE ratio also increases across the ESP, even though, in some cases, the maximum values can be found in the second row (S1 and S3, Table A2). Nevertheless, the comparison of the concentrations normalized to UCC (Rudnick and Gao, 2014) does not show significant REE partitioning (Figure III - 4 III - 3B).

The increase in LREE/HREE ratio across the ESP rows was previously reported for a power plant burning high-S coals from western Kentucky (Hower et al., 2013), however, most of the published data describe a decrease in the LREE/HREE ratio (e.g., P. Liu et al., 2019; Mardon and Hower, 2004), as in S4 (Table A2). Although these trends are not entirely understood but the following may play major roles (Fu et al., 2022; Hower et al., 2020a): (a) the vaporization-condensation of HREE associated with OM; and (b) higher amounts of glass in the FA from the ESP back rows. The organic association of REE is commonly linked with low-rank coals, but it can also be found in minor amounts in high-rank bituminous coals (Finkelman et al., 2018). Considering the lack of REE fractionation, the slight variations observed in the current work are most likely due to the fly ash petrological differences (e.g., amount of glass).

1.3.2. Geochemical associations

The modes of occurrence of the REE in the feed coals and the respective ashes were initially investigated using statistical analysis (hierarchical cluster analysis and Pearson's correlation coefficients), which can provide information concerning organic and inorganic affinities and the potential relations among elements (Eskanazy et al., 2010; Gürdal, 2011; Zhao et al., 2015). Oxides and elements from feed coals with more than one value below the detection limit (bdl) were excluded to avoid skewness in the results. The bdl values considered for the analysis were replaced by bdl/2. The associations between the oxides and trace elements in the feed coals are broadly indicated by the dendrogram in Figure III - 4, the correlation coefficients (CC) are presented in Table A4, and two major groups of elements are distinguished.

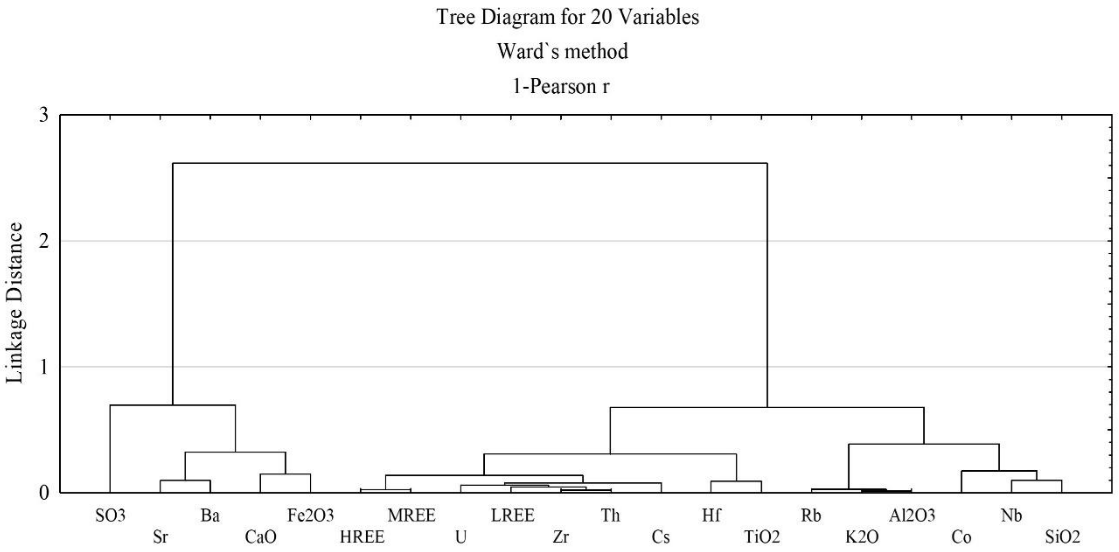

Figure III - 4. Dendrogram developed from cluster analysis on the geochemical data from feed coals (cluster method, Ward's method; interval, Pearson's correlation values).

The first group includes SO_3, Sr, Ba, CaO, and Fe_2O_3 (Figure III - 4). These elements do not show significant positive correlations with ash ($r < 0.64$), SiO_2 ($r < 0.51$) or Al_2O_3 ($r < 0.53$), and, except for SO_3 and Sr, they present a strong negative correlation with carbon:

$r > -0.81$ (Table A4). These correlations are most likely related to the sulfate and sulfide minerals found in feed coals, such as gypsum and pyrite (Table III - 3).

The second group consists of REE and the remaining elements. Except for Hf, they show a strong positive relation to ash ($r > 0.80$, $\rho < 0.05$). Apart from TiO_2, K_2O, and Hf, the elements in this second group also show a significant negative correlation with carbon ($r < -0{,}76$, $\rho < 0.05$), suggesting an inorganic association, which is in line with several studies showing REE primarily associated with minerals in coals (e.g., Finkelman et al., 2018; Hower et al., 2018; Seredin and Dai, 2012). The REE appear to be closely associated with U ($r > 0.91$), Th ($r > 0.94$), Cs ($r > 0.90$), and Zr ($r > 0.95$), and all the elements are significantly correlated with each other, suggesting a common source (Table A4). Since Zr is also found to be positively correlated with SiO_2 ($r >0.78$), these correlations can represent the occurrence of zircon, where lithophile elements, such as REE, U and Th, are commonly found incorporated (Rollinson, 2014).

The REE-bearing phases typically occur in volumetric proportions below the XRD limits, and since SEM/EDS have been proven to be useful for their identification in coal and coal combustion ashes (Dai et al., 2017a; Hood et al., 2017; Montross et al., 2018; Thompson et al., 2018; Valentim et al., 2019), SEM/EDS investigations were conducted on the selected samples.

The examination of the selected feed coals via SEM/EDS enabled the identification of particles containing Ce - La - Nd (Figure III - 5A,C,E,F), Ce (Figure III - 5B), and Y–Dy–Gd (Figure III - 5D), with phosphorous as a major component. In some cases, the occurrence of Ce - La - Nd is associated with Th (Figure III - 5A,F). This corroborates the inorganic association suggested by the statistical analysis, with phosphates, most likely monazite, and xenotime, as the REE carriers. The statistical correlation between REE and P was not assessed because the P_2O_5 concentrations were below the detection limit (Table III - 3). This is in agreement with the study of Finkelman et al., (2018), where sequential leaching experiments in nine samples of bituminous coals were performed and showed that REE are mainly associated with phosphates (70 % LREE, 50 % HREE). No Sc-bearing particles were found, and no REE were detected, outside the particles containing REE. Zirconium-, Ti-, and Ba-bearing particles were found, but no REE were detected in them. The particle sizes ranged from 0.31 to 3.47 µm, with an average of 1.45 µm (measured in the longest section).

The REE-bearing phases were mainly found embedded in clays (Figure III - 5A,B,F), which corroborates the correlations found through statistical analysis. Few particles were found in the organic matter (Figure III - 5C) or embedded in quartz (Figure III - 5E). The spatial association of REE-bearing minerals with other minerals in coals (such as clays) can be an important factor with regard to their incorporation within the aluminosilicate glass of the resulting ashes (Fu et al., 2022).

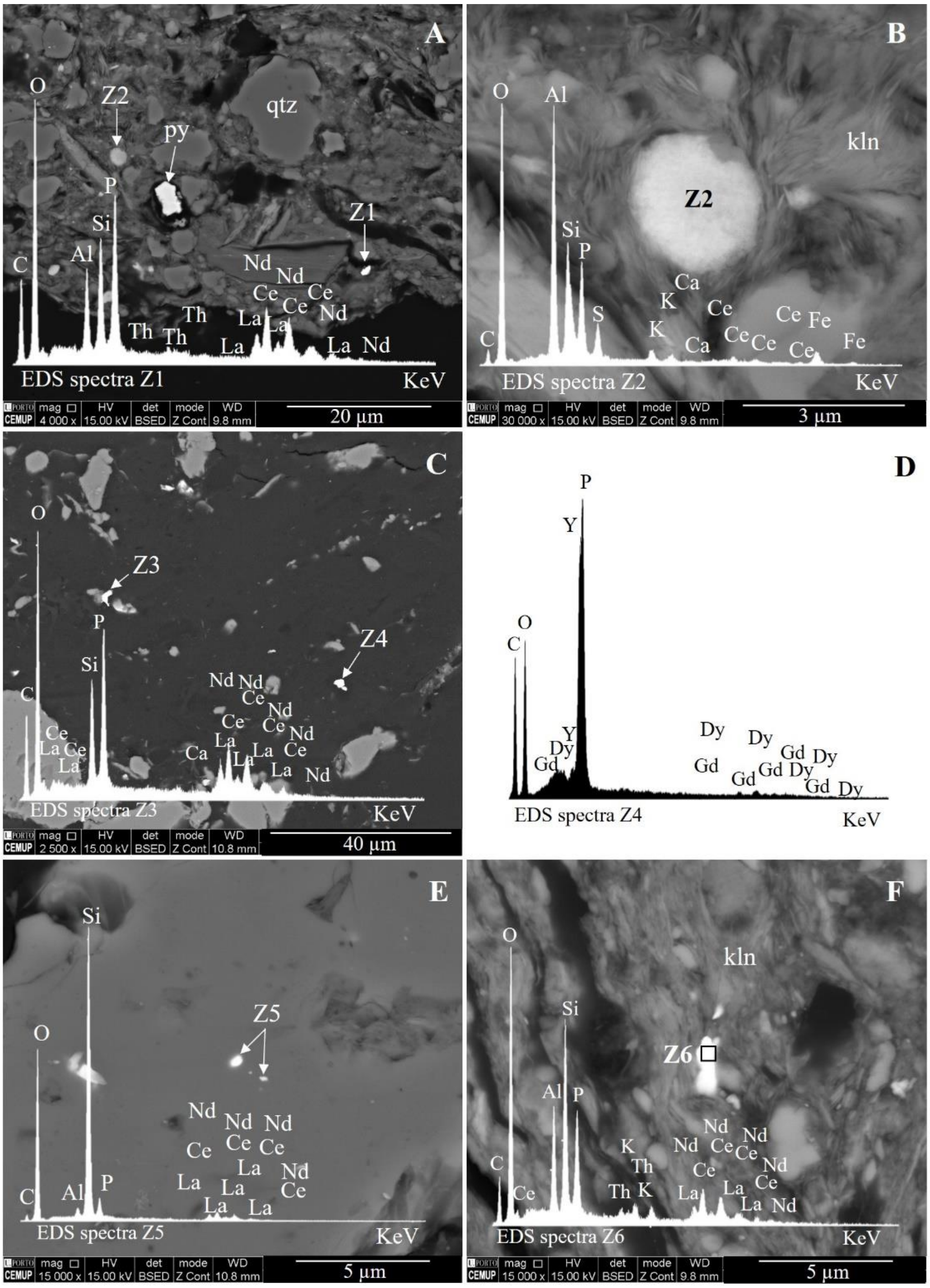

Figure III - 5. Examples of REE-bearing particles found on feed coals via SEM/EDS analysis: (A) general view of coal matrix with particles bearing Ce-La-Nd, with P as major element intermixed with clays, dashed square, Z1, and EDS spectrum (Z1, ×4000); (B) magnification of dashed square, Z2, in "A", and EDS spectrum, Z2, illustrating rounded Ce-bearing particle intermixed with kaolinite (Kln) (×20,000); (C,D) REE-bearing phosphates hosted in organic matter (×2500); (E) particle bearing Ce-La-Nd, with P as major element in quartz (qtz); and (F) particle-bearing Ce-La-Nd and Th, with P as major element intermixed with clays (×15,000); py: pyrite.

The associations between oxides and trace elements in coal combustion ashes are indicated by the hierarchical clustering dendrogram in Figure III - 6, and the correlation coefficients are presented in Table A5 from the supporting information.

Three main groups of elements are identified in the dendrogram. Group 1 includes the elements, Zr and Hf, and the oxides, SiO_2 and Fe_2O_3, which are positively correlated with ash ($r > 0.54$, $\rho < 0.05$), and negatively correlated with carbon ($r > -0.60$, $\rho < 0.05$), which suggests an inorganic occurrence (Table A5). In Group 2, the MREE and HREE are associated with Co, Sr, Ba, Be, SO_3, Na_2O, and CaO (Figure III - 6).

With the exception of SO_3, these elements and oxides do not show significant correlations with either ash or carbon (Table A5), which points to mixed organic and inorganic associations. Nevertheless, significant correlations are not limited within the group, which suggests several modes of occurrence. All the REE exhibited significant positive correlations with the oxides: Al_2O_3 ($r > 0.66$), P_2O_5 ($r > 0.56$), and TiO_2 ($r > 0.67$) (Table A5). The third group includes LREE and the remaining trace elements, which were all significantly correlated with the major oxides: Al_2O_3, K_2O, TiO_2, and P_2O_5 (Table A5). As with MREE and HREE, the LREE do not present significant correlations with ash or with carbon, suggesting that REE can occur in organic and inorganic associations.

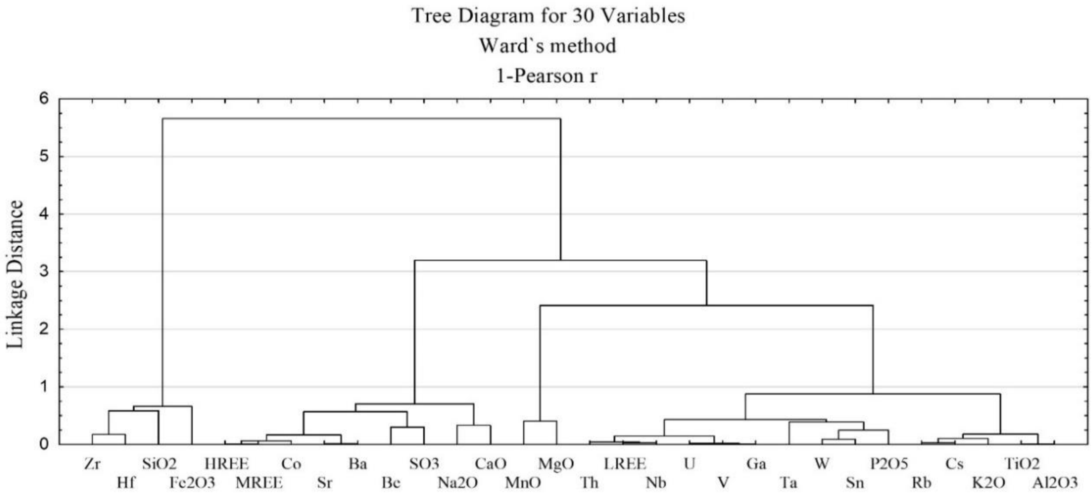

Figure III - 6. Dendrogram from cluster analysis on the geochemical data from bulk ashes (cluster method, Ward's method; interval, Pearson's correlation values).

The relationship with the major oxides suggests the possible occurrence of REE in sulfates, phosphates, and aluminosilicate glass. The existence of nano-sized REE-bearing particles in carbon was reported in fly ashes derived from bituminous coals (Hood et al., 2017; Hower et al., 2019; Hower and Groppo, 2021). Even so, most of the studies show that the REE in coal combustion ashes are mainly associated with aluminosilicate glass (e.g., Bartoňová et al., 2018; Hower et al., 2017b; Izquierdo and

Querol, 2012; Kolker et al., 2017; Lin et al., 2018; P. Liu et al., 2019; Pan et al., 2019; Stuckman et al., 2018; Taggart et al., 2018; Tang et al., 2019).

This association could be the result of the incorporation of the REE-bearing phases, or, less probably, to the REE diffusion into the glass phase (Fu et al., 2022).The results of the REE-bearing phase tracking via SEM/EDS in the bulk ash particulate blocks from S1 are summarized in Table III - 9. A total of 17 REE-bearing particles were identified in nine ash samples, and the numbers of particles found per polished block ranged from 1 to 5. In the BA and the FA from the economizer and silo, three REE-bearing particles were identified, one in each sample. In the FA from the ESP, a total of 14 particles were counted, 9 in the samples from rows 12–32/42, and 5 in the samples from the opposite side. The particle sizes ranged from 0.38 to 8.62 µm, with a corresponding average size of 3.35 µm (Table III - 9).

The particles included Ce - La (one count), Ce-La-Nd (eleven counts), Y (two counts), Y-Dy (one count), Y-Dy-Tb (one count), and Y-Dy-Er-Gd-Yb (one count), with phosphorous or aluminosilicate glass as major components (Table III - 9). Most of the REE-bearing phases were found to occur as discrete particles, with spherical/rounded or angular shapes (Figure III - 7A,B), with few trapped on char pores (Figure III - 7D), and a small number were found embedded in aluminosilicate glass (Figure III - 7C,E,F).

Table III - 9. Descriptions of the REE-bearing grains found in the ash particulate blocks by SEM/EDS.

Sample	Grains Counted	Size (µm)	Major Element (s)	REE Detected	Description
S1-BA	1	[a] 0.76	P	Ce-La-Nd	Particles embedded in glass (Si-Al < Mg-Fe < K-Ti-Ca-Na)
S1-ECO	1	3.07	P	Ce-La-Nd	Spherical particle embedded in glass (Si-Al < Na-K < Fe-Mg-Ca)
S1-ESP 12	2	3.20	Al-Si	Ce-La-Nd	Spherical particle retained on char pore
		1.55	Si-Al	Y	Spherical discrete particle
S1-ESP 15	1	3.10	P	Y-Tb-Dy	Rounded discrete particle
S1-ESP 22	2	[a] 0.38	Zr	Y	Particles embedded in Si-Al glass
		1.54	P	Ce-La-Nd	Spherical discrete particle
S1-ESP 25	3	3.39	P	Ce-La-Nd	Angular discrete particle
		2.14	Al-Si	Ce-La-Nd	Spherical discrete particle
		2.48	Al-Si	Ce-La-Nd	Spherical discrete particle
S1-ESP 32/42	5	2.64	P	Ce-La	Angular discrete particle
		4.22	Si-Al	Y-Dy	Spherical discrete particle
		5.01	Si-Al	Ce-La-Nd	Spherical particle retained on char pore
		8.62	P	Y-Dy-Er-Gd-Yb	Spherical discrete particle
		5.92	P	Ce-La-Nd	Angular discrete particle
S1-ESP 35/45	1	6.13	Al-Si	Ce-La-Nd	Spherical discrete particle
Silo	1	2.89	P	Ce-La-Nd	Spherical discrete particle
Total	17	Mean: 3.35			

SX, sampling campaign; BA, bottom ash; ECO, economizer FA; ESP, electrostatic precipitator fly ash

[a] Average of 10 particles measured

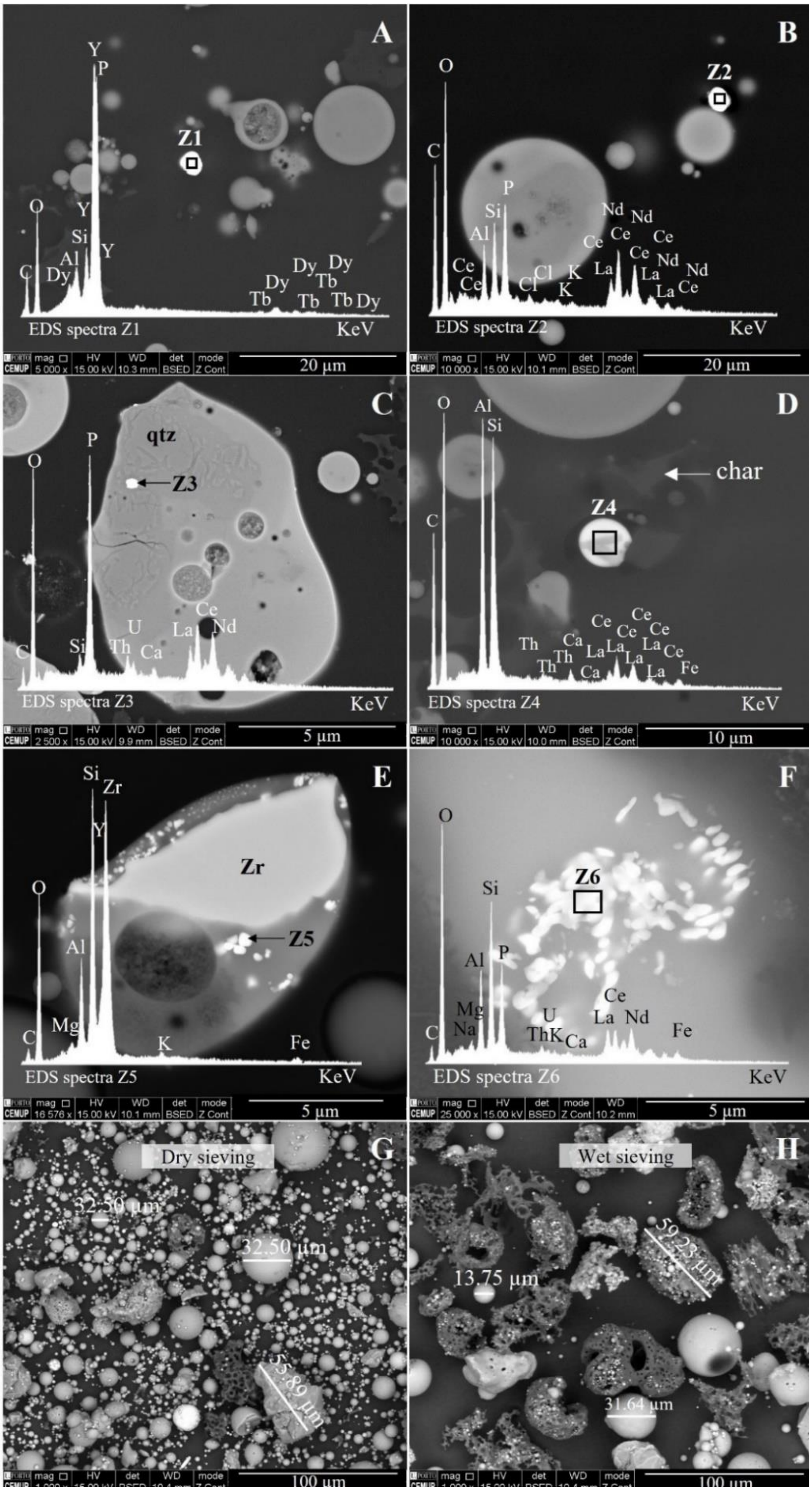

Figure III - 7. Observations under SEM/EDS (BSE mode): (A) discrete Y-Dy-Tb-bearing particle with P as major component (×5000); (B) discrete rounded particle bearing Ce-La-Nd, with P as major component (×10,000); (C) rounded particle bearing Ce-La-Nd, with P as major component, embedded in Al-Si glass beside quartz, qtz (×2500); (D) spherical Ce-La-Nd-bearing particle trapped in char pore (×10,000); (E) Zr-phases incorporated in aluminosilicate glass; (F) Particles with Ce-La-Nd and Th-U embedded within an Al-Si-Ca glass that also contains Ce-La-Nd-Th-U; size-fraction: 42–25 µm from S1-ESP12 sample, before (G) and after (H) wet sieving (BSE mode, ×1000).

The REE-bearing phases identified in the feed coals, such as monazite and xenotime, appear to persist in the combustion ashes. In some discrete particles with P as a major component, Si and Al were also detected, but further analysis would be needed in order to assess the nature of these associations. The existence of discrete particles trapped on char can have an in-fluence on the statistical analysis, and it might indicate an organic correlation that does not exist.

No carrier phases for Sc were found, and REE were not detected in the Ba- and Ti-bearing particles identified. Instead, Zr-bearing particles containing Y (i.e., zircon; Figure 7E) were found embedded in an aluminosilicate glass and were adjacent to a Zr-bearing phase without traceable REE (Figure III - 7E). The particles seem to have resulted from the Zr-bearing phase breakdown with the partitioning of the Y to the melt. Y-bearing zircons have been previously detected in fly ash samples by SEM/EDS and TEM (Hood et al., 2017; P. Liu et al., 2019).

Furthermore, (P. Liu et al., 2019) also observed a Zr-phase exhibiting melting features similar to those observed in this research. Zircon is often considered to be stable at high temperatures (1690 °C; Finch, 2003) and, thus, to be resistant to the combustion process; however, its alteration is well known in natural igneous systems (Watson and Harrison, 1983). Several particles displaying similar features were identified, but no REE were detected in them.

In the bottom ash sample, P-bearing particles with Ca and Ce-La-Nd are visually identical to the Zr-bearing particles with Y (Figure III - 7F). However, in this case, REE were also detected in the aluminosilicate glass (brighter area), which appear to be homogeneous, and the facet observed could have resulted from the REE diffusion into the Si-Al glass. Nevertheless, without further detailed analysis, the occurrence of REE-bearing nanoparticles or REE-enriched domains at the nanoscale must be considered (e.g., (Hood et al., 2017). P. Liu et al., (2019) studied the decomposition of pure typical REE carriers in coals and verified the melting characteristics on REE phosphates. Apatite, which is an important REE carrier in coal, can decompose to other phases at temperatures above 1000 °C (Fu et al., 2022).

1.3.3. Particle Size and Magnetic Fractions

Several studies have shown that greater REE concentrations are usually found within finer-particle-sized and nonmagnetic fractions, particularly in fly ashes (Blissett et al., 2014; Campbell et al., 1978; Lin et al., 2017; Rosita et al., 2020). Moreover, the removal of the Fe-rich fraction before the REE extraction process is important since iron oxides can compete with REE during the hydrometallurgical process (acid leaching) (Nugroho et al., 2019). With consideration to this, the selected ash samples were sieved and magnetically separated, and the resulting fractions were analyzed via ICP-MS to assess the REE distribution.

The ashes from S1 and S4 were used for sieving since all the sampling locations were included (BA, ECO, and ESP FA). The fractions >150 µm from the ESP fly ashes represented <2 wt.% of the bulk ash, so they were added to the 150–75 µm fractions, and this was labelled as >75 µm. A substantial retention of the micrometric particles was spotted on the 45–25 µm fractions via SEM/EDS (Figure III - 7G). Even when using low amounts of sample, the high adhesion forces in the finer particles can cause agglomeration and can lead to its retention (Hrnčířová et al., 2013; Jillavenkatesa et al., 2001; Merkus, 2009). To assess the effect of this on the REE distribution, wet sieving trials were performed on <45 µm fractions from the first ESP row samples, and the fractions were analyzed. Wet sieving removed, on average, 20 wt.% of the fraction (45–25 µm), visibly reducing the amount of the micrometric glass particles retained (Figure III - 7H).

Magnetic separation was performed on six ash samples, BA, ECO, and ESP-12 from S1 and S4. Wet magnetic separation was used to reduce the possibility of particle agglomeration.

The REE enrichment was characterized using the same parameters Lin et al., (2017): the enrichment factor (EF), which is calculated by dividing the REE concentration in the fraction by that in the feed, as given by Equation (1), and the REE recovery, defined by the ratio of the amount of total REE in each fraction to the amount of total REE in the feed, as in Equation (2). To reduce the influence of sample heterogeneity, the REE concentration in the feed was calculated by mass balance (Lin et al., 2017):

$$EF_i = \frac{REE_i}{\sum_{i=1}^{n}(REE_i W_i)} \qquad \text{(Equation 1)}$$

$$R_i\ (\%) = \frac{REE_i W_i}{\sum_{i=1}^{n}(REE_i W_i)} \times 100 \qquad \text{(Equation 2)}$$

where REE_i is the total REE concentration of the fraction; W_i is the weight percentage of the fraction; and n is the total number of fractions.

The results regarding the yield (wt.%), trace elements (ppm), REE anomalies, EF, and recovery of the size and magnetic fractions, are summarized in Table A6. The REE distribution across the size-fractions differs according to the type of material. In the BA size-fractions, the REE concentrations vary by, on average, 29 ppm (184.3 - 213.5 ppm avg.), and the coarser fractions generally have slightly higher concentrations (Table A6). The enrichment factor (EF) varies between 0.92 and 1.10, while the recovery can reach up 39.4%. The fractions greater than 1 mm (comprising >50 wt.% of bulk ash) present recoveries of twice as much of the remaining size-fractions (Figure III - 8). The coarse nature of the particles facilitates their separation and represents a recovery higher than 60 % of the REE present in the BA.

In the FA samples, the REE content is higher in the finer fractions (<25 µm), which is in agreement with what has been reported (Blissett et al., 2014; Lanzerstorfer, 2018a; Liu et al., 2017; Rosita et al., 2020), but some differences are verified between the ECO and ESP. In the ECO FA, the REE content decreases by 20-40 % (42–75 ppm) between the fractions >150 µm and 150-75 µm, before progressively in-creasing till fractions <25 µm (Table A6).

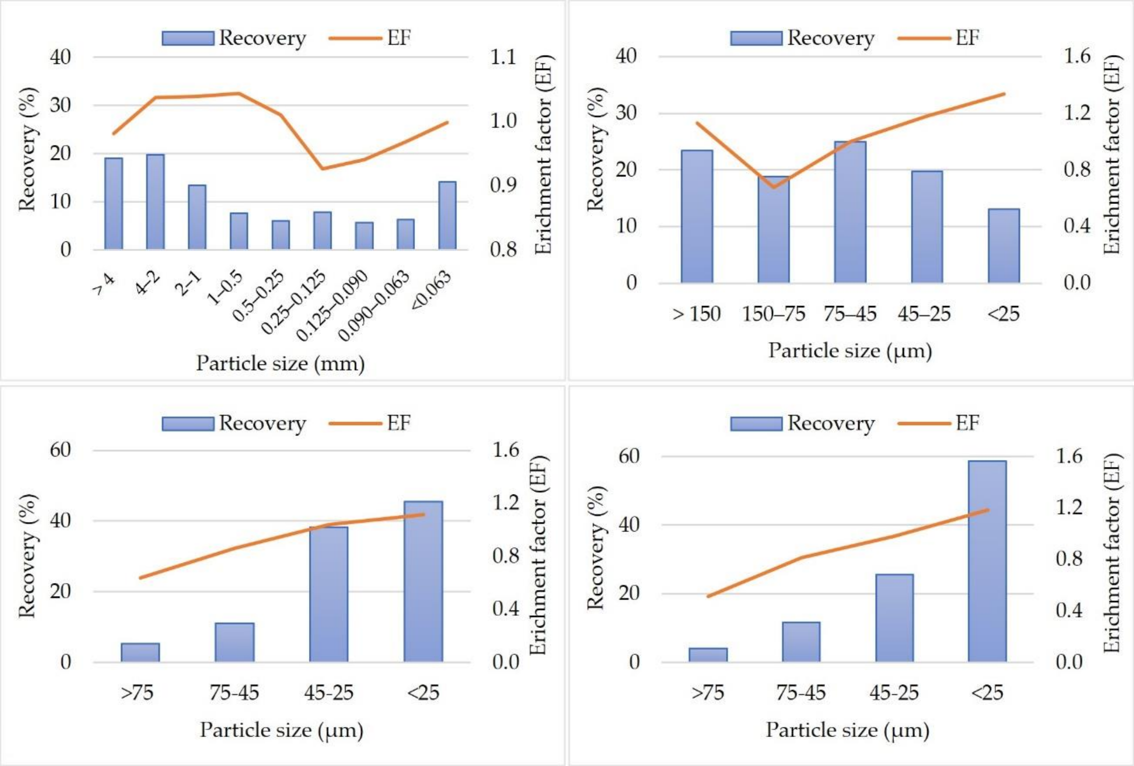

Figure III - 8. REE enrichment factors and recoveries (%) in the size-fractions obtained by dry sieving: (A) BA from S1; (B) ECO fly ash from S1; (C,D) ESP fly ash from S1 and S4, respectively.

The recovery on the ECO size-fractions varies within a range of approx. 10% (13.85–25.79% avg.) (Figure III - 8). Still, the EF can reach up to 1.32-1.34 in the <25 µm fraction, which is higher than the EF found for the same size-fraction from the ESP FA (1.05–1.24). However, as is shown in Figure III - 8, the REE recoveries on fractions <25 µm in the ESP FA are above 40%, while, in the ECO FA, the recoveries are below 17%. The wet sieving led to a decrease in the EF on fractions <25 µm, while the recoveries increased to the range of 78.3–86.2 %. As stated by (Wills and Finch, 2016), the grade and the recovery inversely correlate, which means that higher recoveries imply more impurities on the product, and, consequently, a lower grade (and EF). Ultimately, both parameters should be kept as high as possible during the beneficiation process.

As is observed in this study, and as has been previously reported, the LREE/HREE ratio in the fly ashes from the ESP tends to decrease with the decreasing particle size (Blissett et al., 2014; Dai et al., 2014c; Lanzerstorfer, 2018b; Lin et al., 2017; Liu et al., 2017; Rosita et al., 2020), although, in some cases, there is a slight increase between the fractions >75 µm and from 75–45 µm, before decreasing towards <25 µm fractions (Table A6). In comparison, the REE distributions on the ECO fly ash samples are similar, but their LREE/HREE ratios show the opposite trend (Table A6). The examination of the REE normalized patterns vs. the particle size (Figure III - 9) shows no significant fractionation between the size-fractions, suggesting that the differences found on the LREE/HREE ratio may result from differences in the fly ash petrology, e.g., the amount of glass (Fu et al., 2022). Despite some variations, the remaining trace elements analyzed show distributions similar to those described for the REE (Table A6).

The nonmagnetic fractions of the ESP fly ashes contained up to 53.96 ppm more REE than the respective magnetic fractions, with an EF ranging between 1.06 and 1.10 (Table A7). The REE concentration changes slightly between the magnetic and non-magnetic fractions of the BA and ECO fly ash. Yet, minor enrichments in the magnetic fractions are noted for some REE: (a) S1-ECO, Sm-Eu and Yb; (b) S1-BA, Sm-Eu, Tb-Y, and Yb; and (c) S4-ECO, Gd-Y and Tm (Table A7). The enrichment of REE, such as Pr, Gd, and Tb, have been previously noted in magnetic fractions from fly ashes, despite their lower REE contents (Hower et al., 2021, 2017b).

All the magnetic fractions show slightly higher percentages of critical REE, up to 2.2 %, but the REE recoveries are significantly lower than in nonmagnetic fractions (Table A7). Additionally, they contain slightly higher concentrations of other critical elements, such as Co, Ga, V, and W, compared to the nonmagnetic fractions (Table A7). The removal of Fe-rich fractions, in addition to being beneficial downstream for REE ex-traction, could result in a value-added product.

Overall, the fractions analyzed (size, magnetic, and nonmagnetic) show an enrichment pattern of the H-type ($La_N/Lu_N < 1$), weak positive anomalies of Eu, positive anomalies for Y and Gd, and negative anomalies for Ce (Table A6 and Table A7), resembling the results found for the bulk ashes.

A single trial, combining magnetic separation and dry sieving (cut at 25 µm), was performed on S1-ESP12. The final product corresponded to 42.8 wt.%, and presented an REE content of 240.83 ppm, an enrichment factor of 1.25, and a recovery of 53.3%. This represented an increase of almost 50 ppm in the REE, relative to the raw sample.

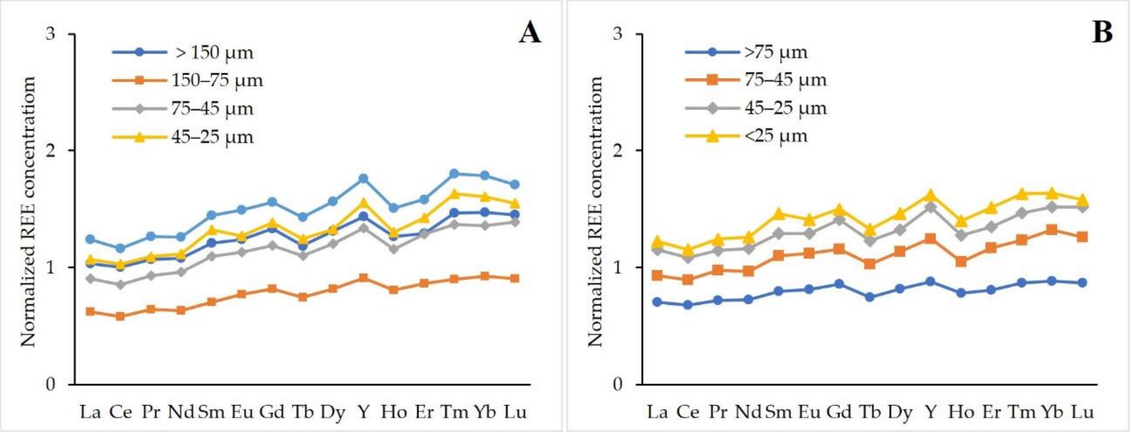

Figure III - 9. Examples of normalized REE distribution patterns (relative to UCC, [32]) of fly ash size-fractions from S1: (A) economizer; and (B) ESP, hopper 12.

1.3.4. Evaluation of REE Potential

The REE potential of the coal combustion ashes and the respective fractions (size, magnetic, and nonmagnetic) analyzed under this research was assessed following the method established by Seredin, (2010) and Seredin & Dai, (2012). This method is based on plotting the percentage of the critical REE (Y + Nd + Eu + Tb + Dy + Er) in the total REE, identified as the $REY_{def,\ rel}$%, versus the ratio of critical/excessive REE ((Nd + Eu + Tb + Dy + Er + Y)/∑REE)/((Ce + Ho + Tm + Yb + Lu)/∑REE)), identified as the “outlook coefficient” (C_{outl}), and it essentially evaluates the quality of the ore. Dai et al., (2017a) updated the method by adding 1000 ppm of REO (rare earth elements as oxides) as the minimum content for an economic extraction.

The bulk ashes exhibit C_{outl} in the range of 0.95-1.18, and a $REY_{def,\ rel}$% between 35.19 and 40.01 %, placing them in the category of a “promising” raw material (Table A6; Figure III - 10A). However, considering the updated version of Dai et al., (2017a), the bulk ashes are not considered to be economical because the REO contents are below 1000 ppm (Figure III - 10B). The size, magnetic, and nonmagnetic fractions present similar C_{outl} and $REY_{def,\ rel}$% to the bulk ashes: 0.93-1.13 and 38.96 %, respectively (Table A6, Table A7; Figure III - 10A). The REO content varies by a slightly wider range (111.35–327.49 ppm), reflecting the REE content variation described in Section 3.3.1., but it is still far below the cutoff (Figure III - 10B).

Even so, it is important to emphasize that the average percentage of critical REE ($REY_{def, rel}$ %) found in either raw ashes or its fractions (37.13 and 36.68 %, respectively) is higher than in some conventional REE ores (Fu et al., 2022).

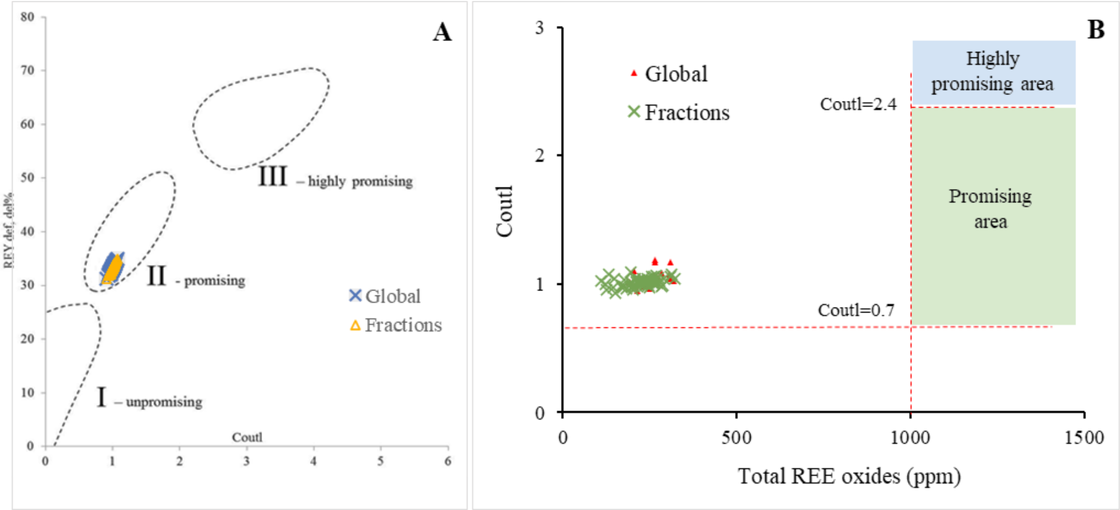

Figure III - 10. REE-potential evaluation of bulk ashes and respective fractions, according to (A) Seredin, (2010) and Seredin & Dai, (2012), $REY_{def, rel}$ vs. Coutl; and the (B) updated version from Dai et al., (2017).

1.4. Conclusions

Samples of commercial Colombian coals and the respective combustion ashes, collected for over a year from the Pego power plant (Portugal), were characterized in order to assess the REE distribution and evaluate the potential of ashes as REE raw materials. Selected ash samples were fractionated and characterized to search for trends that could be used for further REE extraction.

Feed coals were predominantly medium D rank (high-volatile A bituminous coal) and vitrinite-rich, containing low-to-medium ash content and low sulfur content, and were mainly composed of quartz and kaolinite. The respective ashes are Class F, and they are mainly composed of aluminosilicate glass (>71.2 vol.%) and low CaO (<2.38 wt.%).

The coal sample REE concentrations ranged between 6.97 and 23.15 ppm, which is low compared to the world, U.S., and Chinese coals, which is most likely due to their beneficiation. The geochemical associations, corroborated by SEM/EDS, suggest an inorganic association, and Ce,La, Nd, Y, Dy, and Gd were found in <10 µm P-rich grains intermixed with clays.

The ash samples studied presented REE concentrations ranging from 159.9 to 266.6 ppm. The ESP FA present higher REE concentrations (217 ppm average) than the BA (195.45 ppm average) and ECO FA (170.69 ppm average), and generally increase towards the ESP back rows, along with the LREE/HREE ratio. During the SEM/EDS analysis, the REE were mainly detected in <10 µm discrete rounded particles, with P and Al-Si as the major components.

The REE content increases with the decreasing FA particle size. The EF in the ECO FA <25 µm fraction (1.33) was greater than the respective fraction in the ESP FA. However, the REE recovery is low in the former, while it can overcome 50 % in the latter. With regard to the magnetic separation, the ESP FA nonmagnetic fraction is slightly enriched in REE (>40 ppm), compared to the magnetic fraction, while no significant variations were found in the ECO and BA magnetically separated fractions. Meanwhile, the combination of magnetic separation, followed by the dry sieving of the ESP FA, increased the REE content by approx. 50 ppm, and recovered approx. 53 % of the REE.

Overall, the normalized REE patterns and the individual element anomalies show no significant fractionation, either on the bulk ashes or the respective fractions; therefore, the variations found are most likely related to the variations in the fly ash petrology.

All the ash samples studied are promising REE raw materials, but their REO contents are far from the established cutoff of 1000 ppm (Dai et al., 2017a; Seredin and Dai, 2012). Combining sieving and magnetic separation was insufficient to achieve the cutoff, but further trials may be conducted in the fractions proven to be more promising, by resorting to other concentration techniques (e.g., density separation) to try to increase the REE concentrations in the products. Nevertheless, with the increasing demand for REE, the exploration of this type of low-grade secondary resource, requiring no mining and milling, may become profitable in the near future.

2. Carbonaceous solid residue (char)

2.1. Char concentration process

The results obtained from the bulk ash characterization (Part III, chapter 1,Table III - 5), showed that the fly ash from the first row of the ESP was the most promising sample for char recovery. Even though the FA from ESP back rows contain higher carbon grades, the first row represents approximately 80 % of the total FA collected by the ESP. Moreover, BA and economizer FA contain <2 wt.% of carbon (Part III, chapter 1,Table III - 5).

In the context of this thesis, it would be necessary to execute several concentration trials and obtain a char concentrate of approximately 500 g. Thus, one specific sampling task was made to collect approx. 50 kg of fresh FA from the first row of the ESP at Pego power plant. Table III - 10 summarizes the chemical, mineralogical, and petrographic composition of this FA sample which is similar to the FA characterized before (Part III, chapter 1,Table III - 5, Table III - 7).

Table III - 10. Chemical, mineralogical, and petrographic composition of the FA sample selected for char recovery (ESP 1st row, Pego TPP) (adapted from Badenhorst et al., 2019).

Proximate analysis (wt.%)		Mineralogy (wt.%)	
Moisture (air-dry)	0.30	Quartz (SiO_2)	14.7
Ash (dry)	95.09	Mullite ($Al_6Si_2O_{13}$)	4.2
Volatile matter (dry-ash-free)	30.60	Hematite (α-Fe_2O_3)	0.7
		Maghemite (γ-Fe_2O_3)	1.5
Carbon forms (wt.%)		Amorphous	78.9
Total carbon	5.49	Petrography (vol.%)	
Organic carbon	2.90		
Elemental carbon	2.57	Organics	7.2
Inorganic carbon	0.03	Anisotropic char	5.6
		Isotropic char	0.6
Major oxides (wt.%)		Inertinite	1.0
		Partially burned coal	0.0
Al_2O_3	19.9		
CaO	1.38	Inorganics	92.8
Fe_2O_3	6.14	Glass	84.6
K_2O	2.25	Quartz	7.0
MgO	1.75	Mullite	0.0
Na_2O	1.25	Anorthite	0.0
P_2O_5	0.18	Partially Baked clay	0.2
SiO_2	59.1	Dense iron	0.4
TiO_2	0.90	Dendritic iron	0.6
Mn_3O_4	0.08	Other	0.0
SO_3	0.10		
LOI	5.85		

The visual observation of color gradation from the FA size-fractions (Figure III - 11), and their observation under SEM/EDS (e.g., for char particles abundance; Figure III - 12) indicated that char would be more concentrated in the coarser size fractions (>75 µm), which is corroborated by the higher values of total carbon (C_{tot}) (Table A6). This is agreement of have been previously reported (e.g., Badenhorst et al., 2019; Dai et al., 2014c; Hurt and Gibbins, 1995; Külaots et al., 2004; Liu et al., 2017; Lu et al., 2007; Sharonova et al., 2008).

Thus, fixed carbon (FC) and carbon recoveries were used to assess which particle size of the selected ESP FA presented the highest potential for char concentration (Figure III - 13). Despite FC include inorganic, organic and graphitic carbon this method was considered preferable to other methods, such as C_{tot} and petrography, for assess char contents during concentration trials since it can be easily calculated from proximate analysis which are an easy, low-cost and low-time consuming method.

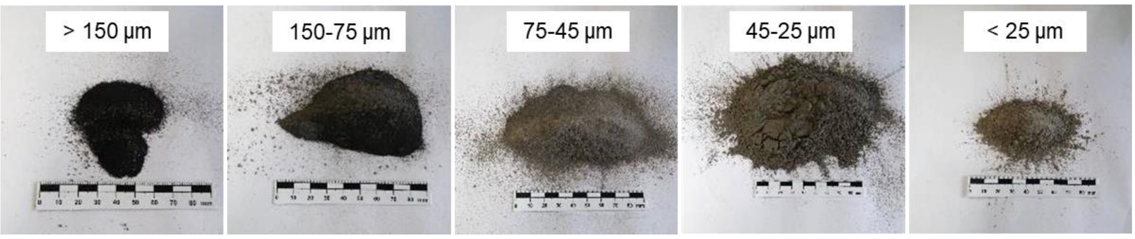

Figure III - 11. Visual comparison of the FA size-fractions obtained by dry sieving revealing the color shift from black to light grey as particle-size decreases and indicating a decrease of the char amount.

The results showed that the >150 µm fraction had a high FC, >25 wt.%, db, but represented less than 2 wt.% of the bulk FA sample and only 12 % of the carbon would be recovered (Figure III - 13A). Therefore, considering cumulative yield and the carbon recovery versus the carbon grade (as FC), the cut-off size was established at 75 µm (Figure III - 13B). As a result, approx. 49 wt.% of the total carbon could be recovered and the FC of the product would be greater than 10 wt.%, db.

Micrometric (<10 µm) glassy spheres were still present on size-fractions >75 µm, either loose or infilling the char pores (Figure III - 12A-C). In particles with dimensions <50 µm the friction forces with the sieve mesh are greater than the gravity, which hinders their passage through the mesh (Merkus, 2009). Moreover, due to high cohesion forces the small particles have a propensity to adhere to larger particle surfaces and form agglomerates, causing their retention in coarser fractions (Merkus, 2009; Rosita et al., 2020).

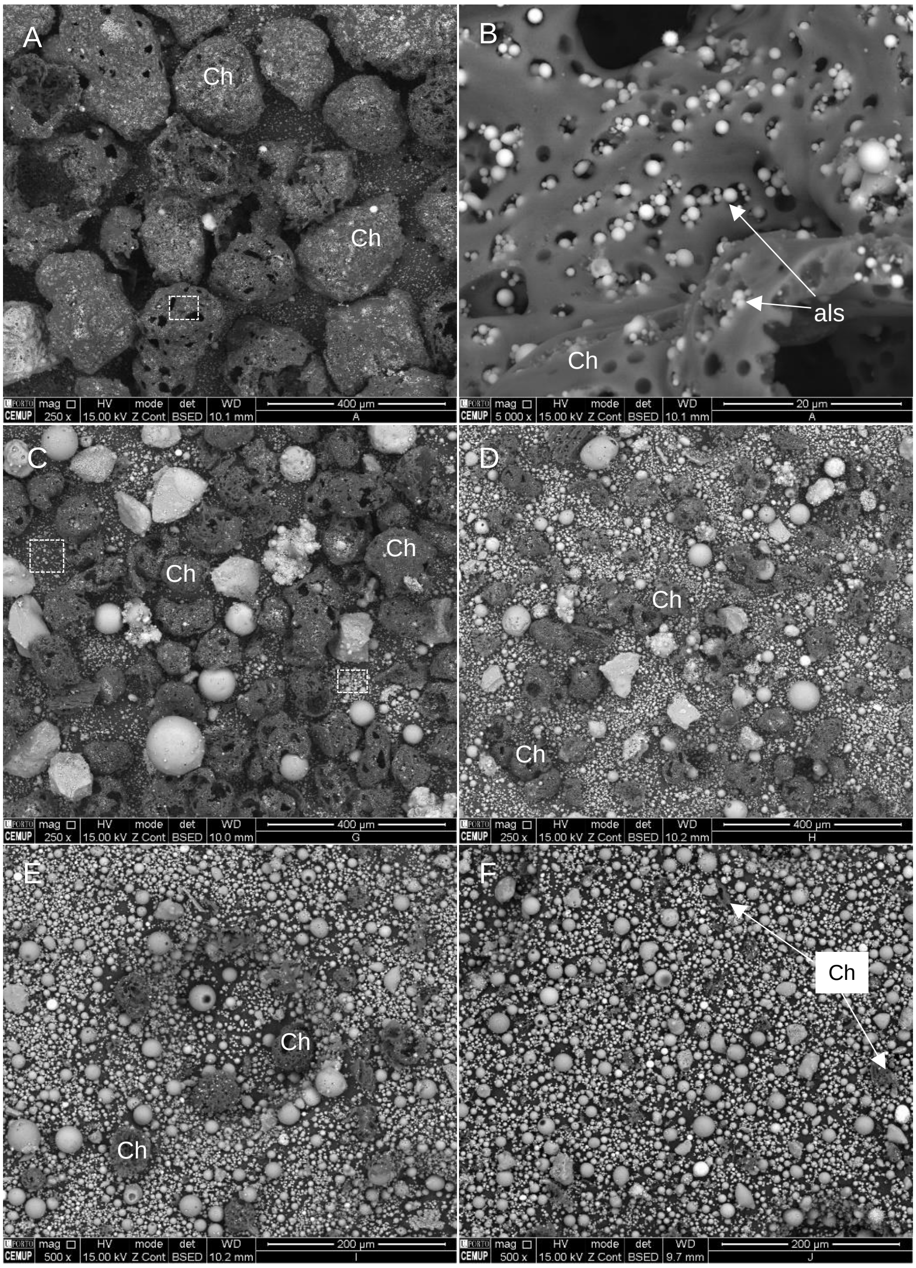

Figure III - 12. Observations of size-fractions obtained by dry sieving under SEM/EDS (BSE mode) showing the decrease in the amount of char particles (Ch) with decreasing particle size: (A) >150 µm (×250); (B) magnification of dashed square in “A” (×5000) where micrometric glassy spheres (als) are observed infilling char pores; (C) 150-75 µm, dashed squares signaling areas with loose micrometric glassy spheres (×250); (D) 75-45 µm (×250); (E) 45-25 µm (×500); (F) <25 µm (×500).

Considering the above mentioned, after dry sieving, two beneficiation methods were further implemented to remove the micrometric glassy aluminosilicate spheres from the >75 µm fraction: gravimetric separation (sink-float) and wet sieving, both using tap water only. The gravimetric separation besides enabling the recovery of a light fraction mainly composed of aluminosilicate hollow spheres (<1.0 g/cm^3; Vassilev et al., 2004b), which is a value-added product with a wide range of applications (e.g., lightweight fillers in polymers and insulators), should also promote the deagglomeration of particles before wet sieving. In this latter process, water is expected to act as dispersant enhancing the passage of the smaller particles through the sieve apertures (Merkus, 2009).

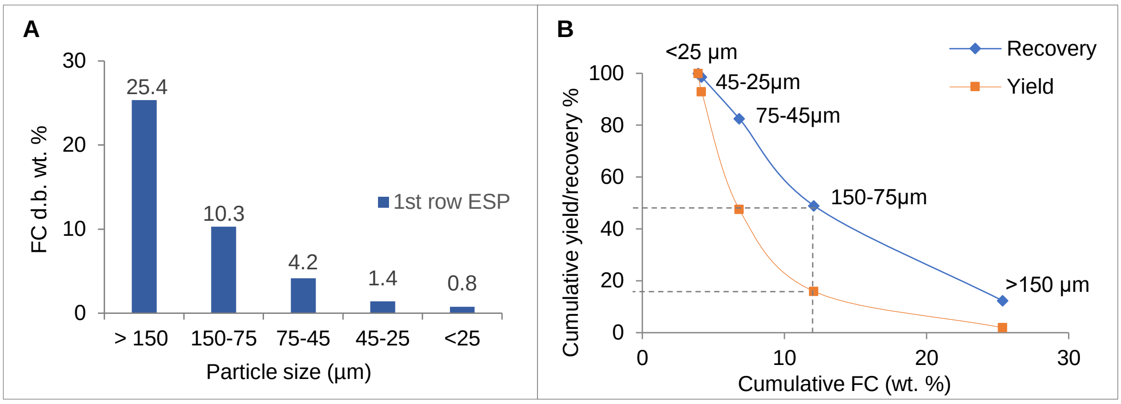

Figure III - 13. (A) Fixed carbon variation across the ESP FA size-fractions obtained via dry sieving, (B) cumulative carbon grade, carbon recovery, and sample yield curves for the ESP FA.

The floating fraction represented a small fraction of the sample (<1 wt.%) and was mainly composed of aluminosilicate glassy spheres and few char particles (Figure III - 14A). The observation of several broken hollow spheres suggested the prevalence of cenospheres (hollow spheres) which was in agreement with previous studies (e.g., Vassilev et al., 2004b). Regarding wet sieving, micrometric glassy spheres were still observed after sieving (Figure III - 14B) even after a significant portion of sample has been discarded (>40 wt.%). As with dry sieving, this can be explained by the temporary blinding of the sieve due to particle agglomeration (Jillavenkatesa et al., 2001).

To release the aluminosilicate glassy spheres infilling the char pores, sonication trials were carried out using a probe-sonicator (Vibra-Cell model VCX 500; Sonics and Materials Inc., Newtown, CT, USA). A total of four trials with 1 g subsamples in 150 mL of water were carried out changing the time and power conditions: (1) 10 min – 50 %; (2) 20 min – 50 %; (3) 20 min – 50 % and (4) 10 min – 70 %. The suspensions were sieved (75 µm sieve), dried and observed under SEM/EDS.

The yield of the fraction retained in the 75 µm sieve after the sonication trials ranged from 7 to 23 wt.%. The sonication essentially promoted fragmentation of the particles, which was also observed by (Zhang et al., 2012), and the liberation of the micrometric glassy spheres infilling the char pores was limited (Figure III - 14C,D; Figure A1). Since the use of this method would lead to a substantial loss of char (as fragments) it was discarded, and it was decided to rather implement a second cycle of gravimetric separation followed by wet sieving to increase the removal of the micrometric particles retained, loose, or infilling char pores.

The discard of particles finer than 75 µm and the floating fraction (dry and wet sieving plus sink-float) from the bulk fly led to the removal over than 50 % of MgO, Na_2O, K_2O, MnO, and TiO_2, 40 % of Al_2O_3, Fe_2O_3 and CaO, and over 20 % of SiO_2, SO_3 and P_2O_3 (Table III – 12). However, some char was lost in the floating fraction leading to a decrease in the carbon content (3.09 wt.%; Table III-12).

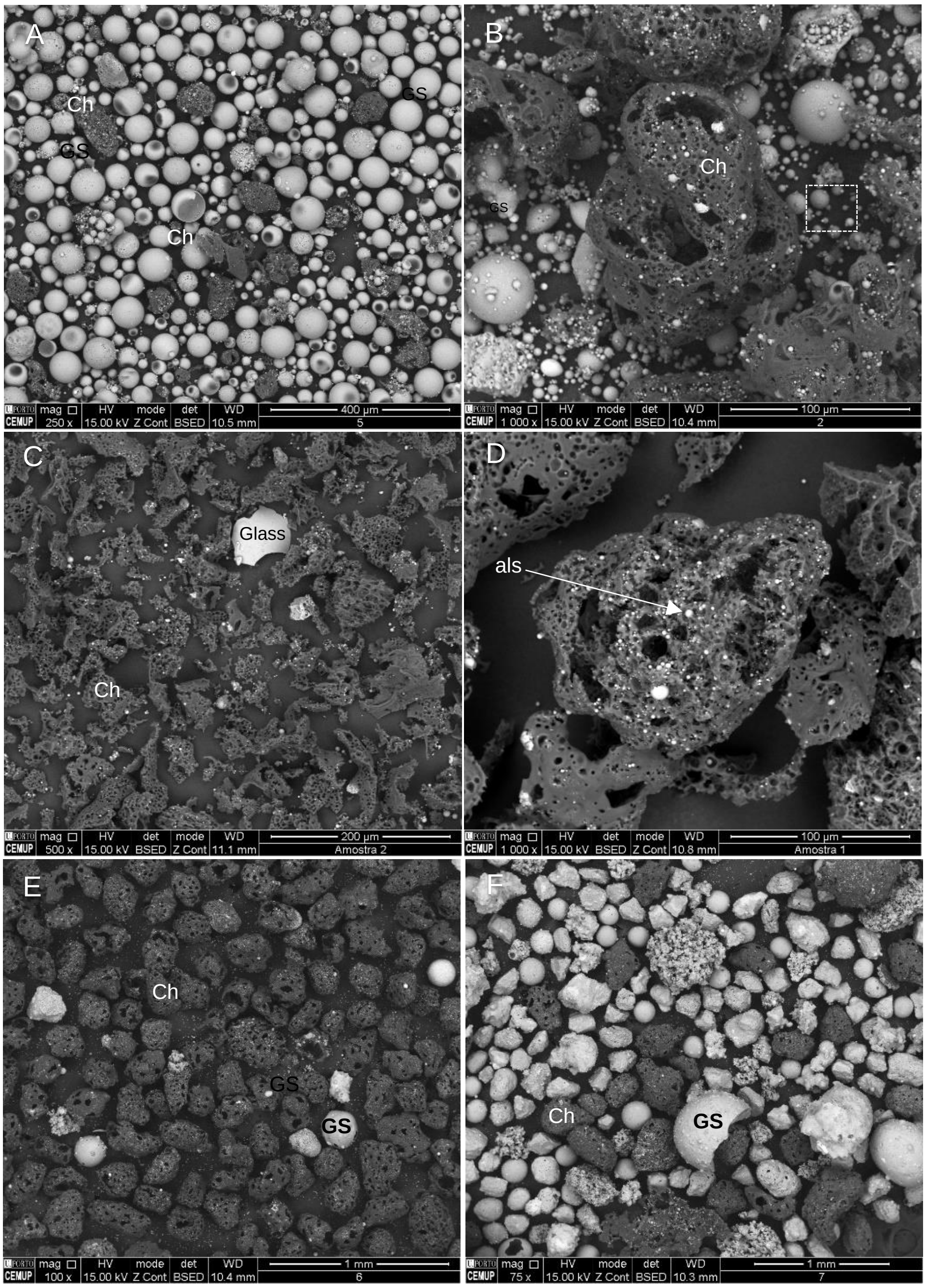

Figure III - 14. Results of fly ash beneficiation (SEM/EDS, BSE mode): (A) float fraction resulting from gravimetric separation essentially composed by aluminosilicate glass spheres (als, ×250), (B) fraction >75 µm after wet sieving where micrometric glass spheres are still retained; after sonication trial (10 min, 50 % power) (C) fraction <75 µm displays broken char and glass and (D) char particle with glassy –(GS) infilling its pores, vibration-induced segregation (E) bottom fraction and (F) top fraction.

Segregation can be a major concern when handling granular materials since sub-samples may not be representative of the bulk sample, but it can be useful for materials beneficiation. For example, vibrational separation systems for particle sorting have been widely used at industrial scale, in the mining industry (Wills and Finch, 2016). Still, as far as known, vibration-induced segregation using a sieving shaker was first applied for char recovery in the current research.

Vibration-induced segregation, also named dry impaction, was initially tested on the bulk FA and on the wet sieved >150 µm and 150-75 µm fractions. No segregation was observed in the bulk FA sample. In contrast, char-rich fractions with FC ranging between 23 and 37 wt.%, db, obtained from both size-fractions (Table III - 11). Observations with SEM/EDS clearly showed the difference in char content of the fractions obtained (Figure III - 14E,F), and corroborated with the FC results listed on Table III - 11. The method was subsequently tested on the bulk >75 µm fraction after wet sieving. The yield and carbon recovery of this trial was positioned between the values of those obtained for the individual size-fractions while FC was slightly below (53.1 wt.%, db) (Table III - 11).

The application of vibration-induced segregation to the >75 µm size-fraction obtained after wet sieving removed more than half of Fe_2O_3, MgO and P_2O_3 and over 40 wt.% of SiO_2, Na_2O, K_2O and CaO (Table III – 12). However, a slight relative increase in SO_3 and total sulfur (S_t) was observed which can be related to insoluble S species associated with char (e.g., partially decomposed pyrite embedded in the char, and some organic S; Valentim et al., 2016).

Table III - 11. Carbon grades and recoveries, and sample yields for the segregation trials carried out on FA size-fractions > 75 µm.

Size-fraction (µm)	Grade after wet sieving (wt.% FC_d)	Yield (wt.%)	Final grade (wt.% FC_d)	Carbon recovery (%)
>150	31.0	55.8	54.5	98.0
150-75	22.2	33.1	59.8	89.1
>75	21.9	38.2	53.1	92.8

FC_d – Fixed carbon on dry basis

Although vibration-induced segregation proved to significantly increase the char concentration, a wet elutriation-based process was tested on the char-rich fraction obtained. It was expected that the dynamics of the char particles being carried by the fluid would be different from the ones of the aluminosilicate glass and other inorganic particles. A trial using manual stirring proved to be efficient for char concentration leading to an increase of 13.06 wt.% in the FC and a carbon recovery of 96.14 %. In this sense, the method was upgraded to reduce operator influence using water pumps to create a water current and a 75 µm sieve to collect the char (Figure II.5, Part II).

The elutriation of the concentrate obtained through vibration-induced segregation removes over 25 % of SiO_2, MgO and Na_2O and more than 15 % of Al_2O_3, CaO, K_2O and TiO_2 (Table III - 12).

Table III - 12. Major and minor oxides and elemental analysis results (wt.%) for the subsamples collected across the char concentration process. Bulk FA is included for comparison purposes (published in Nunes et al., 2022).

	Bulk ESP FA	>75 µm					
		Dry sieving	Sink-float	Wet sieving	Dry impaction	Elutriation	Magnetic separation
Major and minor oxides							
SiO_2	59.10	50.57	55.46	42.93	24.45	15.90	16.12
Al_2O_3	19.90	10.94	11.01	11.16	8.32	6.93	7.13
Fe_2O_3	6.14	3.22	3.60	3.20	1.31	1.20	1.03
CaO	1.38	0.56	0.60	0.78	0.40	0.34	0.32
MgO	1.75	0.64	0.68	0.61	0.27	0.18	0.17
Na_2O	1.25	0.51	0.53	0.46	0.26	0.19	0.18
K_2O	2.25	0.95	0.97	0.96	0.57	0.46	0.45
MnO	0.08	0.03	0.03	0.03	<0.01	<0.01	<0.01
TiO_2	0.90	0.38	0.40	0.38	0.27	0.22	0.21
SO_3	0.10	0.14	0.25	0.07	0.11	0.11	0.19
P_2O_5	0.18	0.06	0.06	0.13	0.04	0.04	0.04
Cr_2O_3	n.d.	<0.01	<0.01	<0.01	<0.01	<0.01	<0.01
Elemental analysis							
C_t	5.49	28.82	25.73	36.62	62.18	71.81	71.37
S_t	n.d.	0.19	0.18	0.19	0.47	0.45	0.32

ESP FA, fly ash from ESP; t, total

To further improve the char concentration, Fe-rich morphotypes were removed via dry magnetic separation using a ferrite magnet. The magnetic fraction yielded <1 wt.% but the occurrence of char particles physically associated with Fe-rich morphotypes (Figure III - 15B), led to a slight decrease in carbon content after magnetic separation (Table III - 12). Nevertheless, this step allowed to remove approximately 0.17 wt.% of Fe_2O_3 (decrease >14 %) from the elutriated sample and most of the ferrospheres.

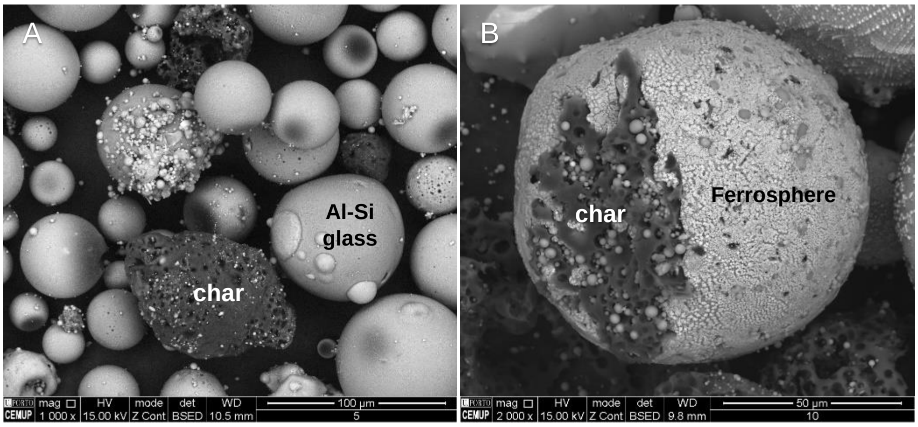

Figure III - 15. SEM micrographs (BSE mode) of (a) floating fraction (×500), and (b) magnetic fraction showing char particles attached to ferrospheres (×2500).

Table III - 13 summarizes the results regarding carbon grades, carbon recoveries, and sample yields across the final char concentration process. Using a sequence of simple physical methods, it was possible to obtain a char concentrate with a 72.55 FC wt.%, db, from a FA bulk sample with an initial carbon content of 5.39 FC wt.%, db, similar to the values obtained by others authors using different methods, such as triboelectrostatic separation, froth flotation, oil agglomeration and incipient fluidization (e.g., Baltrus et al., 2002; Cabielles et al., 2008; Hurt et al., 1995; Hwang et al., 2002; Rubio et al., 2008). Regarding the overall carbon recovery, only 29.28 wt.% of the initial carbon was recovered (Table III - 13). However, the aim of this study was to obtain a char concentrate with as high carbon grade as possible, and without considering carbon recovery which may be addressed in further research.

Despite the success obtaining a char-rich concentrate without recourse to dense liquids, frothing agents or oil, it still contains approx. 25 wt.% of aluminosilicate glass mainly in the form of micrometric glassy spheres infilling the char pores. To avoid clogging in the graphitization chamber, the char-rich concentrate was previously demineralized with HF and HCl (detailed methodology is described in Part II).

Table III - 13. Summary on the whole char concentration process: carbon grades, carbon recoveries, and sample yields.

	Initial grade (FC, wt.%, db)	Sample yield (%)	Final grade (FC, wt.%, db)	Carbon recovery (%)
Dry Sieving	5.39	17.32	20.39	65.51
Sink-Float followed by wet sieving	20.39	58.20	23.13	66.02
Vibration-induced segregation	23.13	31.27	56.56	76.46
Elutriation followed by magnetic separation	56.56	69.03	72.55	88.55
Overall	5.39	2.18	72.55	29.28

FC, fixed carbon; db, dry basis

2.2. Characterization of char concentrates

In this section, characterization results concerning char concentrate (CC), char demineralized (CD) and respective samples after carbonization (C) and graphitization (G) (detailed methodology in Part II) are presented. Meanwhile, for comparison purposes, char concentrates from Poland (PL), Romania (RO), and South Africa (SA) were added to this study. Thus, the sample obtained is from this point hereinafter referred to as Portuguese (PT) sample.

The characterization of the char and demineralized char concentrates included proximate and ultimate analysis, XRF and SEM/EDS (detailed methodology in Part II). The nomenclature used to describe the char types found by SEM/EDS combines terminology from Vleeskens et al., (1994, 1990), Menéndez et al., (1993) and Valentim et al., (2009b). Petrographic components were determined according to the system developed by ICCP (Suárez-Ruiz et al., 2017).

The effects of demineralization, carbonization and graphitization in the morphology, texture and structure of the carbonaceous material were assessed using XRD, carbon forms analysis, optical microscopy (RIS axes and parameters), SEM/EDS, Raman microspectroscopy, and transmitted electronic microscopy (TEM). The description of all the methods can be found in Part II.

Table III - 14 to Table III - 16 list the chemical and petrographic results of the char concentrate samples obtained in this study, and the characterization results of the Romanian, Polish and South Africa samples mentioned above. These chars present carbon contents ranging between 85.15 and 96.63 wt.%, daf (Table III - 14) and, except for the Portuguese char concentrate, organic carbon predominates over elemental (graphitic) carbon (Table III - 18).

Despite the fact that all samples are coal char concentrates, the characterization results show differences between these, which are related to the respective coal genesis and coalification path and impact of thermal transformations during combustion (Suárez-Ruiz and Ward, 2008). The Portuguese char concentrate has the highest carbon content, 96.63 wt.%, daf, and the lowest volatile matter content, 2.59 wt.%, daf, but the H/C ratio is similar to the Polish char concentrate, 0.06. The Romanian char concentrate differs from the remaining samples due to its higher contents of volatile matter (24.87 wt.%, daf), oxygen (10.34 wt.%, daf) and hydrogen (2.16 wt.% daf), due to the high amount of unburned and partially burned coal particles (Table III - 14,Table III - 16; (Badenhorst et al., 2020). It also has higher concentrations of CaO (3.11 wt.%) and SO_3 (1.61 wt.%) and lesser amounts of SiO_2 and Al_2O_3, 4.11 and 1.88 wt.%, respectively (Table III - 15). Observations under SEM/EDS often showed the presence of calcium sulphate (gypsum) and iron sulfide (pyrite) which supports the presence of these elements (Figure 6 in(Badenhorst et al., 2020). On the other hand, the char concentrate from South Africa has the highest amount of SiO_2 and Al_2O_3, 23.93 wt.% and 11.21 wt.%, respectively, which can be related to quartz and aluminosilicate glass interwoven into the char matrix. However, the proximate and ultimate analyses obtained for this sample resemble CC-PT and CC-PL.

Different types of char particles predominate in each studied sample. The char particles in CC-PT sample are mainly rounded, porous-open with perforated thin walls (Figure III - 16A), and the secondary vacuoles are commonly filled by micrometric aluminosilicate glassy spheres (Figure III - 16B).

Table III - 14. Proximate and ultimate analysis (wt.%) of char concentrates, demineralized concentrates, and respective carbonized and graphitized samples.

	Proximate analysis		Ultimate analysis						
	A,db	VM, daf	S,db	C, daf	H, daf	N, daf	O, daf	Atomic ratio H/C	Atomic ratio O/C
CC_PL[a]	22.96	5.91	0.46	94.90	0.38	1.21	3.03	0.05	0.02
CC_PT[a]	22.51	2.59	0.41	96.63	0.48	1.27	1.21	0.06	0.01
CC_RO[a]	14.72	24.87	1.49	85.15	2.16	0.71	10.34	0.30	0.09
CC_SA[a]	18.36	5.08	0.36	95.30	0.23	1.41	2.68	0.03	0.02
CD_PL	2.71[a]	12.88[a]	0.62	84.41	2.31	1.26	11.37	0.33	0.10
CD_PT	0.51[a]	1.93[a]	0.29	93.39	0.18	1.29	4.84	0.02	0.04
CD_RO	7.82[a]	28.69[a]	0.89	81.82	3.32	0.74	13.16	0.48	0.12
CD_SA	7.01[a]	5.06[a]	0.30	90.17	1.05	1.37	7.09	0.14	0.06
CC_PL_C	24.35	3.56	0.26	93.65	0.49	1.18	4.41	0.06	0.04
CC_PT_C	27.89	1.33	0.24	95.56	0.00	1.20	3.00	0.00	0.02
CC_RO_G	2.33	0.53	0.00	99.31	0.00	0.10	0.59	0.00	0.00
CC_SA_C	18.51	3.07	0.18	94.07	0.47	1.42	3.84	0.06	0.03
CD_PL_G	0.23	0.83	0.00	86.67	0.00	0.08	13.25	0.00	0.11
CD_PT_G	0.07	0.79	0.00	96.54	0.00	0.11	3.34	0.00	0.03
CD_RO_G	0.00	0.48	0.00	96.91	0.00	0.08	3.01	0.00	0.02
CD_SA_G	0.20	0.85	0.00	97.54	0.00	0.08	2.38	0.00	0.02

[a] Badenhorst et al., 2020

A, ash; VM, volatile matter; db, dry basis; daf, dry ash free basis; CC, char concentrate; CD, char concentrate demineralized; C, carbonized; graphitized; PL, Poland; PT, Portugal, RO, Romania; SA, South Africa

In the CC-PL sample, the char particles are not as rounded as in the CC-PT and porous-open chars with non-vesiculated walls are more often observed (Figure III - 16C). Furthermore, in char particles with non-vesiculated walls (smooth surface) plastic flow features around the pores were frequently observed (Figure III - 16C,D). The CC-SA sample presents higher abundance of irregularly shaped massive inertinite-derived char particles and mixed morphotypes (Figure III - 16E). The CC-RO sample differs from the remaining samples with a predominance of massive non-porous particles with sharp edges (Figure III - 16F). The angularity of the particles must probably be related with the griding steps applied during the ash beneficiation process (Cruceru et al., 2017).

The demineralization process led to a decrease in the volatile matter (0.66 wt.%, daf) and hydrogen content (0.3 wt.%, daf) in the Portuguese char concentrate (Table III - 14). This may have an impact on the sample graphitization seeing as hydrogen can assist with the mobilization of the BSU to achieve an ordered structure (Atria et al., 2002; González et al., 2004; Suárez-Ruiz and García, 2007). By contrast, the demineralized char from Poland showed a relative enrichment in the volatile matter (almost 7 wt.%, daf) which is explained by the high volume of unreacted particles in this sample, 10.2 vol.% (Table III - 16).

Table III - 15. Major oxides and LOI (wt.%) for char concentrates and respective demineralized samples.

	SiO_2	Al_2O_3	Fe_2O_3	CaO	MgO	Na_2O	K_2O	SO_3	MnO	TiO_2	P_2O_5	Cr_2O_3	LOI
CC-PL	10.90	6.12	0.77	1.47	1.00	0.30	0.51	0.15	<0.01	0.23	0.04	<0.01	77.64
CC-PT	16.12	7.13	1.03	0.32	0.17	0.18	0.45	0.19	<0.01	0.21	0.04	<0.01	73.43
CC-RO	4.11	1.88	1.19	3.11	0.36	<0.01	0.16	0.72	<0.01	0.08	0.02	<0.01	87.64
CC-SA	23.93	11.21	0.82	0.79	0.17	0.04	0.25	0.35	<0.01	0.56	0.14	<0.01	61.51
CD-PL	0.61	1.23	0.38	0.19	<0.01	0.01	<0.01	0.06	<0.01	0.13	<0.01	<0.01	96.91
CD-PT	0.12	0.14	0.01	0.03	<0.01	<0.01	<0.01	<0.002	<0.01	0.02	<0.01	<0.01	99.47
CD-RO	<0.01	3.63	0.41	1.23	0.04	<0.01	0.02	0.42	<0.01	<0.01	0.03	<0.01	93.81
CD-SA	0.74	4.22	0.24	0.12	<0.01	<0.01	<0.01	0.05	<0.01	0.39	0.05	<0.01	93.97

CC, char; CD, char demineralized; PL, Poland; PT, Portugal; RO, Romania; SA, South Africa; LOI, loss on ignition

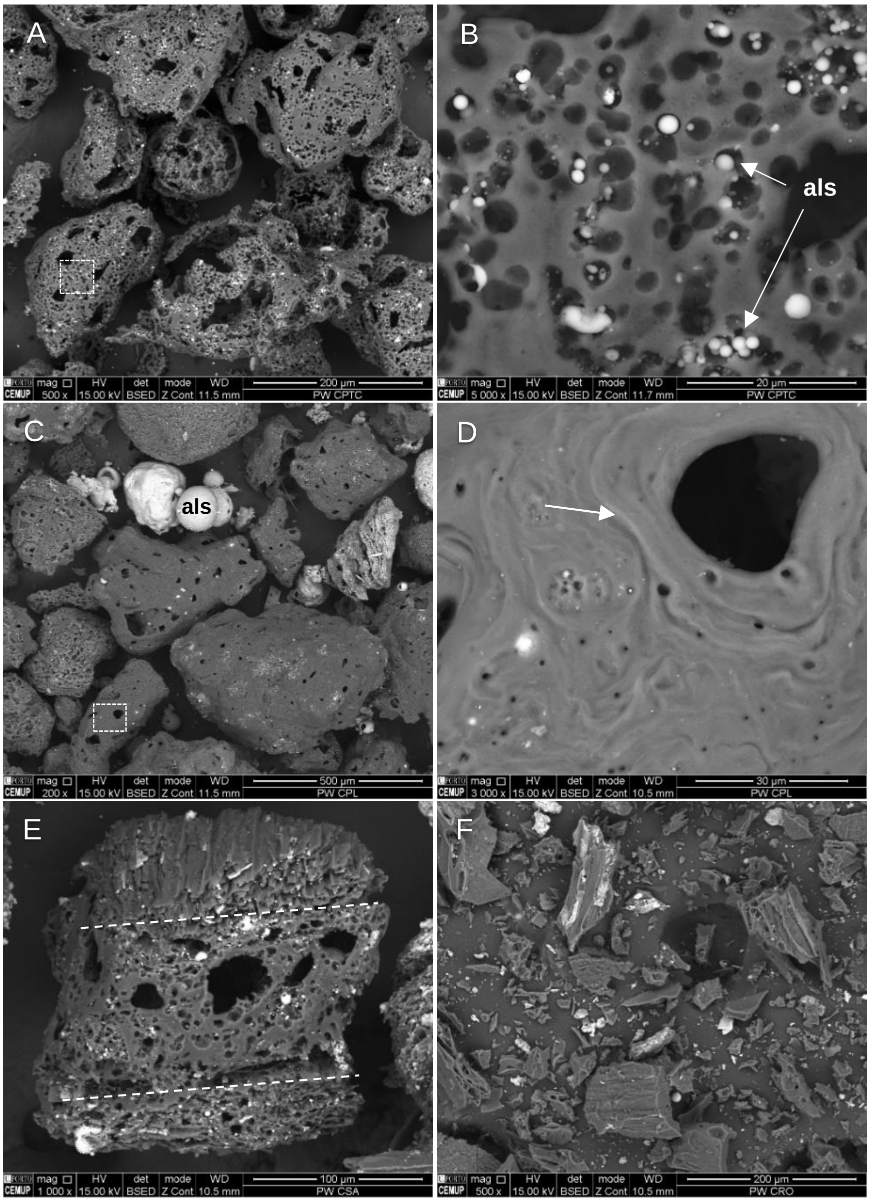

Figure III - 16. Detailed imaging of char concentrates (SEM/EDS, BSE mode): (A) Portugal (CC-PT) rounded thin-wall particles with large vacuoles and perforated walls (×500); (B) magnification of dashed square in A showing aluminosilicate spheres (als) infilling char pores (×5000); (C) Poland (CC-PL) porous char particles exhibiting non-vesiculated (center) and vesiculated (left) walls and aluminosilicate spheres and agglomerates (×200); (D) magnification of dashed square in "C" highlighting plastic flow features around pores (×*3000*); (E) South Africa (CC-SA), mixed char morphotype exhibiting porous-open area with perforated walls between inertinite-derived areas infilled with mineral matter*(×1000)*; (F) Romania (CC-RO) massive non-porous particles with sharp edges *(×1000)*.

In general, inorganic elements, such as Si, Fe and Ca, were effectively removed during demineralization with HF and HCl (Table III - 15). Nevertheless, the CD-RO sample presents a relative enrichment in Al_2O_3, and residues of inorganic elements (S, Cl, Ca) were detected in the surface of some char particles by SEM-EDS analysis (Figure III - 17A,B). In the case of CD-PT sample, it presents the lowest ash content (0.51 wt.%, db), and the SEM-EDS results showed an effective removal of the aluminosilicate glassy spheres infilling the char pores (Figure III - 17C,D).

The removal of silicates embedded in the char structure of the CC-PL and CC-SA samples was limited, and a residue mainly composed of Al, Cl, and F from the demineralization process was found covering the surface of char particles (Figure III - 17E,F). Moreover, some char particles in the CD-SA sample had an aluminum residue infilling its pores (Figure III - 17G,H) which may explain the higher Al_2O_3 content (4.22 wt.%) found in this sample. This can be explained by the mineral matter association with the organic matter in the coal. While in the Colombian coal burned at Pego PP the mineral matter is mostly composed of clay layers, which are transformed into very fine glassy spheres (among others) that infill char pores, the mineral matter in the Polish and South African coals was, in many cases, intimately associated with the organic matter including cell ducts filling, which upon heating became intimately mixed with the char (Badenhorst et al., 2020; Santos et al., 2022). This mineral matter in close association with char is difficult to remove. However, considering that Al has been pointed out as a catalyst in graphitization (e.g., González et al., 2004; Ōya and Ōtani, 1979), it is assumed that the presence of this element in the demineralized char samples would not have a negative impact on the char transformations during high temperature treatments.

The petrographic composition of the four demineralized char presented differences among each other (Table III - 16). The char from CD-PT sample is mainly fused, porous and anisotropic (90.7, 87.6 and 72.2 vol.%, respectively; Table III - 16). This is explained by the feed coal composition and rank, i.e., medium rank D (Bituminous D), moderately high vitrinite (75.96 vol.%,mmf) (Badenhorst et al., 2019; ISO 11760, 2005) since within this rank vitrinite passes through a softening stage where its structure is reorganized originating anisotropic structures (Bend et al., 1992). On contrast, the Romanian sample is mainly composed of isotropic (99.4 vol.%) char particles since the feed coal is a low rank coal, Oltenia lignite (Gorj County, Romania), and contains a significant volume of unreacted particles (33.1 vol.%) (Table III - 16). The latter might be related to poor-efficiency combustion conditions.

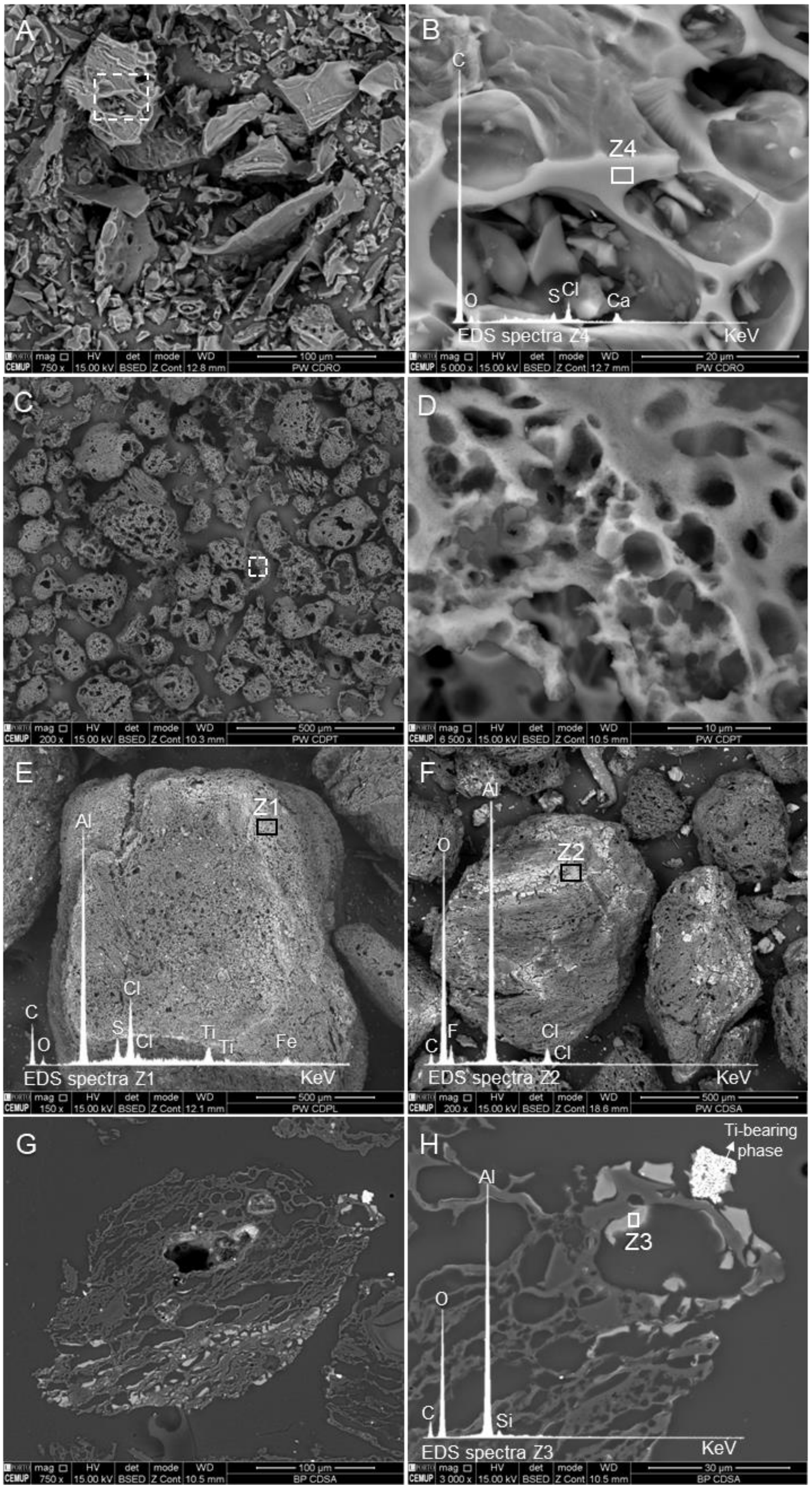

Figure III - 17. Observation of char concentrates after demineralization (SEM/EDS, BSE mode): (A) CD-RO general view with no visible mineral matter (×750); (B) magnification of "A" and respective EDS spectrum demonstrating the presence of impurities (×5000); (C) general overview of CD-PT (×200); (D) magnification of dashed square in "C" showing empty char vacuoles (×6500); (E) CD-PL (×150) and (F) CD-SA (×200) residues of inorganic matter in char following demineralization and the respective EDS spectra; (G) CD-SA mixed dense particle in cross-section (×250), and (H) magnification showing Al-rich residue retained and respective spectra (×3000). Micrographs A and B were published in Badenhorst et al., 2020.

Table III - 16. Petrographic components (vol.%) of the demineralized char according to the ICCP classification (Suárez-Ruiz et al., 2017).

Sample	Nature		Optical character		Structure/Morphology		Optical texture		Unburned coal
	Inorganic	Organic	Fused	Unfused	Porous	Massive	Isotropic	Anisotropic	
CD-PL	2.8	86.9	62.7	37.3	69.9	29.4	45.1	54.2	10.2
CD-PT	4.9	95.1	90.7	9.3	87.6	12.4	27.8	72.2	0.0
CD-RO	0.0	66.9	37.5	62.5	51.2	48.8	99.4	0.6	33.1
CD-SA	0.0	100	63.7	36.3	74.6	25.4	44.8	55.2	0.0

CD, char demineralized, PL, Poland, PT, Portugal, RO, Romania, SA, South Africa

Samples CD-SA and CD-PL are mainly composed of fused, porous, and anisotropic particles (Table III - 16). However, mixed porous morphotypes predominates in the CC-SA sample (40.4 vol.%) while networks (crassi- and tenuinetwork) compose more than 50 vol.% of CC-PL (Badenhorst et al., 2020). This is related to the feed coal composition since the Polish feed coal contained 49.8 vol.% vitrinite while the South African feed coal was mainly composed of inertinite (48.6 vol.%) of which 18.9 vol.% was reactive semifusinite (Badenhorst et al., 2019). This relatively high-volume of reactive inertinite is the main precursor of the distinctive characteristics of SA-chars studied because inertinite-rich coals have been associated with higher density chars, and it is known that low-reflectance inertinite (reactive semifusinite) may originate networks and mixed chars (Bend, 1989; Bend et al., 1992; Thomas et al., 1993a, 1993b).

2.2.1. Assessment of transformations related to demineralization, carbonization, and graphitization

Table III - 17 lists the optical properties of the studied samples. Char concentrates from Portugal, Poland and South Africa presented similar random reflectance (6.66-6.91 %), seeing as the feed coals were of similar rank, i.e., medium rank coals (Badenhorst et al., 2019). The slightly higher texture anisotropy values found for CC-PT and CC-SA (R_{am} parameter) suggest higher spatial arrangement of the BSU, i.e., preferential planar orientation (Marques et al., 2009; Pusz et al., 2003, 2002; Rodrigues et al., 2011a; Suárez-Ruiz and García, 2007) and is in line with the lower interlayer spacing (d_{002}) values found for these samples, 0.3542 and 0.3595 nm, respectively (Table III - 18). The R_{ev} parameter (RIS equivalent volume, Kilby, 1991) is higher for CC-PL samples. This parameter has been associated to the ordering of chemical structure of BSU with greater values indicating a better order (Pusz et al., 2003, 2002; Rodrigues et al., 2011a; Suárez-Ruiz and García, 2007). Nevertheless, the char from South Africa has the highest anisotropy parameters (Table III - 17). The CC-RO sample presented much lower random reflectance (4.25 %), bireflectance (0.98 %), and anisotropy (0.23). The R_{am} close to zero (0.04) for the CC-RO sample supports the high volume of isotropic particles

(Table III - 16), which is in agreement with the low rank of the feed coal. All the samples presented a biaxial negative character (R_{st}, Table III - 17).

According to Oberlin (1984), carbonization (up to 1000 °C) leads to devolatilization, aromatization, and rearrangement of the BSU. In the studied samples, carbonization caused an increase in the biaxial negative character (R_{st}, Table III - 17) and, except for the Romanian char sample, a decrease in anisotropy parameters, all of them more accentuated in the SA sample (Table III - 17). Furthermore, R_{MIN} and R_{ev} parameters increased in the carbonized char from South Africa. The increase in the R_{ev} parameter suggests an improvement in the chemical structure of the BSU in CC-SA-C caused by transformations of chemical nature (Suárez-Ruiz and García, 2007). Regarding random reflectance of carbonized samples, it is generally slightly lower than of the respective char concentrates (Table III - 17). Previous research encompassing high rank coals carbonization, have reported the increase in random reflectance, RIS axes and R_{ev} as general trends (Pusz et al., 2003, 2002; Rodrigues et al., 2011a; Suárez-Ruiz and García, 2007) which was not verified in the studied chars. Nevertheless, one must consider that starting material are fairly different which will reflect in the transformations and the respective optical parameters.

After demineralization, all samples show a slight decrease in their random reflectance compared to the char concentrates, 0.06 % (Romanian sample) to 0.28 % (Polish sample). The RIS axes slightly decreased in samples from Poland and South Africa while in the Portuguese sample only R_{INT} decreased. Regarding the R_{eV} parameter, a decrease in CD-PL and CD-SA, 1.03 and 0.4 % is verified, respectively, while in CD-PT and CD-RO it increased, 0.4 and 0.2 %, respectively (Table III - 17). Except for the char from South Africa, the R_{am} parameter decreased in the demineralized samples suggesting inferior spatial arrangement of the BSU (Table III - 17). Acid leaching is very effective on the removal of mineral matter (as seen from the XRF and SEM results) but can induce changes in the char structure (Bartoňová, 2015). For instance, Li et al., (2021) studied the effects of HF pickling on unburned carbon (UC) from an atmospheric circulating fluidized bed gasification plant and verified that the carbon microcrystalline structure becomes loose due to the break of weak bonds (e.g., hydrogen bonds) and side chains.

Except for the Romanian char, graphitization led to a decrease in the random reflectance in comparison to the respective demineralized char samples, up to -1.48 % in the CD-SA-G sample (Table III - 17). Furthermore, graphitized char from Portugal and South Africa showed a decrease in all RIS axes after graphitization (Table III - 17) while the Polish and Romanian sample showed an increase in R_{MAX} and R_{INT} axes(Table III - 17).

The decrease in reflectance can be related to measurements made on newly formed low reflectance areas where crystallites seem to develop at the expense of the decomposition/reorganization of the adjacent organic matter (Figure III - 18). In some cases, the development of crystalline aggregates (Kwiecińska and Petersen, 2004; Rodrigues et al., 2011b; Suárez-Ruiz and García, 2007) is clearly observed (Figure III - 18A,B) while in others it was only observed the development of an incipient micromosaic texture (Figure III - 18III.C-H). These aspects were more often observed in inertinite-derived chars. Although having a lower reflectance, these areas were in general more ordered than the involving material as verified through Raman microspectroscopy (Table III - 19).

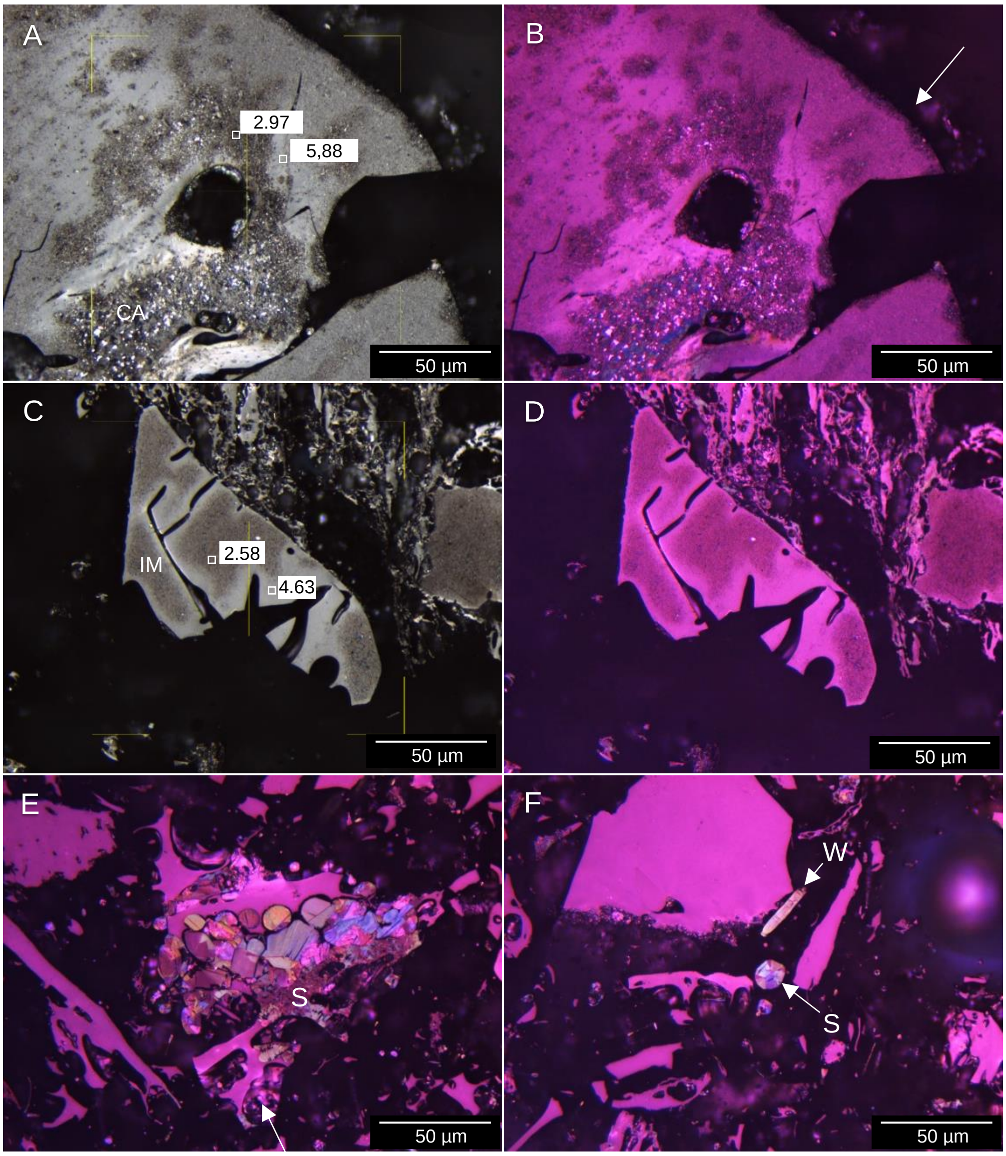

Figure III - 18. Optical photomicrographs of char particles after graphitization (oil immersion objective) under polarized light (A and C), with 1λ retarder plate (B, D, E and F): (A-B) example of crystalline aggregate, CA, formed around a pore and particle edge from CD-PL-G; (C-D) low reflectance incipient micromosaic, IM, texture within a solid particle from CD-SA-G, (E) inertinite-derived char from CD-RO-G showing crystallites being formed at expense of char wall and spherical graphite forms filling the pores; (F) whisker, W, and spherical graphite from CD-RO-G

The graphitized demineralized char from Romania showed an increase in random reflectance and in the R_{MAX} and R_{INT} axes compared to the respective demineralized char (Table III - 17). This reflectance increase may be explained by the development of graphite structures in this sample, which were observed using optical microscopy (Figure III - 18E,F) but more evident and frequently observed via SEM-EDS than in the other samples (results described below).

All the samples maintained their biaxial negative character after graphitization (R_{st}, Table III - 17). The R_{eV} parameter decreased in all graphitized char samples studied relative to the respective demineralized char samples. This parameter is expected to increase with the improvement of the BSU chemical order (Pusz et al., 2003, 2002; Suárez-Ruiz and García, 2007). However, it has been found that after the removal of all heteroatoms and light compounds it stops growing or even decreases (Rodrigues et al., 2011a; Suárez-Ruiz and García, 2007). The structural changes taking place above 2000 °C have been associated to changes in pores namely its dimensions and shape (Duber and Rouzaud, 1999; Pusz et al., 2002; Suárez-Ruiz and García, 2007). Further studies including follow-up of the evolution of RIS parameters and microporosity at different temperature levels would be necessary to verify a possible correlation.

Table III - 17. Random reflectance, mean apparent reflectance values and RIS characteristics of the studied samples.

	Random reflectance	Mean apparent reflectance (%)		RIS characteristics						Anisotropy parameters	
				RIS axes (%)			RIS parameters				
	Rr %	R'_{max}	R'_{min}	R_{MAX}	R_{INT}	R_{MIN}	R_{am}	R_{ev}	R_{st}	B	$(R_{MAX}-R_{MIN})/(R_{MAX})$
CC-PL	6.66	7.84	6.27	9.01	7.49	4.60	0.11	6.66	-13.35	4.41	0.49
CC-PT	6.91	7.86	6.24	9.15	7.40	3.93	0.15	6.29	-13.91	5.22	0.57
CC-RO	4.25	4.09	3.78	4.26	3.87	3.28	0.04	3.77	-8.88	0.98	0.23
CC-SA	6.80	8.08	6.34	9.83	7.57	4.01	0.15	6.36	-13.98	5.82	0.59
CC-PL-C	6.63	7.80	6.28	8.65	7.36	4.60	0.11	6.58	-16.58	4.05	0.47
CC-PT-C	6.58	7.88	6.40	8.84	7.50	3.93	0.14	6.23	-17.79	4.91	0.56
CC-RO-G	3.80	4.29	2.86	5.52	3.57	1.79	0.17	2.85	-11.90	3.72	0.67
CC-SA-C	6.54	7.86	6.32	8.62	7.51	4.46	0.12	6.53	-18.06	4.16	0.48
CD-PL	6.38	6.50	5.31	7.22	6.14	4.17	0.10	5.63	-13.69	3.05	0.42
CD-PT	6.74	7.61	6.02	9.15	7.16	4.36	0.13	6.48	-11.18	4.79	0.52
CD-RO	4.18	4.37	4.06	4.58	4.27	3.72	0.04	4.17	-10.32	0.86	0.19
CD-SA	6.56	8.04	5.65	9.39	7.39	3.47	0.16	5.85	-15.36	5.92	0.63
CD-PL-G	5.18	6.93	4.96	7.60	6.39	2.84	0.16	5.05	-17.56	4.76	0.63
CD-PT-G	5.53	6.56	5.10	7.48	6.31	2.94	0.16	5.10	-18.31	4.55	0.61
CD-RO-G	4.48	5.75	4.08	6.65	5.11	2.03	0.18	3.70	-17.03	4.63	0.70
CD-SA-G	5.09	6.68	3.99	7.74	6.20	1.27	0.25	3.52	-18.56	6.47	0.84

B = R_{MAX}-R_{MIN}; CC, char concentrate; CD, char demineralized, C, carbonized; G, graphitized; PL, Poland, PT, Portugal, RO, Romania, SA, South Africa

For all samples, the R_{am} parameter showed an improvement in the spatial arrangement of the BSU with graphitization, along with an increase in bireflectance and $(R_{MAX}-R_{MIN})/(R_{MAX})$ (Table III - 17). Although the sample from Romania has undergone major changes during graphitization, the graphitized char sample from South Africa ended up with better spatial arrangement of the BSU as shown by the highest R_{am} parameter (Table III - 17). On the other hand, the Portuguese sample that presented initial R_{am} similar to the sample from South Africa did not evolve in a similar way. This may have been influenced by several factors such as the hydrogen loss during demineralization (Table III - 15).

The XRD diffractograms of the char concentrates and the graphitized demineralized char are presented in Figure III - 19, and the d_{002}, Lc and La, <N>, and the graphitization degree (GD) values are provided in Table III - 18.

The diffractograms concerning of the char concentrates presented a broad asymmetrical (002) peak indicating a predominance of aliphatic compounds (Feng et al., 2003; Lu, 2002; Lu et al., 2001). Reflections characteristic of three-dimensional structure, such as (101), (103), (110), and (112), were not present. Nevertheless, the CC-PT sample exhibited the highest degree of structural order, as demonstrated by the X-ray parameters (Table III - 18), which is in line with its higher content of anisotropic particles (Table III - 16), and the RIS parameters (Table III - 17). Still, the d_{002} is far from the one attributed to ideal graphite, 0.3354 nm (Franklin, 1951). Indeed, considering the d_{002} values obtained (>0.3542 nm), one may conclude that all the char concentrates analyzed have a turbostratic structure (Ergun, 1968; Franklin, 1951).

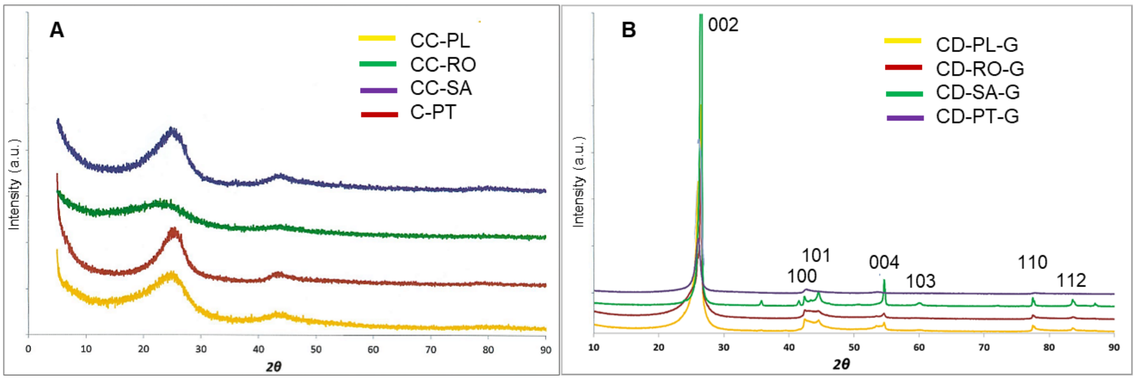

Figure III - 19. X-ray diffraction diffractograms regarding (A) char concentrates and (B) graphitized demineralized char concentrates (already published in Badenhorst et al., 2020).

The XRD diffractograms of the graphitized demineralized char samples have a well-defined (002) peak at 26.6° (2θ) (Figure III - 19). Furthermore, peaks indicative of a three-dimensional structure, such as (101), (110), and (112) (Deurbergue et al., 1987; Jehlicka and Rouzaud, 1990; Kwiecińska and Petersen, 2004; Salver-Disma et al., 1999) were detected in all samples, except the CD-PT-G. The sample CD-SA-G stands out from the remaining samples by a well-defined crystalline (004) peak and for the presence of the (103) peak suggesting a higher degree of structural ordering. The CD-PT-G sample has a small broad asymmetrical two-dimensional (10) peak (between the peaks 100 and 101 in Figure III - 19B) suggesting a turbostratic structure (e.g., Biscoe and Warren, 1942; Ergun, 1968; Franklin, 1951). This is evidence of its lower ability to graphitize despite originally being a char that presented superior spatial arrangement of the BSU (R_{am}, Table III - 17). Nevertheless, it was possible to observe a major decrease in the organic carbon in all graphitized samples (Table III - 18).

The d_{002} ranges between 0.3423 and 0.3360 nm, which is smaller than the d_{002} from the char concentrates (0.3542 – 0.3773 nm). The sample CD-SA-G attained d_{002} values closer to those considered for ideal graphite (0.3354 nm) while in CD-PT-G the d_{002} is closer to a turbostratic structure (0.3440 nm; Ergun, 1968; Franklin, 1951).

The crystal sizes were the highest for CD-SA-G (44.6×98.7 nm) sample with a number of aromatic layers (<N>) of 28 while those values for CD-PT-G sample were 9.3×24.4 nm and 133. The degree of graphitization in the samples decreased as follows: CD-SA-G (93 %), CD-RO-G (80 %), CD-PL-G (53 %), and CD-PT-G (20 %). According to the classification from (Tagiri and Oba, 1986), the CD-PT-G and CD-PL-G samples are classified as disordered graphite, CD-RO-G sample is classified as graphite, and the CD-SA-G sample as fully ordered graphite. The high graphitization degree achieved by the Romanian char can be related among others, e.g., mineral matter and hydrogen, with higher degree of anisotropy of the texture developed during the carbonization as reported by (González et al., 2004). The higher graphitization degree of the CD-SA-G sample agrees with the higher R_{am} parameter, indicating a greater spatial arrangement of the BSU than remaining samples (Table III - 17).

Several authors have verified that a relationship between the amount of mineral matter and the ability to graphitize exists (Atria et al., 2002; Cabielles et al., 2009, 2008; Evans et al., 1972; Garcia et al., 2010; González et al., 2005; Oberlin and Terriere, 1975; Pappano and Schobert, 2009). The samples showed good correlations between ash content and d_{002} (Figure III - 20A) and Al_2O_3 with d_{002} (Figure III - 20B) suggesting that mineral matter, namely Al, may have played a role in the reorganization of BSU. Cabielles et al., (2008) verified that mineral matter mainly promotes growth along the basal plane (L_a) but in the present research the correlation between ash and La, although positive, is weaker (r = 0.71) than the previous referred correlations.

Table III - 18. Carbon forms and XRD parameter for the char concentrates and their respective demineralized graphitized samples.

	Carbon Forms				X-ray diffraction parameters*				GD*
	C_t	C_{org}	C_{gra}	C_{CO2}	d_{002} (nm)	La (nm)	Lc (nm)	<N>	
CC-PL	73.29	42.94	>20.00	0.8	0.3673	n.d.	1.3	4	-
CC-PT	74.00	15.59	>20.00	<0.08	0.3542	n.d.	1.9	5	-
CC-RO	66.51	66.35	0.06	0.39	0.3773	n.d.	1.2	3	-
CC-SA	75.45*	66.58*	7.18*	1.69*	0.3595	n.d.	1.4	4	-
CD-PL-G	99.51	1.15	>20.00	<0.08	0.3394	46.8	10.7	32	19.77
CD-PT-G	96.31	2.11	>20.00	<0.08	0.3423	24.4	9.3	27	53.49
CD-RO-G	98.56	7.45	>20.00	<0.08	0.3371	50.7	22.2	66	80.23
CD-SA-G	98.15	2.31	>20.00	<0.08	0.3360	98.7	44.6	133	93.02

*Badenhorst et al., 2020

C_t - Total carbon; C_{org} - organic carbon, determined by difference: Ct - Cgra - C_{CO2}; C_{gra} - Graphite carbon or elemental carbon; C_{CO2} - Inorganic Carbon, direct CO_2 evolution; d_{002} - interlaying spacing, La - average lateral size; Lc - average stake height; <N> - average number of aromatic layers; GD – graphitization degree; n.d. - not determined

Furthermore, char morphology may have influenced since the samples with lower amounts of spherical and network morphotypes, derived from coals with lower amounts of vitrinite (Badenhorst et al., 2019), graphitized better. It is verified a strong linear negative correlation between the graphitization degree and the sum of spheres and networks morphotypes (r = -0.99).

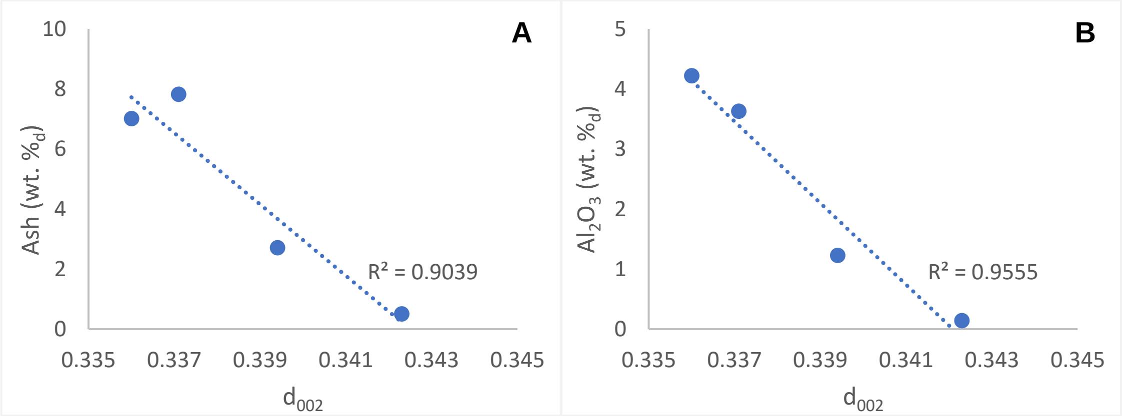

Figure III - 20. Relationship between interlaying spacing (d_{002}) of the demineralized graphitized chars and: (A) ash content of the demineralized chars (B) Al_2O_3 content of the demineralized chars.

Observations of the graphitized char samples under TEM confirmed the presence of graphitized domains with high degree of layer parallelism (Figure III - 21A). Furthermore, graphite crystals were observed, especially in the CD-SA-G sample. In Figure III - 21B-C graphite crystals imaged on CD-SA-G and CD-RO-G samples and the respective selected area electron diffraction (SAED; insets) pattern corresponding to single crystals lying in the 001 plane are showed. Nonetheless, the zigzag texture (wrinkled layers) associated with distorted aromatic layers connection was still observed in all samples (Figure III - 21D).

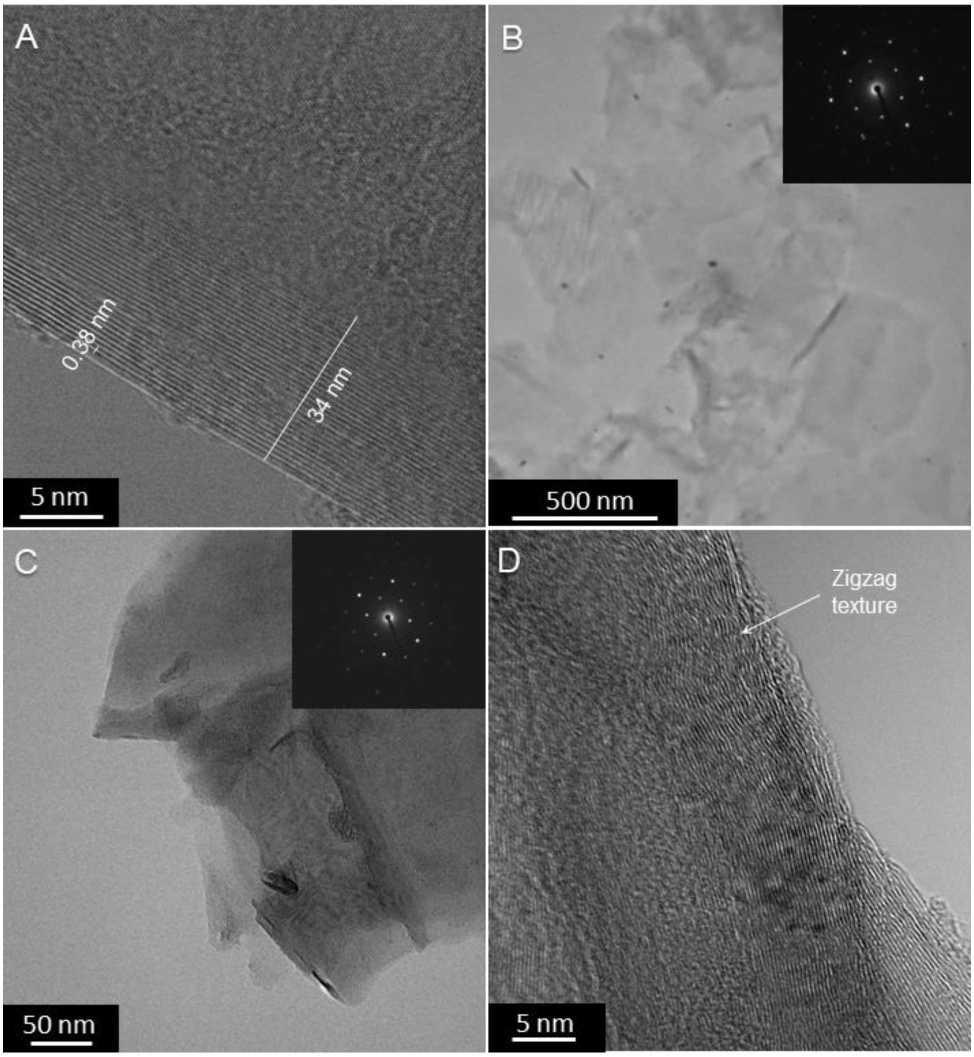

Figure III - 21. TEM images: (A) CD-RO-G lattice fringe of a graphitic structure showing very high degree of layer parallelism; (B) CD-SA-G, graphite crystal and respective SAED pattern (inset); (C) CD-RO-G graphite crystal and respective SAED pattern (inset); (D) lattice fringe showing long distorted layers, wrinkled in a zigzag and disordered carbon domain on left, CD-SA-G.

On the other hand, TEM analysis highlighted the heterogeneity of the graphitized char samples. Even in sample CD-SA-G which according to petrography and XRD responded better to graphitization, disordered carbon domains were observed (Figure III - 22A). In the CD-RO-G sample, isolated microporous disordered carbon structures were frequently observed (Figure III - 22B). By contrast, in CD-PT-G disordered carbon was often found coexisting with polyhedron pores, especially on particle edges (Figure III - 22C). Nevertheless, it must be considered that samples were previously dispersed using an ultrasound bath, so what was being observed were fragments and may not really correspond to the particle boundary. The wrinkled layers harden and dewrinkle above 2100 °C due to annealing of interlayer defects and polygonization occurs for all carbon material (Oberlin, 1984). Nevertheless, with increase in temperature flat lamellae will originate polycrystalline graphite while curved pores will lead to polyhedral pores (Oberlin, 1984). Graphitization depends on the size of the elemental domains in the bulk mesophase (pore walls), the smaller the domains, and the less ability of the carbonaceous material to graphitize (Oberlin, 1984). Polyhedral microtextures were also observed in the remaining samples. Nevertheless, in the CD-SA-G those are similar to the onion-ring structures (Figure III - 22D) described by (Beyssac et al., 2002) without a void in the center.

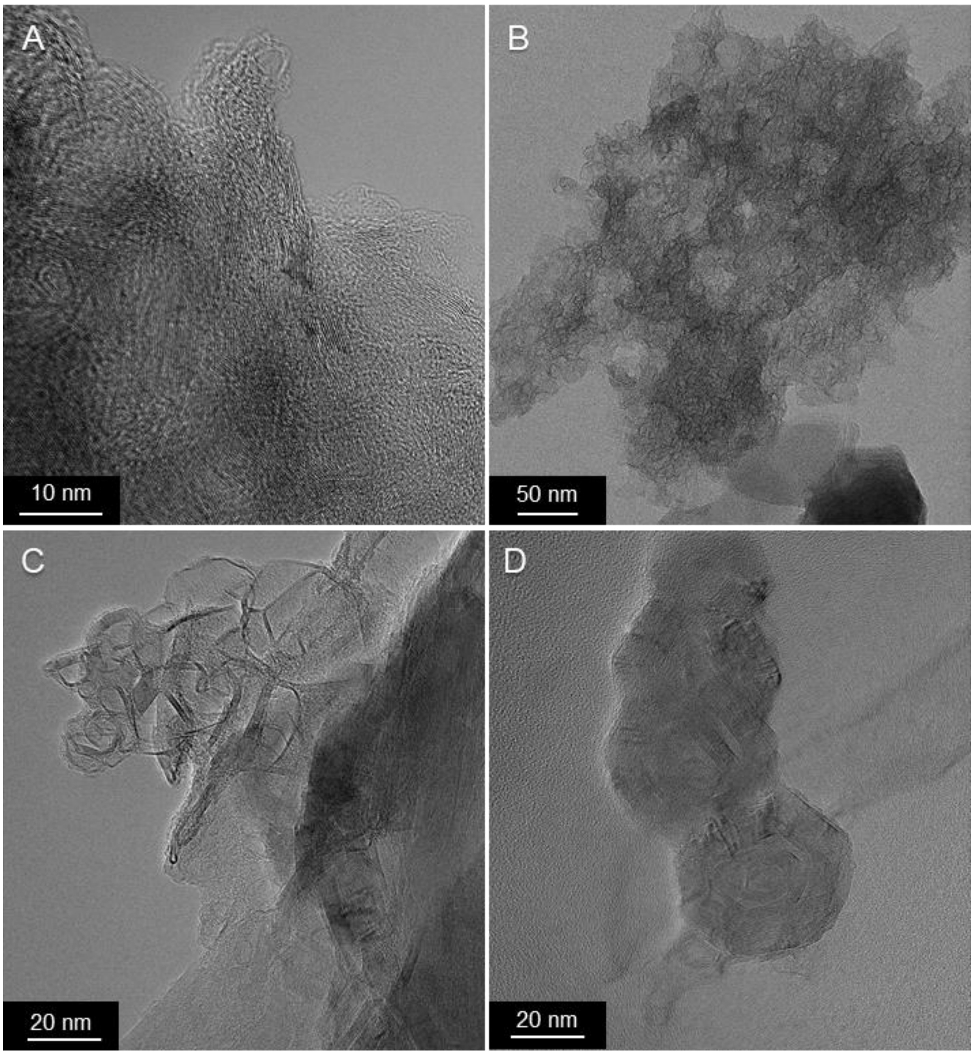

Figure III - 22. TEM images: microporous disordered carbon from CD-SA-G (A) and CD-RO-G (B); (C) polyhedral pores in the edge of the particle bordering disordered carbon and graphitic domains; (D) CD-SA-G polyhedral microtexture.

The SEM/EDS analysis on graphitized demineralized char samples have showed significant morphological changes compared to the char concentrate and demineralized char concentrate samples, and a wide variety of graphite forms, like the ones described for natural and synthetic graphite were observed (Baer, 2020; Barrenechea et al., 2009; Dimovski et al., 2001; Double and Hellawell, 1974; Gogotsi and Dimovski, 2006; Jaszczak et al., 2007, 2003; Kvasnitsa et al., 1999; Kwiecińska and Petersen, 2004; Melvin et al., 2019).

Compared to the other samples, the topography of the chars from the CD-PT-G sample shows less transformations following graphitization. The char surfaces appeared to be smoother (Figure III - 23A,B) and only few submicrometric (<1 µm) whiskers and crystallites were observed on the surface and in the pores of char particles (Figure III - 23B,C), while CD-SA-G and CD-PL-G samples contained discrete plates of imperfect hexagonal graphite crystals on the char surface (Figure III - 23C,D).

The sample CD-RO-G, however, is the one where large graphite forms of all types are present (Figure III - 24). In detail:

- Some char particles present platy-structured walls suggesting a full structural reorganization during the graphitization process (Figure III - 24A).
- Columnar graphite (crystals stacks) was found covering the inner and outer surface of carbonaceous particles (Figure III - 24B). The layered growth and the hollow polyhedron visible in the center of the columnar structures suggest a macro-spiral growth as described by Kvasnitsa et al., (1999) for metamorphic graphite.
- Spherical morphologies appear as aggregates over the char particle surface (Figure III - 24A,C). In a single case, a hollow broken sphere with columnar structures in the inner surface was observed. Spherical forms have been related to the catalytic effect of mineral matter (Deshmukh et al., 2010; Oberlin and Rouchy, 1971). Graphite with this morphology is used as a high value product in Li-ion batteries (Jara et al., 2019). Understanding the formation mechanism of the spheres is an important aspect that can be explored in future research work.
- Whiskers and cones were found attached to the inner and outer surfaces of char particles and loose (Figure III - 24). The morphology of the whiskers varies from cigar-like with a dome-shaped tip to conical with a pointed tip and they can reach up to 80 µm in length. Some of these structures present spiral growth steps indicating a scroll-type structure (Figure III - 24F). The observation of broken whiskers and cross-sections in polished blocks show a solid structure, in some cases with graphite crystals almost perpendicular to the major axis of the whiskers (Figure III - 24G,H). These structures may have resulted from a cone-helix growth as proposed by (Double and Hellawell, 1974), but further studies are needed to confirm the growth mechanism.

Spherical agglomerates, whiskers and cones were observed to a lesser extent in the CD-PL-G sample (Figure III - 23H) and had smaller dimensions. During petrographic observations, it was verified that whiskers and cones in the CD-PL-G sample are mainly found within char pores while in the CD-RO-G sample they are mainly detached.

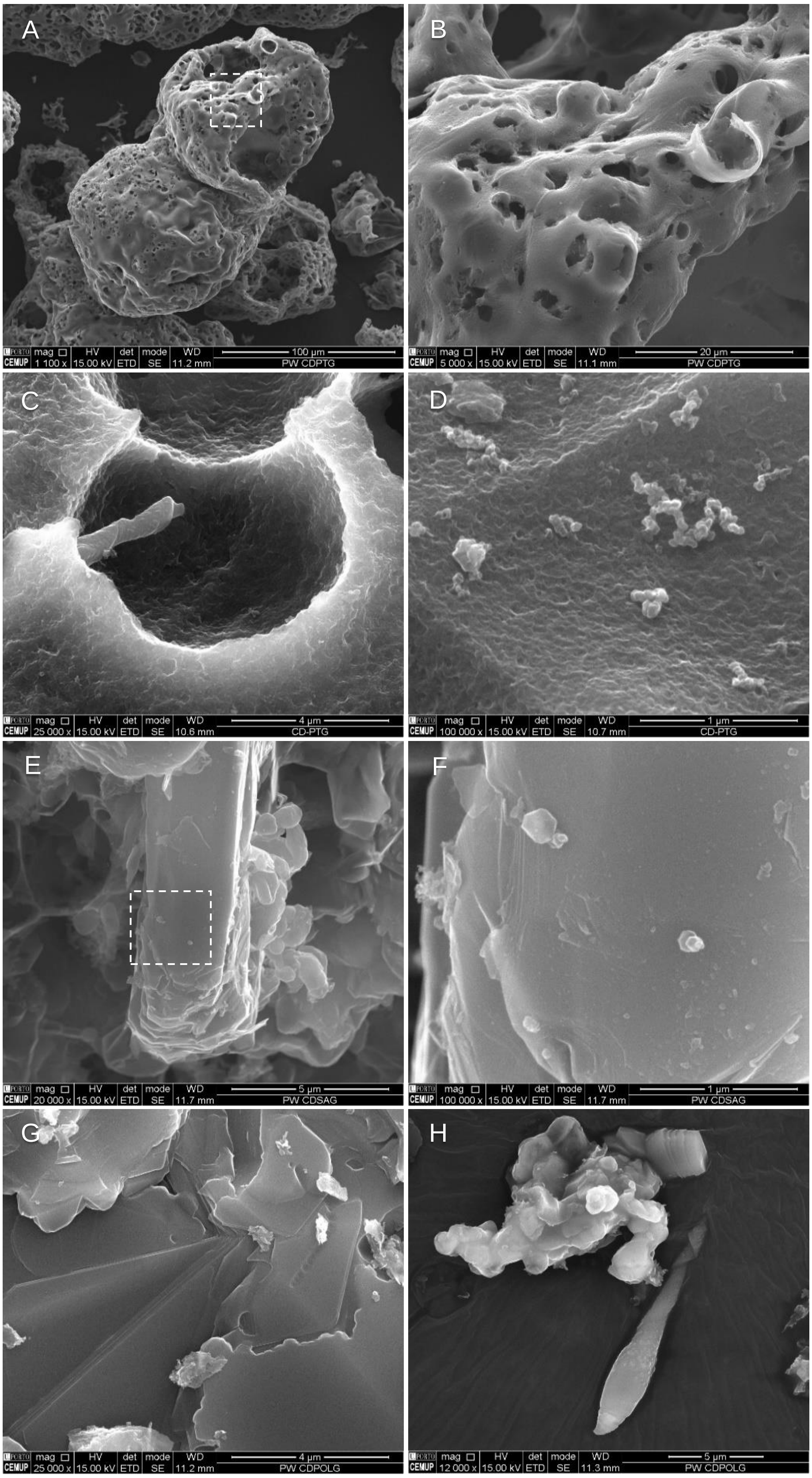

Figure III - 23. Graphitized demineralized chars observed under SEM/EDS (SE mode): (A) rounded char particle from CD-PT-G with the surface appearing smoother (×1100); (B) magnification of dashed square in “A”, surface detail (×5000); (C) whisker inside char pore, CD-PT-G (×25 000); (D) crystallites over char surface, CD-PT-G (×100 000); (E) CD-SA-G exhibiting elongated graphite crystals (×20 000) with (F) imperfect hexagonal graphite crystals as discrete plates over the surface (dashed square in “E”, ×100 000); (G) particle from CD-PL-G exhibiting imperfect graphite crystals (×25 000); (H) whisker presenting spiral growth steps and agglomerate of spherical graphite forms, CD-PL-G (×12 000).

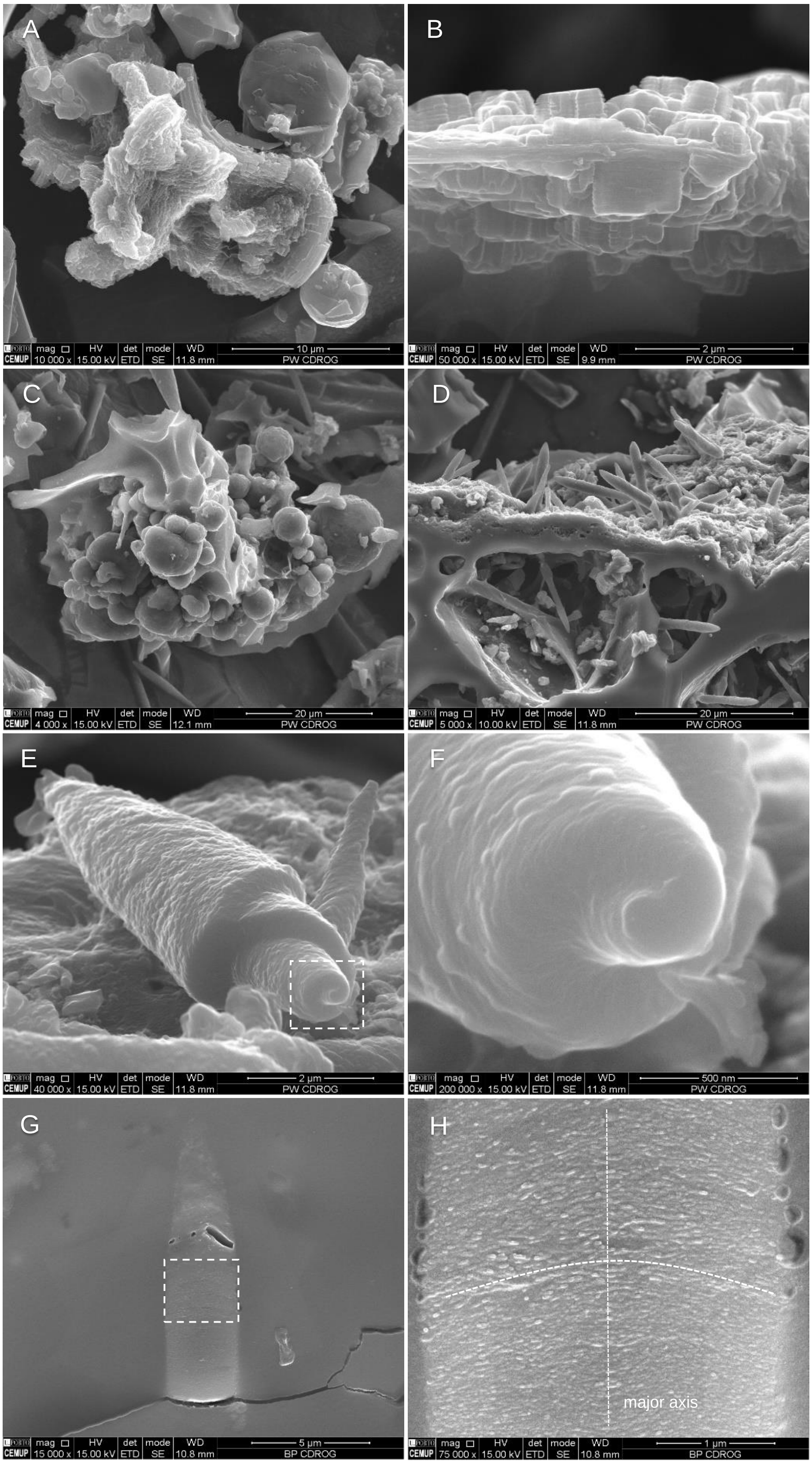

Figure III - 24. Graphitized char from Romania observed under SEM/EDS (SE mode): (A) platy graphitic material composing the char particle wall; (B) graphite stacks on and inside char walls (×50 000); (C) sphere aggregate (×4000); (D) whiskers over the surface and inside char pores (×5000); (E) whisker exhibiting a spiral growth (×40 000); (F) magnification of the dashed square in A showing the solid structure of the whisker and discrepantly stacked graphite crystals (×200 000); (G) whisker cross-section observed on polished block (×15 000); (H) magnification of the dashed square in C showing the graphite crystallites arrangement (×75 000).

It is interesting to note that graphitized samples showing a greater variety of graphite forms (CD-RO-G and CD-PL-G) had the highest amounts of Fe_2O_3, volatile matter, H/C and O/C ratios (Table III - 12 and Table III - 14) and higher volumes of unburned coal particles (Table III - 16) in the respective demineralized samples. Nevertheless, to establish relationships between those parameters and the graphite forms observed further detailed research would be needed.

To understand why the char concentrates from Portugal, Poland and South Africa showed a distinct response to graphitization despite originating from coals of a similar rank, it was decided to assess the Raman properties of different char morphotypes to check the possible relation between the structural transformations observed and the original macerals, the char morphotype and the graphitized char structures. For this purpose, Raman microspectroscopy (detailed methodology in Part II) was used to analyze specific chars and char structures.

Since the pioneer work of (Tuinstra and Koenig, 1970), Raman spectroscopy was extensively used to characterize carbonaceous material and several parameters have been employed to assess structural ordering, namely integrated D/G intensity ratio, relative intensity of ID/It where It = ID + ID2 + IG, position (ω, frequency, cm^{-1}), full width at half maximum (FWHM, cm^{-1}), area of D and G bands and the bands appearing in the second-order spectrum (e.g., Beyssac et al., 2002; Cabielles et al., 2009, 2008; González et al., 2005, 2003, 2002; Guedes et al., 2010; Lespade et al., 1984; Pasteris and Wopenka, 1991; Schito et al., 2017; Suárez-Ruiz and García, 2007; Wopenka and Pasteris, 1993) In the present research, only the graphitized demineralized samples presented a well-defined second-order spectrum so the parameters chosen to characterize and compare the structural ordering were based on the first-order spectra (Table III - 19).

The general spectra obtained on the char concentrates reveal the presence of bands G (1601 – 1612 cm^{-1}) and D (around 1342 – 1362 cm^{-1}), and of weaker bands S_R (around 1053 – 1110 cm^{-1}), S (1159 – 1236 cm^{-1}), Sl (1250 – 1318 cm^{-1}), Vr (1342 – 1362 cm^{-1}), Vl (1454 – 1502 cm^{-1}), Gr (1531 – 1572 cm^{-1}) in the first order spectra. The bands identified resemble those reported by Li, (2007) and Li et al., (2006). The bands Gr (~1540 cm^{-1}), Vl (~1465 cm^{-1}) and Vr (~1380 cm^{-1}) has been assigned to aromatic ring systems typically found in amorphous carbon (3 – 5 fused benzene rings) (Li, 2007; Li et al., 2006). Furthermore, the D2 band usually found at 1620 cm^{-1} as a shoulder of the G band was absent. This feature is characteristic of disordered materials where D2 and G are merged into in a single band at approx. 1600 cm^{-1} (Beny-Bassez and Rozaud, 1985;

Beyssac et al., 2003, 2002; Lahfid et al., 2010; Tuinstra and Koenig, 1970; Wopenka and Pasteris, 1993). Kouketsu et al., (2014) argues that in low grade metamorphism this band is mainly attributed to D2 while the G band is nearly absent.

Differences were found among the spectra of the different morphotypes. For crassispheres and crassinetwork or fused parts of mixed morphotypes the D and G bands have similar intensities (Figure III - 25) and an average integrated ID/IG intensity ratio in the range of 0.93-1.18 (Table III - 19). In contrast, solid, fusinoid and unfused parts of mixed morphotypes have a D band more intense than the G band (Figure III - 25) and higher average integrated ID/IG intensity ratios (1.40 - 1.47) (Table III - 19).

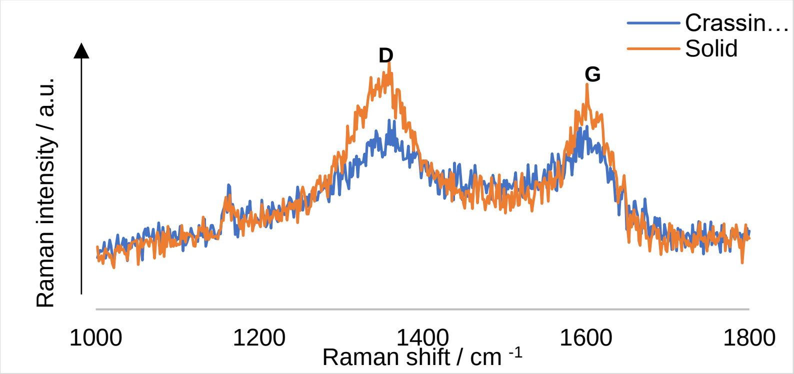

Figure III - 25. Representative Raman spectra for crassinetworks and solid/fusinoid morphotypes.

Since a lower integrated ID/IG intensity ratio is considered an indicator of a higher structural order and since sample CC-PT is mainly composed by spheres and networks (Badenhorst et al., 2020), which are characterized by presenting the lowest ID/IG ratios, it can be deduced that the vitrinitic-derived chars of this sample are the most structurally ordered of the four samples studied. This data is in agreement with petrography (higher reflectance and R_{am} parameter) and XRD (d_{002}) data.

The spectra of the carbonized and demineralized char concentrates are similar to those obtained for the bulk char concentrates and the same bands were assigned to these samples. Changes in the integrated ID/IG intensity ratio were observed with carbonization (0.03 - 0.29) and demineralization (0.02 - 0.15). In general, carbonization leads to an increase in the integrated ID/IG intensity ratio while for demineralization opposite was seen (Table III - 19). During the carbonization process, the devolatilization, aromatization and rearrangement of the BSU occurs (Oberlin, 1984), and the increase in ID/IG can be caused by the relative increase in the concentration of aromatic rings with six or more benzene rings (Li et al., 2006). Regarding the effect of demineralization, a decrease in the spatial arrangement of the BUSs was observed in the bulk samples through the R_{am} parameter (Table III - 17).

Table III - 19. Raman parameters obtained and calculated in the studied samples. FWHM and position (ω) in cm^{-1}.

				D area	G area	ID/IG	D FWHM	G FWHM	D/G FWHM	ωD	ωG	ωG-ωD	ID/It
Poland	Crassinetwork		CC	1369	1163	1.18	96	68	1.42	1356	1607	251	
			CC-C	1398	1221	1.16	99	74	1.35	1355	1606	251	
			CD	1764	1522	1.16	98	69	1.43	1392	1609	253	
			CD-G	1109	879	1.26	38	31	1.24	1353	1587	233	0.44
			IM	1031	878	1.17	35	35	1.02	1353	1586	233	0.43
	Mixed	Fused	CC	1599	1429	1.12	97	73	1.34	1355	1606	251	
			CC-C	1483	1223	1.21	100	73	1.37	1356	1608	251	
			CD	1835	1757	1.06	97	75	1.29	1355	1606	251	
			CD-G	1303	898	1.45	38	30	1.30	1352	1586	234	0.49
		Unfused	CC	1898	1324	1.40	96	65	1.49	1353	1609	256	
			CC-C	2448	1604	1.52	88	66	1.35	1353	1609	255	
			CD	2137	1586	1.35	100	65	1.55	1347	1607	260	
			CD-G	1358	888	1.54	45	22	2.04	1352	1588	236	0.53
	Solid/Fusinoid		CC	2187	1525	1.44	99	65	1.53	1351	1608	257	
			CC-C	1960	1386	1.42	98	67	1.46	1351	1605	254	
			CD	1912	1209	1.59	102	62	1.63	1349	1608	258	
			CD-G	1404	894	1.58	46	22	2.14	1350	1588	237	0.54
			IM	1284	851	1.53	43	26	1.76	1351	1585	235	0.49
Portugal	Crassisphere		CC	1284	1376	0.93	96	79	1.23	1356	1609	253	
			CC-C	1865	1497	1.22	94	64	1.47	1353	1608	255	
			CD	1235	1252	0.98	93	73	1.27	1354	1608	253	
			CD-G	1106	887	1.24	38	28	1.35	1353	1586	233	0.43
	Crassinetwork		CC	1920	1596	1.18	92	68	1.35	1351	1607	256	
			CC-C	1279	1156	1.11	89	76	1.18	1353	1607	254	
			CD	1461	1333	1.10	93	75	1.25	1358	1608	250	
			CD-G	1006	844	1.20	38	29	1.30	1353	1587	233	0.43
			IM	956	901	1.06	37	29	1.28	1353	1586	233	0.41
	Solid/Fusinoid		CC	1854	1281	1.46	81	65	1.25	1352	1608	256	
			CC-C	3138	1931	1.62	85	64	1.33	1352	1605	254	
			CD	2377	1776	1.32	86	67	1.28	1353	1607	254	
			CD-G	1622	964	1.71	47	42	1.14	1351	1588	236	0.54
South Africa	Crassinetwork		CC	1243	1181	1.05	91	68	1.35	1348	1607	258	
			CC-C	1537	1318	1.17	100	69	1.45	1357	1610	253	
			CD	1349	1182	1.15	99	69	1.45	1358	1611	253	
			CD-G	1034	825	1.26	36	29	1.25	1354	1586	233	0.46
	Mixed	Fused	CC	1349	1267	1.09	99	74	1.34	1357	1608	251	
			CC-C	1463	1277	1.17	98	73	1.36	1352	1609	258	
			CD	1409	1486	0.97	98	82	1.22	1352	1607	255	
			CD-G	999	788	1.27	42	31	1.39	1353	1586	234	0.43
		Unfused	CC	2061	1458	1.40	97	67	1.47	1357	1608	251	
			CC-C	1463	1277	1.17	98	73	1.36	1352	1609	258	
			CD	2422	1619	1.49	99	65	1.52	1354	1608	254	
			CD-G	1298	975	1.36	41	35	1.20	1352	1587	235	0.48
			IM	1355	1139	1.19	31	25	1.22	1352	1585	233	0.45
	Solid/Fusinoid		CC	1838	1351	1.40	90	65	1.39	1353	1606	253	
			CC-C	2412	1631	1.46	96	68	1.42	1352	1607	255	
			CD	1739	1186	1.47	100	66	1.51	1357	1610	254	
			CD-G	1222	875	1.41	42	34	1.24	1353	1586	234	0.48

IM – incipient microtexture

It is interesting to note that in the CD-SA sample, the integrated ID/IG intensity ratio slightly increases in the morphotypes analyzed except in fused parts of mixed morphotypes and the R_{ev} parameter (Table III - 17) suggested a slight decrease in chemical ordering of the BSU in this sample.

The typical spectra of the graphitized samples studied present the first order bands G (1581 - 1592 cm^{-1}), D (1347 - 1356 cm^{-1}), D2 (1617 - 1632 cm^{-1}) and D3 (1465 - 1497 cm^{-1}), and in the second-order region the S1 band (~2700 cm^{-1}). The latter corresponds to the overtone of the D band (Nemanich and Solin, 1979), and is the most prominent feature although the S2 band (~2940 cm^{-1}) was also discernible in most spectra. In well-crystalized graphite, the 2D band splits into two bands (Lespade et al., 1984) but this feature was not observed in any of the acquired spectra. Nevertheless, a slight asymmetry in this band was often noted suggesting some development in the third dimension. Overall, ID/It parameters obtained for the morphotypes after graphitization are within the range reported in Badenhorst et al., (2020).

The results evidence a significant increase of the char structural order caused by graphitization since there is a downward shift in the G band position (21 cm^{-1} average) and a narrowing in the FWHM of the D (55 cm^{-1} average), and G (38 cm^{-1} average) bands. However, the same morphotypes show different changes from sample to sample, which is most probably related with the original composition of the char.

Differences in the evolution of integrated ID/IG intensity *vs* D/G FWHM ratios for the crassinetworks and solid/fusinoids before and after graphitization are shown in Figure III - 26B,C.

Regarding crassinetworks, the CD-PT sample present a low integrated ID/IG intensity ratio (1.27) compared to the samples CD-PL and CD-SA (1.43 and 1.43, respectively). Graphitization leads to a similar decrease in FWHM of the D and G bands (approx. 60 %) in CD-PT-G sample while in the CD-PL-G and CD-SA-G samples the D band narrows relatively more than G, leading to a decrease in the D/G FWHM ratio (Figure III - 26B). Nevertheless, in the three samples, the integrated ID/IG intensity ratio of crassinetworks increased with graphitization which corresponds to the general trend observed in the morphotypes analyzed. As mentioned for the carbonized char samples it can result from a relative increase in the concentration of aromatic rings with six or more benzene rings derived from hydroaromatics dehydrogenation and growth of aromatic rings (Li et al., 2006).

The solid/fusinoids changes amongst the three samples can be observed in Figure III - 26C. The initial integrated ID/IG intensity ratio, as verified for crassinetworks, is lower in CD-PT (1.32) than CD-PL and CD-SA, 1.59 and 1.45, respectively (Table III - 19). The narrowing of the D and G bands with graphitization in CD-PT is lower than for the other two samples (45 and 37 %, respectively). The D/G FWHM in CD-PL increases with graphitization since the G band narrows relatively more than the D band. The reverse is observed for CD-SA and CD-PT. The integrated ID/IG intensity ratio changes as follows: (a) it holds in CD-PL, (B) increases in CD-PT, 0.38 and (C) slightly decrease in CD-SA, 0.06.

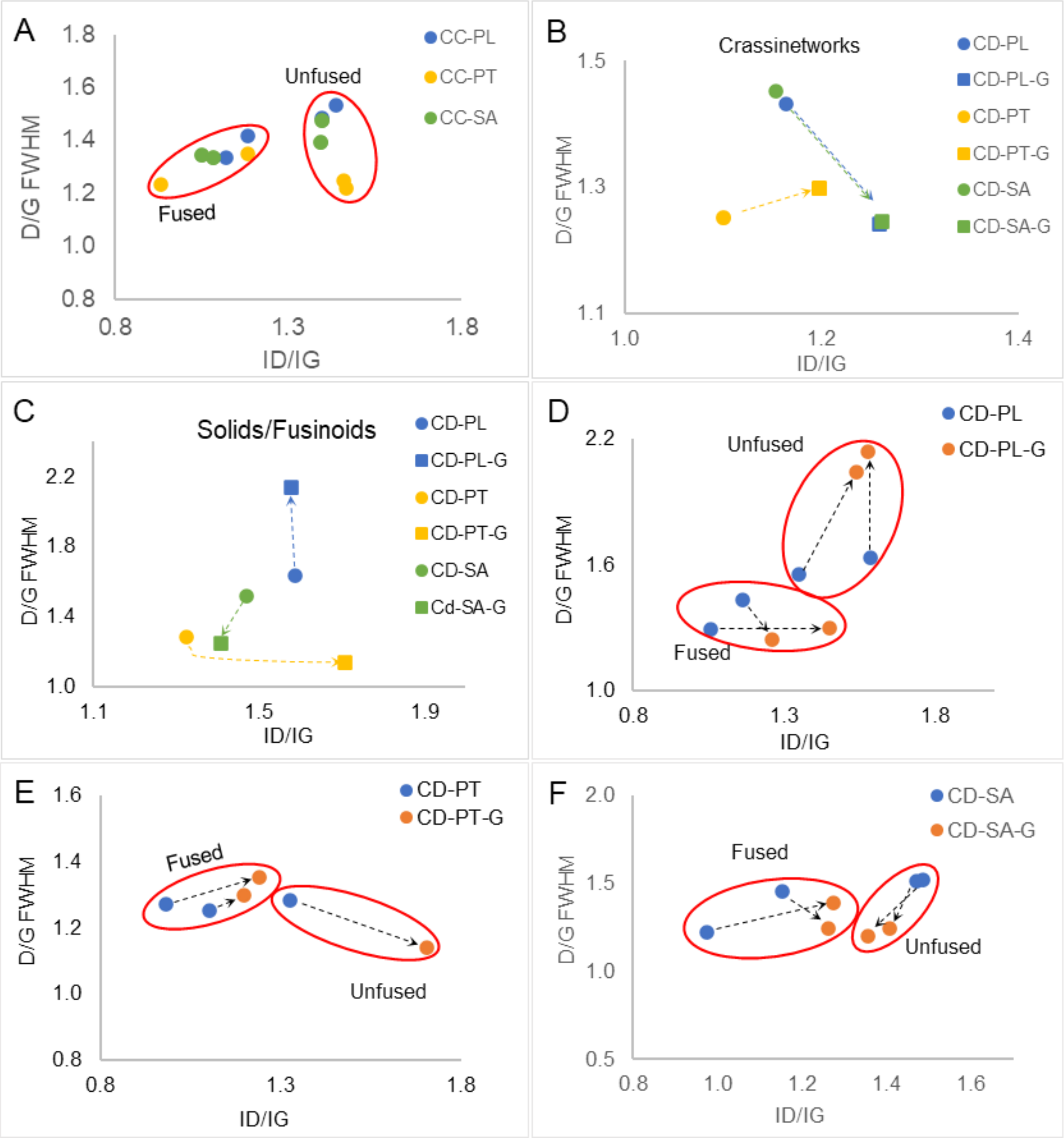

Figure III - 26. Variation of intensity area ratio ID/IG with D/G FWHM ratio: (A) char concentrates, crassinetworks, (C) solid/fusinoid (D) Portuguese sample, (E) Polish sample and (F) South Africa sample.

In Figure III - 26D-E the evolution of integrated ID/IG intensity vs D/G FWHM ratios for each sample is shown, which evidences the influence of the fused or unfused character of the chars on the transformations caused by the graphitization, which in turn depends of the macerals behavior in relation to combustion and carbonization conditions. The unfused particles/parts from the South Africa sample are the only ones exhibiting a decrease in integrated ID/IG intensity ratio, as a result of a higher decrease in D band area (approx. 60 %). This can be related to the type of inertinite in the feed coal, which is mainly inert inertodetrinite (20.8 vol.%) and inert semifusinite (18.4 vol.%) (Badenhorst et al., 2019). Meanwhile, the high amount of mixed morphotypes and solid/fusinoids in C-SA (66.7 vol.%; (Badenhorst et al., 2020) and their higher structural order after graphitization (ID/IG) may be one of the causes of the higher graphitization degrees observed in this sample compared to the Portuguese and Polish samples.

2.3. Application of char in oxygen reduction reaction (ORR)

The substitution of natural graphite by char recovered from FA is a potential hypothesis for its application. However, this requires that a set of preliminary studies are made on different application fields. Therefore, during this study, joint research was proposed and carried out with researchers from the Green Chemistry Laboratory (REQUIMTE, Portugal) to check for an application where the different char materials concentrated and graphitized could act as variables.

Taking into account that graphene is used in oxygen reduction reactions, the question of the possibility of replacing this material by char arose and two hypotheses were constructed:

(1) Being the char a carbonaceous material already in an advanced stage of thermal transformation it may replace to a certain degree graphene in ORR;
(2) The graphitization of the char will produce a material that will replace more efficiently graphene in ORR.

To confirm these hypotheses trials carried out by the REQUIMTE team were then jointly designed and interpreted based on the characterization results discussed above. Here an overview of the most important results obtained is given.

Oxygen reduction reaction trials: comparing char and natural graphite

Detailed trails were made with the Portuguese char samples, where fractions from bulk FA sample to demineralized char concentrate were characterized, tested, and compared with natural graphite from Ancuabe mine (Cabo Delgado province, North of Mozambique). The results are published elsewhere (Nunes et al., 2022).

The study showed that char concentrate, and the respective demineralized char are promising electrocatalysts with good methanol tolerance and long-term electrochemical stability. Nevertheless, all the samples exhibited ORR performance similar or even better than natural graphite, demonstrating their potential to substitute this material in similar energy-related applications (Nunes et al., 2022).

Oxygen reduction reaction trials: influence of char from different provenance

The char concentrates and the respective demineralized and graphitized samples characterized on were tested as electrocatalysts in oxygen reduction reaction (ORR) and the results are published elsewhere (Fernandes et al., 2021).

Char concentrates, demineralized char, carbonized char and graphitized demineralized char from all provenances here mentioned were used), and the trials have showed that all samples have moderate ORR performance comparable or even better than commercial graphene. However, the second hypothesis was not confirmed since demineralization and the subsequent graphitization of the char do not bring significant improvement to the ORR catalytic activity. Furthermore, the influence of degree of graphitization was not clear since CD-SA-G and CD-PT-G had similar ORR catalytic activity. However, the removal of volatile matter via carbonization leads to an improvement of the onset potentials (E_{onset}) and diffusion-limiting currents (j_L) which can be related to the higher accessibility of sites (Fernandes et al., 2021).

In summary, both studies demonstrated the potential of char as substitute of natural graphite in ORR without the need of being demineralized and graphitized. This is quite important seeing as it presents the possibility of a direct application at industrial scale because of the residues and energetic costs.

2.4. Conclusions

To obtain char concentrates from coal fly ash without using dense liquids, a laboratory-scale separation process was successfully conceived. The sequential application of simple methods, such as sieving, gravimetric separation, vibration-induced segregation and elutriation, enabled to obtain a char concentrate with 72.55 FC wt.%, db, while recovering 29.28 % of carbon from the bulk FA sample. These results obtained using simple methods are comparable to previous investigations by other researchers using advanced techniques such as triboelectrostatic separation.

Sequential sieving (dry and wet) and vibration-induced segregation (dry impaction) were crucial to remove mineral matter, reducing the main oxides, SiO_2 and $Al_2O_{3,}$ in almost 60% and increasing the carbon content more than 55 wt.%. The removal of the remaining oxides after these techniques exceeds 70 %, except for SO_3 that relatively enriches most likely due to its association with char.

The char concentrate obtained in this research, also nominated as Portuguese (PT) char sample, and respective demineralized sample, was characterized and compared to samples from Poland (PL), Romania (RO), and South Africa (SA) from the Charphite project. It was concluded that these char concentrates present differences among them that are mainly related to the feed coals (medium rank coals, except lignite from Romania). The CC-PT sample had the highest C content (96.63 wt.%, daf) and intermediate H content (0.48 wt.%, daf), and particles with anisotropic optical texture. By contrast, the C-RO sample, which is derived from a low rank coal, presented the highest VM and H contents, 24.87 and 2.86 wt.%, daf, and char was mostly isotropic with an angular morphology. The C-SA sample, which is derived from a medium rank C, low vitrinite, was characterized by the abundance of inertinitic and mixed morphotypes and had more SiO_2 and Al_2O_3 than other samples due to mineral matter interwoven into the char matrix. The CC-PL sample, which is derived from a medium rank C coal, is chemically similar to CC-PT but char particles were less vesiculated and had flux structures.

The characterization results obtained highlighted different graphitization abilities among the studied chars. It was verified that samples such as CC-PT and C-SA with similar initial reflectance, texture anisotropy (R_{am}) and interlayer spacing (d_{002}), but with different mineral matter contents and different predominant morphotypes present quite different graphitization degrees, 19.77% and 93.02%, respectively. The correlation between d_{002} and Al_2O_3 suggests that aluminum-rich residues infilling char pores of CD-SA after demineralization might have been beneficial during graphitization. In the Portuguese sample, the loss of hydrogen and structural changes during demineralization may have affected its ability to graphitize.

Even the sample CD-SA-G, which responded better to graphitization, had disorder carbon and most of char morphotypes remained identifiable. Detailed Raman microspectroscopy have showed that particles classified as the same morphotype respond differently to graphitization. Unfused morphotypes and unfused parts of mixed morphotypes from South Africa were the only exhibiting a decrease in ID/IG ratio, indicating an increase in the structural ordering. Moreover, even considering the catalytic effect of residual mineral matter left after demineralization, not all morphotypes are affected in a similar way, which may be related with the proprieties of the feed coals and the behavior of macerals during combustion.

The CD-RO which was mostly composed of isotropic and unreacted particles (initial R_{am} close to 0) showed the second highest degree of graphitization 80.23 wt.%, which may be related to its high ash content (7.82 wt.%, db) and high hydrogen (3.32 wt.%, daf) content after demineralization. Nevertheless, the comparison with CD-SA which graphitized best and presented lower contents of ash and hydrogen highlights the influence of other factors in the graphitization ability, such as the spatial arrangement of the BSU. The CD-RO-G sample also presented a wide variety of graphite forms (e.g., spheres and whiskers) which were also the larger and well-developed ones.

All the char concentrates demonstrated potential to substitute graphite as electrocatalysts in oxygen reduction reaction without the need to be demineralized and graphitized. In this sense, future work may focus on the improvement of char recovery process and to fully understand the proprieties influencing the electrocatalytic behavior.

3. Magnetic concentrates (MC)

Magnetic concentrates (MC) were recovered via wet magnetic separation of six ash samples: BA, ECO and ESP12 from campaigns S1 and S4 (samples details and methodologies are provided in Part II). In the S1 samples, a sequential magnetic separation was carried out by using two different magnets: ferrite (Fe) magnet to collect ferromagnetic particles and neodymium (Nd) magnet to recover paramagnetic particles and Fe-poor morphotypes. The MC obtained from the referred sequential process were dry sieved and chemically analyzed for major oxides and trace elements to evaluate elements distribution across the respective size-fractions. Further characterization of bulk ash and bulk MC included magnetic susceptibility, isothermal remanent magnetization (IRM), Mössbauer spectroscopy, reflected microscopy (oil immersion), SEM/EDS and Raman microspectroscopy (methodologies described in Part II). The results of bulk ash samples detailed characterization can be consulted in chapter 1 (Part III).

3.1. Yields and particle-size distribution

The yields using the Fe magnet ranged between 4.5 and 13.1 wt.% while with Nd magnet stand between 8.9 and 53.4 wt.% (Table III - 20). In both cases, the highest yields were obtained for the economizer FA although it does not linearly correlate with the Fe_2O_3 content in bulk ash (Table III - 20).

Sieving results show substantial differences in the particle-size distribution of the MC related to the type of sample and the type of magnet used. In general, the MC collected from BA are significantly coarser than the ones collected from FA, ECO, and ESP, (Figure III - 27), mirroring the coarser nature of BA bulk ash (Santos et al., 2022). The Nd-MC from BA and ECO are coarser than the corresponding Fe-MC, with the fraction >150 µm representing 60.3 wt.% and 28.5 wt.%, respectively (Figure III - 27). The detailed imaging analysis of the referred MC (Figure III - 28A-D) show a greater occurrence of particles with dimensions >1 mm, which are mainly agglomerates, corroborating the differences found by sieving. Furthermore, in the Fe-MC, agglomerates are more often observed in BA than ECO, where discrete Fe-rich morphotypes such as ferrospheres are more common (Figure III - 28A,C). On the other hand, the particle size distribution regarding the MC collected from the ESP FA samples studied are similar, with more than 40 wt.% of the particles being <25 µm in size (Figure III - 27), which is in agreement with reported data (Hower et al., 1999a; Lauf et al., 1982; Vassilev et al., 2004a) .

Given the coarser nature of MC from BA, it was decided to sieve the fraction >150 µm (sieves 4, 2, 1 and 0.5 mm) and select representative size-fractions for chemical characterization.

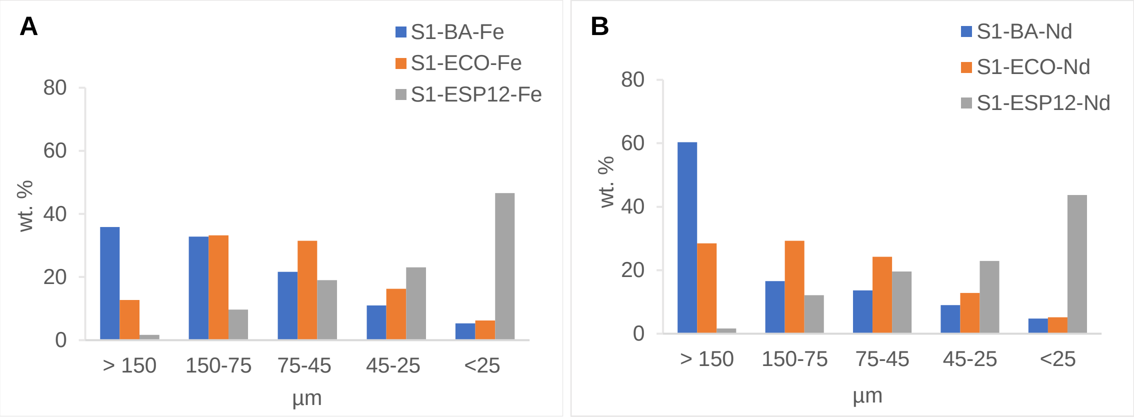

Figure III - 27. Particle size distribution of magnetic concentrates collected from S1-BA, S1-ECO and S1-ESP12 samples with ferrite (A) and neodymium (B) magnet.

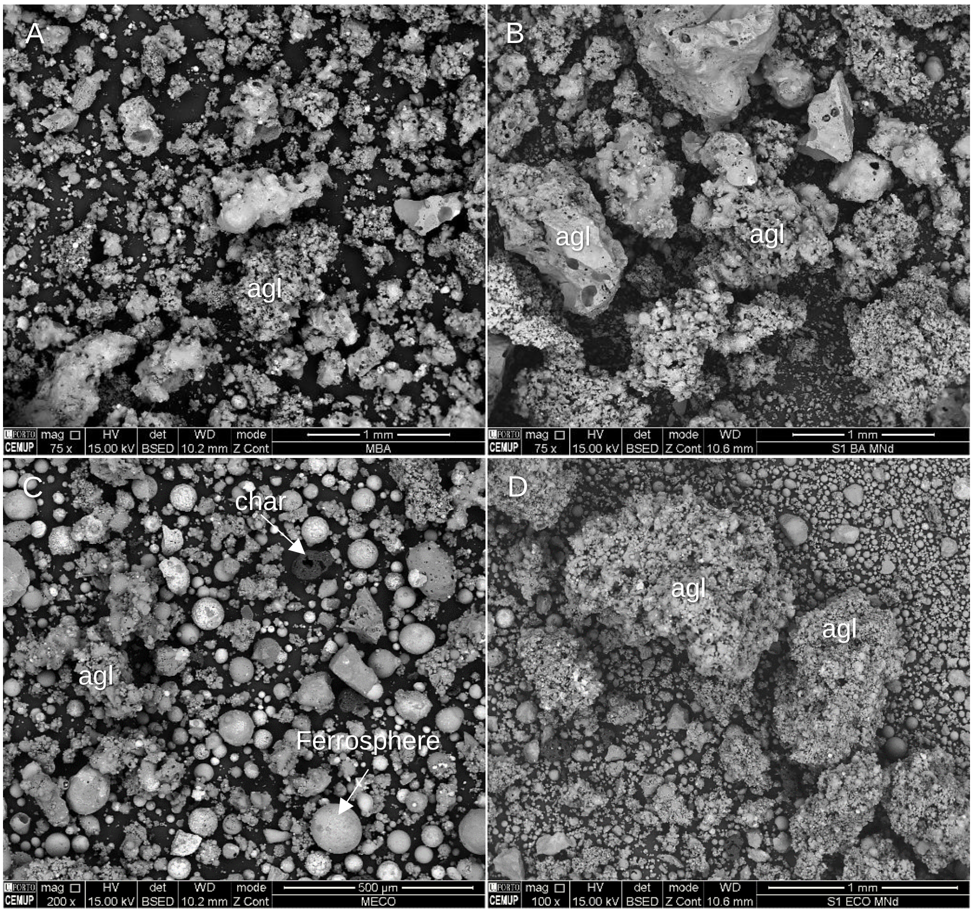

Figure III - 28.Detailed imaging of magnetic concentrates collected from S1-BA (A-B) and S1-ECO (C-D): magnetic concentrates collected with ferrite magnet (A,C) present a finer grain size than the ones collected with neodymium magnet (C,D) where agglomerates, agl, larger than 1 mm are frequent. The MC collected from BA (A-B) are coarser than MC from ECO FA (C-D).

3.2. Occurrence, morphology and microtexture

The SEM/EDS was employed to obtain detailed imaging of powder MC samples to assess Fe-bearing phases modes of occurrence (i.e., spatial relations), morphology and microtexture.

In magnetic concentrates collected from BA and ECO FA the Fe-bearing phases are often found embedded in agglomerates, especially in the coarser fractions (>150 μm). The occurrence of agglomerates in coal combustion ash have been reported previously (Fisher et al., 1976; Kutchko and Kim, 2006; Miller and Schobert, 1994, 1993; Valentim et al., 2009b). These are essentially composed by micrometric particles with variable composition bonded either directly to each other (interrupted coalescence) or through an aluminosilicate matrix (weld pool) (Fisher et al., 1976; Valentim et al., 2009b). Hence, Fe-bearing phases in MC from BA and ECO are found bonded to other particles (Figure III - 29A,B), as exsolutions in the amorphous matrix (Figure III - 29C,D) and as discrete Fe-bearing morphotypes embedded in the aluminosilicate matrix (Figure III - 29E). The aluminosilicate glass matrix itself contains variable amounts of iron as confirmed by EDS spectra (Figure III - 29) which was also observed in the bulk ash samples (Santos et al., 2022).

Most of the Fe-morphotypes in FA MC and finer fractions of ECO and BA MC present spherical morphologies, close to ideal spheres, with sizes ranging from few micrometers up to 100 μm and containing variable amounts of glass matrix (Figure III - 30). A wide range of microtextures are observed and frequently can be directly attributed to the spinel crystals facets (Sokol et al., 2002). That is the case of the sphere showed in Figure III - 30A where the octahedral crystals have the appearance of triangles. Skeletal and dendritical (Figure III - 30B) are the most common microtextures in the studied MC. These microtextures along with predominance of Fe in the EDS spectra (Figure III - 30A,B) are distinctive features of the morphotypes designated as ferrospheres (Lauf et al., 1982; Sokol et al., 2002; Valentim et al., 2018, 2016) so it can be assumed that they are predominant in the studied MC. The formation of skeletal-dendritic spheres has been attributed to several factors such as coal composition, combustion conditions and cooling conditions (e.g., Blaha et al., 2008; Ramsden and Shibaoka, 1982; Sokol et al., 2002). Recently, (Anshits et al., 2019) investigated structure–composition relationships of skeletal-dendritic globules via systematic SEM/EDS analysis and have showed that the aluminosilicate precursor determining the structure is illite. The presence of this mineral in the feed coals that originated the ash used in the current study was previously confirmed by XRD (Santos et al., 2022).

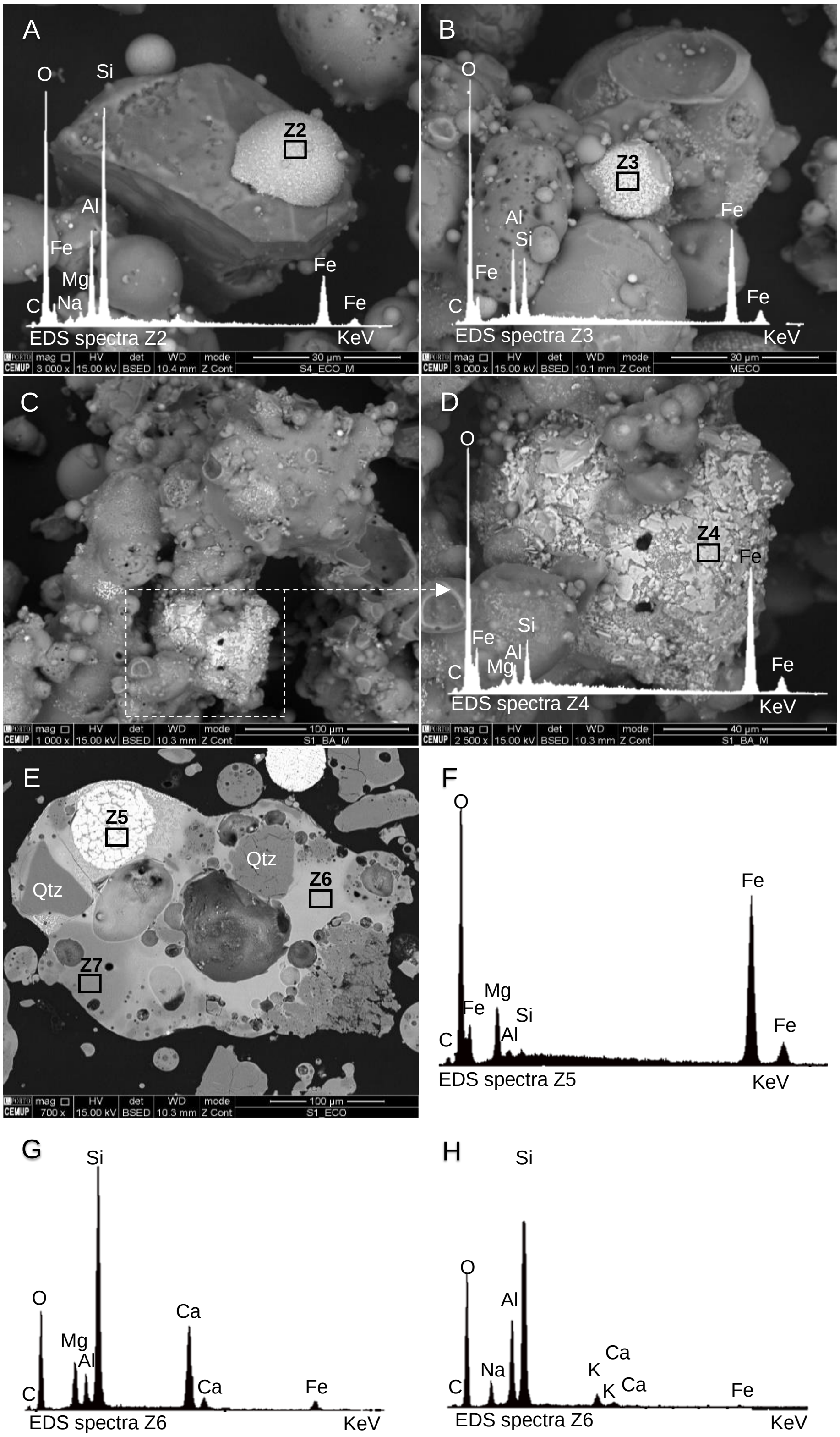

Figure III - 29.Fe-bearing phases in magnetic concentrates (SEM/EDS, BSE mode): (A) ferrosphere bonded to quartz particle with molten surface (×3000); (B) ferrosphere bonded to aluminosilicate in an agglomerate (×3000); (C) aluminosilicate agglomerate with Fe-crystallites (×1000); (D) magnification of dashed square in C and respective EDS spectra of the iron-rich phase: Fe-crystallites; (E) ferrosphere embedded in aluminosilicate glass; (F-H) EDS spectra corresponding to EDS Z locations marked in E.

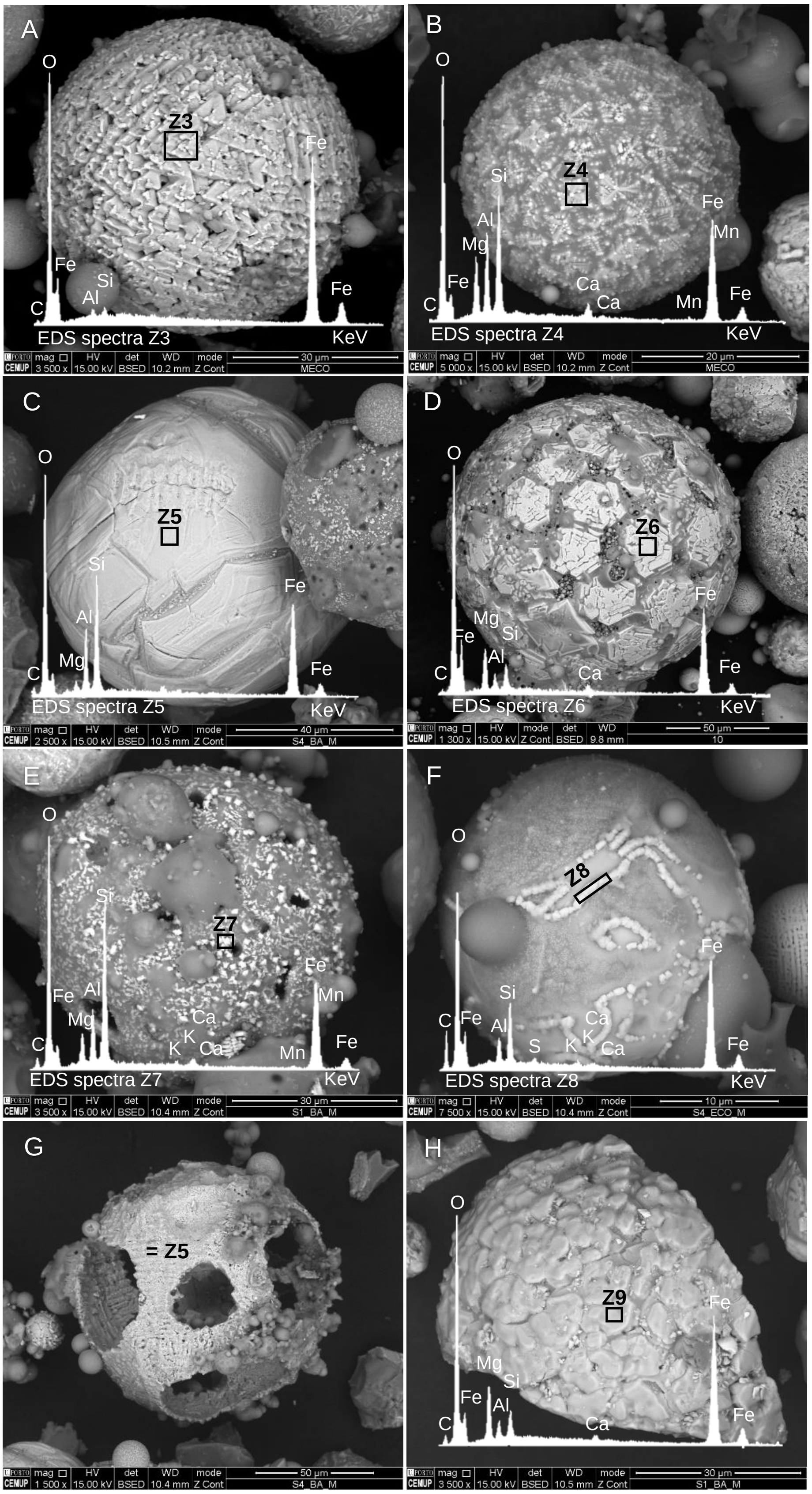

Figure III - 30. Microstructures of ferrospheres and other Fe-morphotypes in magnetic concentrates (SEM/EDS, BSE mode, EDS): (A) skeletal (×3500); (B) dendritic (×5000); (C) monoblock (×2500); (D) blocklike (×1300); (E) molten drop (×3500); (F) mixed (×7500); (G) solid shell (×1500); (H) ferrosphere fragment (×3500).

Monoblock spheres consisting of large crystals without evident glass matrix (Figure III - 30C) and blocklike exhibiting regular polygons embedded in an aluminosilicate matrix (Figure III - 30D) are also observed. According to Anshits et al., (2021, 2020) monoblocks are developed from large, excluded particles of pyrite and siderite containing impurities of Mg and Mn while blocklike derive from sequential conversion of dispersed minerals (pyrite, siderite, quartz, and calcite) with anorthite as the aluminosilicate precursor. Occasionally, molten drop (Figure III - 30E), mixed microtextures (Figure III - 30F), solid shells (no aluminosilicate glass matrix, (Figure III - 30G) and fragments (Figure III - 30H) are observed.

The MC collected with Nd magnet significantly differ from the Fe-MC once aluminosilicate glass is the predominant phase and the Fe-bearing phases are mostly associated with agglomerates while Fe-discrete particles are scarce. This is because the iron-rich particles were previoulsy collected by the ferrite magnet and the final stage with the neodymium magnet mainly collects paramagnetic particles, Fe-poor glass, and glass agglomerates ferrospheres attached.

3.3. Chemical composition

The chemical composition of magnetic concentrates (MC) and respective size-fractions obtained by dry sieving is listed on Table III - 20 and Table A8 (bulk ashes were added for comparison purposes).

The Fe-MC present a Fe-rich (14.87 to 44.16 wt.% Fe_2O_3) aluminosilicate composition (SiO_2 plus Al_2O_3 in the range 45.67 - 76.59 wt.%) which is in agreement with what was previously reported (e.g., Lu et al., 2009; Vassilev et al., 2004a). Besides Fe_2O_3, the Fe-MC present enrichment in MnO, CaO, MgO, Na_2O, K_2O and P_2O_5 (Figure III - 31A), comparatively to the tailings. The enrichment factors (EF) of MnO are the closest to the ones found for Fe_2O_3 (Figure III - 31A) which is most likely related to the Mn ability of substituting Fe in spinel structure (e.g., Hulett et al., 1980).

The average Fe_2O_3 content in Fe-MC decreases as follows: ESP12 (43.07 wt.%) > ECO (35.43 wt.%) > BA (15.88 wt.%). Despite having the lowest Fe-MC yield (5.22 wt.% average), the magnetic particles collected from ESP FA have higher Fe contents. This is in line with the SEM/EDS observations showing that in Fe-MC from FA discrete spherical Fe-rich morphotypes predominate whereas in BA and ECO the Fe is mostly embedded in aluminosilicate agglomerates.

Table III - 20. Yield, major and minor oxides, and loss on ignition (LOI) regarding bulk ash, magnetic concentrates (MC), and respective size-fractions (wt.%) and tailings.

			Yield wt.%	SiO_2	TiO_2	Al_2O_3	Fe_2O_3	MnO	CaO	MgO	Na_2O	K_2O	P_2O_5	SO_3	Cr_2O_3	LOI
S1-BA		Bulk		66.07	0.81	18.28	7.95	0.08	1.50	1.87	1.04	2.11	0.14	0.03	0.02	0.10
	Fe (mm)	MC	5.4	58.85	0.79	17.73	14.87	0.14	1.92	2.59	0.96	1.97	0.15	<0.002	0.02	0.00
		> 500	9.0	65.57	0.84	18.80	7.78	0.07	1.62	1.93	1.09	2.13	0.15	<0.002	0.01	0.00
		500-150	26.8	63.43	0.84	18.68	9.38	0.10	1.91	2.18	1.07	2.11	0.16	<0.002	0.04	0.10
		150-75	32.9	60.65	0.81	18.05	12.77	0.13	1.89	2.49	0.99	2.04	0.16	<0.002	0.01	0.00
		75-45	21.7	57.09	0.81	17.91	16.45	0.15	1.75	2.75	0.92	1.99	0.16	<0.002	0.02	0.00
		<45	16.4	52.50	0.79	17.95	21.00	0.16	1.61	2.91	0.86	1.94	0.15	<0.002	0.02	0.10
		TL	94.2	66.85	0.83	18.60	6.88	0.07	1.46	1.77	1.06	2.13	0.14	<0.002	0.02	0.20
	Nd (mm)	MC	38.3	66.15	0.87	19.25	6.74	0.07	1.45	1.81	1.08	2.23	0.15	<0.002	0.02	0.20
		> 2000	20.9	65.69	0.86	19.43	7.24	0.07	1.48	1.86	1.07	2.23	0.15	<0.002	0.02	-0.10
		2000-500	20.0	65.04	0.88	19.78	7.35	0.07	1.54	1.92	1.09	2.27	0.15	<0.002	0.02	-0.10
		500-150	19.3	65.66	0.85	18.91	7.19	0.07	1.69	1.89	1.09	2.18	0.15	<0.002	0.02	0.30
		150-75	16.6	69.17	0.78	17.52	5.92	0.06	1.46	1.63	1.06	2.04	0.14	<0.002	0.01	0.20
		75-45	13.6	68.49	0.84	18.87	5.27	0.05	1.20	1.58	1.05	2.20	0.14	<0.002	0.01	0.30
		<45	13.8	65.85	0.95	20.53	5.58	0.05	1.08	1.64	1.08	2.40	0.13	<0.002	0.02	0.70
		TL	54.5	66.78	0.79	18.06	7.41	0.07	1.45	1.77	1.05	2.05	0.13	0.31	0.02	0.10
S1-ECO		Bulk		67.77	0.66	15.15	8.13	0.08	1.81	1.86	1.10	1.72	0.13	0.07	0.02	1.51
	Fe (µm)	MC	11.6	41.40	0.57	12.59	35.49	0.33	3.03	4.37	0.66	1.23	0.17	0.05	0.02	0.10
		>150	12.8	58.86	0.82	18.66	10.90	0.11	2.22	2.48	1.11	2.08	0.18	0.03	0.02	2.54
		150-75	33.2	48.97	0.60	13.59	26.42	0.29	3.06	3.81	0.81	1.42	0.17	0.04	0.01	0.80
		75-45	31.5	43.89	0.58	13.16	32.96	0.30	2.84	4.21	0.69	1.29	0.16	0.01	0.01	-0.10
		<45µm	22.5	41.27	0.65	14.43	34.44	0.26	2.56	4.23	0.67	1.37	0.20	0.01	0.02	-0.10
		TL	87.7	71.05	0.68	15.63	4.11	0.04	1.61	1.49	1.14	1.77	0.13	0.03	0.02	2.30
	Nd (µm)	MC	53.4	68.67	0.78	17.22	5.62	0.06	1.79	1.85	1.15	1.98	0.15	<0.002	0.02	0.69
		>150	28.5	64.66	0.88	19.57	6.80	0.07	1.65	1.99	1.18	2.22	0.16	<0.002	0.02	0.81
		150-75	29.3	74.52	0.56	13.14	4.70	0.06	1.89	1.64	1.14	1.53	0.12	<0.002	0.01	0.69
		75-45	24.3	69.94	0.76	16.81	5.05	0.06	1.85	1.82	1.11	1.95	0.15	<0.002	0.01	0.50
		<45	17.9	64.39	0.97	20.47	5.92	0.06	1.78	2.05	1.14	2.34	0.17	<0.002	0.02	0.70
		TL	38.0	75.46	0.56	13.21	2.01	0.02	1.30	0.97	1.15	1.50	0.12	0.01	0.00	3.70
S1-ESP12		Bulk		59.65	0.88	20.22	6.36	0.06	1.34	1.83	1.07	2.37	0.16	0.13	0.02	5.89
	Fe (µm)	MC	4.5	34.03	0.55	12.71	41.95	0.30	2.49	4.24	0.50	1.13	0.23	0.14	0.04	1.69
		> 75	11.3	44.52	0.58	14.58	21.75	0.24	2.74	3.12	0.74	1.56	0.16	0.43	0.01	9.58
		75-45	19.0	42.13	0.57	13.56	32.59	0.27	2.51	3.73	0.62	1.31	0.16	0.15	0.02	2.39
		45-25	23.0	36.78	0.55	12.76	40.59	0.27	2.40	4.03	0.49	1.11	0.18	0.10	0.03	0.71
		<25	46.6	36.21	0.62	14.63	38.78	0.26	2.24	4.21	0.56	1.29	0.31	0.15	0.05	0.69
		TL	94.1	60.63	0.91	21.01	4.71	0.05	1.11	1.69	1.07	2.46	0.16	0.10	0.02	6.07
	Nd (µm)	MC	8.9	56.66	0.85	19.82	7.70	0.07	1.52	2.24	0.96	2.17	0.18	0.08	0.02	7.72
		>75	13.7	53.46	0.69	16.11	5.56	0.07	1.43	1.76	0.97	1.84	0.14	<0.002	0.01	17.95
		75-45	19.6	56.71	0.75	17.41	5.20	0.06	1.46	1.82	0.94	1.96	0.15	<0.002	0.02	13.52
		45-25	23.0	59.35	0.86	19.61	6.47	0.07	1.82	2.10	0.96	2.15	0.18	<0.002	0.02	6.40
		<25	43.7	57.23	0.98	22.30	9.34	0.09	1.52	2.69	1.03	2.45	0.21	0.01	0.03	2.11
		TL	82.9	61.17	0.93	21.21	3.88	0.04	1.05	1.59	1.09	2.49	0.15	0.02	0.01	6.37
S4-BA		Bulk		66.56	0.79	17.60	9.01	0.07	1.56	1.65	0.94	1.88	0.10	0.03	0.02	-0.20
	Fe	MC	5.5	58.99	0.74	16.47	16.88	0.14	1.97	2.24	0.84	1.69	0.12	0.01	0.02	-0.10
		TL	94.1	67.20	0.80	17.73	8.16	0.06	1.52	1.59	0.95	1.87	0.10	<0.002	0.02	0.00
S4-ECO		Bulk		63.11	0.70	16.23	8.37	0.07	1.76	1.63	0.87	1.70	0.11	0.05	0.01	5.38
	Fe	MC	13.1	40.98	0.57	12.96	35.37	0.26	2.44	2.99	0.58	1.20	0.13	0.12	0.02	2.39
		TL	85.7	65.77	0.71	16.68	4.35	0.04	1.58	1.40	0.90	1.74	0.10	0.08	0.02	6.61
S4-ESP 12		Bulk		58.71	0.83	18.97	7.82	0.06	1.57	1.76	1.06	2.08	0.13	0.34	0.02	6.66
	Fe	MC	5.9	33.68	0.51	11.99	44.19	0.25	2.16	3.15	0.49	1.00	0.17	0.10	0.03	2.29
		TL	93.2	60.39	0.86	19.76	4.75	0.05	1.33	1.65	1.08	2.18	0.13	0.13	0.02	7.67

BA, bottom ash; ECO, economizer fly ash; ESP, electrostatic precipitator; MC, magnetic concentrate; TL, tailings

Compared to Fe-MC, the Nd-MC present higher contents of SiO_2 and Al_2O_3, average of 63.83 and 18.76 wt.%, respectively, and lower amounts of Fe_2O_3, MnO, CaO, MgO, P_2O_5, Cr_2O_3, (Figure III - 31B). Furthermore, it is interesting to note that Nd-MC also present higher carbon contents than Fe-MC (Table A8). This one occurs mainly as char particles, which are the predominant form of carbon in ashes, and most probably were collected by the Nd-magnet due to particles with variable amounts of Fe infilling char pores (Figure III - 31D-E).

After sequential separation using Fe and Nd magnets, the tailings are depleted in almost all minor oxides and trace elements relatively to the bulk ash samples (Table III - 20). The sharpest decrease in Fe_2O_3 comparatively to the bulk sample is verified for ECO FA, approx. 75 wt.% Table III - 20. In ESP FA the Fe_2O_3 content decreases about 40 wt.% while in BA does not reach 10 wt.%.

Among the trace elements analyzed, Fe-MC present slight enrichments in the following elements relatively to the tailings (average EF: 2.2 - 1.2): Mo > Co > As > W > Cr > Ni > V > Sc > Sb > Sn > U (Figure III - 31C). Other elements such as Cu and Zn are enriched in Fe-MC from BA and ECO (EF 1.2 – 1.3) while Bi, Cd and Pb are enriched in BA Fe-MC (EF 1.0 – 2.0) (Figure III - 31C). Comparatively to the world coal ashes (WCA, Ketris & Yudovich, 2009), only V is slightly enriched in Fe-MC from ESP FA (2 < CC < 5), and one may conclude that FA could be a secondary source of this element, which is a critical raw material (European Commission, 2020), but the contents found are below the stablished economical cut-off (1000 ppm; Dai and Finkelman, 2018).

Hierarchical cluster analysis and Pearson’s correlation coefficients were used to obtain information concerning organic and inorganic affinities and potential relations among the elements (Eskanazy et al., 2010; Gürdal, 2011; Zhao et al., 2015). Elements with more than 10% values below the detection limit (bdl) were excluded to avoid skewness in the results. The bdl values considered for the analysis were replaced by bdl/2.

The associations between major and trace elements in Fe-MC are broadly indicated by the dendrogram in Figure III - 32, and the correlation coefficients (CC) are presented in Table A9. Iron presents significant positive correlations (at $\rho < 0.05$) with Mo and Sc ($r > 0.92$), Mn and As ($r > 0.90$), Cd (0.86) and Ni ($r > 0.85$) (Table A9, Figure III - 32). Among these elements two groups are distinguish based on their positive relations ($r > 0.9$, at $\rho < 0.05$) which suggest a common occurrence: (a) Mn and Sc; (b) Mo, As, Cd, and Ni (Figure III - 32). On the other hand, Fe is negatively correlated with elements usually associated with the glass phase such as Al, K, Na and Ti ($r > -0.94$ at $\rho < 0.05$) (Table A9). This does not mean that the referred elements do not coexist, even because it is known that Fe-bearing morphotypes usually have an aluminosilicate matrix, only that there is no linear correlation between them. Most likely, however, the Fe-coming from pyrite and carbonates decomposition is the main source of Fe in these ashes, which explains its weak correlation with aluminosilicates.

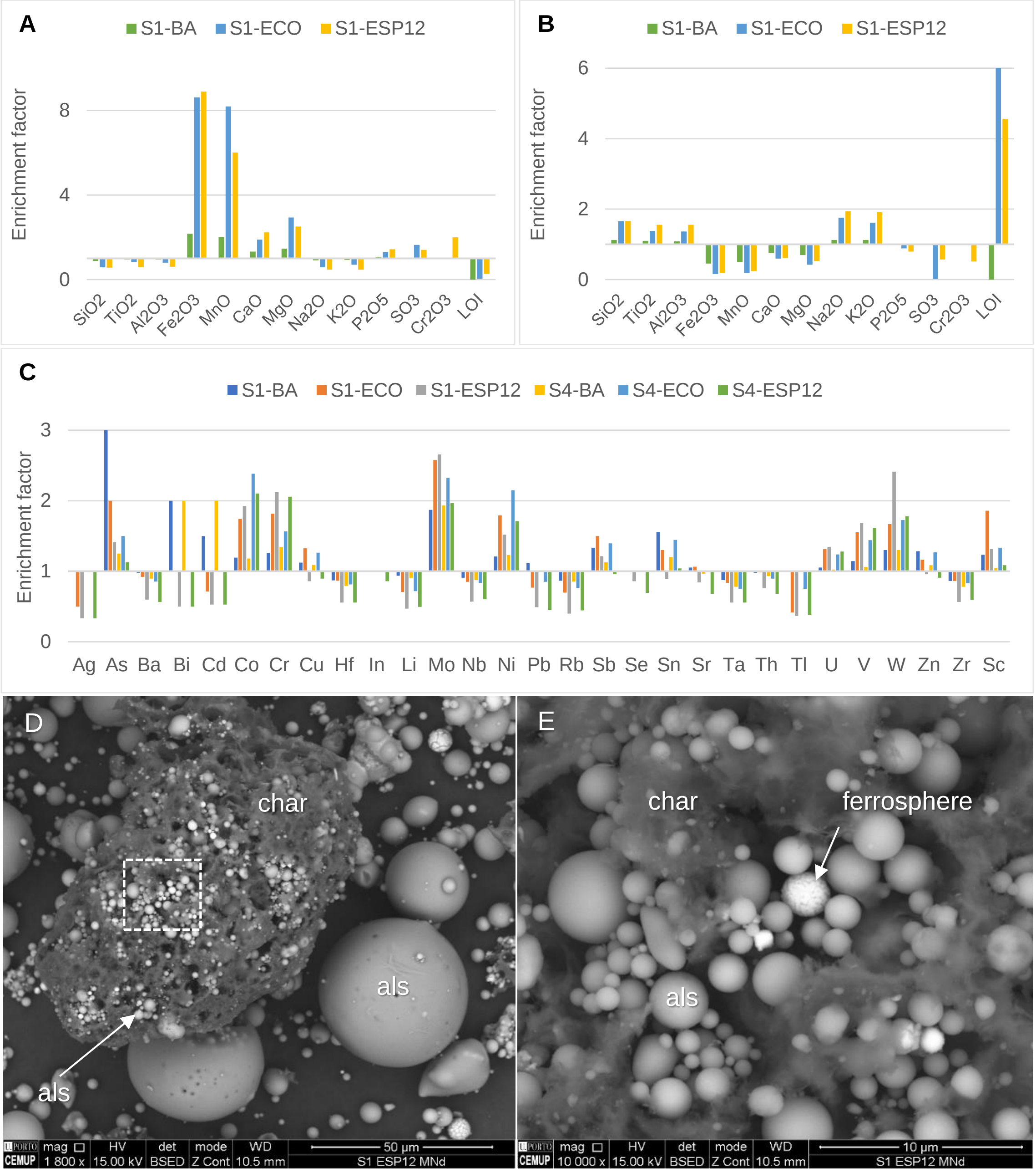

Figure III - 31. Enrichment factor relatively to the tailings: (A) Fe-MC major oxides, (B) Nd-MC major oxides, (C) trace elements Fe-MC. Detail imaging of char particle from ECO Nd-MC (D) with char pores mainly infilled with aluminosilicate, als, glassy spheres (BSE mode, x1800) and magnification of dashed square in “D” showing a ferrosphere intermixed with aluminosilicate glass spheres infilling char pores (E).

Transition metals such as Mn and Ni that were found significantly correlated with Fe in MC have long been reported to be enriched in magnetic fractions from coal combustion ashes, which was mainly assigned to their ability for isomorphically replace Fe ions in the crystal lattice of spinels (Hansen et al., 1981; Hulett et al., 1980; Kukier et al., 2003; Lu et al., 2009; Querol et al., 1995; Strzałkowska, 2021; Vassilev et al., 2004a; Vassilev and Vassileva, 1996). Nevertheless, these elements may be also found absorbed at particles surface, in the aluminosilicate matrix or in discrete minerals associated with Fe-bearing morphotypes in agglomerates (Vassilev and Vassileva, 1996).

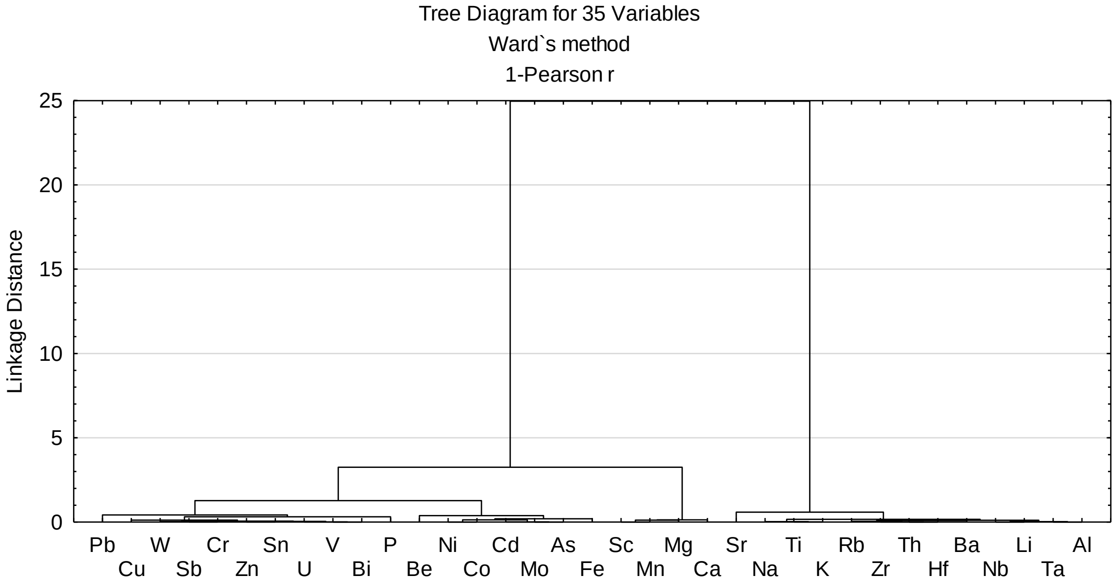

Figure III - 32. Dendrogram from cluster analysis on the geochemical data from bulk Fe-MC (cluster method, Ward's method; interval, Pearson's correlation values).

The Fe-MC size-fractions show that the content of Fe and the elements associated with it (e.g., Mg, Co, Cr, Cu, Mo, and Ni) increase with decreasing particle size (Table A8). A similar trend was observed by (Hower et al., 1999a) for Fe, Cr and Ni in MC collected from FA derived from high-sulfur coal from Illinois Basin. The highest variation in the Fe content is observed for ECO Fe-MC sample which triples from the >150 µm to the >45 µm fraction, 7.04 to 23.39 % (Table A8). Pearson´s correlation coefficients based on size-fractions geochemistry reinforce Fe positive correlations found in bulk MC (Table A10) and reveals other significant positive correlations (at $\rho < 0.05$) with Mg ($r = 0.97$), Co ($r = 0.81$), Ca ($r = 0.72$), Cr ($r = 0.64$), Sb and U ($r = 0.60$), and V ($r = 0.64$) (Table A10). Except for Ca, the referred elements present positive correlations among each other suggesting a common source. The Co, Cr and V as previously referred for Mn and Ni can substitute Fe in the spinel structure which may justify the correlations found. Calcium appears positively correlated ($r > 0.57$, at $\rho < 0.05$) with Mg, Mn, and Sc (Table A10) which was later explained by their common occurrence in morphotypes as the one presented in Figure III - 39. The negative correlation of Fe with Al although significant at $\rho < 0.05$ is not as strong as observed for bulk Fe-MC ($r = - 0.68$,Table A10).

Elements concentration in the Nd-MC size-fractions vary within a narrower range revealing a more homogeneous composition than in the Fe-MC (Table A8). Nevertheless, it is observed an increase in Fe content with the decreasing particle size in Nd-MC from FA and in fractions <150 μm from ECO, 1.5 % in average (Table A8). By contrast, in Nd-MC from BA the Fe content along with Mg and Mn, decrease with decreasing particle size, approx. 1 % (Table A8).

3.4. Magnetic parameters

Magnetic susceptibility and isothermal remanent magnetization (IRM) were used to characterize magnetic minerals in bulk ash samples Table III - 21.

Mass specific magnetic susceptibility (χ) results from the contribution of the magnetic susceptibilities of all the constituent minerals. Ferromagnetic minerals, such as magnetite, contribute more due to their greater magnetic susceptibility compared to paramagnetic and diamagnetic minerals, e.g., clay and quartz (e.g., (Dekkers, 1997; Evans and Heller, 2003; Maher and Thompson, 1999; Verosub and Roberts, 1995).

Magnetic susceptibility (χ, Table III - 21) ranges from 834.79×10^{-8} m^3/Kg to 2375.18×10^{-8} m^3/Kg and the average values decrease as follows: ECO (2200.06×10^{-8} m^3/Kg) > ESP FA (1245.43×10^{-8} m^3/Kg) > BA (853.79×10^{-8} m^3/Kg). The values obtained are within the range formerly reported for coal combustion ashes (Kapička et al., 2001; Lu et al., 2009; Veneva et al., 2004). Veneva et al., (2004) noted differences on the magnetic susceptibility regarding the sampling locations (mechanical collectors *vs* electrostatic precipitators) and attributed it to differences in combustion technologies which is not the case in the current research. Although no significant linear correlations were found, bulk ECO FA presents higher contents of ferromagnetic minerals (Part III, chapter 1, Table III - 6) explaining the higher magnetic susceptibilities determined.

Examples of isothermal remanent magnetization (IRM) acquisition plots for the studied samples are shown in Figure III - 33. The IRM curves depend on the relative concentrations of low-coercivity minerals (e.g., magnetite) versus high-coercivity (e.g., hematite) minerals and its deconvolution can provide information about the contributions of the different components in the total remanence (e.g., Kruiver et al., 2001; Thompson and Oldfield, 1986).

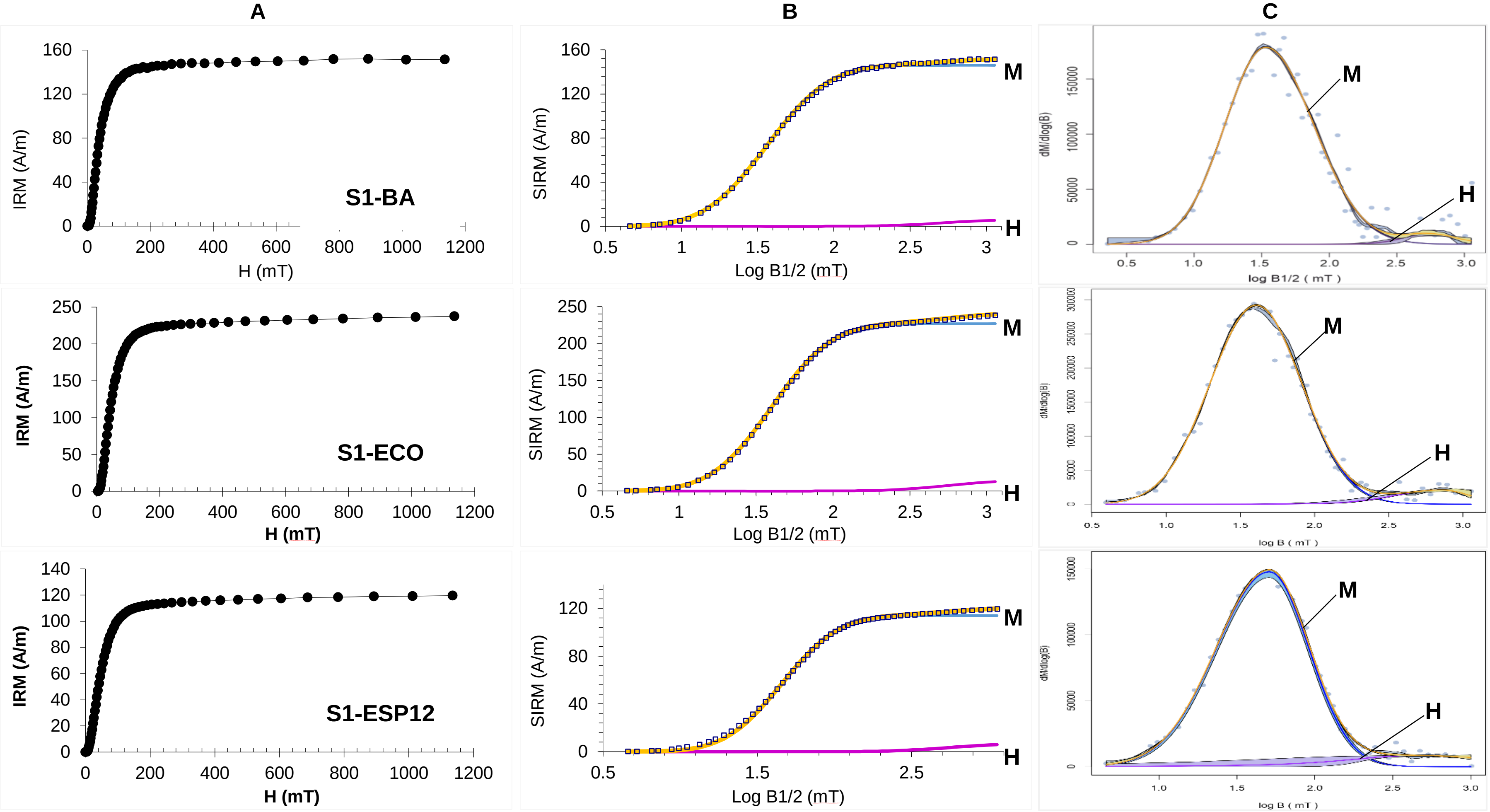

Figure III - 33. A) IRM curves obtained for bulk ashes from S1 (BA, ECO and ESP FA), B) IRM curves unmixed using Kruiver et al., (2001) and C) coercivity distribution derived from IRM curves obtained unmixed using Max UnMix application (Maxbauer et al., 2016). H, hematite; M, magnetite.

The S ratio (Table III - 21) close to 1 indicates a predominance of low coercivity magnetic phase such as magnetite and maghemite (Bloemendal et al., 1988), but the lack of saturation at the field applied indicates the presence of high coercive phases such as hematite and goethite. Statistical analysis of the raw IRM data using the cumulative log-Gaussian (CLG) function (Kruiver et al., 2001; Robertson and France, 1994b), revealed that optimal fits could be obtained considering two components (Table III - 21;Figure III - 33).

Component 1 represents a low coercive phase with $B_{1/2}$ in the range 36-49 mT, interpreted as magnetite/maghemite, while component 2 corresponds to a high coercive phase with $B_{1/2}$ 355-562 mT, though as hematite (Abrajevitch and Kodama, 2011; Kruiver et al., 2001). Component 1 predominates in all samples analyzed contributing to 92-96% of the total remanence (Table III - 21, Figure III - 33). All components identified present a large dispersion parameter (DP), 0.29-0.33, indicating a large variability on the physical and chemical parameters affecting microcoercivity (Egli, 2004). The presence of these minerals is corroborated by the mineralogical composition determined by XRD (Table III - 7, Part III, chapter 1).

Table III - 21. Magnetic susceptibility, χ and Isothermal remanent magnetization (IRM) parameter obtained from IRM curve deconvolution.

		X (×10^{-8} m^3/kg)	Method	S ratio	Component									
					1					2				
					SIRM (A/m)	$B_{1/2}$ (mT)	DP	Cont. (%)	S	SIRM (A/m)	B1/2 (mT)	DP	Cont. (%)	S
S1	BA	872.79	CLG	0.943	146000	36	0.32	96	n.a.	6000	501	0.28	4	n.a.
			Max UnMix	n.a.	n.a.	37	0.33	97	1.09	n.a.	578	0.21	3	1.11
	ECO	2375.18	CLG	0.921	227000	40	0.31	94	n.a.	15000	562	0.30	6	n.a.
			Max UnMix	n.a.	n.a.	40	0.31	95	0.99	n.a.	573	0.27	5	0.77
	ESP12	1164.99	CLG	0.923	114000	46	0.29	94	n.a.	7000	562	0.30	6	n.a.
			Max UnMix	n.a.	n.a.	44	0.30	93	0.87	n.a.	527	0.57	7	1.09
S4	BA	834.79	CLG	0.925	133000	34	0.33	93	n.a.	9500	355	0.30	7	n.a.
			Max UnMix	n.a.	n.a.	35	0.35	95	1.11	n.a.	460	0.28	5	0.92
	ECO	2024.94	CLG	0.909	176000	47	0.31	92	n.a.	15000	562	0.29	8	n.a.
			Max UnMix	n.a.	n.a.	47	0.32	94	0.97	n.a.	632	0.25	6	1.14
	ESP12	1325.87	CLG	0.944	145500	49	0.28	96	n.a.	6000	562	0.28	4	n.a.
			Max UnMix	n.a.	n.a.	48	0.29	96	0.85	n.a.	422	0.22	4	0.94

BA; bottom ash; ECO, economizer; ESP, electrostatic precipitator; S-ratio (I'-IRM-0.3T/IRM1T); SIRM, saturation of isothermal remanent magnetization; B1/2, field at which half of the SIRM was reached; DP, dispersion parameter; S, skewness; n.a.—not attributed value.

As a result of the asymmetry observed in the IRM curves during CLG from ESP FA samples, it was decided to also use the Max UnMix software (Maxbauer, 2016) to get more suitable fittings. As verified for CLG method, the best fitting is achieved using two components, one of low coercivity, 35-47 mT, and other of high coercivity 422-578 mT (Table III - 21; Figure III - 33).

Variations observed for the second component are mainly due to noise in that range of the curve that makes fitting less accurate. As expected, the first component is more asymmetric in ESP FA samples than the remaining samples, 0.86 average (Table III - 21). According to Helsop et al. (2004) skew-left distributions ($S<1$) result from thermal relaxation and magnetic interactions. Nevertheless, further studies would be needed to explain the difference found.

3.5. Mineralogy

The minerals and phases present in the MC were assessed using XRD and Mössbauer spectroscopy and the results are listed on Table III - 22-Table III - 24.

All MC are mainly composed by an amorphous phase (46.2 - 77.1 wt.%) and Nd-MC present in average 15 wt.% more amorphous than Fe-MC (Table III - 22). The amorphous phase is mainly attributed to the aluminosilicate glass, but also includes char. The parameters obtained from Mössbauer spectra confirms that some iron is found associated with aluminosilicate glass, in the form of Fe^{2+} and Fe^{3+} (Table III - 23) corroborating what was previously verified using SEM/EDS and corroborating other authors work (e.g., Lu et al., 2009; Matjie et al., 2011; Sokol et al., 2002, 2000; Wang, 2014; Zhao et al., 2006).

The main crystalline phases (>10 wt.% average) composing Fe-MC are quartz (5.5 - 17.4 wt.%), magnetite (4.4 - 19.9 wt.%) and mullite (6.2 - 14.2 wt.%), while minor phases (1 - 10 wt.% avg.) comprise magnesioferrite (0.8 - 8.3 wt.%), hematite (2.0 – 5.1 wt.%), diopside (0.9 - 5.5 wt.%), albite (1.3 - 2.4 wt.%) and maghemite (up to 2.3 wt.%) (Table III - 22). Accessory minerals (<1 wt.%) include rutile, hercynite, calcite, gypsum, calcium aluminate, cordierite, anhydrite, and cristobalite. The association of non-magnetic minerals/phases to MC was previously reported and it was generally assigned to intrinsic features of the material, i.e., Fe-oxides crystallization on aluminosilicate matrix and intimate association among different particles (e.g., Hansen et al., 1981; Hower et al., 1999a; Kukier et al., 2003; Lu et al., 2009; Sokol et al., 2002; Vassilev et al., 2004a; Zhao et al., 2006). However, the particles control equipment also plays a role in the distribution of these phases. For example, magnesioferrite occurs in higher amounts in the MC recovered from ECO FA, 8.3 wt.%, which may be due to higher size and density particles being mostly captured in this intermediate point.

In the Nd-MC, quartz (11.4 - 29.6 wt.%) and mullite (5.4 - 13.2 wt.%) are the major crystalline phases followed by albite (0.9 - 2.0 wt.%) (Table III - 22), while magnesioferrite, is absent and the remaining Fe-crystalline phases detected occur below 1 wt.%.

Table III - 22. XRD results for MC collected from S1 ash samples (wt.%).

	S1 BA			S1 ECO			S1 ESP-12		
	Bulk*	Fe	Nd	Bulk*	Fe	Nd	Bulk*	Fe	Nd
Quartz (SiO_2)	11.5	17.4	18.1	24.8	11.2	29.6	12.5	5.5	11.4
Cristobalite (SiO_2)	0.3	0.1	0.1	0.1	0.2	0.1	0.0	0.0	0.1
Mullite ($Al_6Si_2O_{13}$)	6.6	14.2	13.2	8.3	7.6	11.4	4.7	6.2	5.4
Cordierite ($Mg_2Al_4Si_5O_{18}$)	0.2	0.3	0.1	0.1	0.2	0.2	0.2	0.1	0.0
Albite ($NaAlSi_3O_8$)	0.0	1.3	1.6	1.4	1.4	0.9	0.9	2.4	2.0
Diopside ($(Ca,Mg,Fe)_2Si_2O_6$))	0.1	0.9	0.3	0.7	3.9	0.9	0.8	5.5	0.0
Calcium aluminate ($Ca_3Al_2O_6$)	0.0	0.5	0.2	0.5	0.2	0.0	0.1	0.0	0.3
Rutile (TiO_2)	0.0	0.7	0.3	0.5	0.8	0.3	0.3	0.4	0.5
Hematite (α-Fe_2O_3)	0.7	2.0	0.5	0.6	5.0	0.6	0.7	5.1	0.7
Maghemite (γ-Fe_2O_3)	0.9	2.3	0.7	1.2	0.0	0.6	0.2	1.9	0.8
Magnetite (Fe_3O_4)	0.0	4.4	0.8	2.0	8.6	0.4	0.9	19.9	0.7
Magnesioferrite ($MgFe_2O_4$)	0.0	0.8	0.0	0.2	8.3	0.0	0.4	5.5	0.0
Hercynite ($FeAl_2O_4$)	0.0	0.7	0.2	0.4	0.7	0.0	0.0	0.0	0.4
Calcite ($CaCO_3$)	0.0	0.2	0.1	0.1	0.7	0.2	0.1	0.7	0.6
Gypsum ($CaSO_4 \cdot 2H_2O$)	1.4	0.2	0.5	0.4	0.6	0.0	0.3	0.5	0.1
Anhydrite ($CaSO_4$)	0.0	0.0	0.0	0.1	0.0	0.0	0.1	0.2	0.1
Amorphous	78.3	54.1	63.4	58.5	50.8	54.9	78.0	46.2	77.1

S1, sampling campaign 1; BA, Bottom ash; ECO, Economizer; ESP-12, fly ash from electrostatic precipitator from first row (bin 12)

Therefore, the predominant Fe-bearing minerals in Fe-MC are magnetite, hematite and magnesioferrite (Table III - 22) which is agreement with previous works (e.g., Vassilev et al., 2004). These phases derive from thermochemical conversion of Fe-bearing minerals present in feed coals (e.g., pyrite, siderite and illite; Table III - 3) which originate melts of complex composition ($FeO{-}SiO_2{-}Al_2O_3{-}CaO{-}MgO$) that later will cool and crystallize (Anshits et al., 2001; Sokol et al., 2000; Vassilev and Vassileva, 1996). During the cooling of the melt drops, the oxidation potential increases and Fe^{2+} partially oxidizes to Fe^{3+} leading to the precipitation of magnetite or a mixture of magnetite and hematite (Sokol et al., 2002), as observed in the studied MC. Magnesioferrite is the highest temperature mineral in the magnetite spinel series and its occurrence suggests the involvement of other minerals rather than pyrite since Mg tends to be associated with silicates or dolomite in coal (Hansen et al., 1981; Sokol et al., 2002).

Mössbauer spectra of the Fe-MC are showed in Figure III - 34. Three sextets are necessary to fit the outer peaks of the spectra which is particularly clear in the spectra from ECO and FA Fe-MC (Figure III - 34). The estimated parameters (Table III - 23) are typical of Fe^{3+} in hematite, magnetite/maghemite and $Fe^{2.5+}$ on the octahedral sites of magnetite (Murad, 1998; Vandenberghe et al., 2000). The sextet attributed to Fe^{3+} in magnetite/maghemite results from the contribution of Fe^{3+} in magnetite phases with different oxidation degrees that may reach almost complete oxidation corresponding to maghemite. It should be noted that Fe in $MgFe_2O_4$ detected by XRD (Table III - 22) has hyperfine parameters very similar to those of Fe^{3+} in magnetite, maghemite or hematite (de Grave et al., 1976; Murad, 1998; Vandenberghe et al., 2000). Therefore, when present, the $MgFe_2O_4$ spectrum is not resolved from those of the binary Fe oxides.

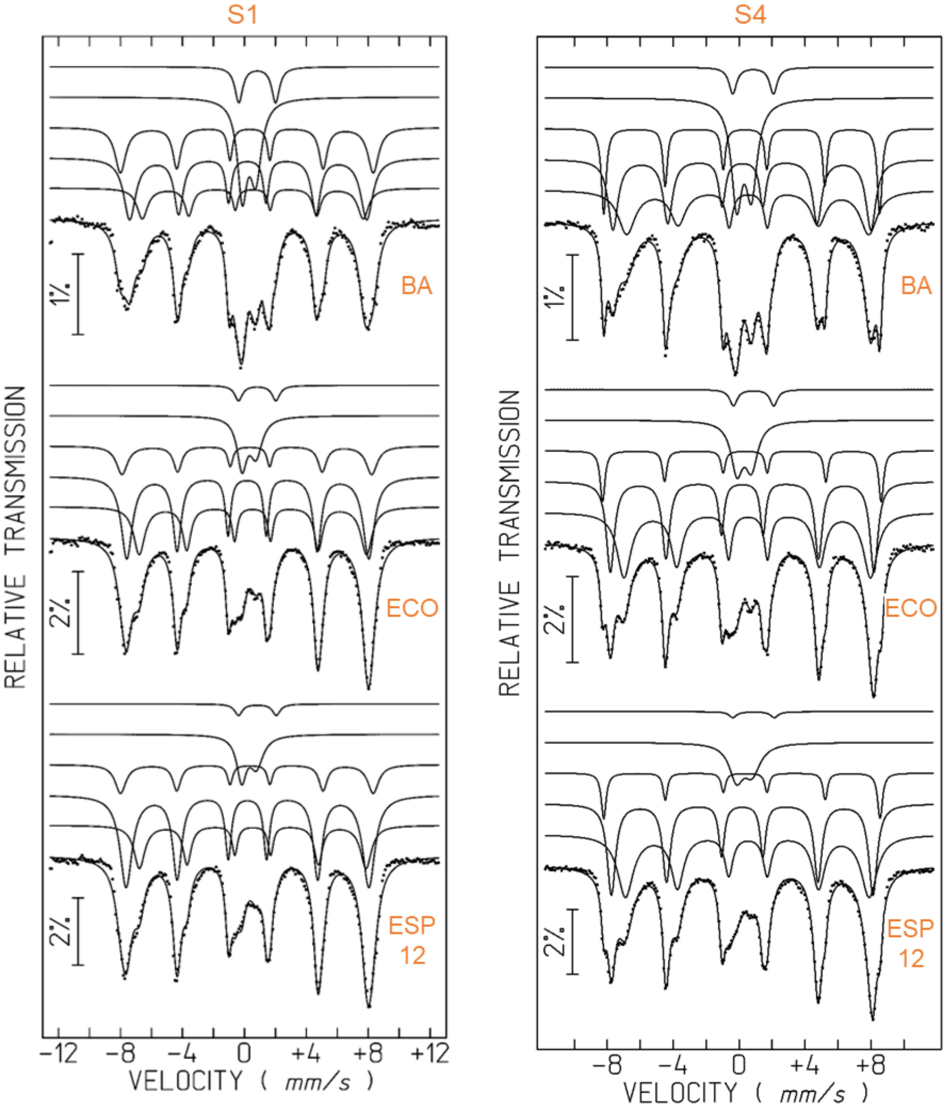

Figure III - 34. Mössbauer spectra regarding magnetic concentrates collected with ferrite magnet. The lines over the experimental points are the sum of sextets and doublets (shown slightly shifted for clarity) corresponding to Fe atoms on different sites and in different phases. The estimated parameters for these sextets and doublets are collected in Table III - 23.

The remaining resonant absorption may be fitted with two doublets, which represent average spectra of Fe^{3+} and Fe^{2+} in paramagnetic phases. Considering the phases detected by XRD, Fe^{3+} is present in aluminosilicates, Fe^{2+} in silicates and hercynite (Waerenborgh et al., 1994). Both Fe^{3+} and Fe^{2+} are also present in the Fe-containing silicate glasses as observed by SEM/EDS (Ferreira et al., 2017; Jayasuriya et al., 2004; Santos et al., 2022). The asymmetry of the Fe^{3+} doublet is typical of distributions of quadrupole splittings in amorphous phases (Ferreira et al., 2017; Jayasuriya et al., 2004). The composition of the Fe-MC deduced from the present Mössbauer data are comparable with other examples reported in the literature (Szumiata et al., 2014; Vandenberghe et al., 2009; Wang, 2014; Zhao et al., 2006).

Table III - 23. Estimated parameters from the Mössbauer spectra of Fe-MC.

Fe-MC	Fe species	IS, mm/s	QS, ε, mm/s	B_{hf}, tesla	I
S1-BA	Fe$^{2.5+}$ magnetite	0.65	0	44.2	15%
	Fe^{3+} magnetite + maghemite	0.33	0.06	47.5	35%
	Fe^{3+} hematite	0.37	-0.2	50.6	23%
	Fe^{3+} aluminosilicate phases	0.41	0.87	-	21%
	Fe^{2+} aluminosilicate phases	0.94	2.38	-	6%
S1-ECO	Fe$^{2.5+}$ magnetite	0.65	-0.02	45.5	26%
	Fe^{3+} magnetite + maghemite	0.31	0.04	48.5	44%
	Fe^{3+} hematite	0.37	-0.2	50	15%
	Fe^{3+} aluminosilicate phases	0.41	0.91	-	12%
	Fe^{2+} aluminosilicate phases	0.94	2.42	-	3%
S1-ESP12	Fe$^{2.5+}$ magnetite	0.65	0	45.3	23%
	Fe^{3+} magnetite + maghemite	0.31	0	48.6	49%
	Fe^{3+} hematite	0.37	-0.2	50.4	17%
	Fe^{3+} aluminosilicate phases	0.49	0.93	-	8%
	Fe^{2+} aluminosilicate phases	0.95	2.56	-	3%
S4-BA	Fe$^{2.5+}$ magnetite	0.65	-0.03	45.5	29%
	Fe^{3+} magnetite + maghemite	0.3	-0.03	48.5	31%
	Fe^{3+} hematite	0.37	-0.2	51.9	16%
	Fe^{3+} aluminosilicate phases	0.41	0.87	-	20%
	Fe^{2+} aluminosilicate phases	0.96	2.47	-	4%
S4-ECO	Fe$^{2.5+}$ magnetite	0.63	-0.05	46.3	39%
	Fe^{3+} magnetite + maghemite	0.3	-0.01	49.6	35%
	Fe^{3+} hematite	0.38	-0.2	52.4	10%
	Fe^{3+} aluminosilicate phases	0.42	0.88	-	13%
	Fe^{2+} aluminosilicate phases	0.99	2.44	-	3%
S4-ESP12	Fe$^{2.5+}$ magnetite	0.62	-0.04	45.8	43%
	Fe^{3+} magnetite + maghemite	0.3	-0.01	49.2	37%
	Fe^{3+} hematite	0.38	-0.19	50.4	9%
	Fe^{3+} aluminosilicate phases	0.42	0.95	-	10%
	Fe^{2+} aluminosilicate phases	0.99	2.61	-	1%

IS (mm/s) isomer shift relative to metallic a-Fe at 295 K; QS (mm/s) quadrupole splitting and ε (mm/s) quadrupole shift estimated for quadrupole doublets and magnetic sextets, respectively. B_{hf} (tesla) magnetic hyperfine field; I relative area. Estimated errors £ 0.02 mm/s for IS, QS, ε, < 0.2 T for B_{hf} and <2% for I.

Assuming that the recoil free fractions are similar for all the Fe species in these samples (Jayasuriya et al., 2004) the relative areas of the doublets and sextets fitted to the spectra are a good approximation of the fraction of Fe atoms contributing to them. The Fe^{3+}/total Fe ratios for each sample (Table III - 24) are calculated considering that half of the Fe cations giving rise to the $Fe^{2.5+}$ sextet of magnetite is on the 3+ oxidation state and the other half on the 2+ oxidation state.

The Fe-MC from campaign S1 have higher content of hematite (Table III - 23), and higher Fe^{3+}/total Fe ratio (Table III - 24) than the samples from S4. In Fe-MC from both sampling campaigns the fraction of Fe in magnetically ordered oxides increase along the series BA < ECO < ESP12, corroborating the XRD results obtained for Fe-MC from S1 (Table III - 22).

Table III - 24. Parameters calculated from the relative areas estimated from the Mössbauer spectra of Fe-MC.

	S1-BA	S1-ECO	S1-ESP12	S4-BA	S4-ECO	S4-ESP12
Fe fraction in Fe oxides ($MgFe_2O_4$ included when present)	73%	85%	89%	76%	84%	89%
Fe^{3+} / total Fe	86.5%	84%	85.5%	81.5%	77.5%	77.5%

3.6. Cross-sections integrated characterization: petrography, SEM/EDS and Raman microspectroscopy

Taking in consideration the geochemical and mineralogical data, random areas of polished blocks were characterized combining petrography, SEM/EDS, and Raman microspectroscopy to assess features within Fe-bearing morphotypes.

In general, the cross-sections of the iron-bearing morphotypes show that the character of surface microtextures (e.g., skeletal, dendritic, etc.) observed in the powder samples often extends across the entire spheres (Figure III - 35). Moreover, Fe-morphotypes are predominantly massive suggesting that were originated from low viscosity melts, i.e., enriched in basic elements such as Mg (e.g., Anshits et al., 2001; Sokol et al., 2000). As observed in powder samples, ferrospheres exhibiting skeletal-dendritic microtextures with variable amount of aluminosilicate glass are the most common morphotypes.

The observations under reflected light microscopy (oil immersion) highlighted aspects that go unnoticed using SEM/EDS. One example is the presence oxidation rims with red internal reflections that are often observed in the particles outer surface (Figure III - 35B-C). Furthermore, ferrospheres frequently exhibit martitization textures, i.e., replacement of magnetite by pseudomorphic hematite (martite). High reflectance martite often presents a blue hue and appears substituting spinel crystals and as lamellae (Figure III - 35A,D). These aspects were not restricted to a particular type of microstructure as observed by Sharonova et al., (2015). These rimes are not detected under SEM/EDS

(Figure III - 35C,F) because corresponds to change in the oxidation state (magnetite to hematite) and not composition.

Martitization in Fe-rich morphotypes from coal combustion ashes has been previously reported by several authors (Ramsden and Shibaoka, 1982; Strzałkowska, 2021; Valentim et al., 2016; Vassilev and Vassileva, 1996), but the mechanism beneath this transformation it is yet to be understood. In natural conditions, the transformation from magnetite to hematite can be direct or through maghemite (γ-Fe_2O_3) intermediate stage and has been attributed to several processes such as dissolution-precipitation and deformation ((Orberger et al., 2014) and references therein). The oxidation state of the Fe-bearing phases on the surface of the particles, may explain some Mössbauer results, such as the higher content of hematite in Fe-MC from campaign S1, and can set a drawback in the use of the iron-rich morphotypes in further applications, such as the use as catalysts since chemical reactions unfold at active sites over the surface.

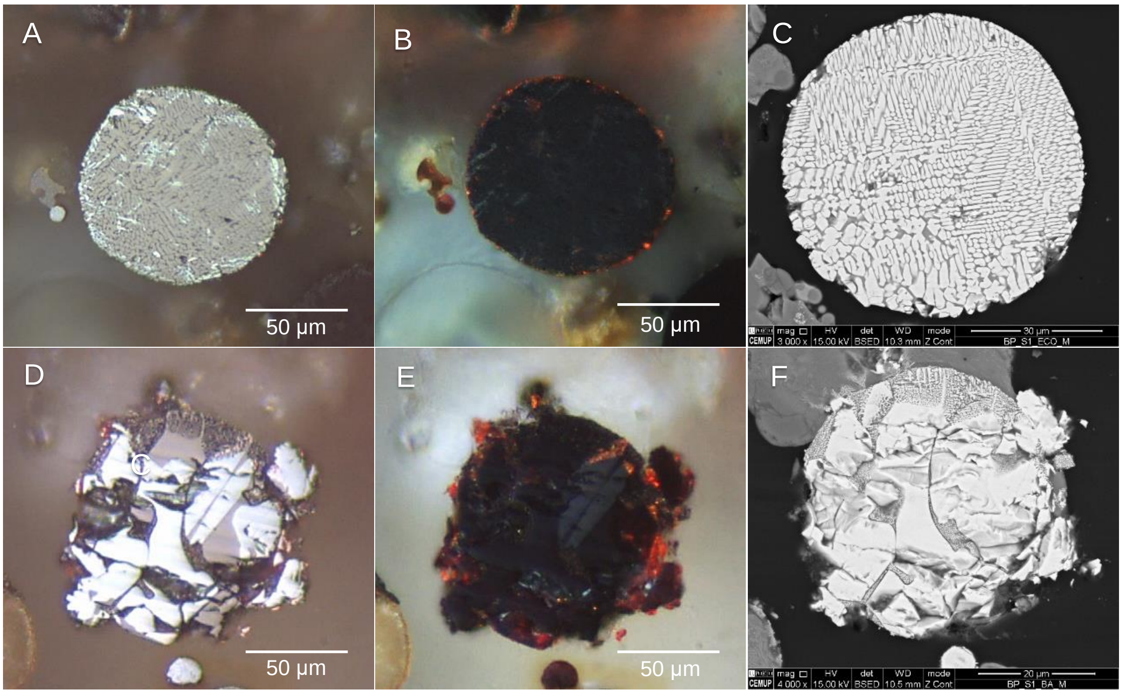

Figure III - 35. Ferrospheres presenting oxidation rims and martitization textures observed under reflected microscopy (oil immersion), parallel and crossed nicols, respecttively (A-B, D-E) and SEM/EDS, BSE mode (C,F).

Raman microspectroscopy enabled the confirmation of the martization process. Magnetite spectrum presents a high intensity Raman shift at 671 - 688 cm^{-1}(A_{1g}) (Figure III - 36B), and less frequently low intensity peaks at 300 - 338 cm^{-1} (E_g), 424 - 458 cm^{-1} (T_{2g}) and 522 - 553 cm^{-1}(T_{2g}), are also detected (Guedes et al., 2008). Hematite (α-Fe_2O_3) exhibited peaks corresponding to the phonon modes A_{1g} (Fe^{+3} displacements, 224 - 229 cm^{-1}), Eg (Fe^{+3} displacements, 245 - 250 and 290 - 295 cm^{-1}), ρ1 - E_g (O = displacements, 406 - 413 cm^{-1}), a – A_{1g} (O = displacements, 495 - 500 cm^{-1}), and a - E_g (O =

displacements, 608 - 618 cm^{-1}) (Figure III - 36F) (Guedes et al., 2008). An additional peak was identified at 658 - 667 cm^{-1}, which may be attributed to the incomplete transformation of magnetite (Chourpa et al., 2005; de Faria and Lopes, 2007; Minitti et al., 2005; Owens and Orosz, 2006) or to a longitudinal optical (LO) Eu mode very sensitive to the crystallite size (Chernyshova et al., 2007; Lopez et al., 2009; Xu et al., 2009).

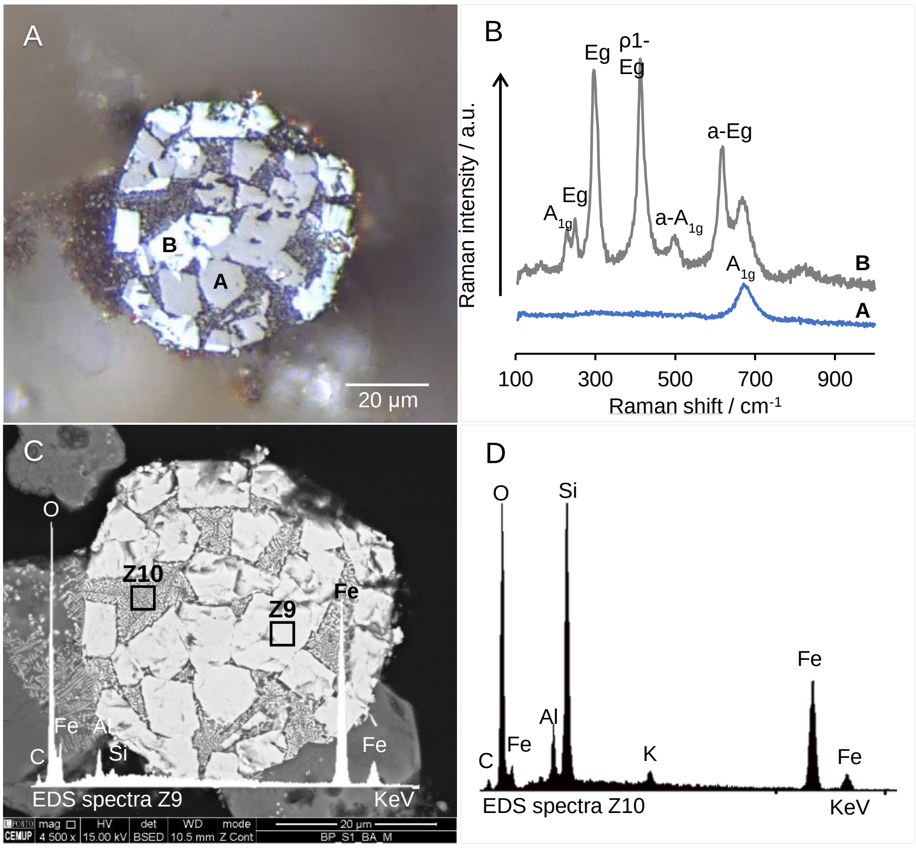

Figure III - 36. Ferrosphere under reflected light 98(A) exhibiting martitization aspect; (B) Raman spectra corresponding to the letters signed in “A”; (C) ferrosphere under SEM/EDS (BSE mode; ×4500) and spectra corresponding to Z9; (D) Spectra corresponding to Z10 marked in ”C”.

Nevertheless, there are particles presenting a chemical zonation which is distinguishable using SEM/EDS (Figure III - 37A,B) and under reflected light it looks similar to a martitization aspect (Figure III - 37C).

Indeed, the Fe-rich phase without Mg present red internal reflections and the Raman spectra confirms that it is oxidized to hematite (Figure III - 37E – Z11). The spectra corresponding to the Mg-rich phase presents a strong Raman shift at 686 cm $^{-1}$ with a shoulder at 621 cm^{-1} and low intensity peaks at 333 and 459 cm^{-1} (Figure III - 37E). The splitting of A_{1g} phonon mode observed in the spectra is typical of magnesioferrite and occurs due to the substitution of Fe^{3+} by Mg^{2+} in spinel structure (D’Ippolito et al., 2015; Nakagomi et al., 2009).

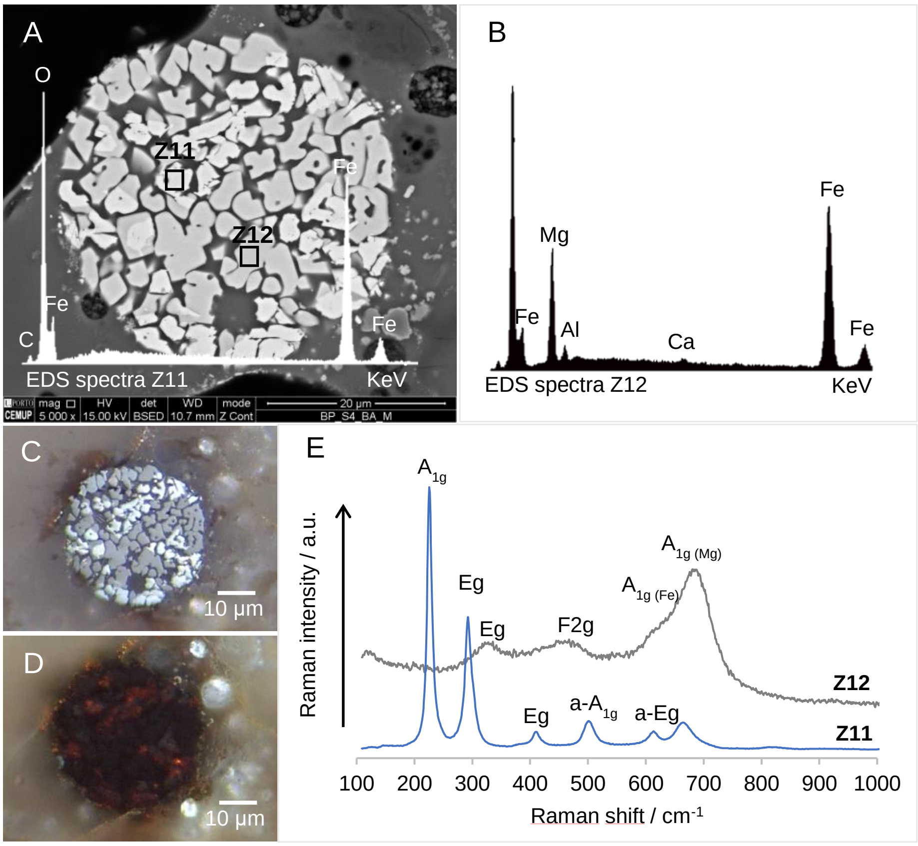

Figure III - 37. Magnesiaferrosphere observed under (A-B) SEM (BSE mode, ×5000) and EDS spectra obtained on areas marked (Z11 and Z12) , (C) and (D) reflected microscopy (oil immersion), parallel and crossed nicols, respectively; (E) Raman spectra corresponding to Z11 and Z12.

Nonetheless, not in all particles where a compositional variation was observed the Mg-containing phase was magnesioferrite but rather magnetite containing Mg. The association of Mg to magnetite and the occurrence of magnesioferrite corroborates the slight enrichment of Mg observed in MC (Figure III - 31).

Figure III - 38 shows an example of a magnesiaferrosphere (Valentim et al., 2018) that was analyzed. Although not being the most common morphotype it was selected given that magnesioferrite has suitable properties for being used as a heterogeneous catalyst (Yang et al., 1991).

The morphotype is mainly composed by magnesioferrite crystals (Figure III - 38E) embedded in a Ca-rich matrix with typical yellow reflections (Figure III - 38B,G) containing MgO nodules (Figure III - 38F). The Raman spectra obtained in this morphotype (Figure III - 38H) are similar to those assigned by (D'Ippolito et al., 2015; Nakagomi et al., 2009) to magnesioferrite and the differences among the spectra obtained are probably related with variation on Mg-content.

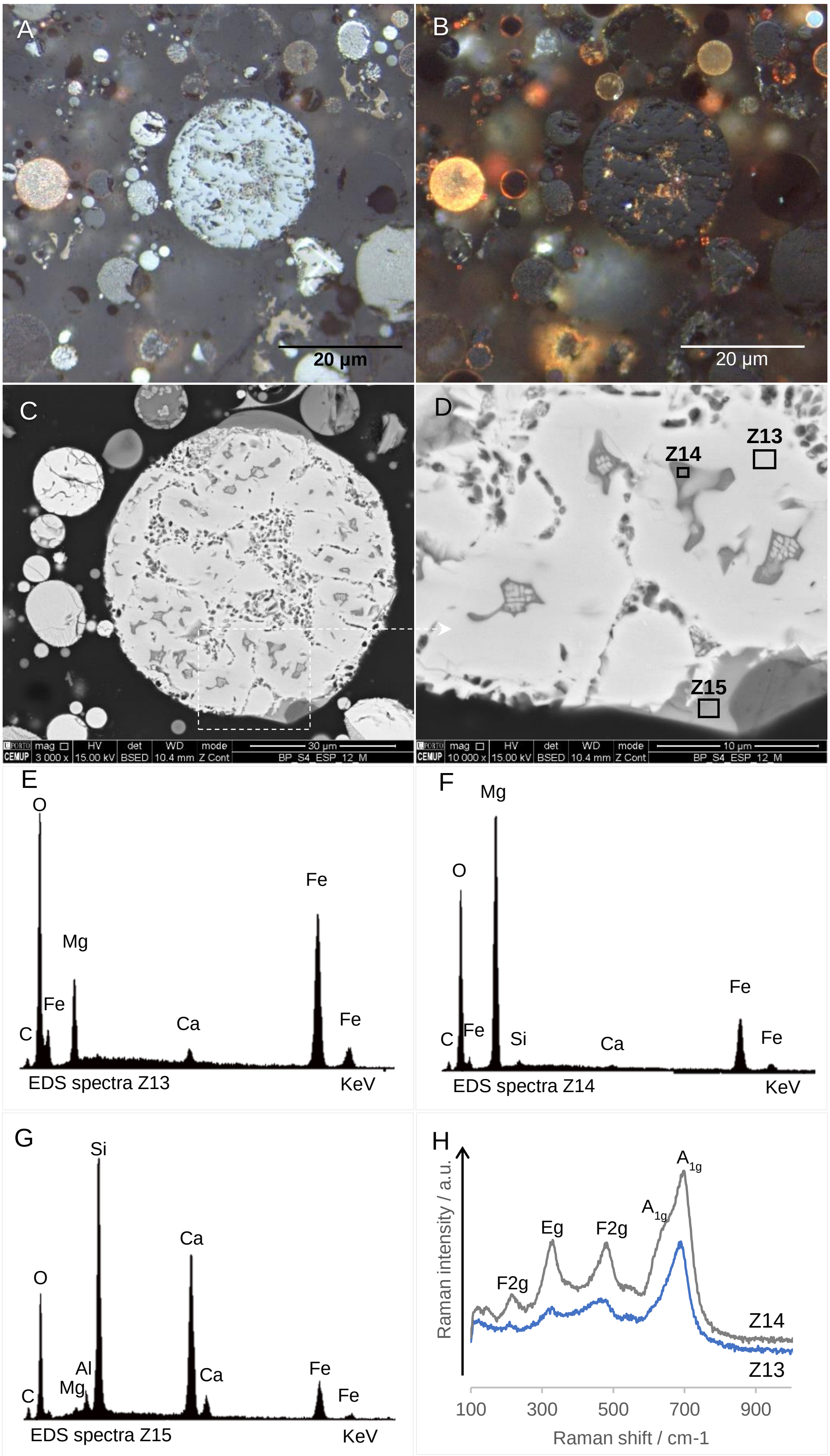

Figure III - 38. Magnesiaferrosphere observed under (A-B) reflected microscopy (oil immersion), parallel and crossed nicols, respectively and (C-D) SEM (BSE mode, ×5000) and EDS spectra obtained on areas marked (Z13 and Z14); (E) Raman spectra corresponding to Z11 and Z12.

A Ca-rich morphotypes stand out in Figure 11 (left side of magnesiaferrosphere) by their yellow internal reflections and Ca-sugar texture (Valentim et al., 2018). Due to the low amounts of Ca-bearing phases in the feed coals (Table III – 3) these morphotypes are residual in the coal ashes studied and in the respective MC. Figure III - 39 shows an example of a calcimagnesiasphere in which the different components were analyzed.

The main phase is a (Ca,Mg)-silicate (Figure III - 39C) embedded in a matrix with Al–Si–Ca–(Mg–Fe-Mn) composition (Figure III - 39D), where exsolutions of (Al-Si)-Ca are found (Figure III - 39E) together with (Mg-Ca)-silicate nodules (Figure III - 39F). The coexistence of Ca, Mn and Mg corroborate the geochemical associations previously found through statistical analysis (Figure III - 32).

3.7. Application in nitrophenol (4-Nph) reduction reaction

To find new solutions for recycling the magnetic concentrates, collaborative research was developed with Green Chemistry Laboratory (REQUIMTE) (Kuźniarska-Biernacka et al., 2021; Mendes et al., 2022; Santos et al., 2021b, 2021a). The trials carried out by the REQUIMTE team were jointly designed and interpreted based on the characterization results described above.

The Fe-MC obtained under this study were tested as catalysts in the nitrophenol (4-Ph) reduction reaction. The catalytic conversion as the advantage of selectively convert 4-NPh, toxic compound commonly found in wastewaters (Nemanashi and Meijboom, 2013), to 4-aminophenol (4-APh) which has a wide variety of applications, e.g., pharmaceutics production (Cho et al., 2019). The trials were carried out using standard solutions of 4-NPh (>99%, Sigma-Aldrich).

It was found that, except for BA Fe-MC sample, the other samples studied are active for 4-Nph reaction (Santos et al., 2021a,b; Mendes et al., 2022). The non-catalytic performance of BA was mainly attributed to the mode of occurrence of Fe-bearing morphotypes, which are mainly embedded in the aluminosilicate matrix.

Considering the best catalytic performance showed by Fe-MC from ESP fly ash, further trials with this sample were made (Kuźniarska-Biernacka et al., 2022). The best catalytic performance was achieved for the <75 μm fraction after washing with NaOH where nearly total 4-Ph reduction was achieved in 5 min with no induction time, which is comparable to noble metal containing nanocatalysts (Kuźniarska-Biernacka et al., 2022). Thus, the Fe-MC from ESP FA was proven to be a promising catalyst in 4-Ph reduction and consequently production of 4-Ph. Given their magnetic proprieties MC can be easily obtained from the FA and recovered after the application to be reused (Kuźniarska-Biernacka et al., 2022).

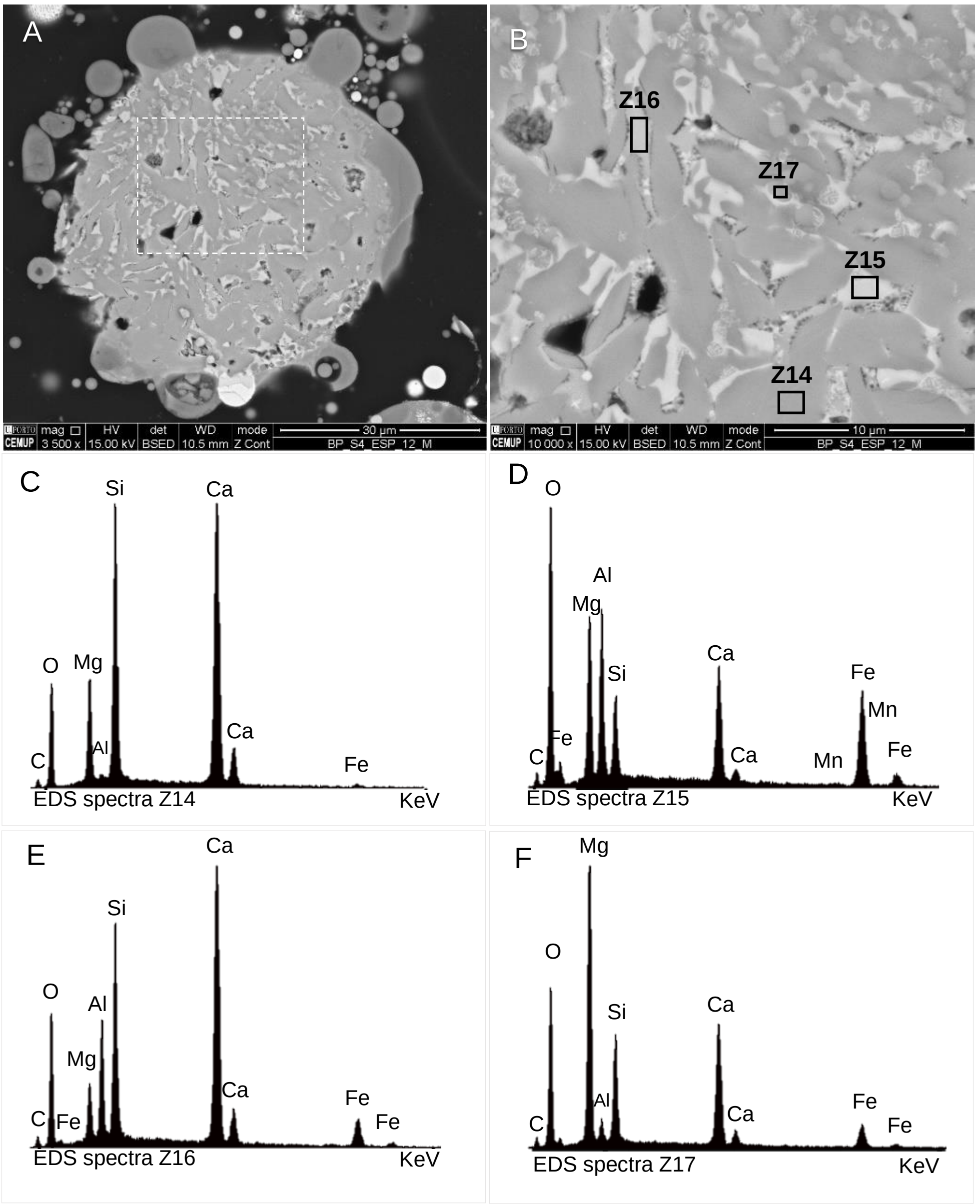

Figure III - 39. Detailed imaging of a (A) calcimagnesiasphere (BSE mode, ×3500), (B) magnification of dashed square in "A" showing the locations where spectra were acquired (BSE mode, ×10 000). (C-F) Z14-Z17 EDS spectra.

3.8. Conclusions

Magnetic concentrates were collected from six coal combustion ashes via wet magnetic separation and characterized in detail. Three of the six samples were subjected to sequential separation using a ferrite and a neodymium magnet. The MC obtained from the sequential separation were dry sieved and chemically characterized to assess elemental distribution.

The yields using Nd magnet (8.9-53.4 wt.%) were superior to the ones achieved using the ferrite magnet (4.5-13.1 wt.%). However, as the separation was sequential, most of the iron-rich morphotypes were initially captured by the Fe magnet while the Nd magnet mainly captured paramagnetic phases (glass). Sequential separation with both magnets leads to a decrease in the Fe-content of approx. 75 wt.% in ECO FA and 40 wt.% in ESP FA.

Among the Fe-MC, the ESP FA had the lowest yield but highest Fe-content (>40 wt.% Fe_2O_3). This is related to Fe-bearing phases mode of occurrence: (a) ESP FA, primarily discrete iron-rich particles mainly <25 μm while (b) BA, and coarser fractions from ECO FA, Fe-bearing phases/minerals are often found embedded in aluminosilicate agglomerates.

Several elements such as Mo, Sc, Mn, As, Cd and Ni were found to be enriched in Fe-MC and significantly correlated to iron, which can be attributed to their ability to substitute Fe in spinel structure. The content of iron as well as the elements associated with it increase with decreasing particle size. Seemingly, the finer fractions could be considered more promising to be used as catalyst due to their higher Fe-content. However, it must be considered that smaller melt droplets suffer more rapidly cooling that quenches Fe-minerals growth which may affect catalytic performance. The Nd-MC show homogeneous chemical composition among the size-fractions with negligible variations in the Fe content.

Magnetic parameters revealed the predominance of a low coercivity magnetic phase, magnetite/maghemite and a small contribution of a high coercivity phase, hematite/goethite. The XRD results confirmed that magnetite, hematite and magnesioferrite were the predominant iron-bearing minerals in MC. Still, non-magnetic phases such amorphous glass, quartz and mullite occur in significant amounts in MC most likely due to intimate association with Fe-bearing phases and low efficiency of magnetic separation process. Iron speciation by Mössbauer spectroscopy revealed the presence of Fe^{2+} and Fe^{3+} in silicates from the magnetic fractions apart from magnetite and hematite corroborating the SEM/EDS analysis.

The characterization of MC cross-sections provided new chemical and mineralogical insights regarding local variations within Fe-morphotypes, whereas Raman microspectroscopy was fundamental to distinguish the mineral phases, namely where martitization aspects (polymorphic substitution of magnetite by hematite) were identified using reflected light microscopy. Nevertheless, the process that leads to magnetite oxidation into hematite in ashes is still not understood. It was verified that sometimes chemical variations observed in SEM/EDS and under optical reflected light appear similar to martitization aspects, however the phase co-existing with martite is magnesioferrite. Ferrospheres are the morphotypes prevalent in the studied MC and are generally characterized by skeletal-dentritic crystals embedded in an aluminossilicate matrix.

The Fe-MC were tested as electrocatalysts in the reduction of 4-NPh and except for the ones derived from BA, catalytic activity was verified. Furthermore, MC from ESP FA after washing with NaOH the MC showed a catalytic efficiency comparable to the verified for noble metal nanocatalysts. These results highlight the potential of reutilization of MC in wastewater treatment and encourages research to continue to be done in this direction.

Part IV | Main conclusions and final remarks

The main objective of this thesis was to assess the potential of combustion ashes derived from commercial coal burned in Portugal as raw materials for REE, graphitic precursors (char; to substitute natural graphite) and Fe catalysts (Fe-bearing morphotypes, to substitute noble metals), starting from an integrated analysis where time and space variations would be taken in consideration.

For these purposes, four sampling campaigns were carried out at Pego power plant (Abrantes, Portugal) over a year to collect samples of feed coals and ashes in different locations of the system. The feed coals and respective bulk ash samples were characterized, and ash samples were selected for fractionation (size and magnetic proprieties) and characterization to gather information regarding elements/morphotypes distribution.

After petrographic and chemical characterization, it was concluded that the feed coals were predominantly medium rank D vitrinite-rich, with very low-to-medium ash, low sulfur, and mainly composed by silicates such as quartz and kaolinite. All feed coals presented low REE concentrations (<25 ppm), which may have resulted from beneficiation prior commercialization to meet Portuguese criteria regarding sulfur emissions and for an efficient combustion. Meanwhile, the geochemical associations found suggested that REE were inorganically associated and occur in micrometric P-rich phases, often intermixed with clays.

All ashes studied were low-Ca, class F, sialic with medium acidity, and mainly composed of an amorphous phase (mostly aluminosilicate glass), quartz and mullite. Regarding the glass phase in these ashes, two main types of glass were distinguished: (a) main type with chemical composition similar to illite/smectite, occurring as large masses in BA and as subrounded/rounded particles in FA; and (b) a phase essentially composed of Al-Si occurring in minor amounts. This phase is distinguished by its vesiculated structure and slightly darker tone under SEM BSE mode and easily distinguished in optical microscopy by its white color and vesicular texture.

The distribution of char among the different types of combustion ashes as inferred from carbon analysis and verified by petrographic examination was consistent over time, with ESP FA presenting higher carbon content and char volume than BA and ECO FA. However, variations across the ESP hoppers/bins were not consistent over time most probably due to changes in combustion conditions and performance of the ESP. Considered that that the first row collects about 80% of the total FA collected by the ESP, this ash would be the most suitable for char recovery.

Bulk ashes presented low REE concentrations, <270 ppm, reflecting the low contents found in feed coals. The REE were consistently found in higher concentrations in ESP fly ashes, tending to increase towards the back rows along with the LREE/HREE ratio, which seems to be related likely related to the variations in the fly ash petrology, e.g., amount of glass. The REE were mainly found in <10 µm discrete particles having P and Al-Si as the major components.

Chemical analysis from size and magnetic fractions showed that in fly ashes the REE were more concentrated in the nonmagnetic <25 µm fraction, which was not observed for BA. A single trial made in a FA sample from the first row of the ESP combining dry sieving and magnetic separation enabled to increase the ΣREE in 50 ppm recovering 53 % of total REE. Finally, the assessment of the potential of coal ashes and respective fractions as REE-raw material allowed to conclude that were promising materials for REE extraction regarding ore quality, but the concentrations found were below the economical cut-off of 1000 ppm REO.

Char was found to be mainly concentrated in the coarser fractions of ESP FA, and for that reason fraction >75 µm was chosen for char recovery. A concentrate with 72.55 wt.% FC, db, was obtained from a sample initially with 5.39 wt.% FC, db. This was possible using a sequence of simple methods: sieving (dry and wet), sink-float, vibration induced segregation, elutriation, and magnetic separation. Finally, after demineralization, the FC exceeded 95 wt.%, db.

The char concentrate (CC-PT sample) obtained from Pego power plant ash and respective heat-treated sample were characterized along with samples from difference provenances (Poland, Romania, and South Africa) that underwent through the same processes (demineralization and high temperature treatments) to determine their proprieties and the transformations occurred. The results have showed that chars had different graphitization abilities, and several factors affected their responses.

The CD-PT sample which presented the highest volume of anisotropic particles, high spatial arrangement of the BSU, lowest mineral matter and H contents compared to the remaining samples showed the lowest ability to graphitize. By contrast, the CD-RO sample which was mainly composed of isotropic particles and had the highest contents of ash and H, attained the second-best graphitization degree and the wider variety and size of graphite forms. The comparison between these two samples pointed to the importance of mineral matter and H in graphitization, both reduced in CC-PT during the demineralization. However, the sample that graphitized better, CD-SA, had lower H content than CD-RO sample. The CD-SA sample besides presenting higher preferential orientation of BSU relatively to CD-RO, had a higher content of Al_2O_3 that may have acted as catalyst.

It was also concluded that same char morphotypes derived from coals of similar rank suffer different structural transformations during graphitization, which might be related to other differences in the respective feed coals and macerals behavior during combustion.

Nevertheless, after electrocatalysis experiments all char concentrates studied demonstrated potential to substitute graphite as electrocatalysts in ORR. Unexpectedly, however, it was concluded that the best results were provided by non-graphitized chars, which increases the potential utilization of coal chars as catalysts.

The characterization of magnetic concentrates (MC) showed that adding an additional step using a Nd magnet greatly improved the recovery yield than if only the Fe magnet was used. Nevertheless, given the sequential nature of the procedure, the Fe magnet collected Fe-rich particles, including most of the ferrospheres, while the Nd magnet collected mainly paramagnetic phases, which includes Fe embedded in aluminosilicate glass. The Fe-MC from ESP FA had higher Fe content because was predominantly composed by discrete Fe-rich morphotypes such as ferrospheres. In the analogous MC from BA and ECO these phases were often observed embedded in aluminosilicate glass.

Regarding the chemical composition of the MC, elements such as Mn and Ni were enriched in Fe-MC relatively to the tailings and significantly correlated to Fe, which is related to their ability to substitute Fe in spinel structure. Furthermore, it was verified that those elements tend to increase with decreasing Fe-MC particle size. By contrast, Nd-MC show negligible variations in chemical composition across the size-fractions. The amorphous phase is predominant in all MC, and it is mainly composed by aluminosilicate glass where some iron was found as Fe^{2+} and Fe^{3+}.

Magnetite, hematite, magnesioferrite and maghemite were the predominant iron-bearing minerals in Fe-MC. In the Nd-MC magnesioferrite was absent and the remaining Fe-bearing minerals were residual. Observation of MC cross-section enabled the identification of oxidation rims in particles surface and martitization aspects (polymorphic substitution of magnetite by hematite). Furthermore, it was verified that aspects similar to martitization under reflected microscopy might correspond the co-existence of hematite and magnesioferrite.

The Fe-MC were tested as electrocatalysts in the reduction of 4-NPh and, except for the ones derived from BA, catalytic activity was verified. Furthermore, MC from ESP FA after washing with NaOH the MC showed a catalytic efficiency comparable to that of noble metal nanocatalysts, which is a very important conclusion since FA magnetics is an abundant material easily to collect, not desirable in FA based concrete, bricks and ceramics, and may replace expensive and scarce noble metals.

Overall, among the samples studied, fly ash samples from the ESP were the most promising for the recovery of the targeted elements and morphotypes, and it was demonstrated that both char and Fe-rich fractions can easily be recovered and applied in high value applications.

The Pego power plant was closed in November 2021 and as such, no more ashes such as those studied under the scope of this research will be produced. Nevertheless, the information gathered during this research can be applied to ashes being produced in power plants worldwide. Despite the policies to achieve carbon neutrality, there are still numerous power plants in operation and others planned to be installed, especially in developing countries, such as India, where coal remains the most abundant or affordable source of energy. The ashes produced in those countries are now being exported to EU for concrete production and will need to meet EU requirements. Moreover, there is plenty ash landfilled that can be characterized to further be recycled and reutilized.

References

Abrajevitch, A., Kodama, K., 2011. Diagenetic sensitivity of paleoenvironmental proxies: A rock magnetic study of Australian continental margin sediments. Geochemistry, Geophysics, Geosystems 12, n/a-n/a. https://doi.org/10.1029/2010GC003481

Ahmaruzzaman, M., 2010. A review on the utilization of fly ash. Prog Energy Combust Sci 36, 327–363. https://doi.org/10.1016/j.pecs.2009.11.003

Ahn, Y.C., Lee, J.K., 2006. Physical, chemical, and electrical analysis of aerosol particles generated from industrial plants. J Aerosol Sci 37, 187–202. https://doi.org/10.1016/j.jaerosci.2005.04.008

Alonso, M.J.G., Borrego, A.G., Alvarez, D., Menendez, R., 1999. Conference: 10. international conference on coal science: ICCS ’99, in: An Assessment of the Variations in the Structure of Chars Materials by Different Microscopy Techniques. Taiyuan (China).

Alonso, M.J.G., Borrego, A.G., Alvarez, D., Parra, J.B., Menéndez, R., 2001. Influence of pyrolysis temperature on char optical texture and reactivity. J Anal Appl Pyrolysis 58–59, 887–909. https://doi.org/10.1016/S0165-2370(00)00186-8

Annamalai, K., Ryan, W., 1993. Interactive processes in gasification and combustion—II. Isolated carbon, coal and porous char particles. Prog Energy Combust Sci 19, 383–446. https://doi.org/10.1016/0360-1285(93)90010-C

Anshits, A.G., Bayukov, O.A., Kondratenko, E.V., Anshits, N.N., Pletnev, O.N., Rabchevskii, E.V., Solovyov, L.A., 2016. Catalytic properties and nature of active centers of ferrospheres in oxidative coupling of methane. Appl Catal A Gen 524, 192–199. https://doi.org/10.1016/j.apcata.2016.06.032

Anshits, A.G., Kondratenko, E.V., Fomenko, E.V., Kovalev, A.M., Anshits, N.N., Bajukov, O.A., Sokol, E.V., Salanov, A.N., 2001. Novel glass crystal catalysts for the processes of methane oxidation. Catal Today 64, 59–67. https://doi.org/10.1016/S0920-5861(00)00509-5

Anshits, A.G., Kondratenko, E.V., Fomenko, E.V., Kovalev, A.M., Bajukov, O.A., Anshits, N.N., Sokol, E.V., Kochubey, D.I., Boronin, A.I., Salanov, A.N., Koshcheev, S.V., 2000. Physicochemical and catalytic properties of glass crystal catalysts for the oxidation of methane. J Mol Catal A Chem 158, 209–214. https://doi.org/10.1016/S1381-1169(00)00067-4

Anshits, A.G., Sharonova, O.M., Anshits, N.N., Vereshchagin, S.N., Rabchevskii, E.V., Solovjev, L.A., 2011. Ferrospheres from fly ashes: Composition and Catalytic proprieties in high-temperature oxidation of methane, in: World of Coal Ash. Denver, CO, USA.

Anshits, N.N., Fedorchak, M.A., Fomenko, E.V., Mazurova, E.V., Anshits, A.G., 2020. Composition, Structure, and Formation Routes of Blocklike Ferrospheres Separated from Coal and Lignite Fly Ashes. Energy & Fuels 34, 3743–3754. https://doi.org/10.1021/acs.energyfuels.9b04034

Anshits, N.N., Fedorchak, M.A., Zhizhaev, A.M., Anshits, A.G., 2019. Composition–Structure Relationship of Skeletal–Dendritic Ferrospheres Formed during Industrial

Combustion of Lignite and Coal. Energy & Fuels 33, 6788–6796. https://doi.org/10.1021/acs.energyfuels.9b01077

Anshits, N.N., Fedorchak, M.A., Zhizhaev, A.M., Sharonova, O.M., Anshits, A.G., 2018. Composition and Structure of Block-Type Ferrospheres Isolated from Calcium-Rich Power Plant Ash. Inorganic Materials 54, 187–194. https://doi.org/10.1134/S0020168518020012

Anshits, N.N., Fomenko, E.V., Anshits, A.G., 2021. Composition–Structure Relationship and Routes of Formation of Blocklike Ferrospheres Produced by Pulverized Combustion of Two Coal Types. ACS Omega 6, 26004–26015. https://doi.org/10.1021/acsomega.1c02880

Anthony, J., Bideaux, R., Bladh, K., Nichols, M., 1990. Handbook of mineralogy. Vol. 1. Elements, Sulfides, Sulfosalts. Mineral Data Publishing, Tucson, Arizona.

Arbuzov, S.I., Finkelman, R.B., Il'enok, S.S., Maslov, S.G., Mezhibor, A.M., Blokhin, M.G., 2019. Modes of Occurrence of Rare-Earth Elements (La, Ce, Sm, Eu, Tb, Yb, Lu) in Coals of Northern Asia (Review). Solid Fuel Chemistry 53, 1–21. https://doi.org/10.3103/S0361521919010026

ASTM C618, 2005. Coal Fly Ash and Raw or Calcined Natural Pozzolan for Use in Concrete. American Society for Testing and Materials 3. https://doi.org/10.1520/C0618-19

ASTM D388, 1999. Standard Classification of Coals by Rank. American Society for Testing and Materials 8. https://doi.org/10.1520/D0388-19A

ASTM D4239, 2017. Standard Test Method for Sulfur in the Analysis Sample of Coal and Coke Using High-Temperature Tube Furnace Combustion. American Society for Testing and Materials 7. https://doi.org/10.1520/D4239-17

ASTM D5373, 2016. Standard Test Methods for Determination of Carbon, Hydrogen and Nitrogen in Analysis Samples of Coal and Carbon in Analysis Samples of Coal and Coke. American Society for Testing and Materials 11. https://doi.org/10.1520/D5373-16

ASTM D7348, 2013. Standard Test Methods for Loss on Ignition (LOI) of Solid Combustion Residues. https://doi.org/10.1520/D7348-13

ASTM D7582, 2015. Standard Test Methods for Proximate Analysis of Coal and Coke by Macro Thermogravimetric Analysis. American Society for Testing and Materials 9. https://doi.org/10.1520/D7582-15

Atria, J. v., Rusinko, F., Schobert, H.H., 2002. Structural Ordering of Pennsylvania Anthracites on Heat Treatment to 2000−2900 °C. Energy & Fuels 16, 1343–1347. https://doi.org/10.1021/ef010295h

Badenhorst, C., Santos, C., Lázaro-Martínez, J., Białecka, B., Cruceru, M., Guedes, A., Guimarães, R., Moreira, K., Predeanu, G., Suárez-Ruíz, I., Cameán, I., Valentim, B., Wagner, N., 2020. Assessment of Graphitized Coal Ash Char Concentrates as a Potential Synthetic Graphite Source. Minerals 10, 986. https://doi.org/10.3390/min10110986

Badenhorst, C., Wagner, N., Valentim, B., Santos, A.C., Guedes, A., Białecka, B., Mozco, J.C., Popescu, L., Cruceru, M., Predeanu, G., Vijoen, K.S., Lázaro-

Martínez, J.M., Abagiu, T.A., 2019. Char from coal ash as a possible precursor for synthetic graphite – Recent developments of the Charphite project, in: Ash Library - Flyash.Org. World of Coal Ash (WOCA), St. Louis.

Bae, S., Gim, S., Kim, H., Dorcet, V., Pasturel, M., Grenèche, J.-M., Darbha, G.K., Hanna, K., 2017. New Features and Uncovered Benefits of Polycrystalline Magnetite as Reusable Catalyst in Reductive Chemical Conversion. The Journal of Physical Chemistry C 121, 25195–25205. https://doi.org/10.1021/acs.jpcc.7b08178

Baer, W., 2020. Chunky Graphite in Ferritic Spheroidal Graphite Cast Iron: Formation, Prevention, Characterization, Impact on Properties: An Overview. International Journal of Metalcasting 14, 454–488. https://doi.org/10.1007/s40962-019-00363-8

Baltrus, J.P., Diehl, J.R., Soong, Y., Sands, W., 2002. Triboelectrostatic separation of fly ash and charge reversal. Fuel 81, 757–762. https://doi.org/10.1016/S0016-2361(01)00196-X

Ban, H., Li, T.X., Hower, J.C., Schaefer, J.L., Stencel, J.M., 1997. Dry triboelectrostatic beneficiation of fly ash. Fuel 76, 801–805. https://doi.org/10.1016/S0016-2361(97)00045-8

Barranco, R., Cloke, M., Lester, E., 2003. Prediction of the burnout performance of some South American coals using a drop-tube furnace. Fuel 82, 1893–1899. https://doi.org/10.1016/S0016-2361(03)00192-3

Barrenechea, J.F., Luque, F.J., Millward, D., Ortega, L., Beyssac, O., Rodas, M., 2009. Graphite morphologies from the Borrowdale deposit (NW England, UK): Raman and SIMS data. Contributions to Mineralogy and Petrology 158, 37–51. https://doi.org/10.1007/s00410-008-0369-y

Bartoňová, L., 2015. Unburned carbon from coal combustion ash: An overview. Fuel Processing Technology 134, 136–158. https://doi.org/10.1016/j.fuproc.2015.01.028

Bartoňová, L., Klika, Z., Spears, D.A., 2007. Characterization of unburned carbon from ash after bituminous coal and lignite combustion in CFBs. Fuel 86, 455–463. https://doi.org/10.1016/j.fuel.2006.07.024

Bartoňová, L., Serenčíšová, J., Čech, B., 2018. Yttrium partitioning and associations in coal-combustion ashes prior to and after their leaching in HCl. Fuel Processing Technology 173, 205–215. https://doi.org/10.1016/j.fuproc.2018.01.011

Bau, M., Dulski, P., 1996. Distribution of yttrium and rare-earth elements in the Penge and Kuruman iron-formations, Transvaal Supergroup, South Africa. Precambrian Res 79, 37–55. https://doi.org/10.1016/0301-9268(95)00087-9

Bend, S.L., 1989. Coal characterization and coal combustion. University of Newcastle, Upon Tyne, England.

Bend, S.L., Edwards, I.A.S., Marsh, H., 1992. The influence of rank upon char morphology and combustion. Fuel 71, 493–501. https://doi.org/10.1016/0016-2361(92)90145-E

Benfell, K.E., Liu, G.-S., Roberts, D.G., Harris, D.J., Lucas, J.A., Bailey, J.G., Wall, T.F., 2000. Modeling char combustion: The influence of parent coal petrography and pyrolysis pressure on the structure and intrinsic reactivity of its char. Proceedings of the Combustion Institute 28, 2233–2241. https://doi.org/10.1016/S0082-0784(00)80633-5

Benson, E.E., Kubiak, C.P., Sathrum, A.J., Smieja, J.M., 2009. Electrocatalytic and homogeneous approaches to conversion of CO $_2$ to liquid fuels. Chem. Soc. Rev. 38, 89–99. https://doi.org/10.1039/B804323J

Beny-Bassez, C.,, Rozaud, J.N., 1985. Characterization of carbonaceous materials by correlated electron and optical microscopy and Raman microspectroscopy. Scan Electron Microsc 119–132.

Beyssac, O., Goffé, B., Petitet, J.-P., Froigneux, E., Moreau, M., Rouzaud, J.-N., 2003. On the characterization of disordered and heterogeneous carbonaceous materials by Raman spectroscopy. Spectrochim Acta A Mol Biomol Spectrosc 59, 2267–2276. https://doi.org/10.1016/S1386-1425(03)00070-2

Beyssac, O., Rouzaud, J.-N., Goffé, B., Brunet, F., Chopin, C., 2002. Graphitization in a high-pressure, low-temperature metamorphic gradient: a Raman microspectroscopy and HRTEM study. Contributions to Mineralogy and Petrology 143, 19–31. https://doi.org/10.1007/s00410-001-0324-7

Beyssac, O., Rumble, D., 2014. Graphitic Carbon: A Ubiquitous, Diverse, and Useful Geomaterial. Elements 10, 415–420. https://doi.org/10.2113/gselements.10.6.415

Bhatt, A., Priyadarshini, S., Acharath Mohanakrishnan, A., Abri, A., Sattler, M., Techapaphawit, S., 2019. Physical, chemical, and geotechnical properties of coal fly ash: A global review. Case Studies in Construction Materials 11, e00263. https://doi.org/10.1016/j.cscm.2019.e00263

Bibby, D., 1977. Composition and variation of pulverized fuel ash obtained from the combustion of sub-bituminous coals, New Zealand. Fuel 56, 427–431. https://doi.org/10.1016/0016-2361(77)90071-0

Biscoe, J., Warren, B.E., 1942. An X-Ray Study of Carbon Black. J Appl Phys 13, 364–371. https://doi.org/10.1063/1.1714879

Blaha, U., Sapkota, B., Appel, E., Stanjek, H., Rosler, W., 2008. Micro-scale grain-size analysis and magnetic properties of coal-fired power plant fly ash and its relevance for environmental magnetic pollution studies. Atmos Environ 42, 8359–8370. https://doi.org/10.1016/j.atmosenv.2008.07.051

Blissett, R.S., Rowson, N.A., 2012. A review of the multi-component utilisation of coal fly ash. Fuel 97, 1–23. https://doi.org/10.1016/j.fuel.2012.03.024

Blissett, R.S., Smalley, N., Rowson, N.A., 2014. An investigation into six coal fly ashes from the United Kingdom and Poland to evaluate rare earth element content. Fuel 119, 236–239. https://doi.org/10.1016/j.fuel.2013.11.053

Bloemendal, J., Lamb, B., King, J., 1988. Paleoenvironmental implications of rock-magnetic properties of Late Quaternary sediment cores from the eastern equatorial Atlantic. Paleoceanography 3, 61–87. https://doi.org/10.1029/PA003i001p00061

Borrego, A.G., Alvarez, D., Menéndez, R., 1997. Effects of Inertinite Content in Coal on Char Structure and Combustion. Energy & Fuels 11, 702–708. https://doi.org/10.1021/ef960130m

Brown, R., 1995. Systematic errors in the use of loss-on-ignition to measure unburned carbon in fly ash. Fuel 74, 570–574. https://doi.org/10.1016/0016-2361(95)98360-Q

Bryers, R.W., 1986. Influence of Segregated Mineral Matter in Coal on Slagging, in: Mineral Matter and Ash in Coal, ACS Symposium Series. American Chemical Society, pp. 353–374. https://doi.org/doi:10.1021/bk-1986-0301.ch025

Burgess-Clifford, C.E., Narayanan, D.L., van Essendelft, D.T., Jain, P., Sakti, A., Lueking, A.D., 2009. The effect of calcination on reactive milling of anthracite as potential precursor for graphite production. Fuel Processing Technology 90, 1515–1523. https://doi.org/10.1016/j.fuproc.2009.07.017

Cabielles, M., Montes-Morán, M.A., Garcia, A.B., 2008. Structural Study of Graphite Materials Prepared by HTT of Unburned Carbon Concentrates from Coal Combustion Fly Ashes. Energy & Fuels 22, 1239–1243. https://doi.org/10.1021/ef700603t

Cabielles, M., Rouzaud, J.-N., Garcia, A.B., 2009. High-Resolution Transmission Electron Microscopy Studies of Graphite Materials Prepared by High-Temperature Treatment of Unburned Carbon Concentrates from Combustion Fly Ashes. Energy & Fuels 23, 942–950. https://doi.org/10.1021/ef800763s

Cameán, I., Garcia, A.B., 2011. Graphite materials prepared by HTT of unburned carbon from coal combustion fly ashes: Performance as anodes in lithium-ion batteries. J Power Sources 196, 4816–4820. https://doi.org/10.1016/j.jpowsour.2011.01.041

Campbell, J.A., Laul, J.C., Nielson, K.K., Smith, R.D., 1978. Separation and chemical characterization of finely-sized fly-ash particles. Anal Chem 50, 1032–1040. https://doi.org/10.1021/ac50030a009

Cangialosi, F., Notarnicola, M., Liberti, L., Stencel, J., 2009. The role of weathering on fly ash charge distribution during triboelectrostatic beneficiation. J Hazard Mater 164, 683–688. https://doi.org/10.1016/j.jhazmat.2008.08.050

Castor, S.B., Hedrick, J.B., 2006. Rare earth elements., in: Kogel, J.E., Trivedi, N.C., Barker, J.M., Krukowski, S.K. (Eds.), Industrial Minerals and Rocks:Commodities, Markets, and Uses. Society for Mining, Metallurgy, and Exploration, pp. 769–792.

Chernyshova, I. v., Hochella Jr, M.F., Madden, A.S., 2007. Size-dependent structural transformations of hematite nanoparticles. 1. Phase transition. Physical Chemistry Chemical Physics 9, 1736. https://doi.org/10.1039/b618790k

Cho, D.-W., Kim, S., Tsang, Y.F., Song, H., 2019. Preparation of nitrogen-doped Cu-biochar and its application into catalytic reduction of p-nitrophenol. Environ Geochem Health 41, 1729–1737. https://doi.org/10.1007/s10653-017-9966-x

Chou, C.-L., 2012. Sulfur in coals: A review of geochemistry and origins. Int J Coal Geol 100, 1–13. https://doi.org/10.1016/j.coal.2012.05.009

Chourpa, I., Douziech-Eyrolles, L., Ngaboni-Okassa, L., Fouquenet, J.-F., Cohen-Jonathan, S., Soucé, M., Marchais, H., Dubois, P., 2005. Molecular composition of iron oxide nanoparticles, precursors for magnetic drug targeting, as characterized by confocal Raman microspectroscopy. Analyst 130, 1395. https://doi.org/10.1039/b419004a

Clarke, L.B., 1993. The fate of trace elements during coal combustion and gasification: an overview. Fuel 72, 731–736. https://doi.org/10.1016/0016-2361(93)90072-A

Clarke, L.B., Sloss, L.L., 1992. Trace elements: emissions from coal combustion and gasification. IEA Coal Research, London.

Connelly, N.G., 2005. Nomenclature of Inorganic Chemistry: IUPAC Recommendations 2005. The Red-Book. Royal Society of Chemistry.

Crelling, J.C., Hippo, E.J., Woerner, B.A., West, D.P., 1992. Combustion characteristics of selected whole coals and macerals. Fuel 71, 151–158. https://doi.org/10.1016/0016-2361(92)90003-7

Cruceru, M., Diaconu, B., Anghelescu, L., Abagiu, T.A., 2017. Study on char recovery from bottom coal ash. International Journal of Energy and Environment 11, 64–68.

Dai, S., Chou, C.-L., 2007. Occurrence and origin of minerals in a chamosite-bearing coal of Late Permian age, Zhaotong, Yunnan, China. American Mineralogist 92, 1253–1261. https://doi.org/10.2138/am.2007.2496

Dai, S., Finkelman, R.B., 2018. Coal as a promising source of critical elements: Progress and future prospects. Int J Coal Geol 186, 155–164. https://doi.org/10.1016/j.coal.2017.06.005

Dai, S., Graham, I.T., Ward, C.R., 2016a. A review of anomalous rare earth elements and yttrium in coal. Int J Coal Geol 159, 82–95. https://doi.org/10.1016/j.coal.2016.04.005

Dai, S., Li, T., Seredin, V.V., Ward, C.R., Hower, J.C., Zhou, Y., Zhang, M., Song, X., Song, W., Zhao, C., 2014a. Origin of minerals and elements in the Late Permian coals, tonsteins, and host rocks of the Xinde Mine, Xuanwei, eastern Yunnan, China. Int J Coal Geol 121, 53–78. https://doi.org/10.1016/j.coal.2013.11.001

Dai, S., Liu, J., Ward, C.R., Hower, J.C., French, D., Jia, S., Hood, M.M., Garrison, T.M., 2016b. Mineralogical and geochemical compositions of Late Permian coals and host rocks from the Guxu Coalfield, Sichuan Province, China, with emphasis on enrichment of rare metals. Int J Coal Geol 166, 71–95. https://doi.org/10.1016/j.coal.2015.12.004

Dai, S., Seredin, V.V., Ward, C.R., Hower, J.C., Xing, Y., Zhang, W., Song, W., Wang, P., 2015. Enrichment of U–Se–Mo–Re–V in coals preserved within marine carbonate successions: geochemical and mineralogical data from the Late Permian Guiding Coalfield, Guizhou, China. Miner Depos 50, 159–186. https://doi.org/10.1007/s00126-014-0528-1

Dai, S., Seredin, V.V., Ward, C.R., Jiang, J., Hower, J.C., Song, X., Jiang, Y., Wang, X., Gornostaeva, T., Li, X., Liu, H., Zhao, L., Zhao, C., 2014b. Composition and modes of occurrence of minerals and elements in coal combustion products derived from high-Ge coals. Int J Coal Geol 121, 79–97. https://doi.org/10.1016/j.coal.2013.11.004

Dai, S., Tian, L., Chou, C.-L., Zhou, Y., Zhang, M., Zhao, L., Wang, J., Yang, Z., Cao, H., Ren, D., 2008. Mineralogical and compositional characteristics of Late Permian coals from an area of high lung cancer rate in Xuan Wei, Yunnan, China: Occurrence and origin of quartz and chamosite. Int J Coal Geol 76, 318–327. https://doi.org/10.1016/j.coal.2008.09.001

Dai, S., Xie, P., Jia, S., Ward, C.R., Hower, J.C., Yan, Xi., French, D., 2017a. Enrichment of U-Re-V-Cr-Se and rare earth elements in the Late Permian coals of the Moxinpo Coalfield, Chongqing, China: Genetic implications from geochemical and mineralogical data. Ore Geol Rev 80, 1–17. https://doi.org/10.1016/j.oregeorev.2016.06.015

Dai, S., Xie, P., Ward, C.R., Yan, X., Guo, W., French, D., Graham, I.T., 2017b. Anomalies of rare metals in Lopingian super-high-organic-sulfur coals from the Yishan Coalfield, Guangxi, China. Ore Geol Rev 88, 235–250. https://doi.org/10.1016/j.oregeorev.2017.05.007

Dai, S., Zhao, L., Hower, J.C., Johnston, M.N., Song, W., Wang, P., Zhang, S., 2014c. Petrology, Mineralogy, and Chemistry of Size-Fractioned Fly Ash from the Jungar Power Plant, Inner Mongolia, China, with Emphasis on the Distribution of Rare Earth Elements. Energy & Fuels 28, 1502–1514. https://doi.org/10.1021/ef402184t

Dai, S., Zhao, L., Peng, S., Chou, C.-L., Wang, X., Zhang, Y., Li, D., Sun, Y., 2010. Abundances and distribution of minerals and elements in high-alumina coal fly ash from the Jungar Power Plant, Inner Mongolia, China. Int J Coal Geol 81, 320–332. https://doi.org/10.1016/j.coal.2009.03.005

Dakič, D., van der Honing, G., Valk, M., 1989. Fragmentation and swelling of various coals during devolatilization in a fluidized bed. Fuel 68, 911–916. https://doi.org/10.1016/0016-2361(89)90129-4

de Boer, G.B.J., de Weerd, C., Thoenes, D., Goossens, H.W.J., 1987. Laser Diffraction Spectrometry: Fraunhofer Diffraction Versus Mie Scattering. Particle & Particle Systems Characterization 4, 14–19. https://doi.org/10.1002/ppsc.19870040104

de Faria, D.L.A., Lopes, F.N., 2007. Heated goethite and natural hematite: Can Raman spectroscopy be used to differentiate them? Vib Spectrosc 45, 117–121. https://doi.org/10.1016/j.vibspec.2007.07.003

de Grave, E., Vanleerberghe, R., Dauwe, C., de Sitter, J., Govaert, A., 1976. Magnetic hyperfine field distributions in ferrimagnetic spinels Fe2(1-y)Mg1+yTiyO4 with y ≤ 0.5. Le Journal de Physique Colloques 37, C6-97-C6-100. https://doi.org/10.1051/jphyscol:1976623

Dekkers, M.J., 1997. Environmental magnetism: an introduction. Geologie en Mijnbouw (Geology and Mining) 76, 163–182. https://doi.org/10.1023/A:1003122305503

Demir, U., Yamik, A., Kelebek, S., Oteyaka, B., Ucar, A., Sahbaz, O., 2008. Characterization and column flotation of bottom ashes from Tuncbilek power plant. Fuel 87, 666–672. https://doi.org/10.1016/j.fuel.2007.05.040

Deshmukh, A.A., Mhlanga, S.D., Coville, N.J., 2010. Carbon spheres. Materials Science and Engineering: R: Reports 70, 1–28. https://doi.org/10.1016/j.mser.2010.06.017

Deurbergue, A., Oberlin, A., Oh, J.H., Rouzaud, J.N., 1987. Graphitization of Korean anthracites as studied by transmission electron microscopy and X-ray diffraction. Int J Coal Geol 8, 375–393. https://doi.org/10.1016/0166-5162(87)90074-7

Dimovski, S., Libera, J.A., Gogotsi, Y., 2001. A Novel Class of Carbon Nanocones. MRS Proceedings 706, Z6.27.1. https://doi.org/10.1557/PROC-706-Z6.27.1

D'Ippolito, V., Andreozzi, G.B., Bersani, D., Lottici, P.P., 2015. Raman fingerprint of chromate, aluminate and ferrite spinels. Journal of Raman Spectroscopy 46, 1255–1264. https://doi.org/10.1002/jrs.4764

Double, D.D., Hellawell, A., 1974. Cone-helix growth forms of graphite. Acta Metallurgica 22, 481–487. https://doi.org/10.1016/0001-6160(74)90101-1

Duber, S., Pusz, S., Kwiecińska, B.K., Rouzaud, J.N., 2000. On the optically biaxial character and heterogeneity of anthracites. Int J Coal Geol 44, 227–250. https://doi.org/10.1016/S0166-5162(00)00012-4

Duber, S., Rouzaud, J.N., 1999. Calculation of reflectance values for two models of texture of carbon materials. Int J Coal Geol 38, 333–348. https://doi.org/10.1016/S0166-5162(98)00037-8

Egli, R., 2004. Characterization of Individual Rock Magnetic Components by Analysis of Remanence Curves, 1. Unmixing Natural Sediments. Studia Geophysica et Geodaetica 48, 391–446. https://doi.org/10.1023/B:SGEG.0000020839.45304.6d

Ehlers, E.G., Stiles, D.V., 1965. Melanterite-rozenite equilibrium. American Mineralogist 50, 1457–1458.

Ergun, S., 1968. Structure of carbon. Carbon N Y 6, 141–159. https://doi.org/10.1016/0008-6223(68)90299-6

Eskanazy, G., Finkelman, R.B., Chattarjee, S., 2010. Some considerations concerning the use of correlation coefficients and cluster analysis in interpreting coal geochemistry data. Int J Coal Geol 83, 491–493. https://doi.org/10.1016/j.coal.2010.05.006

Eskenazy, G.M., 1999. Aspects of the geochemistry of rare earth elements in coal: an experimental approach. Int J Coal Geol 38, 285–295. https://doi.org/10.1016/S0166-5162(98)00027-5

Eskenazy, G.M., 1987a. Rare earth elements in a sampled coal from the Pirin deposit, Bulgaria. Int J Coal Geol 7, 301–314. https://doi.org/10.1016/0166-5162(87)90041-3

Eskenazy, G.M., 1987b. Zirconium and hafnium in Bulgarian coals. Fuel 66, 1652–1657. https://doi.org/10.1016/0016-2361(87)90357-7

Eskenazy, G.M., 1987c. Rare earth elements and yttrium in lithotypes of Bulgarian coals. Org Geochem 11, 83–89. https://doi.org/10.1016/0146-6380(87)90030-1

European Commission, 2020. Critical Raw Materials Resilience: Charting a Path towards greater Security and Sustainability. Brussels.

European Commission, 2019. The European Green Deal. Brussels.

European Commission, Directorate-General for Internal Market, I.E. and Sme., Blengini, G., el Latunussa, C., Eynard, U., Torres De Matos, C., Wittmer, D., Georgitzikis, K., Pavel, C., Carrara, S., Mancini, L., Unguru, M., Grohol, M., Mathieux, F., Pennington, D., 2020. Study on the EU's list of critical raw materials (2020) : critical raw materials factsheets. Publications Office. https://doi.org/doi/10.2873/92480

Evans, E.L., Jenkins, J.L., Thomas, J.M., 1972. Direct electron microscopic studies of graphitic regions in heat-treated coals and coal extracts. Carbon N Y 10, 637–642. https://doi.org/10.1016/0008-6223(72)90102-9

Evans, M.E., Heller, F., 2003. Environmental Magnetism. Principles and Applications of Enviromagnetics. Academic Press Elsevier.

Fan, M., Brown, R.C., 2001. Comparison of the Loss-on-Ignition and Thermogravimetric Analysis Techniques in Measuring Unburned Carbon in Coal Fly Ash. Energy & Fuels 15, 1414–1417. https://doi.org/10.1021/ef0100496

Feng, B., Bhatia, S.K., Barry, J.C., 2003. Variation of the Crystalline Structure of Coal Char during Gasification. Energy & Fuels 17, 744–754. https://doi.org/10.1021/ef0202541

Fernandes, D.M., Abdelkader-Fernández, V.K., Badenhorst, C., Bialecka, B., Guedes, A., Predeanu, G., Santos, A.C., Valentim, B., Wagner, N., Freire, C., 2021. Coal chars recovered from fly ash as promising electrocatalysts for oxygen reduction reaction. Int J Hydrogen Energy 46, 34679–34688. https://doi.org/10.1016/j.ijhydene.2021.08.009

Ferreira, N.M., Kovalevsky, A.V., Valente, M.A., Waerenborgh, J.C., Frade, J.R., Costa, F.M., 2017. Structural and redox effects in iron-doped magnesium aluminosilicates. J Cryst Growth 457, 19–23. https://doi.org/10.1016/j.jcrysgro.2016.01.039

Finch, R.J., 2003. Structure and Chemistry of Zircon and Zircon-Group Minerals. Rev Mineral Geochem 53, 1–25. https://doi.org/10.2113/0530001

Finkelman, R.B., 1999. Trace elements in coal. Biol Trace Elem Res 67, 197–204. https://doi.org/10.1007/BF02784420

Finkelman, R.B., 1993. Trace and Minor Elements in Coal, in: Engel M.H., M.S.A. (Ed.), Organic Geochemistry. Topics in Geobiology. Springer, Boston, MA, pp. 593–607. https://doi.org/10.1007/978-1-4615-2890-6_28

Finkelman, R.B., Palmer, C.A., Wang, P., 2018. Quantification of the modes of occurrence of 42 elements in coal. Int J Coal Geol 185, 138–160. https://doi.org/10.1016/j.coal.2017.09.005

Fisher, G.L., Chang, D.P.Y., Brummer, M., 1976. Fly Ash Collected from Electrostatic Precipitators: Microcrystalline Structures and the Mystery of the Spheres. Science (1979) 192, 553–555. https://doi.org/10.1126/science.192.4239.553

Fisher, G.L., Prentice, B.A., Silberman, D., Ondov, J.M., Biermann, A.H., Ragaini, R.C., McFarland, A.R., 1978. Physical and morphological studies of size-classified coal fly ash. Environ Sci Technol 12, 447–451. https://doi.org/10.1021/es60140a008

Fitzer, E., Kochling, K.-H., Boehm, H.P., Marsh, H., 1995. Recommended terminology for the description of carbon as a solid (IUPAC Recommendations 1995). Pure and Applied Chemistry 67, 473–506. https://doi.org/10.1351/pac199567030473

Folk, R.L., Ward, W.C., 1957. Brazos River bar [Texas]; a study in the significance of grain size parameters. Journal of Sedimentary Research 27, 3–26. https://doi.org/10.1306/74D70646-2B21-11D7-8648000102C1865D

Francis, W., 1961. Coal: its formation and composition. E. Arnold.

Franklin, R.E., 1951. The structure of graphitic carbons. Acta Crystallogr 4, 253–261. https://doi.org/10.1107/S0365110X51000842

Franus, W., Wiatros-Motyka, M.M., Wdowin, M., 2015. Coal fly ash as a resource for rare earth elements. Environmental Science and Pollution Research 22, 9464–9474. https://doi.org/10.1007/s11356-015-4111-9

Fu, B., Hower, J.C., Zhang, W., Luo, G., Hu, H., Yao, H., 2022. A review of rare earth elements and yttrium in coal ash: content, modes of occurrences, combustion behavior, and extraction methods. Prog Energy Combust Sci 88, 100954. https://doi.org/10.1016/j.pecs.2021.100954

Gadiou, R., 2002. The devolatilisation of millimetre sized coal particles at high heating rate: the influence of pressure on the structure and reactivity of the char. Fuel 81, 2121–2130. https://doi.org/10.1016/S0016-2361(02)00144-8

Garcia, A.B., Cameán, I., Pinilla, J.L., Suelves, I., Lázaro, M.J., Moliner, R., 2010. The graphitization of carbon nanofibers produced by catalytic decomposition of methane: Synergetic effect of the inherent Ni and Si. Fuel 89, 2160–2162. https://doi.org/10.1016/j.fuel.2010.03.046

Gluskoter, H.J., 1977. Inorganic Sulfur in Coal. Energy Sources 3, 125–131. https://doi.org/10.1080/00908317708945974

Godoy, M.L.D.P., Godoy, J.M., Roldao, L.A., 2001. Determination of trace elements in coal and coal ash samples by ICP-MS. At Spectrosc 22.

Gogotsi, Y., Dimovski, S., 2006. Graphite Whiskers, Cones, and Polyhedral Crystals. pp. 149–174. https://doi.org/10.1201/9781420009378.ch4

Golab, A., Ward, C.R., Permana, A., Lennox, P., Botha, P., 2013. High-resolution three-dimensional imaging of coal using microfocus X-ray computed tomography, with special reference to modes of mineral occurrence. Int J Coal Geol 113, 97–108. https://doi.org/10.1016/j.coal.2012.04.011

Gollakota, A.R.K., Volli, V., Shu, C.-M., 2019. Progressive utilisation prospects of coal fly ash: A review. Science of The Total Environment 672, 951–989. https://doi.org/10.1016/j.scitotenv.2019.03.337

González, D., Montes-Morán, M., Suárez-Ruiz, I., Garcia, A.B., 2004. Structural Characterization of Graphite Materials Prepared from Anthracites of Different Characteristics: A Comparative Analysis. Energy and Fuels 18, 365–370.

González, D., Montes-Morán, M.A., Garcia, A.B., 2005. Influence of Inherent Coal Mineral Matter on the Structural Characteristics of Graphite Materials Prepared from Anthracites. Energy & Fuels 19, 263–269. https://doi.org/10.1021/ef049893x

González, D., Montes-Morán, M.A., Garcia, A.B., 2003. Graphite Materials Prepared from an Anthracite: A Structural Characterization. Energy & Fuels 17, 1324–1329. https://doi.org/10.1021/ef0300491

González, D., Montes-Morán, M.A., Young, R.J., Garcia, A.B., 2002. Effect of temperature on the graphitization process of a semianthracite. Fuel Processing Technology 79, 245–250. https://doi.org/10.1016/S0378-3820(02)00181-9

Graedel, T.E., Reck, B.K., 2016. Six Years of Criticality Assessments: What Have We Learned So Far? J Ind Ecol 20, 692–699. https://doi.org/10.1111/jiec.12305

Gray, M.L., Champagne, K.J., Soong, Y., Killmeyer, R.P., Maroto-Valer, M.M., Andrésen, J.M., Ciocco, M.V., Zandhuis, P.H., 2002. Physical cleaning of high carbon fly ash. Fuel Processing Technology 76, 11–21. https://doi.org/10.1016/S0378-3820(02)00006-1

Gray, R.J., Devanney, K.F., 1986. Coke carbon forms: Microscopic classification and industrial applications. Int J Coal Geol 6, 277–297. https://doi.org/10.1016/0166-5162(86)90005-4

Gruner, D., Hood, W.C., 1971. Three Iron Sulfate Minerals from Coal Mine Refuse Dumps in Perry County, Illinois. Transactions Illinois State Academy of Science 156–158.

Guedes, A., Valentim, B., Prieto, A.C., Noronha, F., 2012. Raman spectroscopy of coal macerals and fluidized bed char morphotypes. Fuel 97, 443–449. https://doi.org/10.1016/j.fuel.2012.02.054

Guedes, A., Valentim, B., Prieto, A.C., Rodrigues, S., Noronha, F., 2010. Micro-Raman spectroscopy of collotelinite, fusinite and macrinite. Int J Coal Geol 83, 415–422. https://doi.org/10.1016/j.coal.2010.06.002

Guedes, A., Valentim, B., Prieto, A.C., Sanz, A., Flores, D., Noronha, F., 2008. Characterization of fly ash from a power plant and surroundings by micro-Raman spectroscopy. Int J Coal Geol 73, 359–370. https://doi.org/10.1016/j.coal.2007.09.001

Gürdal, G., 2011. Abundances and modes of occurrence of trace elements in the Çan coals (Miocene), Çanakkale-Turkey. undefined 87, 157–173. https://doi.org/10.1016/J.COAL.2011.06.008

Hansen, L.D., Silberman, David., Fisher, G.L., 1981. Crystalline components of stack-collected, size-fractionated coal fly ash. Environ Sci Technol 15, 1057–1062. https://doi.org/10.1021/es00091a004

Haque, N., Hughes, A., Lim, S., Vernon, C., 2014. Rare Earth Elements: Overview of Mining, Mineralogy, Uses, Sustainability and Environmental Impact. Resources 3, 614–635. https://doi.org/10.3390/resources3040614

Harja, M., Barbuta, M., Rusu, L., Apostolescu, N., 2008. Utilization of coal fly ash from power plants - I. Ash characterization. Environ Eng Manag J 7, 289–293. https://doi.org/10.30638/eemj.2008.037

Henry, J., Towler, M., Stanton, K., Querol, X., Moreno, N., 2004. Characterisation of the glass fraction of a selection of European coal fly ashes. Journal of Chemical Technology & Biotechnology 79, 540–546. https://doi.org/10.1002/jctb.1023

Hood, M.M., Taggart, R.K., Smith, R.C., Hsu-Kim, H., Henke, K.R., Graham, U., Groppo, J.G., Unrine, J.M., Hower, J.C., 2017. Rare Earth Element Distribution in Fly Ash Derived from the Fire Clay Coal, Kentucky. Coal Combustion and Gasification Products 9, 22–33. https://doi.org/10.4177/CCGP-D-17-00002.1

Hower, J.C., 2012. Petrographic examination of coal-combustion fly ash. Int J Coal Geol 92, 90–97. https://doi.org/10.1016/j.coal.2011.12.012

Hower, J.C., Berti, D., Hochella, M.F., Mardon, S.M., 2018. Rare earth minerals in a “no tonstein” section of the Dean (Fire Clay) coal, Knox County, Kentucky. Int J Coal Geol 193, 73–86. https://doi.org/10.1016/j.coal.2018.05.001

Hower, J.C., Dai, S., Seredin, V.V., Zhao, L., Kostova, I.J., Silva, L.F.O., Mardon, S.M., Gurdal, G., 2013. A Note on the Occurrence of Yttrium and Rare Earth Elements in Coal Combustion Products. Coal Combustion and Gasification Products 5, 39–47. https://doi.org/10.4177/CCGP-D-13-00001.1

Hower, J.C., Eble, C.F., Dai, S., Belkin, H.E., 2016. Distribution of rare earth elements in eastern Kentucky coals: Indicators of multiple modes of enrichment? Int J Coal Geol 160–161, 73–81. https://doi.org/10.1016/j.coal.2016.04.009

Hower, J.C., Fu, B., Dai, S., 2020a. Geochemical partitioning from pulverized coal to fly ash and bottom ash. Fuel 279, 118542. https://doi.org/10.1016/j.fuel.2020.118542

Hower, J.C., Groppo, J.G., 2021. Rare Earth-bearing particles in fly ash carbons: Examples from the combustion of eastern Kentucky coals. Energy Geoscience 2, 90–98. https://doi.org/10.1016/j.engeos.2020.09.003

Hower, J.C., Groppo, J.G., Graham, U.M., Ward, C.R., Kostova, I.J., Maroto-Valer, M.M., Dai, S., 2017a. Coal-derived unburned carbons in fly ash: A review. Int J Coal Geol 179, 11–27. https://doi.org/10.1016/j.coal.2017.05.007

Hower, J.C., Groppo, J.G., Henke, K.R., Graham, U.M., Hood, M.M., Joshi, P., Preda, D.V., 2017b. Ponded and Landfilled Fly Ash as a Source of Rare Earth Elements from a Kentucky Power Plant. Coal Combustion and Gasification Products 9, 1–21. https://doi.org/10.4177/CCGP-D-17-00003.1

Hower, J.C., Groppo, J.G., Jewell, R.B., Wiseman, J.D., Duvallet, T.Y., Oberlink, A.E., Hopps, S.D., Morgan, T.D., Henke, K.R., Joshi, P., Preda, D.V., Gamliel, D.P., Beers, T., Schrock, M., 2021. Distribution of rare earth elements in the pilot-scale processing of fly ashes derived from eastern Kentucky coals: Comparisons of the feed and processed ashes. Fuel 295, 120562. https://doi.org/10.1016/j.fuel.2021.120562

Hower, J.C., Groppo, J.G., Joshi, P., Preda, D.V., Gamliel, D.P., Mohler, D.T., Wiseman, J.D., Hopps, S.D., Morgan, T.D., Beers, T., Schrock, M., 2020b. Distribution of Lanthanides, Yttrium, and Scandium in the Pilot-Scale Beneficiation of Fly Ashes Derived from Eastern Kentucky Coals. Minerals 10, 105. https://doi.org/10.3390/min10020105

Hower, J.C., Hood, M.M., Taggart, R.K., Hsu-Kim, H., 2017c. Chemistry and petrology of paired feed coal and combustion ash from anthracite-burning stoker boilers. Fuel 199, 438–446. https://doi.org/10.1016/j.fuel.2017.03.007

Hower, J.C., Qian, D., Briot, N.J., Santillan-Jimenez, E., Hood, M.M., Taggart, R.K., Hsu-Kim, H., 2019. Nano-Scale Rare Earth Distribution in Fly Ash Derived from the Combustion of the Fire Clay Coal, Kentucky. Minerals 2019, Vol. 9, Page 206 9, 206. https://doi.org/10.3390/MIN9040206

Hower, J.C., Rathbone, R.F., Robertson, J.D., Peterson, G., Trimble, A.S., 1999a. Petrology, mineralogy, and chemistry of magnetically-separated sized fly ash. Fuel 78, 197–203. https://doi.org/10.1016/S0016-2361(98)00132-X

Hower, J.C., Ruppert, L.F., Eble, C.F., 1999b. Lanthanide, yttrium, and zirconium anomalies in the Fire Clay coal bed, Eastern Kentucky. Int J Coal Geol 39, 141–153. https://doi.org/10.1016/S0166-5162(98)00043-3

Hower, J.C., Senior, C.L., Suuberg, E.M., Hurt, R.H., Wilcox, J.L., Olson, E.S., 2010. Mercury capture by native fly ash carbons in coal-fired power plants. Prog Energy Combust Sci 36, 510–529. https://doi.org/10.1016/j.pecs.2009.12.003

Hower, J.C., Suárez-Ruiz, I., Mastalerz, M., 2005. An Approach Toward a Combined Scheme for the Petrographic Classification of Fly Ash: Revision and Clarification. Energy & Fuels 19, 653–655. https://doi.org/10.1021/ef0498061

Hower, J.C., Thomas, G.A., Palmer, J., 1999c. Impact of the conversion to low-NOx combustion on ash characteristics in a utility boiler burning Western US coal. Fuel Processing Technology 61, 175–195. https://doi.org/10.1016/S0378-3820(99)00054-5

Hrnčířová, M., Pospíšil, J., Michalšpiláček, M.M., 2013. Size analysis of solid particles using laser diffraction and sieve analysis. Engineering MECHANICS 20, 309–318.

Huang, Z., Fan, M., Tiand, H., 2018. Coal and coal byproducts: A large and developable unconventional resource for critical materials – Rare earth elements. Journal of Rare Earths 36, 337–338. https://doi.org/10.1016/j.jre.2018.01.002

Hulett, L.D., Weinberger, A.J., 1980. Some etching studies of the microstructure and composition of large aluminosilicate particles in fly ash from coal-burning power plants. Environ Sci Technol 14, 965–970. https://doi.org/10.1021/es60168a013

Hulett, L.D., Weinberger, A.J., Northcutt, K.J., Ferguson, M., 1980. Chemical Species in Fly Ash from Coal-Burning Power Plants. Science (1979) 210, 1356–1358. https://doi.org/10.1126/science.210.4476.1356

Hurt, R.H., Davis, K.A., Yang, N.Y.C., Headley, T.J., Mitchell, G.D., 1995. Residual carbon from pulverized-coal-fired boilers. 2. Morphology and physicochemical properties. Fuel 74, 1297–1306. https://doi.org/10.1016/0016-2361(95)00100-J

Hurt, R.H., Gibbins, J.R., 1995. Residual carbon from pulverized coal fired boilers: 1. Size distribution and combustion reactivity. Fuel 74, 471–480. https://doi.org/10.1016/0016-2361(95)98348-I

Hwang, J.Y., Sun, X., Li, Z., 2002. Unburned Carbon from Fly Ash for Mercury Adsorption: I. Separation and Characterization of Unburned Carbon. Journal of Minerals and Materials Characterization and Engineering 01, 39–60. https://doi.org/10.4236/jmmce.2002.11004

ICCP, 2001. The new inertinite classification (ICCP System 1994). Fuel 80, 459–471. https://doi.org/10.1016/S0016-2361(00)00102-2

ICCP, 1998. The new vitrinite classification (ICCP System 1994). Fuel 77, 349–358. https://doi.org/10.1016/S0016-2361(98)80024-0

Inagaki, M., 2001. Applications of Polycrystalline Graphite, in: Delhaès, P. (Ed.), Graphite and Precursors. Gordon and Breach, Amsterdam, pp. 179–198.

International Energy Agency (IEA), 2020. Coal 2020. Paris, France.

ISO, 2013a. 11722. Solid mineral fuels — Hard coal — Determination of moisture in the general analysis test sample by drying in nitrogen, International Organization for Standardization. International Organization for Standardization, Geneva, Switzerland.

ISO, 2013b. 1170. Coal and coke — Calculation of analyses to different bases, International Organization for Standardization. International Organization for Standardization, Geneva, Switzerland.

ISO, 2010a. 1171. Solid mineral fuels — Determination of ash, International Organization for Standardization. International Organization for Standardization, Geneva, Switzerland.

ISO, 2010b. 562. Hard coal and coke — Determination of volatile matter, International Organization for Standardization. International Organization for Standardization, Geneva, Switzerland.

ISO, 2005. 17246. Coal — Proximate analysis, International Organization for Standardization. International Organization for Standardization, Geneva, Switzerland.

ISO 7404-2, 2009. Methods for the petrographic analysis of coals — Part 2: Methods of preparing coal samples. International Organization for Standardization 12.

ISO 7404-3, 2009. Methods for the petrographic analysis of coals — Part 3: Method of determining maceral group composition. International Organization for Standardization 7.

ISO 7404-5, 2009. Methods for the petrographic analysis of coals — Part 5: Method of determining microscopically the reflectance of vitrinite.

ISO 11760, 2005. Classification of coals. International Organization for Standardization 9.

ISO/IEC 17025, 2017. General requirements for the competence of testing and calibration laboratories 30.

Izquierdo, M., Querol, X., 2012. Leaching behaviour of elements from coal combustion fly ash: An overview. Int J Coal Geol 94, 54–66. https://doi.org/10.1016/j.coal.2011.10.006

Jara, A.D., Betemariam, A., Woldetinsae, G., Kim, J.Y., 2019. Purification, application and current market trend of natural graphite: A review. Int J Min Sci Technol 29, 671–689. https://doi.org/10.1016/j.ijmst.2019.04.003

Jaszczak, J.A., Dimovski, S., Hackney, S.A., Robinson, G.W., Bosio, P., Gogotsi, Y., 2007. Micro- and nanoscale graphite cones and tubes from hackman valley, Kola Peninsula, Russia. The Canadian Mineralogist 45, 379–389. https://doi.org/10.2113/gscanmin.45.2.379

Jaszczak, J.A., Robinson, G.W., Dimovski, S., Gogotsi, Y., 2003. Naturally occurring graphite cones. Carbon N Y 41, 2085–2092. https://doi.org/10.1016/S0008-6223(03)00214-8

Jayasuriya, K.D., O'Neill, H.St.C., Berry, A.J., Campbell, S.J., 2004. A Mössbauer study of the oxidation state of Fe in silicate melts. American Mineralogist 89, 1597–1609. https://doi.org/10.2138/am-2004-11-1203

Jehlicka, J., Rouzaud, J.-N., 1990. Organic geochemistry of precambrian shales and schists (Bohemian massif, Central Europe). Org Geochem 16, 865–872. https://doi.org/10.1016/0146-6380(90)90123-H

Jiao, Y., Zheng, Y., Jaroniec, M., Qiao, S.Z., 2015. Design of electrocatalysts for oxygen- and hydrogen-involving energy conversion reactions. Chem Soc Rev 44, 2060–2086. https://doi.org/10.1039/C4CS00470A

Jillavenkatesa, A., Dapkunas, S.J., Lum, L.-S.H., 2001. NIST Recommended Practice Guide: Particle Size Characterization, Special Publication (NIST SP). National Institute of Standards and Technology, Gaithersburg, MD. https://doi.org/10.6028/NBS.SP.960-1

Jones, R.B., McCourt, C.B., Morley, C., King, K., 1985. Maceral and rank influences on the morphology of coal char. Fuel 64, 1460–1467. https://doi.org/10.1016/0016-2361(85)90351-5

Kapička, A., Jordanova, N., Petrovský, E., Ustjak, S., 2001. Effect of different soil conditions on magnetic parameters of power-plant fly ashes. J Appl Geophy 48, 93–102. https://doi.org/10.1016/S0926-9851(01)00082-9

Ketris, M.P., Yudovich, Y.. E., 2009. Estimations of Clarkes for Carbonaceous biolithes: World averages for trace element contents in black shales and coals. Int J Coal Geol 78, 135–148. https://doi.org/10.1016/j.coal.2009.01.002

Kilby, W.E., 1991. Vitrinite reflectance measurement — Some technique enhancements and relationships. Int J Coal Geol 19, 201–218. https://doi.org/10.1016/0166-5162(91)90021-A

Kilby, W.E., 1988. Recognition of vitrinite with non-uniaxial negative reflectance characteristics. Int J Coal Geol 9, 267–285. https://doi.org/10.1016/0166-5162(88)90017-1

Kirik, N.P., Anshits, N.N., Rabchevskii, E.V., Solov'ev, L.A., Anshits, A.G., 2019. Effect of HF Modification on the Catalytic Properties of Ferrospheres in the Oxidative Coupling of Methane. Kinetics and Catalysis 60, 196–204. https://doi.org/10.1134/S0023158419020034

Kızgut, S., Bilen, M., Toroğlu, İ., Barış, K., 2016. Size-Related Evaluation of Unburned Carbon. Combustion Science and Technology 188, 439–450. https://doi.org/10.1080/00102202.2015.1125345

Klyucharev, D.S., Volkova, N.M., Comyn, M.F., 2013. The problems associated with using non-conventional rare-earth minerals. J Geochem Explor 133, 138–148. https://doi.org/10.1016/j.gexplo.2013.03.006

Kolker, A., Scott, C., Hower, J.C., Vazquez, J.A., Lopano, C.L., Dai, S., 2017. Distribution of rare earth elements in coal combustion fly ash, determined by SHRIMP-RG ion microprobe. Int J Coal Geol 184, 1–10. https://doi.org/10.1016/j.coal.2017.10.002

Kossenberg, M., Cook, A.C., 1961. Weathering of sulphide minerals in coal: production of ferrous sulphate heptahydrate. Mineralogical Magazine and Journal of the Mineralogical Society 32, 829–830. https://doi.org/10.1180/minmag.1961.032.253.11

Kouketsu, Y., Mizukami, T., Mori, H., Endo, S., Aoya, M., Hara, H., Nakamura, D., Wallis, S., 2014. A new approach to develop the Raman carbonaceous material geothermometer for low-grade metamorphism using peak width. Island Arc 23, 33–50. https://doi.org/10.1111/iar.12057

Kruiver, P.P., Dekkers, M.J., Heslop, D., 2001. Quantification of magnetic coercivity components by the analysis of acquisition curves of isothermal remanent magnetisation. Earth Planet Sci Lett 189, 269–276. https://doi.org/10.1016/S0012-821X(01)00367-3

Kukier, U., Ishak, C.F., Sumner, M.E., Miller, W.P., 2003. Composition and element solubility of magnetic and non-magnetic fly ash fractions. Environmental Pollution 123, 255–266. https://doi.org/10.1016/S0269-7491(02)00376-7

Külaots, I., Hurt, R.H., Suuberg, E.M., 2004. Size distribution of unburned carbon in coal fly ash and its implications. Fuel 83, 223–230. https://doi.org/10.1016/S0016-2361(03)00255-2

Kutchko, B., Kim, A., 2006. Fly ash characterization by SEM–EDS. Fuel 85, 2537–2544. https://doi.org/10.1016/j.fuel.2006.05.016

Kuźniarska-Biernacka, I., Santos, A.C., Guedes, A., Jarrais, B., Peixoto, A.F., Valentim, B., Freire, C., 2021. Application of coal fly ash in wastewater treatment , in: XXVII National Meeting of the Portuguese Chemical Society. Braga, Portugal, p. 152.

Kuźniarska-Biernacka, I., Santos, A.C., Jarrais, B., Valentim, B., Guedes, A., Freire, C., Peixoto, A.F., 2022. Application of Fe-rich coal fly ashes to enhanced reduction of 4-nitrophenol. Cleaner Chemical Engineering 2, 100019. https://doi.org/10.1016/j.clce.2022.100019

Kvasnitsa, V.N., Yatsenko, V.G., Jaszczak, J.A., 1999. Disclinations in unusual graphite crystals from anorthosites of Ukraine. The Canadian Mineralogist 37, 951–960.

Kwiecińska, B., Petersen, H.I., 2004. Graphite, semi-graphite, natural coke, and natural char classification—ICCP system. Int J Coal Geol 57, 99–116. https://doi.org/10.1016/j.coal.2003.09.003

Laggoun-Défarge, F., Lallier-Vergès, E., Suárez-Ruiz, I., Cohaut, N., Bautista, A.J., Landais, P., Prado, J.G., 1994. Evolution of Vitrinite Ultrafine Structures During Artificial Thermal Maturation. pp. 194–205. https://doi.org/10.1021/bk-1994-0570.ch012

Lahfid, A., Beyssac, O., Deville, E., Negro, F., Chopin, C., Goffé, B., 2010. Evolution of the Raman spectrum of carbonaceous material in low-grade metasediments of the Glarus Alps (Switzerland). Terra Nova 22, 354–360. https://doi.org/10.1111/j.1365-3121.2010.00956.x

Lanzerstorfer, C., 2018a. Fly ash from coal combustion: Dependence of the concentration of various elements on the particle size. Fuel 228, 263–271. https://doi.org/10.1016/j.fuel.2018.04.136

Lanzerstorfer, C., 2018b. Pre-processing of coal combustion fly ash by classification for enrichment of rare earth elements. Energy Reports 4, 660–663. https://doi.org/10.1016/j.egyr.2018.10.010

Laskowski, J.S., 2001. Coal Flotation and Fine Coal Utilization, 1st ed. Elsevier Science, Netherlands.

Lauf, R.J., 1982. Microstructures of coal fly ash particles. American Ceramic Society Bulletin 61:4.

Lauf, R.J., Harris, L.A., Rawlston, S.S., 1982. Pyrite framboids as the source of magnetite spheres in fly ash. Environ Sci Technol 16, 218–220. https://doi.org/10.1021/es00098a009

Lespade, P., Marchand, A., Couzi, M., Cruege, F., 1984. Caracterisation de materiaux carbones par microspectrometrie Raman. Carbon N Y 22, 375–385. https://doi.org/10.1016/0008-6223(84)90009-5

Lester, E., Alvarez, D., Borrego, A.G., Valentim, B., Flores, D., Clift, D.A., Rosenberg, P., Kwiecinska, B., Barranco, R., Petersen, H.I., Mastalerz, M., Milenkova, K.S., Panaitescu, C., Marques, M.M., Thompson, A., Watts, D., Hanson, S., Predeanu, G., Misz, M., Wu, T., 2010. The procedure used to develop a coal char classification—Commission III Combustion Working Group of the International Committee for Coal and Organic Petrology. Int J Coal Geol 81, 333–342. https://doi.org/10.1016/j.coal.2009.10.015

Li, C.-Z., 2007. Some recent advances in the understanding of the pyrolysis and gasification behaviour of Victorian brown coal. Fuel 86, 1664–1683. https://doi.org/10.1016/j.fuel.2007.01.008

Li, J., Chen, Z., Yuan, L., Qiao, Y., Yuan, Z., Zeng, L., Li, Z., 2021. Effects of flotation and acid treatment on unburned carbon recovery from atmospheric circulating fluidized bed coal gasification fine ash and application evaluation of residual carbon. Waste Management 136, 283–294. https://doi.org/10.1016/j.wasman.2021.10.024

Li, X., Hayashi, J., Li, C., 2006. FT-Raman spectroscopic study of the evolution of char structure during the pyrolysis of a Victorian brown coal. Fuel 85, 1700–1707. https://doi.org/10.1016/j.fuel.2006.03.008

Li, Z., Ward, C.R., Gurba, L.W., 2010. Occurrence of non-mineral inorganic elements in macerals of low-rank coals. Int J Coal Geol 81, 242–250. https://doi.org/10.1016/j.coal.2009.02.004

Li, Z., Ward, C.R., Gurba, L.W., 2007. Occurrence of non-mineral inorganic elements in low-rank coal macerals as shown by electron microprobe element mapping techniques. Int J Coal Geol 70, 137–149. https://doi.org/10.1016/j.coal.2006.04.009

Lin, R., Howard, B.H., Roth, E.A., Bank, T.L., Granite, E.J., Soong, Y., 2017. Enrichment of rare earth elements from coal and coal by-products by physical separations. Fuel 200, 506–520. https://doi.org/10.1016/j.fuel.2017.03.096

Lin, R., Stuckman, M., Howard, B.H., Bank, T.L., Roth, E.A., Macala, M.K., Lopano, C., Soong, Y., Granite, E.J., 2018. Application of sequential extraction and hydrothermal treatment for characterization and enrichment of rare earth elements from coal fly ash. Fuel 232, 124–133. https://doi.org/10.1016/j.fuel.2018.05.141

Liu, J., Dai, S., He, X., Hower, J., Sakulpitakphon, T., 2017. Size-Dependent Variations in Fly Ash Trace Element Chemistry: Examples from a Kentucky Power Plant and with Emphasis on Rare Earth Elements. Energy & Fuels 31, 438–447. https://doi.org/10.1021/acs.energyfuels.6b02644

Liu, J., Song, H., Dai, S., Nechaev, V., Graham, I., French, D., Nechaeva, E., 2019. Mineralization of REE-Y-Nb-Ta-Zr-Hf in Wuchiapingian coals from the Liupanshui Coalfield, Guizhou, southwestern China: Geochemical evidence for terrigenous input. Ore Geol Rev 115, 103190. https://doi.org/10.1016/j.oregeorev.2019.103190

Liu, P., Huang, R., Tang, Y., 2019. Comprehensive Understandings of Rare Earth Element (REE) Speciation in Coal Fly Ashes and Implication for REE Extractability. Environ Sci Technol 53, 5369–5377. https://doi.org/10.1021/acs.est.9b00005

Long, G.J., Cranshaw, T.E., Longworth, G., 1983. The ideal Mössbauer effect absorber thickness. Mössbauer effect reference and data journal 43–49.

Lopez, L.B.M., Pasteris, J.D., Biswas, P., 2009. Sensitivity of Micro-Raman Spectrum to Crystallite Size of Electrospray-Deposited and Post-Annealed Films of Iron-Oxide Nanoparticle Suspensions. Appl Spectrosc 63, 627–635. https://doi.org/10.1366/000370209788559539

Lu, L., 2002. Char structural ordering during pyrolysis and combustion and its influence on char reactivity. Fuel 81, 1215–1225. https://doi.org/10.1016/S0016-2361(02)00035-2

Lu, L., Sahajwalla, V., Kong, C., Harris, D., 2001. Quantitative X-ray diffraction analysis and its application to various coals. Carbon N Y 39, 1821–1833. https://doi.org/10.1016/S0008-6223(00)00318-3

Lu, S.G., Chen, Y.Y., Shan, H.D., Bai, S.Q., 2009. Mineralogy and heavy metal leachability of magnetic fractions separated from some Chinese coal fly ashes. J Hazard Mater 169, 246–255. https://doi.org/10.1016/j.jhazmat.2009.03.078

Lu, Y., Rostam-Abadi, M., Chang, R., Richardson, C., Paradis, J., 2007. Characteristics of Fly Ashes from Full-Scale Coal-Fired Power Plants and Their Relationship to Mercury Adsorption. Energy & Fuels 21, 2112–2120. https://doi.org/10.1021/ef070145s

Ma, Z., Shan, X., Cheng, F., 2019. Distribution Characteristics of Valuable Elements, Al, Li, and Ga, and Rare Earth Elements in Feed Coal, Fly Ash, and Bottom Ash from a 300 MW Circulating Fluidized Bed Boiler. ACS Omega 4, 6854–6863. https://doi.org/10.1021/acsomega.9b00280

Maher, B.A., Thompson, R., 1999. Quaternary climates, environments, and magnetism. Cambridge University Press.

Mandlimath, T.R., Gopal, B., 2011. Catalytic activity of first row transition metal oxides in the conversion of p-nitrophenol to p-aminophenol. J Mol Catal A Chem 350, 9–15. https://doi.org/10.1016/j.molcata.2011.08.009

Mardon, S.M., Hower, J.C., 2004. Impact of coal properties on coal combustion by-product quality: examples from a Kentucky power plant. Int J Coal Geol 59, 153–169. https://doi.org/10.1016/j.coal.2004.01.004

Maroto-Valer, M.M., Taulbee, D.N., Hower, J.C., 1999. Novel Separation of the Differing Forms of Unburned Carbon Present in Fly Ash Using Density Gradient Centrifugation. Energy & Fuels 13, 947–953. https://doi.org/10.1021/ef990029s

Marques, M., Suárez-Ruiz, I., Flores, D., Guedes, A., Rodrigues, S., 2009. Correlation between optical, chemical and micro-structural parameters of high-rank coals and graphite. Int J Coal Geol 77, 377–382. https://doi.org/10.1016/j.coal.2008.06.002

Matjie, R.H., French, D., Ward, C.R., Pistorius, P.C., Li, Z., 2011. Behaviour of coal mineral matter in sintering and slagging of ash during the gasification process. Fuel Processing Technology 92, 1426–1433. https://doi.org/10.1016/j.fuproc.2011.03.002

Matjie, R.H., van Alphen, C., Pistorius, P.C., 2006. Mineralogical characterisation of Secunda gasifier feedstock and coarse ash. Miner Eng 19, 256–261. https://doi.org/10.1016/j.mineng.2005.06.010

Maxbauer, D.P., Feinberg, J.M., Fox, D.L., 2016. MAX UnMix: A web application for unmixing magnetic coercivity distributions. Comput Geosci 95, 140–145. https://doi.org/10.1016/j.cageo.2016.07.009

McLennan, A.R., Bryant, G.W., Stanmore, B.R., Wall, T.F., 2000. Ash Formation Mechanisms during pf Combustion in Reducing Conditions. Energy & Fuels 14, 150–159. https://doi.org/10.1021/ef990095u

Meij, R., 1995. The Distribution of Trace Elements During the Combustion of Coal, in: Swaine D.J., G.F. (Ed.), Environmental Aspects of Trace Elements in Coal. Energy & Environment. Springer, Dordrecht, pp. 111–127. https://doi.org/https://doi.org/10.1007/978-94-015-8496-8_7

Melvin, G.J.H., Wang, Z., Morimoto, S., Fujishige, M., Takeuchi, K., Hashimoto, Y., Endo, M., 2019. Graphite Whiskers Derived from Waste Coffee Grounds Treated at High Temperature. Global Challenges 3, 1800107. https://doi.org/10.1002/gch2.201800107

Mendes, J., Santos, A.C., Valentim, B., Kuźniarska-Biernacka, I., Peixoto, A.F., Freire, C., 2022. Recycling industrial Coal Fly Ashes for catalytic reduction of nitroarenes, in: 13th Inorganic & Bioinorganic Chemistry, 13IBCC. Aveiro, Portugal.

Menéndez, R., Vleeskens, J.M., Marsh, H., 1993. The use of scanning electron microscopy for classification of coal chars during combustion. Fuel 72, 611–617. https://doi.org/10.1016/0016-2361(93)90572-J

Merkus, H.G., 2009. Particle Size, Size Distributions and Shape, in: Particle Size Measurements. Particle Technology Series. Springer Dordrecht, pp. 13–42. https://doi.org/10.1007/978-1-4020-9016-5_2

Mernagh, T.P., Cooney, R.P., Johnson, R.A., 1984. Raman spectra of Graphon carbon black. Carbon N Y 22, 39–42. https://doi.org/10.1016/0008-6223(84)90130-1

Miller, S.F., Schobert, H.H., 1994. Effect of the Occurrence and Composition of Silicate and Aluminosilicate Compounds on Ash Formation in Pilot-Scale Combustion of Pulverized Coal and Coal-Water Slurry Fuels. Energy & Fuels 8, 1197–1207. https://doi.org/10.1021/ef00048a006

Miller, S.F., Schobert, H.H., 1993. Effect of fuel particle and droplet size distribution on particle size distribution of char and ash during pilot-scale combustion of pulverized coal and coal-water slurry fuels. Energy & Fuels 7, 520–531. https://doi.org/10.1021/ef00040a013

Ministério da Agricultura, do M. do A. e do O. do T., 2013. Decreto-Lei n.º 127/2013 .

Minitti, M.E., Lane, M.D., Bishop, J.L., 2005. A new hematite formation mechanism for Mars. Meteorit Planet Sci 40, 55–69. https://doi.org/10.1111/j.1945-5100.2005.tb00364.x

Montross, S.N., Verba, C.A., Chan, H.L., Lopano, C., 2018. Advanced characterization of rare earth element minerals in coal utilization byproducts using multimodal image analysis. Int J Coal Geol 195, 362–372. https://doi.org/10.1016/j.coal.2018.06.018

Murad, E., 1998. Clays and clay minerals: What can Mössbauer spectroscopy do to help understand them? Hyperfine Interact 117, 39–70. https://doi.org/10.1023/A:1012635124874

Mushtaq, F., Zahid, M., Bhatti, I.A., Nasir, S., Hussain, T., 2019. Possible applications of coal fly ash in wastewater treatment. J Environ Manage 240, 27–46. https://doi.org/10.1016/j.jenvman.2019.03.054

Mutlu, B.K., Cantoni, B., Turolla, A., Antonelli, M., Hsu-Kim, H., Wiesner, M.R., 2018. Application of nanofiltration for Rare Earth Elements recovery from coal fly ash leachate: Performance and cost evaluation. Chemical Engineering Journal 349, 309–317. https://doi.org/10.1016/j.cej.2018.05.080

Nakagomi, F., da Silva, S.W., Garg, V.K., Oliveira, A.C., Morais, P.C., Franco, A., 2009. Influence of the Mg-content on the cation distribution in cubic Mg Fe3O4 nanoparticles. J Solid State Chem 182, 2423–2429. https://doi.org/10.1016/j.jssc.2009.06.036

Nemanashi, M., Meijboom, R., 2013. Synthesis and characterization of Cu, Ag and Au dendrimer-encapsulated nanoparticles and their application in the reduction of 4-nitrophenol to 4-aminophenol. J Colloid Interface Sci 389, 260–267. https://doi.org/10.1016/j.jcis.2012.09.012

Nemanich, R.J., Solin, S.A., 1979. First- and second-order Raman scattering from finite-size crystals of graphite. Phys Rev B 20, 392–401. https://doi.org/10.1103/PhysRevB.20.392

Nugroho, N.D., Rosita, W., Perdana, I., Bendiyasa, I.M., Mufakhir, F.R., Astuti, W., 2019. Iron bearing oxide minerals separation from rare earth elements (REE) rich coal fly ash. IOP Conf Ser Mater Sci Eng 478, 012026. https://doi.org/10.1088/1757-899X/478/1/012026

Nunes, M.S., Pereira, C., Guedes, A., Santos, A.C., Valentim, B., Freire, C., 2022. Assessment of coal fly ash char as a substituting material of graphite with electrocatalytic activity for the oxygen reduction reaction. Sustain Chem Pharm 27, 100705. https://doi.org/10.1016/j.scp.2022.100705

Oberlin, A., 1984. Carbonization and graphitization. Carbon N Y 22, 521–541. https://doi.org/10.1016/0008-6223(84)90086-1

Oberlin, A., Rouchy, J.P., 1971. Transformation des carbones non graphitables par traitement thermique en presence de fer. Carbon N Y 9, 39–46. https://doi.org/10.1016/0008-6223(71)90142-4

Oberlin, A., Terriere, G., 1975. Graphitization studies of anthracites by high resolution electron microscopy. Carbon N Y 13, 367–376. https://doi.org/10.1016/0008-6223(75)90004-4

Oliveira, M.L.S., Ward, C.R., French, D., Hower, J.C., Querol, X., Silva, L.F.O., 2012. Mineralogy and leaching characteristics of beneficiated coal products from Santa Catarina, Brazil. Int J Coal Geol 94, 314–325. https://doi.org/10.1016/j.coal.2011.10.004

Orberger, B., Wagner, C., Tudryn, A., Wirth, R., Morgan, R., Fabris, J.D., Greneche, J.M., Rosière, C., 2014. Micro- to nano-scale characterization of martite from a banded iron formation in India and a lateritic soil in Brazil. Phys Chem Miner 41, 651–667. https://doi.org/10.1007/s00269-014-0679-8

Owens, F.J., Orosz, J., 2006. Effect of nanosizing on lattice and magnon modes of hematite. Solid State Commun 138, 95–98. https://doi.org/10.1016/j.ssc.2006.01.049

Ōya, A., Ōtani, S., 1979. Catalytic graphitization of carbons by various metals. Carbon N Y 17, 131–137. https://doi.org/10.1016/0008-6223(79)90020-4

Pan, J., Zhou, C., Tang, M., Cao, S., Liu, C., Zhang, N., Wen, M., Luo, Y., Hu, T., Ji, W., 2019. Study on the modes of occurrence of rare earth elements in coal fly ash by statistics and a sequential chemical extraction procedure. Fuel 237, 555–565. https://doi.org/10.1016/j.fuel.2018.09.139

Pappano, P.J., Schobert, H.H., 2009. Effect of Natural Mineral Inclusions on the Graphitizability of a Pennsylvania Anthracite. Energy & Fuels 23, 422–428. https://doi.org/10.1021/ef800515r

Park, J., Bae, S., 2019. Highly efficient and magnetically recyclable Pd catalyst supported by iron-rich fly ash@fly ash-derived SiO2 for reduction of p-nitrophenol. J Hazard Mater 371, 72–82. https://doi.org/10.1016/j.jhazmat.2019.02.105

Park, J., Bae, S., 2018. Formation of Fe nanoparticles on water-washed coal fly ash for enhanced reduction of p-nitrophenol. Chemosphere 202, 733–741. https://doi.org/10.1016/j.chemosphere.2018.03.152

Park, J., Dattatraya Saratale, G., Cho, S.-K., Bae, S., 2020. Synergistic effect of Cu loading on Fe sites of fly ash for enhanced catalytic reduction of nitrophenol. Science of The Total Environment 705, 134544. https://doi.org/10.1016/j.scitotenv.2019.134544

Pasteris, J.D., Wopenka, B., 1991. Raman spectra of graphite as indicators of degree of metamorphism. The Canadian Mineralogist 29, 1–9.

Permana, A.K., Ward, C.R., Li, Z., Gurba, L.W., 2013. Distribution and origin of minerals in high-rank coals of the South Walker Creek area, Bowen Basin, Australia. Int J Coal Geol 116–117, 185–207. https://doi.org/10.1016/j.coal.2013.03.001

Pickel, W., Kus, J., Flores, D., Kalaitzidis, S., Christanis, K., Cardott, B.J., Misz-Kennan, M., Rodrigues, S., Hentschel, A., Hamor-Vido, M., Crosdale, P., Wagner, N., 2017. Classification of liptinite – ICCP System 1994. Int J Coal Geol 169, 40–61. https://doi.org/10.1016/j.coal.2016.11.004

Pierson, H.O., 1994. Handbook of Carbon, Graphite, Diamonds and Fullerenes. Noyes Publications, Park Ridge, New Jersey, U.S.A.

Pusz, S., Duber, S., Kwiecińska, B.K., 2002. The study of textural and structural transformations of carbonized anthracites. Fuel Processing Technology 77–78, 173–180. https://doi.org/10.1016/S0378-3820(02)00068-1

Pusz, S., Kwiecińska, B.K., Duber, S., 2003. Textural transformation of thermally treated anthracites. Int J Coal Geol 54, 115–123. https://doi.org/10.1016/S0166-5162(03)00024-7

Querol, X., Fernández-Turiel, J., López-Soler, A., 1995. Trace elements in coal and their behaviour during combustion in a large power station. Fuel 74, 331–343. https://doi.org/10.1016/0016-2361(95)93464-O

Raask, E., 1985. Mineral impurities in coal combustion: behavior, problems, and remedial measures. Hemisphere Pub.

Ramsden, A.R., Shibaoka, M., 1982. Characterization and analysis of individual fly-ash particles from coal-fired power stations by a combination of optical microscopy, electron microscopy and quantitative electron microprobe analysis. Atmospheric Environment (1967) 16, 2191–2206. https://doi.org/10.1016/0004-6981(82)90290-6

Rao, C.P., Gluskoter, H.J., 1973. Occurrence and distribution of minerals in Illinois coals. Circular no. 476.

Ratafia-Brown, J.A., 1994. Overview of trace element partitioning in flames and furnaces of utility coal-fired boilers. Fuel Processing Technology 39, 139–157. https://doi.org/10.1016/0378-3820(94)90177-5

Robertson, D.J., France, D.E., 1994. Discrimination of remanence-carrying minerals in mixtures, using isothermal remanent magnetisation acquisition curves. Physics of the Earth and Planetary Interiors 82, 223–234. https://doi.org/10.1016/0031-9201(94)90074-4

Rodrigues, S., Suárez-Ruiz, I., Marques, M., Camean, I., Flores, D., 2011a. Microstructural evolution of high temperature treated anthracites of different rank. Int J Coal Geol 87, 204–211. https://doi.org/10.1016/j.coal.2011.06.009

Rodrigues, S., Suárez-Ruiz, I., Marques, M., Flores, D., 2012. Catalytic role of mineral matter in structural transformation of anthracites during high temperature treatment. Int J Coal Geol 93, 49–55. https://doi.org/10.1016/j.coal.2012.01.012

Rodrigues, S., Suárez-Ruiz, I., Marques, M., Flores, D., Camean, I., García, A.B., 2011b. Development of graphite-like particles from the high temperature treatment of carbonized anthracites. Int J Coal Geol 85, 219–226. https://doi.org/10.1016/j.coal.2010.11.007

Rollinson, H.R., 2014. Using Geochemical Data : Evaluation, Presentation, Interpretation. Using Geochemical Data. https://doi.org/10.4324/9781315845548

Rosato, A.D., Blackmore, D.L. (Eds.), 2000. IUTAM Symposium on Segregation in Granular Flows. Springer Netherlands, Dordrecht. https://doi.org/10.1007/978-94-015-9498-1

Rosita, W., Bendiyasa, I.M., Perdana, I., Anggara, F., 2020. Sequential particle-size and magnetic separation for enrichment of rare-earth elements and yttrium in Indonesia coal fly ash. J Environ Chem Eng 8, 103575. https://doi.org/10.1016/j.jece.2019.103575

Rouzaud, J.N., Duval, B., Leroy, J., 1991. Reactive surface area: an old but new concept in reactivity, in: Lahaye, J., Ehrburger, P. (Eds.), Fundamental Issues in Control of Carbon Gasification Reactivity. Kluwer Academic Publishers, Dordrecht, The Netherlands, pp. 257–268.

Rouzaud, J.N., Oberlin, A., 1989. Structure, microtexture, and optical properties of anthracene and saccharose-based carbons. Carbon N Y 27, 517–529. https://doi.org/10.1016/0008-6223(89)90002-X

Rubio, B., Izquierdo, M.T., Mayoral, M.C., Bona, M.T., Martínez-Tarazona, R.M., 2008. Preparation and characterization of carbon-enriched coal fly ash. J Environ Manage 88, 1562–1570. https://doi.org/10.1016/j.jenvman.2007.07.027

Rudnick, R.L., Gao, S., 2014. Composition of the Continental Crust, in: Holland, H.D., Turekian, K.K. (Eds.), Treatise on Geochemistry. Elsevier, pp. 1–51. https://doi.org/10.1016/B978-0-08-095975-7.00301-6

Sadezky, A., Muckenhuber, H., Grothe, H., Niessner, R., Pöschl, U., 2005. Raman microspectroscopy of soot and related carbonaceous materials: Spectral analysis and structural information. Carbon N Y 43, 1731–1742. https://doi.org/10.1016/j.carbon.2005.02.018

Salver-Disma, F., Tarascon, J.-M., Clinard, C., Rouzaud, J.-N., 1999. Transmission electron microscopy studies on carbon materials prepared by mechanical milling. Carbon N Y 37, 1941–1959. https://doi.org/10.1016/S0008-6223(99)00059-7

Samson, I.M., Chassé, M., 2018. Scandium 1323–1326. https://doi.org/10.1007/978-3-319-39312-4_281

Santos, A.C., Guedes, A., French, D., Futuro, A., Valentim, B., 2022. Integrative Study Assessing Space and Time Variations with Emphasis on Rare Earth Element (REE) Distribution and Their Potential on Ashes from Commercial (Colombian) Coal. Minerals 12, 194. https://doi.org/10.3390/min12020194

Santos, A.C., Kuźniarska-Biernacka, I., Freire, C., Guedes, A., Jarrais, B., Peixoto, A.F., Valentim, B., 2021a. Characterization of coal fly ash applied in wastewater treatment, in: XXVII National Meeting of the Portuguese Chemical Society. Braga, Portugal., p. 286.

Santos, A.C., Kuźniarska-Biernacka, I., Guedes, A., Peixoto, A., Valentim, B., 2021b. Magnetic fraction from coal combustion ashes as catalyst in the 4-nitrophenol (4-NPh) reduction reaction , in: Institute of Earth Sciences (ICT) Journeys . pp. 22–23.

Schito, A., Romano, C., Corrado, S., Grigo, D., Poe, B., 2017. Diagenetic thermal evolution of organic matter by Raman spectroscopy. Org Geochem 106, 57–67. https://doi.org/10.1016/j.orggeochem.2016.12.006

Schobert, H.H., Song, C., 2002. Chemicals and materials from coal in the 21st century. Fuel 81, 15–32. https://doi.org/10.1016/S0016-2361(00)00203-9

Schulz, K.J., DeYoung, J.H., Seal, R.R., Bradley, D.C., 2017. Critical mineral resources of the United States: economic and environmental geology and prospects for future supply. Geological Survey.

Schulze, D., 2007. Powders and Bulk Solids. Springer Berlin Heidelberg, Berlin, Heidelberg. https://doi.org/10.1007/978-3-540-73768-1

Senneca, O., 2008. Burning and physico-chemical characteristics of carbon in ash from a coal fired power plant. Fuel 87, 1207–1216. https://doi.org/10.1016/j.fuel.2007.07.033

Seredin, V.V., 2010. A new method for primary evaluation of the outlook for rare earth element ores. Geology of Ore Deposits 52, 428–433. https://doi.org/10.1134/S1075701510050077

Seredin, V.V., 1996. Rare earth element-bearing coals from the Russian Far East deposits. Int J Coal Geol 30, 101–129. https://doi.org/10.1016/0166-5162(95)00039-9

Seredin, V.V., Dai, S., 2012. Coal deposits as potential alternative sources for lanthanides and yttrium. Int J Coal Geol 94, 67–93. https://doi.org/10.1016/j.coal.2011.11.001

Severin, K.P., 2004. Energy Dispersive Spectrometry of Common Rock Forming Minerals. Kluwer Academic Publishers, Dordrecht, The Netherlands.

Sharonova, O.M., Anshits, N.N., Fedorchak, M.A., Zhizhaev, A.M., Anshits, A.G., 2015a. Characterization of Ferrospheres Recovered from High-Calcium Fly Ash. Energy & Fuels 29, 5404–5414. https://doi.org/10.1021/acs.energyfuels.5b01618

Sharonova, O.M., Anshits, N.N., Solovyov, L.A., Salanov, A.N., Anshits, A.G., 2013. Relationship between composition and structure of globules in narrow fractions of ferrospheres. Fuel 111, 332–343. https://doi.org/10.1016/j.fuel.2013.03.059

Sharonova, O.M., Anshits, N.N., Yumashev, V.V., Anshits, A.G., 2008. Composition and morphology of char particles of fly ashes from industrial burning of high-ash coals with different reactivity. Fuel 87, 1989–1997. https://doi.org/10.1016/j.fuel.2007.10.007

Sharonova, O.M., Fedorchak, M.A., Zhizhaev, A.M., Mazurova, E.V., Anshits, A.G., 2015b. Composition of individual ferrospheres of different morphological types. Inorganic Materials 51, 1143–1150. https://doi.org/10.1134/S0020168515110114

Sokol, E.V., Kalugin, V.M., Nigmatulina, E.N., Volkova, N.I., Frenkel, A.E., Maksimova, N.V., 2002. Ferrospheres from fly ashes of Chelyabinsk coals: chemical composition, morphology and formation conditions. Fuel 81, 867–876. https://doi.org/10.1016/S0016-2361(02)00005-4

Sokol, E.V., Maksimova, N.V., Volkova, N.I., Nigmatulina, E.N., Frenkel, A.E., 2000. Hollow silicate microspheres from fly ashes of the Chelyabinsk brown coals (South Urals, Russia). Fuel Processing Technology 67, 35–52. https://doi.org/10.1016/S0378-3820(00)00084-9

Solomon, P.R., Hamblen, D.G., Carangelo, R.M., Serio, M.A., Deshpande, G. v., 1988. General model of coal devolatilization. Energy & Fuels 2, 405–422. https://doi.org/10.1021/ef00010a006

Solomon, P.R., Hamblen, D.G., Serio, M.A., Yu, Z.-Z., Charpenay, S., 1993. A characterization method and model for predicting coal conversion behaviour. Fuel 72, 469–488. https://doi.org/10.1016/0016-2361(93)90106-C

Speight, J.G., 2015. Handbook of coal analysis, 2nd ed. John Wiley & Sons, Hoboken, New Jersey. https://doi.org/10.1002/9781119037699

Srinivasachar, S., Boni, A.A., 1989. A kinetic model for pyrite transformations in a combustion environment. Fuel 68, 829–836. https://doi.org/10.1016/0016-2361(89)90116-6

Srinivasachar, S., Helble, J.J., Boni, A.A., 1990. Mineral behavior during coal combustion 1. Pyrite transformations. Prog Energy Combust Sci 16, 281–292. https://doi.org/10.1016/0360-1285(90)90037-4

Stach, E., Mackowsky, M.-T., Teichmuller, M., Taylor, G.H., Chandra, D., Teichmuller, R., 1982. Stach's textbook of coal petrology: Gebruder Borntraeger. Berlin, 535p.

Strzałkowska, E., 2021. Morphology, chemical and mineralogical composition of magnetic fraction of coal fly ash. Int J Coal Geol 240, 103746. https://doi.org/10.1016/j.coal.2021.103746

Stuckman, M.Y., Lopano, C.L., Granite, E.J., 2018. Distribution and speciation of rare earth elements in coal combustion by-products via synchrotron microscopy and spectroscopy. Int J Coal Geol 195, 125–138. https://doi.org/10.1016/j.coal.2018.06.001

Suárez-Ruiz, I., García, A.B., 2007. Optical Parameters as a Tool To Study the Microstructural Evolution of Carbonized Anthracites during High-Temperature Treatment. Energy & Fuels 21, 2935–2941. https://doi.org/10.1021/ef700221r

Suárez-Ruiz, I., Hower, J.C., Thomas, G.A., 2007. Hg and Se Capture and Fly Ash Carbons from Combustion of Complex Pulverized Feed Blends Mainly of Anthracitic Coal Rank in Spanish Power Plants. Energy & Fuels 21, 59–70. https://doi.org/10.1021/ef0603481

Suárez-Ruiz, I., Valentim, B., Borrego, A.G., Bouzinos, A., Flores, D., Kalaitzidis, S., Malinconico, M.L., Marques, M., Misz-Kennan, M., Predeanu, G., Montes, J.R., Rodrigues, S., Siavalas, G., Wagner, N., 2017. Development of a petrographic classification of fly-ash components from coal combustion and co-combustion. (An ICCP Classification System, Fly-Ash Working Group – Commission III.). Int J Coal Geol 183, 188–203. https://doi.org/10.1016/j.coal.2017.06.004

Suárez-Ruiz, I., Ward, C., 2008. Chapter 4 - Coal Combustion, in: Suárez-Ruiz, I., Crelling, J.C. (Eds.), Applied Coal Petrology. Elsevier, Burlington, pp. 85–117. https://doi.org/https://doi.org/10.1016/B978-0-08-045051-3.00004-X

Szumiata, T., Brzózka, K., Górka, B., Gawroński, M., Gzik-Szumiata, M., Świetlik, R., Trojanowska, M., 2014. Iron speciation in coal fly ashes—chemical and Mössbauer analysis. Hyperfine Interact 226, 483–487. https://doi.org/10.1007/s10751-013-0950-2

Taggart, R.K., Hower, J.C., Dwyer, G.S., Hsu-Kim, H., 2016. Trends in the Rare Earth Element Content of U.S.-Based Coal Combustion Fly Ashes. Environ Sci Technol 50, 5919–5926. https://doi.org/10.1021/acs.est.6b00085

Taggart, R.K., Rivera, N.A., Levard, C., Ambrosi, J.-P., Borschneck, D., Hower, J.C., Hsu-Kim, H., 2018. Differences in bulk and microscale yttrium speciation in coal combustion fly ash. Environ Sci Process Impacts 20, 1390–1403. https://doi.org/10.1039/C8EM00264A

Tagiri, M., Oba, T., 1986. Hydrothermal syntheses of graphite from bituminous coal at 0.5-5 kbar water vapor pressure and 300-600.DEG.C. The Journal of the Japanese Association of Mineralogists, Petrologists and Economic Geologists 81, 260–271. https://doi.org/10.2465/ganko1941.81.260

Tang, M., Zhou, C., Zhang, N., Pan, J., Cao, S., Hu, T., Ji, W., Wen, Z., Nie, T., 2019. Extraction of rare earth elements from coal fly ash by alkali fusion–acid leaching: Mechanism analysis. International Journal of Coal Preparation and Utilization 1–20. https://doi.org/10.1080/19392699.2019.1623206

Taylor, J.C., 1991. Computer Programs for Standardless Quantitative Analysis of Minerals Using the Full Powder Diffraction Profile. Powder Diffr 6, 2–9. https://doi.org/10.1017/S0885715600016778

Thomas, C.G., Gosnell, M.E., Gawronski, E., Phont-anant, D., Shibaoka, M., 1993a. The behaviour of inertinite macerals under pulverised fuel (pf) combustion conditions. Org Geochem 20, 779–788. https://doi.org/10.1016/0146-6380(93)90062-G

Thomas, C.G., Shibaoka, M., Gawronski, E., Gosnell, M.E., Phong-anant, D., 1993b. Reactive (fusible) inertinite in pulverized fuel combustion. Fuel 72, 913–919. https://doi.org/10.1016/0016-2361(93)90287-C

Thompson, R., Oldfield, F., 1986. Environmental Magnetism. Allen & Unwin: Springer Netherlands, Dordrecht. https://doi.org/10.1007/978-94-011-8036-8

Thompson, R.L., Bank, T., Montross, S., Roth, E., Howard, B., Verba, C., Granite, E., 2018. Analysis of rare earth elements in coal fly ash using laser ablation inductively coupled plasma mass spectrometry and scanning electron microscopy. Spectrochim Acta Part B At Spectrosc 143, 1–11. https://doi.org/10.1016/j.sab.2018.02.009

Ting, F.T.C., 1981. Uniaxial and biaxial vitrinite reflectance models and their relationship to paleotectonics, in: Brooks, J. (Ed.), Organic Maturation Studies and Fossil Fuel Exploration. Academic Press, London, pp. 379–392.

Ting, F.T.C., 1978. Petrographic Techniques in Coal Analysis, in: Karr, C. (Ed.), Analytical Methods for Coal and Coal Products. Academic Press, New York, pp. 3–26. https://doi.org/10.1016/B978-0-12-399901-6.50007-4

Tomeczek, J., Palugniok, H., 2002. Kinetics of mineral matter transformation during coal combustion. Fuel 81, 1251–1258. https://doi.org/10.1016/S0016-2361(02)00027-3

Tsai, C.Y., Scaroni, A.W., 1987. Pyrolysis and combustion of bituminous coal fractions in an entrained-flow reactor. Energy & Fuels 1, 263–269. https://doi.org/10.1021/ef00003a007

Tuinstra, F., Koenig, J.L., 1970. Raman Spectrum of Graphite. J Chem Phys 53, 1126–1130. https://doi.org/10.1063/1.1674108

Valentim, B., 2020. Petrography of coal combustion char: A review. Fuel 277, 118271. https://doi.org/10.1016/j.fuel.2020.118271

Valentim, B., Abagiu, A.T., Anghelescu, L., Flores, D., French, D., Gonçalves, P., Guedes, A., Popescu, L.G., Predeanu, G., Ribeiro, J., Santos, A.C., Slăvescu, V., Ward, C.R., 2019. Assessment of bottom ash landfilled at Ceplea Valley (Romania) as a source of rare earth elements. Int J Coal Geol 201. https://doi.org/10.1016/j.coal.2018.11.019

Valentim, B., Białecka, B., Gonçalves, P.A., Guedes, A., Guimarães, R., Cruceru, M., Całus-Moszko, J., Popescu, L.G., Predeanu, G., Santos, A.C., 2018. Undifferentiated inorganics in coal fly ash and bottom ash: Calcispheres, magnesiacalcispheres, and magnesiaspheres. Minerals 8. https://doi.org/10.3390/min8040140

Valentim, B., Guedes, A., Flores, D., Ward, C.R., Hower, J.C., 2009a. Variations in fly ash composition with sampling location: Case study from a Portuguese power plant. Coal Combustion and Gasification Products 1, 14–24. https://doi.org/10.4177/CCGP-D-09-00017.1

Valentim, B., Hower, J.C., Flores, D., Guedes, A., 2008. Notes on the efficacy of wet versus dry screening of fly ash. Min Metall Explor 25, 143–148. https://doi.org/10.1007/BF03403400

Valentim, B., Hower, J.C., Guedes, A., Flores, D., 2009b. Scanning Electron Miccroscopy and Energy-dispersive X-ray spectroscopy of low-sulfur coal fly ash. International Journal of Energy for a Clean Environment 10, 147–166. https://doi.org/10.1615/InterJEnerCleanEnv.2011001526

Valentim, B., Lemos de Sousa, M.J., Abelha, P., Boavida, D., Gulyurtlu, I., 2006. The identification of unusual microscopic features in coal and their derived chars: Influence on coal fluidized bed combustion. Int J Coal Geol 67, 202–211. https://doi.org/10.1016/j.coal.2005.11.003

Valentim, B., Shreya, N., Paul, B., Gomes, C.S., Sant'Ovaia, H., Guedes, A., Ribeiro, J., Flores, D., Pinho, S., Suárez-Ruiz, I., Ward, C.R., 2016. Characteristics of ferrospheres in fly ashes derived from Bokaro and Jharia (Jharkand, India) coals. Int J Coal Geol 153, 52–74. https://doi.org/10.1016/j.coal.2015.11.013

van Krevelen, D.W., 1993. Coal: typology, physics, chemistry, constitution, 3rd ed. Elsevier.

Vandenberghe, R.E., Barrero, C.A., da Costa, G.M., van San, E., de Grave, E., 2000. Mössbauer characterization of iron oxides and (oxy)hydroxides: the present state of the art. Hyperfine Interact 126, 247–259. https://doi.org/10.1023/A:1012603603203

Vandenberghe, R.E., de Resende, V.G., de Grave, E., 2009. Mössbauer effect study of fly and bottom ashes from an electric generating plant, in: ISIAME 2008. Springer Berlin Heidelberg, Berlin, Heidelberg, pp. 341–346. https://doi.org/10.1007/978-3-642-01370-6_44

Vassilev, S. v, Menendez, R., Borrego, A.G., Diaz-Somoano, M., Rosa Martinez-Tarazona, M., 2004a. Phase-mineral and chemical composition of coal fly ashes as a basis for their multicomponent utilization. 3. Characterization of magnetic and char concentrates. Fuel 83, 1563–1583. https://doi.org/10.1016/j.fuel.2004.01.010

Vassilev, S. v, Menendez, R., Diaz-Somoano, M., Martinez-Tarazona, M.R., 2004b. Phase-mineral and chemical composition of coal fly ashes as a basis for their multicomponent utilization. 2. Characterization of ceramic cenosphere and salt concentrates. Fuel 83, 585–603. https://doi.org/10.1016/j.fuel.2003.10.003

Vassilev, S. v., Vassileva, C.G., 2007. A new approach for the classification of coal fly ashes based on their origin, composition, properties, and behaviour. Fuel 86, 1490–1512. https://doi.org/10.1016/j.fuel.2006.11.020

Vassilev, S. v., Vassileva, C.G., 1996. Mineralogy of combustion wastes from coal-fired power stations. Fuel Processing Technology 47, 261–280. https://doi.org/10.1016/0378-3820(96)01016-8

Veneva, L., Hoffmann, V., Jordanova, D., Jordanova, N., Fehr, Th., 2004. Rock magnetic, mineralogical and microstructural characterization of fly ashes from Bulgarian power plants and the nearby anthropogenic soils. Physics and Chemistry of the Earth, Parts A/B/C 29, 1011–1023. https://doi.org/10.1016/j.pce.2004.03.011

Vereshchagin, S.N., Kondratenko, E. v., Rabchevskii, E. v., Anshits, N.N., Solov'ev, L.A., Anshits, A.G., 2012. New approach to the preparation of catalysts for the oxidative coupling of methane. Kinetics and Catalysis 53, 449–455. https://doi.org/10.1134/S0023158412040131

Vereshchagina, T.A., Fedorchak, M.A., Sharonova, O.M., Fomenko, E.V., Shishkina, N.N., Zhizhaev, A.M., Kudryavtsev, A.N., Frank, L.A., Anshits, A.G., 2016. Ni2+-zeolite/ferrosphere and Ni2+-silica/ferrosphere beads for magnetic affinity separation of histidine-tagged proteins. Dalton Transactions 45, 1582–1592. https://doi.org/10.1039/C5DT03827H

Verosub, K.L., Roberts, A.P., 1995. Environmental magnetism: Past, present, and future. J Geophys Res Solid Earth 100, 2175–2192. https://doi.org/10.1029/94JB02713

Vidano, R.P., Fischbach, D.B., Willis, L.J., Loehr, T.M., 1981. Observation of Raman band shifting with excitation wavelength for carbons and graphites. Solid State Commun 39, 341–344. https://doi.org/10.1016/0038-1098(81)90686-4

Vleeskens, J., Kwiecińska, B., Roos, M., Hamburg, G., 1994. Coke forms in nature and in power utilities: interpretation with SEM. Fuel 73, 816–822. https://doi.org/10.1016/0016-2361(94)90273-9

Vleeskens, J.M., Kwiecinska, B.K., Hamburg, G., Roos, C.M., 1990. Identification of coal pyrolysis products by scanning electron microscopy. Fuel Processing Technology 24, 35–43. https://doi.org/10.1016/0378-3820(90)90040-Y

Vleeskens, J.M., Menéndez, R.M., Roos, C.M., Thomas, C.G., 1993. Combustion in the burnout stage: the fate of inertinite. Fuel Processing Technology 36, 91–99. https://doi.org/10.1016/0378-3820(93)90014-U

Waerenborgh, J.C., Figueiredo, M.O., Cabral, J.M.P., Pereira, L.C.J., 1994. Powder XRD structure refinements and 57Fe Mössbauer effect study of synthetic Zn1-xFexAl2O4 (0 < x ≦ 1) spinels annealed at different temperatures. Phys Chem Miner 21. https://doi.org/10.1007/BF00202276

Waerenborgh, J.C., Salamakha, P., Sologub, O., Gonçalves, A.P., Cardoso, C., Sério, S., Godinho, M., Almeida, M., 2000. Influence of Thermal Treatment and Crystal Growth on the Final Composition and Magnetic Properties of the YFe $_{x}$ Al $_{12-x}$ (4 ≤

x ≤ 4.2) Intermetallics. Chemistry of Materials 12, 1743–1749. https://doi.org/10.1021/cm990760c

Wagner, N.J., Matiane, A., 2018. Rare earth elements in select Main Karoo Basin (South Africa) coal and coal ash samples. Int J Coal Geol 196, 82–92. https://doi.org/10.1016/j.coal.2018.06.020

Wang, S., 2008. Application of Solid Ash Based Catalysts in Heterogeneous Catalysis. Environ Sci Technol 42, 7055–7063. https://doi.org/10.1021/es801312m

Wang, S., Li, H., 2005. Dye adsorption on unburned carbon: Kinetics and equilibrium. J Hazard Mater 126, 71–77. https://doi.org/10.1016/j.jhazmat.2005.05.049

Wang, X.S., 2014. Mineralogical and chemical composition of magnetic fly ash fraction. Environ Earth Sci 71, 1673–1681. https://doi.org/10.1007/s12665-013-2571-0

Wang, Y., Alsmeyer, D.C., McCreery, R.L., 1990. Raman spectroscopy of carbon materials: structural basis of observed spectra. Chemistry of Materials 2, 557–563. https://doi.org/10.1021/cm00011a018

Wang, Z., Dai, S., Zou, J., French, D., Graham, I.T., 2019. Rare earth elements and yttrium in coal ash from the Luzhou power plant in Sichuan, Southwest China: Concentration, characterization and optimized extraction. Int J Coal Geol 203, 1–14. https://doi.org/10.1016/j.coal.2019.01.001

Ward, C.R., 2016. Analysis, origin and significance of mineral matter in coal: An updated review. Int J Coal Geol 165, 1–27. https://doi.org/10.1016/j.coal.2016.07.014

Ward, C.R., French, D., 2006. Determination of glass content and estimation of glass composition in fly ash using quantitative X-ray diffractometry. Fuel 85, 2268–2277. https://doi.org/10.1016/j.fuel.2005.12.026

Watson, E.B., Harrison, T.M., 1983. Zircon saturation revisited: temperature and composition effects in a variety of crustal magma types. Earth Planet Sci Lett 64, 295–304. https://doi.org/10.1016/0012-821X(83)90211-X

Wei, Q., Song, W., 2020. Mineralogical and Chemical Characteristics of Coal Ashes from Two High-Sulfur Coal-Fired Power Plants in Wuhai, Inner Mongolia, China. Minerals 10, 323. https://doi.org/10.3390/min10040323

Wilczyńska-Michalik, W., Moryl, R., Sobczyk, J., Michalik, M., 2014. Composition of coal combustion by-products: The importance of combustion technology. Fuel Processing Technology 124, 35–43. https://doi.org/10.1016/j.fuproc.2014.02.016

Wills, B.A., Finch, J.A., 2016. Wills' Mineral Processing Technology, Eighth. ed, Wills' Mineral Processing Technology. Elsevier, Oxford. https://doi.org/10.1016/B978-075064450-1/50003-5

Wolfschmidt, H., Paschos, O., Stimming, U., 2010. Hydrogen Reactions on Nanostructured Surfaces, in: Fuel Cell Science. John Wiley & Sons, Inc., Hoboken, NJ, USA, pp. 1–70. https://doi.org/10.1002/9780470630693.ch1

Wood, K.N., O'Hayre, R., Pylypenko, S., 2014. Recent progress on nitrogen/carbon structures designed for use in energy and sustainability applications. Energy Environ. Sci. 7, 1212–1249. https://doi.org/10.1039/C3EE44078H

Wopenka, B., Pasteris, J.D., 1993. Structural characterization of kerogens to granulite-facies graphite: Applicability of Raman microprobe spectroscopy. American Mineralogist 78, 533–557.

Xu, Y.Y., Zhao, D., Zhang, X.J., Jin, W.T., Kashkarov, P., Zhang, H., 2009. Synthesis and characterization of single-crystalline α-Fe2O3 nanoleaves. Physica E Low Dimens Syst Nanostruct 41, 806–811. https://doi.org/10.1016/j.physe.2008.12.015

Yang, B.L., Cheng, D.S., Lee, S.B., 1991. Effect of steam on the oxidative dehydrogenation of butene over magnesium ferrites with and without chromium substitution. Appl Catal 70, 161–173. https://doi.org/10.1016/S0166-9834(00)84161-5

Yao, Z.T., Ji, X.S., Sarker, P.K., Tang, J.H., Ge, L.Q., Xia, M.S., Xi, Y.Q., 2015. A comprehensive review on the applications of coal fly ash. Earth Sci Rev 141, 105–121. https://doi.org/10.1016/j.earscirev.2014.11.016

Yu, J., Strezov, V., Lucas, J., Wall, T., 2003. Swelling behaviour of individual coal particles in the single particle reactor. Fuel 82, 1977–1987. https://doi.org/10.1016/S0016-2361(03)00159-5

Yuan, Y., Tang, S., Zhang, S., 2019. Geochemical and Mineralogical Characteristics of the Middle Jurassic Coals from the Tongjialiang Mine in the Northern Datong Coalfield, Shanxi Province, China. Minerals 9, 184. https://doi.org/10.3390/min9030184

Zhang, L., Hou, J., Bi, X.T., Grace, J.R., Janke, T., Arato, C., 2012. Electrostatic beneficiation of fly ash in a free-falling system. Particuology 10, 154–160. https://doi.org/10.1016/j.partic.2011.07.006

Zhao, L., Ward, C.R., French, D., Graham, I., 2015. Major and Trace Element Geochemistry of Coals and Intra-Seam Claystones from the Songzao Coalfield, SW China. Minerals 5, 870–893. https://doi.org/10.3390/min5040531

Zhao, Y., Zhang, J., Sun, J., Bai, X., Zheng, C., 2006. Mineralogy, Chemical Composition, and Microstructure of Ferrospheres in Fly Ashes from Coal Combustion. Energy & Fuels 20, 1490–1497. https://doi.org/10.1021/ef060008f

Zhou, B., Li, Z., Chen, C., 2017. Global Potential of Rare Earth Resources and Rare Earth Demand from Clean Technologies. Minerals 7, 203. https://doi.org/10.3390/min7110203

Appendices

Table A1 - Trace elements (ppm), enrichment patterns and anomalies for individual REE for feed coals.

	S1	S2		S3		S4		Minimum	Average	Maximum	CV (%)
	C	C1	C2	C1	C2	C1	C2				
Ba	46	129	185	100	154	158	86	46	123	185	36.3
Be	<1	<1	<1	<1	<1	<1	<1	<1	n.a.	<1	n.a.
Co	1.3	2.3	2.3	2.7	2.8	3.3	1.9	1.30	2.37	3.30	25.4
Cs	<0.1	0.6	0.5	0.7	0.4	0.8	0.5	0.4	0.6	0.8	23.0
Ga	<0.5	1.3	0.6	1.3	1.2	1.3	<0.5	<0.5	0.9	1.3	52.3
Hf	0.2	0.6	0.4	0.5	0.3	0.6	0.5	0.2	0.4	0.6	31.6
Nb	<0.1	0.9	1.1	1.4	1.1	1.3	0.8	<0.1	1.0	1.4	43.7
Rb	1.5	7.3	7.4	10	6.4	9.1	8.4	1.5	7.2	10.0	35.8
Sn	<1	<1	<1	<1	<1	<1	<1	<1	n.a.	<1	n.a.
Sr	31.4	44.5	58.8	33	45.8	45.3	26.6	26.6	40.8	58.8	25.1
Ta	<0.1	<0.1	<0.1	<0.1	<0.1	<0.1	<0.1	<0.1	n.a.	<0.1	n.a.
Th	0.3	1.1	0.9	1	0.8	1.1	0.8	0.3	0.9	1.1	29.8
U	0.3	0.6	0.6	0.6	0.5	0.6	0.5	0.3	0.5	0.6	19.5
V	<8	30	<8	29	25	32	<8	<8	18	32	65.4
W	<0.5	<0.5	0.5	<0.5	<0.5	<0.5	<0.5	<0.5	n.a.	0.50	n.a.
Zr	6.7	20.9	16.7	18.1	17.7	21.3	15.5	6.7	16.7	21.3	27.1
La	1.5	4.4	3.4	4.2	3.5	4	3.4	1.5	3.5	4.4	25.6
Ce	2.3	6.5	5.9	7.3	6.1	7.2	6.5	2.3	6.0	7.3	26.4
Pr	0.25	0.75	0.69	0.83	0.65	0.83	0.7	0.25	0.67	0.83	27.3
Nd	1	2.9	2.9	3.1	2.6	3.3	2.4	1.0	2.6	3.3	27.3
Sm	0.21	0.53	0.64	0.67	0.53	0.63	0.57	0.21	0.54	0.67	26.7
Eu	0.05	0.13	0.11	0.16	0.15	0.16	0.13	0.05	0.13	0.16	28.1
Gd	0.19	0.62	0.61	0.58	0.58	0.73	0.49	0.19	0.54	0.73	29.2
Tb	0.03	0.09	0.1	0.1	0.09	0.12	0.08	0.03	0.09	0.12	29.9
Dy	0.22	0.65	0.58	0.61	0.58	0.71	0.44	0.22	0.54	0.71	28.1
Y	0.9	4	3.7	3.4	3.9	4.3	2.9	0.90	3.30	4.30	32.3
Ho	0.04	0.13	0.12	0.1	0.12	0.14	0.11	0.04	0.11	0.14	28.0
Er	0.14	0.38	0.39	0.35	0.35	0.49	0.3	0.14	0.34	0.49	28.8
Tm	0.01	0.06	0.05	0.05	0.05	0.06	0.04	0.01	0.05	0.06	34.8
Yb	0.12	0.35	0.3	0.29	0.3	0.42	0.25	0.12	0.29	0.42	29.5
Lu	0.01	0.05	0.05	0.04	0.04	0.06	0.04	0.01	0.04	0.06	35.2
∑REE	6.97	21.54	19.54	21.78	19.54	23.15	18.35	6.97	18.70	23.15	26.9
REO	8.36	25.92	23.52	26.19	23.55	27.86	22.09	8.36	22.50	27.86	26.9
L/H	6.99	6.53	6.20	7.67	6.41	5.90	7.83	5.90	6.79	7.83	10.0
Critical	2.34	8.15	7.78	7.72	7.67	9.08	6.25	2.34	7.00	9.08	29.3
Uncritical	2.15	6.3	5.34	6.28	5.26	6.19	5.16	2.15	5.24	6.30	25.7
Excessive	2.48	7.09	6.42	7.78	6.61	7.88	6.94	2.48	6.46	7.88	26.3
La_N/Lu_N	1.50	0.88	0.68	1.05	0.88	0.67	0.85	0.67	0.93	1.50	28.3
La_N/Sm_N	1.08	1.26	0.81	0.95	1.00	0.96	0.90	0.81	1.00	1.26	13.4
Gd_N/Lu_N	1.47	0.96	0.95	1.12	1.12	0.94	0.95	0.94	1.07	1.47	16.7
Y_N/Ho_N	0.89	1.22	1.22	1.34	1.28	1.21	1.04	0.89	1.17	1.34	12.3
Eu_N/Eu^*	1.13	1.10	0.79	1.12	1.27	1.09	1.09	0.79	1.09	1.27	12.2
Ce_N/Ce_N^*	0.87	0.83	0.91	0.92	0.95	0.93	0.99	0.83	0.91	0.99	5.1
Gd_N/Gd_N^*	1.09	1.26	1.08	1.02	1.18	1.15	1.05	1.02	1.12	1.26	6.8
REYdef, rel%	33.57	37.84	39.82	35.45	39.25	39.22	34.06	33.57	37.03	39.82	6.6
C_{outl}	0.94	1.15	1.21	0.99	1.16	1.15	0.90	0.90	1.07	1.21	10.7

CV, coefficient of variation; REO, REE as oxides, L/H, ratio between light REE and heavy REE; REYdef, rel%, (Y+Nd+Eu+Tb+Dy+Er)/∑REE; C_{outl}, ((Nd+Eu+Tb+Dy+Er+Y)/∑REE)/((Ce+Ho+Tm+Yb+Lu)/∑REE))

Table A2 - Trace elements (ppm), enrichment patterns, anomalies for individual REE for bulk coal combustion ashes.

Campaign	Sample	Ba	Be	Co	Cs	Ga	Hf	Nb	Rb	Sn	Sr	Ta	Th	U	V	W	Zr	La	Ce	Pr	Nd	Sm	Eu	Gd	Tb	Dy	Y	Ho	Er
S1	BA	794	3	16.6	6.6	13.9	5.5	11.8	92.5	1	234	0.9	11.1	4.2	207	1.3	211	33	64.3	7.71	30.5	5.34	1.24	5.22	0.86	4.74	28.8	0.99	3.11
	ECO	699	2	14.2	5.1	11.9	4.9	9.1	72.7	1	206	0.7	9	3.6	172	1	197	28.8	53.4	6.41	24.8	4.76	1.04	4.34	0.72	4.24	24.8	0.87	2.63
	ESP12	861	3	18.6	7.2	21.7	4.7	12	103	6	255	1	10.4	5.1	235	4.6	182	34.4	66	7.8	30.1	5.62	1.2	5.13	0.83	5.19	29.1	1.02	3.15
	ESP15	728	4	17.9	6.3	18.4	4.7	10.8	87.2	3	247	0.8	9.9	4.4	211	1.8	173	32.3	61.5	7.25	27.2	5.21	1.23	4.67	0.78	4.68	25.9	0.95	2.92
	ESP22	894	4	18.3	7.8	24.4	4.7	12.1	104	3	250	0.7	10.8	5.2	252	2.6	173	34.4	66.2	7.94	30.7	6	1.25	5.14	0.83	4.98	29.1	1.02	3.02
	ESP25	879	4	19.1	7.3	25.1	5.1	13.1	96	3	275	0.8	12.1	5.3	266	2.2	190	36.1	70.1	8.41	31.9	6.4	1.42	5.75	0.9	5.25	32.2	1.1	3.22
	ESP32/42	853	3	17	7.2	20.4	5.1	11.6	98.7	2	246	0.9	10.4	4.8	224	1.8	182	34.3	63.9	7.64	30	5.72	1.22	5.21	0.83	4.72	29.7	0.98	3.03
	ESP35/45	866	3	18.9	7.3	22.9	4.6	12	96.1	3	272	0.9	11	5.6	247	2.3	177	34.3	66.1	8.01	30.6	5.95	1.3	5.16	0.84	4.89	29.3	1.04	3.03
	Silo	946	3	19.9	8.3	24.5	4.9	12.6	108	3	264	0.9	11.9	6	270	2.2	185	36.8	71.6	8.54	32.2	6.05	1.4	5.5	0.89	5.26	31	1.11	3.35
S2	ECO	1053	4	20.5	4.9	11.2	5	9.4	59.5	1	387	0.7	9	3.8	173	1.1	206	28.2	54.8	6.48	25.2	5.11	1.14	4.93	0.81	4.92	30.4	0.97	3.04
	ESP12	1806	4	26.3	6.7	26.7	5.6	12.2	84	3	603	0.9	12	6.1	282	2.8	206	36.3	68	8.19	32.3	6.6	1.53	6.62	1.08	6.71	42.2	1.48	4.29
	ESP22	2336	10	34.1	7.4	47.1	5.3	14.1	98.2	5	775	0.9	12.9	8	368	4.2	206	42.7	80.5	9.86	38.7	7.54	1.87	7.93	1.24	7.73	48.2	1.67	4.87
	ESP32/42	1712	7	29	8.4	46.7	5.1	14.5	111	6	530	1	13.9	8.5	398	4.6	189	45	82.9	10.2	39.9	7.7	1.77	7.33	1.15	6.95	42	1.42	4.35
	Silo	1770	7	25.3	6.7	27.3	5.2	12.6	86.1	3	600	0.8	12.7	6	269	3.2	210	37.1	68.6	8.32	32.4	6.84	1.53	6.86	1.08	6.86	41.3	1.41	4.35
S3	BA	907	4	18.5	6.1	13.2	5.2	11.5	84.8	1	295	0.8	10.5	4.6	202	1	202	34	65.1	7.8	29.8	5.87	1.32	5.72	0.9	5.49	32.6	1.16	3.45
	ESP12	1182	4	22.7	7.6	24.4	5.2	13.2	99.5	3	377	0.8	12.4	5.9	269	2	200	37.7	71.8	8.49	32.3	6.58	1.48	6.18	0.99	6.34	37.7	1.25	3.84
	ESP22	1378	3	27.6	8	35.4	5	14.3	105	4	426	1	13.3	7.6	327	3.1	187	40.7	77.1	9.41	36.4	7.27	1.63	6.81	1.07	6.71	40.1	1.38	4.09
	ESP32	1614	7	32.1	8.7	51.4	5	16	114	7	470	1.1	14.7	10.2	424	5	188	48.2	87.8	10.7	40.6	8.04	1.9	7.5	1.16	6.93	42.2	1.45	4.38
	Silo	1152	4	22.8	7.2	26.8	5.1	12.5	94.5	3	365	0.9	11.6	6.5	276	2.6	186	37.4	71.3	8.38	32.4	6.35	1.41	6	0.94	5.85	34.4	1.2	3.74
S4	BA	905	3	20	6.3	12.9	5.6	12.1	86	<1	286	0.9	11.2	4.3	200	1.3	204	33.9	66.6	7.94	30.7	6.03	1.35	5.77	0.89	5.41	31.8	1.14	3.37
	ECO	804	5	18.2	5.6	11.1	5	10.8	76.8	<1	271	0.6	10	3.9	185	1.2	189	31.6	61	7.18	27.9	5.43	1.18	5.06	0.8	4.89	29.5	0.99	3.13
	ESP12	1053	4	21.8	7	23.3	4.7	11.9	94.3	2	326	0.9	11.2	5.5	246	1.9	181	35.4	68.1	8.03	31.3	6.27	1.36	5.66	0.91	5.26	33.8	1.18	3.63
	ESP22	1291	8	26.6	7.5	36	4.6	13.8	106	4	391	1	12.6	7.3	322	4	176	40.4	74.9	9.15	35.6	6.64	1.54	6.27	0.99	6.23	36.7	1.32	3.71
	ESP32	1582	9	32.6	8.2	48.7	4.7	14.4	113	6	449	1	14.6	9.2	392	6	184	44.9	84.8	10.2	39.9	7.89	1.81	7.34	1.12	7.14	41.1	1.43	4.35
	Silo	1095	2	23.9	7.4	25	4.8	12.8	99.6	3	346	1	12.1	5.8	265	4.6	187	37.4	72.5	8.59	33.2	6.52	1.42	6.18	0.96	5.69	35.5	1.18	3.64
Minimum		699	2	14.2	4.9	11.1	4.6	9.1	59.5	<1	206	0.6	9	3.6	172	1	173	28.2	53.4	6.41	24.8	4.76	1.04	4.34	0.72	4.24	24.8	0.87	2.63
Average		1166	4.56	22.5	7.07	26	5.01	12.4	94.8	3.08	366	0.88	11.7	5.9	267	2.74	191	36.6	69.6	8.34	32.3	6.31	1.42	5.93	0.94	5.72	34.4	1.19	3.59
Maximum		2336	10	34.1	8.7	51.4	5.6	16	114	7	775	1.1	14.7	10.2	424	6	211	48.2	87.8	10.7	40.6	8.04	1.9	7.93	1.24	7.73	48.2	1.67	4.87
CV (%)		35.2	46.4	23.6	13.5	45.4	5.71	12.3	13.5	57.8	37.7	13.4	12.9	28.8	25.8	51.3	6.02	13	11.9	12.8	12.9	13.7	16	15.8	14.2	16.3	17.2	17.1	16.1

Table A2 – Continuation.

Campaign	Sample	Tm	Yb	Lu	∑REE	REO	L/H	Critical	Uncritical	Excessive	La_N/Lu_N	La_N/Sm_N	Gd_N/Lu_N	Y_N/Ho_N	Eu_N/Eu^*	Ce_N/Ce_N^*	Gd_N/Gd_N^*	REYdef, rel%	C_{outl}
S1	BA	0.45	3.02	0.45	189.73	228.09	7.54	69.25	51.27	69.21	0.73	0.94	0.90	1.15	1.06	0.95	1.09	36.50	1.00
	ECO	0.37	2.38	0.38	159.94	192.28	7.48	58.23	44.31	57.40	0.76	0.92	0.89	1.13	1.02	0.93	1.06	36.41	1.01
	ESP12	0.45	2.87	0.46	193.32	232.42	7.60	69.57	52.95	70.80	0.75	0.93	0.86	1.13	1.01	0.95	1.08	35.99	0.98
	ESP15	0.42	2.75	0.43	178.19	214.17	7.65	62.71	49.43	66.05	0.75	0.94	0.84	1.08	1.11	0.95	1.05	35.19	0.95
	ESP22	0.45	3.05	0.45	194.53	233.84	7.73	69.88	53.48	71.17	0.76	0.87	0.89	1.13	1.00	0.94	1.06	35.92	0.98
	ESP25	0.48	3.12	0.5	206.85	248.76	7.59	74.89	56.66	75.30	0.72	0.86	0.89	1.16	1.06	0.95	1.10	36.20	0.99
	ESP32/42	0.44	2.99	0.46	191.14	229.81	7.65	69.50	52.87	68.77	0.75	0.91	0.88	1.20	1.01	0.93	1.09	36.36	1.01
	ESP35/45	0.43	2.96	0.46	194.37	233.67	7.78	69.96	53.42	70.99	0.75	0.87	0.87	1.11	1.04	0.94	1.06	35.99	0.99
	Silo	0.44	3.2	0.46	207.80	249.84	7.75	74.10	56.89	76.81	0.80	0.92	0.93	1.10	1.09	0.95	1.08	35.66	0.96
S2	ECO	0.45	2.9	0.44	169.79	204.38	6.55	65.51	44.72	59.56	0.64	0.84	0.87	1.24	1.03	0.95	1.09	38.58	1.10
	ESP12	0.59	3.77	0.58	220.24	265.18	6.09	88.11	57.71	74.42	0.63	0.83	0.88	1.13	1.06	0.93	1.11	40.01	1.18
	ESP22	0.66	4.34	0.65	258.46	311.12	6.23	102.61	68.03	87.82	0.66	0.86	0.95	1.14	1.13	0.92	1.16	39.70	1.17
	ESP32/42	0.59	3.98	0.6	255.82	307.62	7.11	96.12	70.21	89.49	0.75	0.89	0.95	1.17	1.08	0.91	1.12	37.57	1.07
	Silo	0.6	3.81	0.58	221.64	266.75	6.06	87.52	59.12	75.00	0.64	0.82	0.92	1.16	1.03	0.92	1.13	39.49	1.17
S3	BA	0.5	3.28	0.49	197.48	237.53	6.86	73.56	53.39	70.53	0.69	0.88	0.90	1.11	1.05	0.94	1.12	37.25	1.04
	ESP12	0.52	3.38	0.53	219.08	263.65	6.88	82.65	58.95	77.48	0.71	0.87	0.90	1.19	1.05	0.95	1.10	37.73	1.07
	ESP22	0.56	3.67	0.56	237.46	285.65	6.94	90.00	64.19	83.27	0.73	0.85	0.94	1.15	1.06	0.93	1.11	37.90	1.08
	ESP32	0.58	4.04	0.6	266.07	319.91	7.40	97.17	74.43	94.47	0.80	0.91	0.97	1.15	1.12	0.91	1.12	36.52	1.03
	Silo	0.5	3.34	0.51	213.72	257.04	7.12	78.74	58.13	76.85	0.73	0.89	0.91	1.13	1.05	0.95	1.11	36.84	1.02
S4	BA	0.48	3.28	0.49	199.15	239.49	7.03	73.52	53.64	71.99	0.69	0.85	0.91	1.10	1.06	0.96	1.13	36.92	1.02
	ECO	0.42	2.8	0.45	182.33	219.32	7.24	67.40	49.27	65.66	0.70	0.88	0.87	1.18	1.03	0.95	1.10	36.97	1.03
	ESP12	0.49	3.21	0.49	205.09	246.73	7.22	76.26	55.36	73.47	0.72	0.86	0.90	1.13	1.03	0.95	1.08	37.18	1.04
	ESP22	0.53	3.44	0.54	227.96	274.12	7.30	84.77	62.46	80.73	0.75	0.92	0.90	1.10	1.09	0.92	1.11	37.19	1.05
	ESP32	0.59	3.94	0.61	257.14	309.17	7.15	95.42	70.35	91.37	0.74	0.86	0.93	1.14	1.10	0.93	1.13	37.11	1.04
	Silo	0.53	3.36	0.51	217.18	261.27	7.24	80.41	58.69	78.08	0.73	0.87	0.94	1.19	1.03	0.95	1.12	37.02	1.03
Minimum		0.37	2.38	0.38	159.34	192.28	6.06	58.23	44.31	57.40	0.63	0.82	0.84	1.08	1.00	0.91	1.05	35.19	0.95
Average		0.5	3.32	0.51	210.58	253.27	7.17	78.31	57.20	75.07	0.72	0.88	0.90	1.14	1.06	0.94	1.10	37.13	1.04
Maximum		0.66	4.34	0.65	274.52	319.91	7.78	102.61	74.43	94.47	0.80	0.94	0.97	1.24	1.13	0.96	1.16	40.01	1.18
CV (%)		14.1	13.9	13	218.11	13.11	6.90	14.72	13.17	11.95	6.15	3.75	3.37	3.11	3.26	1.48	2.42	3.26	5.77

BA, bottom ash; ECO, economizer; ESP, Electrostatic precipitator; CV, coefficient of variations; REO, rare earth elements as oxides; L/H, ratio between light REE and heavy REE; REYdef, rel%, (Y+Nd+Eu+Tb+Dy+Er)/∑REE; Coutl, ((Nd+Eu+Tb+Dy+Er+Y)/∑REE)/((Ce+Ho+Tm+Yb+Lu)/∑REE))

Table A3 – Relative enrichments (RE) for trace elements according to Meij, (1995).

Campaign	Sample	Ba	Be	Co	Cs	Ga	Hf	Nb	Rb	Sn	Sr	Ta	Th	U	V	W	Zr	REE
S1	BA	0.6	0.2	0.4	4.3	1.8	0.9	7.7	2.0	0.1	0.2	0.6	1.2	0.5	1.7	0.2	1.0	0.9
	ECO	0.5	0.1	0.4	3.3	1.6	0.8	6.0	1.6	0.1	0.2	0.5	1.0	0.4	1.4	0.1	1.0	0.8
	ESP12	0.6	0.2	0.5	4.7	2.8	0.8	7.9	2.2	0.4	0.3	0.7	1.1	0.6	1.9	0.6	0.9	0.9
	ESP15	0.5	0.3	0.5	4.1	2.4	0.8	7.1	1.9	0.2	0.3	0.5	1.1	0.5	1.7	0.2	0.8	0.8
	ESP22	0.6	0.3	0.5	5.1	3.2	0.8	7.9	2.3	0.2	0.3	0.5	1.2	0.6	2.1	0.3	0.8	0.9
	ESP25	0.6	0.3	0.5	4.8	3.3	0.8	8.6	2.1	0.2	0.3	0.5	1.3	0.6	2.2	0.3	0.9	1.0
	ESP32/42	0.6	0.2	0.4	4.7	2.7	0.8	7.6	2.2	0.1	0.3	0.6	1.1	0.5	1.8	0.2	0.9	0.9
	ESP35/45	0.6	0.2	0.5	4.8	3.0	0.8	7.9	2.1	0.2	0.3	0.6	1.2	0.6	2.0	0.3	0.9	0.9
	Silo	0.7	0.2	0.5	5.4	3.2	0.8	8.3	2.4	0.2	0.3	0.6	1.3	0.7	2.2	0.3	0.9	1.0
S2	ECO	0.5	0.6	0.7	0.7	0.9	0.8	0.7	0.6	0.2	0.6	1.1	0.7	0.5	0.8	0.2	0.9	0.6
	ESP12	0.9	0.6	0.9	1.0	2.2	0.9	1.0	0.9	0.5	0.9	1.4	0.9	0.8	1.3	0.6	0.9	0.8
	ESP22	1.2	1.6	1.2	1.1	3.9	0.8	1.1	1.0	0.8	1.2	1.4	1.0	1.0	1.7	0.9	0.9	1.0
	ESP32/42	0.9	1.1	1.0	1.2	3.8	0.8	1.1	1.2	0.9	0.8	1.6	1.1	1.1	1.8	1.0	0.8	1.0
	Silo	0.9	1.1	0.9	1.0	2.2	0.8	1.0	0.9	0.5	0.9	1.3	1.0	0.8	1.2	0.7	0.9	0.8
S3	BA	0.7	0.8	0.6	1.1	1.0	1.3	0.9	1.0	0.2	0.7	1.5	1.1	0.8	0.7	0.4	1.1	0.9
	ESP12	0.9	0.8	0.8	1.3	1.9	1.3	1.0	1.2	0.6	0.9	1.5	1.3	1.0	1.0	0.8	1.1	1.0
	ESP22	1.0	0.6	1.0	1.4	2.7	1.2	1.1	1.2	0.8	1.0	1.9	1.4	1.3	1.2	1.2	1.0	1.1
	ESP32	1.2	1.4	1.1	1.5	4.0	1.2	1.2	1.3	1.4	1.2	2.1	1.6	1.8	1.5	1.9	1.0	1.2
	Silo	0.9	0.8	0.8	1.3	2.1	1.2	1.0	1.1	0.6	0.9	1.7	1.2	1.1	1.0	1.0	1.0	1.0
S4	BA	0.7	0.6	0.7	0.9	1.6	1.0	1.1	0.9	0.1	0.8	1.7	1.1	0.7	1.1	0.5	1.1	0.9
	ECO	0.6	1.0	0.7	0.8	1.4	0.9	1.0	0.8	0.1	0.7	1.1	1.0	0.7	1.0	0.5	1.0	0.8
	ESP12	0.8	0.8	0.8	1.0	2.9	0.8	1.1	1.0	0.4	0.9	1.7	1.1	1.0	1.3	0.7	0.9	0.9
	ESP22	1.0	1.5	1.0	1.1	4.4	0.8	1.3	1.2	0.8	1.0	1.9	1.3	1.3	1.7	1.5	0.9	1.0
	ESP32	1.2	1.7	1.2	1.2	6.0	0.8	1.3	1.2	1.1	1.2	1.9	1.5	1.6	2.1	2.3	1.0	1.2
	Silo	0.9	0.4	0.9	1.1	3.1	0.8	1.2	1.1	0.6	0.9	1.9	1.2	1.0	1.4	1.8	1.0	1.0

BA, bottom ash; ECO, economizer; ESP, Electrostatic precipitator; REE, rare earth elements.

Table A4 - Pearson correlation coefficients for feed coals. Statistically significant relations for ρ > 0.05 in bold.

	C	Ash	SiO_2	Al_2O_3	Fe_2O_3	SO_3	K_2O	CaO	TiO_2	Ba	Co	Cs	Hf	Nb	Rb	Sr	Th	U	Zr	LREE	MREE	HREE
C	1.00																					
Ash	**-0.86**	1.00																				
SiO_2	**-0.76**	**0.94**	1.00																			
Al_2O_3	**-0.76**	**0.94**	**0.93**	1.00																		
Fe_2O_3	**-0.91**	0.64	0.51	0.53	1.00																	
SO_3	-0.47	0.08	0.10	0.00	0.50	1.00																
K_2O	-0.65	**0.89**	**0.88**	**0.99**	0.41	-0.10	1.00															
CaO	**-0.81**	0.64	0.40	0.60	**0.85**	0.25	0.54	1.00														
TiO_2	-0.73	**0.81**	**0.81**	**0.89**	0.46	0.32	**0.89**	0.56	1.00													
Ba	**-0.87**	0.58	0.38	0.39	**0.87**	0.58	0.26	**0.80**	0.42	1.00												
Co	**-0.83**	**0.84**	**0.79**	0.70	0.59	0.19	0.60	0.51	0.60	0.71	1.00											
Cs	**-0.78**	**0.87**	**0.82**	**0.89**	0.48	0.15	**0.87**	0.61	**0.91**	0.54	**0.82**	1.00										
Hf	-0.53	0.65	0.61	0.72	0.19	0.21	0.75	0.43	**0.91**	0.34	0.56	**0.90**	1.00									
Nb	**-0.94**	**0.95**	**0.90**	**0.90**	**0.76**	0.23	**0.82**	0.71	**0.80**	0.70	**0.90**	**0.89**	0.63	1.00								
Rb	**-0.80**	**0.95**	**0.89**	**0.98**	0.56	0.09	**0.97**	0.66	**0.93**	0.48	0.73	**0.94**	**0.81**	**0.91**	1.00							
Sr	-0.63	0.19	0.01	0.03	0.75	0.64	-0.10	0.68	0.13	**0.90**	0.44	0.24	0.08	0.40	0.13	1.00						
Th	**-0.84**	**0.81**	**0.77**	**0.81**	0.58	0.44	**0.76**	0.63	**0.93**	0.66	**0.79**	**0.95**	**0.89**	**0.87**	**0.88**	0.40	1.00					
U	**-0.91**	**0.82**	0.74	**0.83**	0.72	0.44	**0.77**	**0.78**	**0.91**	0.73	0.75	**0.92**	**0.81**	**0.90**	**0.89**	0.50	**0.97**	1.00				
Zr	**-0.86**	**0.82**	**0.78**	**0.76**	0.59	0.50	0.69	0.57	**0.88**	0.71	**0.85**	**0.91**	**0.83**	**0.86**	**0.84**	0.44	**0.98**	**0.93**	1.00			
LREE	**-0.88**	**0.92**	**0.89**	**0.92**	0.63	0.33	**0.87**	0.65	**0.95**	0.62	**0.81**	**0.95**	**0.83**	**0.94**	**0.96**	0.30	**0.97**	**0.95**	**0.95**	1.00		
MREE	**-0.94**	**0.84**	**0.76**	0.73	0.72	0.52	0.64	0.67	**0.80**	**0.83**	**0.88**	**0.87**	0.72	**0.90**	**0.81**	0.57	**0.94**	**0.92**	**0.98**	**0.93**	1.00	
HREE	**-0.87**	**0.80**	0.69	0.70	0.62	0.42	0.63	0.67	**0.78**	**0.81**	**0.88**	**0.90**	**0.79**	**0.85**	**0.79**	0.56	**0.94**	**0.91**	**0.96**	**0.90**	**0.97**	1.00

LREE, light rare earth elements (La-Sm), MREE, medium rare earth elements (Eu-Y), HREE, heavy earth elements (Ho-Lu)

Table A5 - Pearson correlation coefficients for bulk ashes. Statistically significant relations for $\rho > 0.05$ in bold.

	C	Ash	Al_2O_3	CaO	Fe_2O_3	K_2O	MgO	MnO	Na_2O	P_2O_5	SO_3	SiO_2	TiO_2	Ba	Be	Co	Cs	Ga	Hf	Nb	Rb	Sn	Sr	Ta	Th	U	V	W	Zr	LREE	MREE	HREE
C	1.00																															
Ash	**-0.98**	1.00																														
Al_2O_3	0.36	**-0.47**	1.00																													
CaO	-0.25	0.23	0.02	1.00																												
Fe_2O_3	**-0.60**	**0.54**	-0.29	0.39	1.00																											
K_2O	**0.52**	**-0.59**	**0.84**	-0.32	**-0.57**	1.00																										
MgO	**0.43**	**-0.50**	**0.43**	-0.25	-0.33	**0.75**	1.00																									
MnO	-0.09	0.06	-0.31	-0.37	0.15	0.05	**0.59**	1.00																								
Na_2O	0.04	-0.11	**0.69**	**0.67**	-0.03	**0.41**	0.17	**-0.44**	1.00																							
P_2O_5	0.21	-0.36	**0.81**	0.10	-0.08	**0.67**	**0.54**	0.02	**0.63**	1.00																						
SO_3	0.31	**-0.41**	**0.51**	0.29	0.18	0.23	0.18	-0.20	**0.43**	**0.54**	1.00																					
SiO_2	**-0.68**	**0.78**	**-0.88**	-0.06	0.28	**-0.77**	**-0.53**	0.20	**-0.59**	**-0.77**	**-0.68**	1.00																				
TiO_2	0.33	**-0.44**	**0.99**	0.07	-0.25	**0.83**	**0.44**	-0.30	**0.71**	**0.82**	**0.52**	**-0.87**	1.00																			
Ba	-0.11	0.02	**0.56**	**0.68**	0.34	0.07	-0.26	**-0.61**	**0.80**	**0.50**	**0.61**	**-0.49**	**0.58**	1.00																		
Be	0.07	-0.19	**0.49**	**0.56**	0.32	0.14	0.04	-0.21	**0.61**	**0.57**	**0.70**	**-0.57**	**0.50**	**0.77**	1.00																	
Co	0.06	-0.19	**0.68**	**0.47**	0.37	0.24	0.00	-0.38	**0.69**	**0.67**	**0.78**	**-0.68**	**0.69**	**0.91**	**0.79**	1.00																
Cs	**0.41**	**-0.52**	**0.95**	-0.15	-0.32	**0.89**	**0.52**	-0.19	**0.54**	**0.76**	**0.47**	**-0.86**	**0.94**	**0.42**	0.35	**0.59**	1.00															
Ga	0.25	-0.39	**0.86**	0.32	0.06	**0.57**	0.32	-0.25	**0.77**	**0.88**	**0.75**	**-0.86**	**0.87**	**0.78**	**0.75**	**0.91**	**0.79**	1.00														
Hf	**-0.73**	**0.74**	-0.15	0.30	**0.42**	-0.38	**-0.53**	-0.26	0.11	-0.24	-0.28	**0.46**	-0.13	0.28	-0.02	0.07	-0.21	-0.13	1.00													
Nb	0.21	-0.34	**0.91**	0.11	0.07	**0.66**	0.36	-0.21	**0.62**	**0.79**	**0.60**	**-0.82**	**0.91**	**0.65**	**0.58**	**0.82**	**0.88**	**0.89**	0.02	1.00												
Rb	**0.45**	**-0.56**	**0.92**	-0.19	-0.33	**0.94**	**0.66**	-0.03	**0.50**	**0.75**	**0.44**	**-0.86**	**0.91**	0.31	0.33	**0.51**	**0.97**	**0.75**	-0.28	**0.85**	1.00											
Sn	0.34	**-0.46**	**0.84**	0.14	-0.17	**0.65**	**0.40**	-0.22	**0.66**	**0.87**	**0.63**	**-0.82**	**0.85**	**0.59**	**0.57**	**0.73**	**0.78**	**0.89**	-0.30	**0.79**	**0.76**	1.00										
Sr	-0.17	0.10	**0.45**	**0.73**	0.38	-0.07	-0.39	**-0.66**	**0.75**	0.39	**0.54**	-0.37	**0.47**	**0.98**	**0.73**	**0.85**	0.28	**0.68**	0.34	**0.54**	0.16	**0.49**	1.00									
Ta	0.16	-0.27	**0.71**	-0.03	0.00	**0.61**	**0.42**	-0.05	**0.45**	**0.61**	**0.48**	**-0.64**	**0.74**	**0.41**	0.25	**0.60**	**0.72**	**0.68**	-0.07	**0.75**	**0.74**	**0.71**	0.31	1.00								
Th	0.12	-0.26	**0.83**	0.24	0.17	**0.54**	0.28	-0.25	**0.66**	**0.74**	**0.71**	**-0.77**	**0.85**	**0.72**	**0.63**	**0.87**	**0.82**	**0.90**	0.07	**0.96**	**0.76**	**0.75**	**0.62**	**0.70**	1.00							
U	0.21	-0.36	**0.84**	0.23	0.14	**0.54**	0.30	-0.21	**0.68**	**0.87**	**0.74**	**-0.83**	**0.85**	**0.75**	**0.69**	**0.91**	**0.81**	**0.98**	-0.11	**0.92**	**0.75**	**0.86**	**0.64**	**0.73**	**0.93**	1.00						
V	0.21	-0.36	**0.87**	0.28	0.09	**0.58**	0.32	-0.24	**0.74**	**0.87**	**0.73**	**-0.84**	**0.88**	**0.77**	**0.71**	**0.91**	**0.82**	**0.99**	-0.08	**0.93**	**0.77**	**0.87**	**0.66**	**0.70**	**0.94**	**0.99**	1.00					
W	0.37	**-0.47**	**0.75**	0.24	-0.03	**0.55**	0.35	-0.24	**0.61**	**0.71**	**0.76**	**-0.81**	**0.77**	**0.63**	**0.60**	**0.79**	**0.71**	**0.86**	-0.29	**0.77**	**0.72**	**0.91**	**0.53**	**0.73**	**0.77**	**0.84**	**0.84**	1.00				
Zr	**-0.83**	**0.85**	-0.34	**0.44**	**0.59**	**-0.63**	**-0.66**	-0.23	0.04	-0.33	-0.12	**0.57**	-0.33	0.32	0.06	0.09	**-0.42**	-0.19	**0.83**	-0.14	**-0.49**	-0.33	**0.41**	-0.21	-0.02	-0.17	-0.16	-0.26	1.00			
LREE	0.18	-0.32	**0.88**	0.22	0.15	**0.60**	0.34	-0.20	**0.68**	**0.82**	**0.69**	**-0.82**	**0.88**	**0.73**	**0.67**	**0.89**	**0.85**	**0.95**	-0.01	**0.97**	**0.81**	**0.82**	**0.62**	**0.75**	**0.97**	**0.97**	**0.97**	**0.82**	-0.12	1.00		
MREE	-0.06	-0.05	**0.66**	**0.53**	0.37	0.19	-0.15	**-0.53**	**0.74**	**0.56**	**0.66**	**-0.58**	**0.67**	**0.96**	**0.73**	**0.95**	**0.55**	**0.83**	0.28	**0.80**	**0.45**	**0.63**	**0.92**	**0.53**	**0.86**	**0.83**	**0.84**	**0.68**	0.27	**0.85**	1.00	
HREE	-0.07	-0.04	**0.68**	**0.52**	0.37	0.22	-0.12	**-0.52**	**0.74**	**0.57**	**0.65**	**-0.58**	**0.69**	**0.95**	**0.74**	**0.95**	**0.57**	**0.84**	0.28	**0.81**	**0.48**	**0.63**	**0.91**	**0.55**	**0.87**	**0.84**	**0.85**	**0.68**	0.25	**0.86**	**0.99**	1.00

LREE, light rare earth elements (La-Sm), MREE, medium rare earth elements (Eu-Y), HREE, heavy earth elements (Ho-Lu)

Table A6 - Trace elements (ppm), enrichment patterns, anomalies for individual REE for coal combustion ashes size-fractions.

Sample	Fraction	wt.%	C_t	Ba	Be	Co	Cs	Ga	Hf	Nb	Rb	Sn	Sr	Ta	Th	U	V	W	Zr	La	Ce	Pr	Nd	Sm	Eu	Gd	Tb	Dy	Y	Ho
S1 BA	>4	19.42	0.1	833	4	17.2	6.4	14	5.7	12.7	90.5	1	235	0.9	11.6	4.2	208	2.1	216	33.3	65.6	7.88	30.2	6.15	1.29	5.58	0.88	5.43	31.1	1.08
(mm)	4-2	19.05	0.08	869	4	17.3	6.9	14.4	5.9	12.7	94.5	3	243	1	12.3	4.6	219	1.1	219	35.1	69.2	8.44	32.6	6.22	1.41	5.94	0.91	5.49	32.8	1.1
	2-1	12.95	0.08	860	2	17.8	7.1	15.7	5.8	12.8	95.8	1	248	0.8	12.8	4.8	220	1.1	216	35.3	68.9	8.4	32	6.27	1.42	5.87	0.94	5.36	34.1	1.19
	1-0.5	7.29	0.15	868	5	17.6	7.1	15.7	5.5	13.3	95.7	1	248	0.9	12	4.9	221	1.4	211	35.6	71	8.57	31.6	6.46	1.35	5.84	0.93	5.4	32.5	1.09
	0.5-0.25	5.97	0.46	862	5	17.7	6.9	14.3	5.5	12.4	89.5	4	244	0.9	13.1	4.6	209	1.1	205	33.9	68.5	8.27	32.1	6.22	1.34	5.74	0.89	5.12	31	1.09
	0.25-0.125	8.54	0.48	779	3	16.3	5.9	12.5	4.9	11.3	83.3	3	230	0.8	10.7	4.1	191	0.9	188	31.9	62.3	7.43	28.2	5.69	1.26	5.31	0.83	4.84	29	1.04
	0.125-0.090	6.06	0.39	777	4	16.2	5.7	12.1	5.3	11.3	82.7	1	214	0.7	10.8	3.9	188	1	192	32.1	62.9	7.63	29.4	6.04	1.24	5.48	0.83	5.02	28.9	1.06
	0.090-0.063	6.56	0.44	787	4	15.7	6.4	12	5.9	11.7	87.2	1	224	0.8	11.5	4.1	191	1.2	217	32.9	65.7	7.82	29.6	5.88	1.33	5.39	0.85	5.14	30.4	1.06
	<0.063	14.13	0.95	817	4	16.9	6.6	13.2	5.9	12.1	92.7	2	226	0.8	11.1	4.1	200	1.3	217	34.8	66.3	8.15	30.9	6.12	1.31	5.59	0.87	5.31	31.4	1.09
S1 Eco	> 150	20.74	1.93	806	2	16.5	6.1	16.5	4.8	11.5	84	1	239	0.7	10.5	4.5	215	1.5	174	32.1	63.2	7.61	29.1	5.68	1.24	5.33	0.83	5.11	30.1	1.05
(µm)	150-75	27.74	1.64	552	2	9.6	3.4	7	3.4	6.4	49.1	<1	156	0.5	6.2	2.6	115	0.8	127	19.2	36.7	4.55	17.1	3.31	0.77	3.26	0.52	3.19	19.1	0.67
	75-45	24.96	1.19	680	5	12.6	4.7	8.8	6.1	9.6	66.8	<1	196	0.6	11.6	3.7	157	1.1	234	28.1	53.9	6.6	25.9	5.14	1.13	4.75	0.77	4.7	28.1	0.96
	45-25	16.76	1.49	784	4	15.7	5.6	11.7	7.8	11.7	79.9	1	231	0.8	11.3	4.2	194	1.5	296	33.2	64.9	7.76	30.1	6.21	1.27	5.54	0.87	5.17	32.6	1.08
	<25	9.80	2.4	960	5	19.9	7.4	18.1	6.7	13.7	95.8	2	270	1	12.2	5.1	234	1.7	252	38.4	73.1	8.98	34	6.79	1.49	6.24	1	6.1	37	1.25
S1 ESP12	>75	8.18	22.93	519	3	11.3	3.9	12.3	2.7	7.2	57.3	3	157	0.5	6.8	3.2	151	1.2	105	21.8	42.7	5.09	19.5	3.74	0.81	3.44	0.52	3.18	18.5	0.65
	75-45	12.80	12.57	729	3	14.2	5.6	14.4	4.3	9.8	78.4	2	198	0.7	10.8	4	193	1.9	164	28.9	56.4	6.92	26.1	5.17	1.12	4.62	0.72	4.43	26.2	0.87
	45-25	36.82	3.54	865	3	18.4	7.6	18.9	5.5	12.2	94.3	2	246	0.9	11.5	4.9	229	2	197	35.7	68.3	8.15	31.4	6.08	1.29	5.64	0.86	5.16	31.9	1.06
	<25	40.73	1.53	949	3	20.1	8.5	26.4	4.9	13.3	107	3	274	0.9	12.5	5.5	255	2.3	179	37.9	72.5	8.82	34	6.86	1.41	6	0.93	5.7	34.1	1.16
	45-25 ws	6.44	5.65	717	2	14.1	6.1	10.3	5.1	10.7	81.9	2	206	0.8	10.6	3.9	177	1	197	31.5	60.1	7.33	28.3	5.59	1.23	5.01	0.79	4.84	27.7	0.93
	<25 ws	72.26	1.66	900	5	19.6	7.9	24.6	5.2	13.4	104	3	263	0.9	12.4	5	234	3.2	184	36.8	71	8.73	33.7	6.65	1.41	5.88	0.93	5.52	32.9	1.12
S1 ESP15	>75	10.88	17.16	410	2	8.8	3	7.4	2.6	6	46.8	1	147	0.4	6	2.3	111	1	95.2	18.5	35.1	4.24	15.7	3.13	0.7	2.95	0.47	2.87	16.3	0.59
	75-45	15.35	7.36	552	1	11.6	4.5	8.8	4.6	8.9	65.5	<1	182	0.6	8.7	3.1	152	1.2	166	25.7	50.7	5.99	23.2	4.63	1.01	4.28	0.68	3.95	22.3	0.83
	45-25	32.21	2.65	759	2	18	6.7	18.1	5.6	12	89.6	2	264	0.8	11.3	4.7	214	2	209	34.1	64.7	7.83	29.9	5.81	1.3	5.65	0.85	4.91	31.6	1.09
	<25	39.11	1.62	957	5	21.9	8	26.2	5.4	14.2	108	3	319	1	13	5.5	262	2.5	201	40.6	77.6	9.41	35.8	7.12	1.54	6.54	1.03	6.25	36.1	1.25
	45-25 ws	9.00	3.38	688	2	15.8	6.2	11.6	6.1	11.4	81.3	1	235	0.7	11.4	3.9	174	1.2	226	32.2	61.4	7.6	28.5	5.78	1.24	5.22	0.82	5.18	29.6	1
	<25 ws	64.10	1.64	893	6	21.2	7.6	26.2	5.3	13.9	103	3	305	0.9	12.7	5.1	242	1.8	193	38.2	72.9	8.82	33.3	6.59	1.48	6.09	0.97	5.74	35	1.17
S1 ESP22	>75	8.16	26.76	570	2	11.1	4.1	14.1	3	7.5	58.7	2	159	0.5	6.9	3.4	152	1.4	102	22.3	41.1	5.11	19.7	3.84	0.84	3.61	0.55	3.31	19.9	0.71
	75-45	13.11	12.84	775	3	15	6.1	16.9	4.3	10	79.4	2	199	0.7	10.7	4.6	203	1.9	153	30.9	57.4	7.02	26.9	5.39	1.17	4.73	0.74	4.29	24.8	0.88
	45-25	35.47	4.31	926	5	18.9	7.7	24.7	5.3	13.1	102	3	262	0.8	12.7	5.4	268	2.2	197	38.9	75.1	9.3	35.4	6.85	1.51	6.25	0.96	5.84	33.5	1.21
	<25	41.74	1.29	1014	4	21.9	8.8	30.9	5.4	15	116	3	287	1	14.8	6.1	285	2.7	196	42.5	82.5	10.1	37.7	7.34	1.69	6.94	1.07	6.51	37.1	1.35
S1 ESP25	>75	10.59	18.91	626	3	13.6	4.8	17.9	3.1	8.5	67.3	2	204	0.6	8.3	4.2	181	2.7	114	26	48.3	5.95	22.3	4.53	0.98	4.04	0.64	3.75	21.6	0.81
	75-45	14.26	9.41	688	3	14.1	5.4	15	4.3	9.7	74.4	2	220	0.7	9.3	4.3	188	5.8	155	28.4	55.3	6.72	25.8	5.13	1.13	4.74	0.73	4.31	25.7	0.88
	45-25	35.35	3.79	860	6	18.1	6.8	21.9	5.3	12.4	91.6	3	269	0.9	12.8	5.5	247	2.1	198	36.5	69.5	8.58	31.9	6.31	1.44	6.03	0.91	5.61	32.5	1.17
	<25	38.45	1.75	1045	4	22.7	8.3	30.2	5.5	14.7	110	4	310	1.1	14.2	6.5	291	2.2	196	41.7	82	9.99	37.2	7.32	1.64	7.05	1.07	6.52	35.9	1.36
S1 ESP 32/42	>75	10.51	24.92	582	<1	11.7	4.5	14.8	2.9	7.8	61.2	9	179	0.4	6.9	3.5	174	1.7	112	23.1	44.4	5.16	19	3.85	0.86	3.49	0.58	3.28	18.7	0.67
	75-45	16.19	10.24	787	1	14.6	6.5	17.8	4.6	10.8	84.2	2	212	0.9	10.5	4.7	223	1.7	177	30.5	59.3	7.17	26.9	5.19	1.19	4.87	0.78	4.44	26.3	0.95
	45-25	32.74	3.88	873	4	16.6	7.1	18.3	5.3	12.1	91.8	3	243	0.8	12	5	227	1.9	201	35.3	68	8.37	31.8	6.34	1.35	5.78	0.87	5.32	30.3	1.12
	<25	36.43	1.49	951	5	20.2	8.1	26	5.1	13.5	105	3	264	0.9	13.3	5.7	255	2.1	186	37.6	74.8	9.06	35.3	6.85	1.54	6.45	0.98	6.18	34.2	1.22

Table A6 – Continuation.

Sample	Fraction	Er	Tm	Yb	Lu	∑REE	REO	L/H	Critical	Uncritical	Excessive	EF	Recovery	La_N/Lu_N	La_N/Sm_N	Gd_N/Lu_N	Y_N/Ho_N	Eu_N/Eu^*	Ce_N/Ce_N^*	Gd_N/Gd_N^*	REYdef, rel%	C_{outl}
S1 BA (mm)	>4	3.25	0.47	3.03	0.46	195.7	235.34	7.16	72.15	52.91	70.64	0.98	19.07	0.72	0.82	0.94	1.14	1.00	0.95	1.09	36.87	1.02
	4-2	3.41	0.48	3.23	0.5	206.83	248.72	7.26	76.62	55.70	74.51	1.04	19.77	0.70	0.86	0.92	1.18	1.07	0.95	1.14	37.04	1.03
	2-1	3.31	0.49	3.17	0.5	207.22	249.30	7.31	77.13	55.84	74.25	1.04	13.46	0.71	0.85	0.91	1.13	1.06	0.94	1.10	37.22	1.04
	1-0.5	3.47	0.48	3.22	0.49	208	250.17	7.39	75.25	56.47	76.28	1.04	7.61	0.73	0.84	0.92	1.18	0.99	0.96	1.09	36.18	0.99
	0.5-0.25	3.27	0.47	3.01	0.5	201.42	242.19	7.48	73.72	54.13	73.57	1.01	6.04	0.68	0.83	0.89	1.12	1.03	0.96	1.11	36.60	1.00
	0.25-0.125	3.12	0.42	2.88	0.44	184.66	222.06	7.24	67.25	50.33	67.08	0.93	7.91	0.73	0.85	0.94	1.10	1.05	0.95	1.11	36.42	1.00
	0.125-0.090	3.13	0.45	2.83	0.44	187.45	225.34	7.24	68.52	51.25	67.68	0.94	5.69	0.73	0.81	0.97	1.08	0.99	0.95	1.12	36.55	1.01
	0.090-0.063	3.23	0.44	2.95	0.47	193.16	232.33	7.33	70.55	51.99	70.62	0.97	6.35	0.70	0.85	0.89	1.13	1.07	0.96	1.10	36.52	1.00
	<0.063	3.22	0.47	3.03	0.47	199.03	239.32	7.36	73.01	54.66	71.36	1.00	14.11	0.74	0.86	0.92	1.14	1.02	0.93	1.11	36.68	1.02
S1 Eco (µm)	> 150	2.97	0.44	2.88	0.45	188.09	226.23	7.29	69.35	50.72	68.02	1.13	23.43	0.71	0.86	0.92	1.13	1.03	0.95	1.12	36.87	1.02
	150-75	1.99	0.27	1.81	0.28	112.72	135.60	6.81	42.67	30.32	39.73	0.68	18.78	0.69	0.88	0.90	1.13	1.07	0.92	1.12	37.85	1.07
	75-45	2.96	0.41	2.66	0.43	166.51	200.28	6.85	63.56	44.59	58.36	1.00	24.96	0.65	0.83	0.86	1.16	1.03	0.93	1.08	38.17	1.09
	45-25	3.28	0.49	3.15	0.48	196.1	235.92	7.15	73.29	52.71	70.10	1.18	19.74	0.69	0.81	0.89	1.19	0.98	0.95	1.09	37.37	1.05
	<25	3.64	0.54	3.5	0.53	222.56	267.73	7.14	83.23	60.41	78.92	1.34	13.09	0.72	0.86	0.91	1.17	1.04	0.93	1.09	37.40	1.05
S1 ESP12	>75	1.85	0.26	1.73	0.27	124.04	149.14	7.87	44.36	34.07	45.61	0.64	5.22	0.81	0.88	0.99	1.12	1.04	0.95	1.13	35.76	0.97
	75-45	2.69	0.37	2.59	0.39	167.49	201.41	7.47	61.26	45.61	60.62	0.86	11.02	0.74	0.85	0.92	1.19	1.04	0.94	1.10	36.58	1.01
	45-25	3.1	0.44	2.98	0.47	202.53	243.59	7.66	73.71	55.57	73.25	1.04	38.33	0.76	0.89	0.93	1.19	1.01	0.94	1.13	36.39	1.01
	<25	3.48	0.49	3.21	0.49	217.05	260.99	7.53	79.62	59.58	77.85	1.12	45.44	0.77	0.84	0.95	1.16	1.00	0.93	1.09	36.68	1.02
	45-25 ws	2.79	0.41	2.75	0.41	179.68	216.00	7.48	65.65	49.43	64.60	0.91	5.89	0.77	0.85	0.95	1.18	1.05	0.93	1.09	36.54	1.02
	<25 ws	3.33	0.49	3.18	0.48	212.12	255.02	7.56	77.79	58.06	76.27	1.09	78.03	0.77	0.84	0.95	1.16	1.02	0.93	1.08	36.67	1.02
S1 ESP15	>75	1.65	0.23	1.49	0.24	104.16	125.26	7.38	37.69	28.82	37.65	0.56	6.04	0.77	0.90	0.95	1.09	1.05	0.93	1.10	36.18	1.00
	75-45	2.45	0.33	2.27	0.35	148.67	178.71	7.35	53.59	40.60	54.48	0.79	12.17	0.73	0.84	0.95	1.06	1.03	0.96	1.10	36.05	0.98
	45-25	3.1	0.45	3.06	0.45	194.8	234.31	7.34	71.66	53.39	69.75	1.04	33.47	0.76	0.89	0.97	1.15	1.06	0.93	1.16	36.79	1.03
	<25	3.71	0.53	3.58	0.54	231.6	278.46	7.34	84.43	63.67	83.50	1.24	48.32	0.75	0.86	0.94	1.14	1.03	0.93	1.10	36.46	1.01
	45-25 ws	3.12	0.44	2.88	0.46	185.44	222.98	7.15	68.46	50.80	66.18	0.97	8.76	0.70	0.84	0.88	1.17	1.02	0.92	1.10	36.92	1.03
	<25 ws	3.42	0.52	3.35	0.52	218.07	262.29	7.41	79.91	59.70	78.46	1.14	73.33	0.73	0.88	0.91	1.18	1.06	0.94	1.09	36.64	1.02
S1 ESP22	>75	2.06	0.29	1.96	0.3	125.58	150.96	7.26	46.36	34.86	44.36	0.59	4.80	0.74	0.88	0.93	1.11	1.04	0.91	1.13	36.92	1.05
	75-45	2.69	0.38	2.48	0.38	170.15	204.44	7.77	60.59	48.04	61.52	0.80	10.46	0.81	0.87	0.96	1.11	1.05	0.92	1.09	35.61	0.98
	45-25	3.66	0.51	3.29	0.51	222.79	267.77	7.52	80.87	61.30	80.62	1.04	37.07	0.76	0.86	0.95	1.09	1.06	0.93	1.12	36.30	1.00
	<25	3.97	0.57	3.66	0.57	243.52	292.76	7.38	88.04	66.83	88.65	1.14	47.67	0.75	0.88	0.94	1.09	1.09	0.94	1.13	36.15	0.99
S1 ESP25	>75	2.35	0.34	2.2	0.35	144.14	173.22	7.46	51.62	40.52	52.00	0.70	7.46	0.74	0.87	0.89	1.05	1.03	0.91	1.09	35.81	0.99
	75-45	2.68	0.39	2.51	0.4	164.82	198.17	7.36	60.35	44.99	59.48	0.80	11.47	0.71	0.84	0.92	1.15	1.05	0.94	1.12	36.62	1.01
	45-25	3.43	0.48	3.08	0.5	207.94	250.01	7.27	75.79	57.42	74.73	1.02	35.90	0.73	0.88	0.93	1.10	1.08	0.92	1.15	36.45	1.01
	<25	3.97	0.57	3.65	0.57	240.51	289.09	7.26	86.30	66.06	88.15	1.17	45.17	0.73	0.86	0.96	1.04	1.06	0.95	1.15	35.88	0.98
S1 ESP 32/42	>75	2.01	0.3	2.01	0.3	127.71	153.53	7.62	44.43	35.60	47.68	0.68	7.11	0.77	0.91	0.90	1.10	1.05	0.96	1.06	34.79	0.93
	75-45	2.76	0.4	2.6	0.42	173.77	208.92	7.56	62.37	47.73	63.67	0.92	14.92	0.73	0.89	0.90	1.09	1.07	0.94	1.10	35.89	0.98
	45-25	3.3	0.46	3.01	0.47	201.79	242.52	7.44	72.94	55.79	73.06	1.07	35.03	0.75	0.84	0.95	1.07	1.03	0.93	1.13	36.15	1.00
	<25	3.73	0.52	3.34	0.52	222.29	267.22	7.20	81.93	59.96	80.40	1.18	42.94	0.72	0.83	0.96	1.11	1.07	0.95	1.14	36.86	1.02

Table A6 – Continuation.

Sample	Fraction	wt.%	Ct	Ba	Be	Co	Cs	Ga	Hf	Nb	Rb	Sn	Sr	Ta	Th	U	V	W	Zr	La	Ce	Pr	Nd	Sm	Eu	Gd	Tb	Dy	Y	Ho
S1 ESP 35/45	>75	10.7	18.41	709	2	15.3	5.4	20.1	3.4	9.8	75.5	2	228	0.6	9.2	4.7	196	2.2	127	28.3	53.1	6.28	24	4.7	1.06	4.24	0.68	3.92	22.7	0.87
	75-45	13.6	8.77	782	2	15.5	5.9	16.6	4.7	10.9	81.9	2	238	0.7	11	4.7	207	2	173	31.2	57.7	7.15	27.9	5.17	1.18	4.88	0.78	4.73	27.4	0.97
	45-25	23.5	4.32	797	4	16.5	6.2	16.7	5.6	11.9	86	2	251	0.8	11.9	4.8	217	2	209	33.6	66.1	8.06	30.2	6.06	1.28	5.69	0.88	5.33	31.1	1.1
	<25	50.9	2.04	1022	3	22.4	8.7	30	5.4	14.4	107	3	301	1	14.2	6.5	285	2.3	196	41.1	78.3	9.7	37.4	7.29	1.6	6.85	1.03	6.3	36	1.3
S4 BA (mm)	>4	38.9	0.08	915	4	21	6.5	13	6	13.3	87.8	<1	293	1	12.2	4.7	197	3.5	219	37.1	72.3	8.35	30.8	6.25	1.37	5.79	0.94	5.61	33.7	1.13
	4-2	19.4	0.14	1004	5	21.1	6.9	14.3	5.9	13.5	91.3	1	311	1	12.8	5.1	214	1.1	219	37.6	73.7	8.73	33.5	6.64	1.43	6.4	1.01	5.87	34.5	1.23
	2-1	10.7	0.17	1023	2	20.7	7.1	15.3	6.1	13.6	92.6	1	323	0.9	12.2	5.3	223	1.8	220	36.9	71.9	8.67	33	6.52	1.49	6.24	1.03	6.08	36.7	1.26
	1-0.5	5.09	0.19	947	1	18.7	6.5	14.9	5.4	13.8	83.5	1	292	0.9	11.5	4.7	210	1.4	206	35.9	68.5	8.36	31.9	6.25	1.36	5.97	0.93	5.54	32.6	1.16
	0.5-0.25	4.57	0.45	920	5	18.2	6	14.2	5.4	13.4	81.5	2	292	0.8	11.2	4.8	204	1.7	211	34.2	67	8.2	30.1	5.89	1.34	5.87	0.91	5.35	32.4	1.14
	0.25-0.125	6.29	0.62	869	3	18.3	5.8	12.9	5.3	12	76.3	1	274	0.8	11.1	4.6	190	1.6	189	32.9	64.5	7.92	29.2	5.86	1.28	5.55	0.89	5.34	29.5	1.12
	0.125-0.090	3.38	0.37	809	6	16.6	5.5	11.7	4.9	11.4	73.9	<1	258	0.8	10.1	4.3	178	1.2	186	31.7	61.4	7.46	28.5	5.38	1.24	5.32	0.85	5.15	28.9	1.08
	0.090-0.063	3.93	0.32	876	5	17.7	5.7	11.4	5.4	12.2	77.1	1	265	0.8	11.8	4.4	185	1.5	198	33.1	66.6	7.99	31	5.88	1.3	5.63	0.9	5.53	31.6	1.19
	<0.063	7.58	0.48	900	4	18.6	5.9	13.6	5.7	12.6	81.1	1	274	0.8	11.7	4.5	191	1.5	209	33.6	66.3	8.02	30.6	6.03	1.34	5.83	0.89	5.5	31	1.12
S4 ECO (µm)	> 150	13.5	7.76	888	4	17.9	5.7	15.5	4.6	11.6	76.1	1	291	0.8	10.5	4.7	198	1.9	170	32.3	62	7.59	28.7	5.45	1.29	5.4	0.86	5.37	29.7	1.08
	150-75	27.3	9.21	638	3	12.4	4.3	8.3	3.3	8.7	59.5	<1	205	0.6	8.1	3.2	140	1.1	136	25	49.5	6.02	22.3	4.32	0.96	4	0.65	3.88	21.6	0.81
	75-45	26.7	2.9	738	4	15.4	5.3	8.8	5.2	10.6	72.3	<1	231	0.8	11.1	3.7	163	1.5	191	29.9	59.4	7.06	26.4	5.01	1.12	4.96	0.78	4.6	25.5	0.95
	45-25	17.8	1.71	844	4	17.9	5.8	10.1	6.7	11.9	75.6	<1	261	0.8	10.8	4.4	176	1.1	241	32.5	63.2	7.7	29	5.53	1.21	5.34	0.85	5.15	29.4	1.11
	<25	12.5	2.75	1131	5	23.2	7.1	18.7	7.2	14.4	93.5	2	371	1	13	5.8	227	1.6	258	37.4	74.9	9.17	35.2	6.82	1.56	6.75	1.06	6.62	38.3	1.41
S4 ESP12	>75	8.02	27.22	456	<1	9.6	3.5	6.5	2.5	6.2	46.6	<1	147	0.5	6.2	2.7	126	1.5	94.9	18.6	36.6	4.37	16.2	3.35	0.72	3.07	0.46	2.78	15.7	0.59
	75-45	14.4	10.14	743	5	14.4	5.1	10.7	4.4	9.7	71.3	1	223	0.7	9.3	4.1	176	1.6	170	29.4	57.6	6.99	27.6	4.97	1.12	4.57	0.7	4.14	24.5	0.89
	45-25	26.1	4.84	999	3	20	6.9	19.9	5.5	12.5	88.9	2	319	0.9	11.5	5.9	241	2.6	203	34.6	68.1	8.31	31.7	6.11	1.36	5.78	0.91	5.45	32	1.18
	<25	49.6	1.62	1334	6	26.3	8.5	31.8	5.5	15.2	109	3	393	1.1	13.8	6.9	293	2.9	200	41.4	81.2	9.85	38.2	7.45	1.71	7.06	1.12	6.89	39.6	1.47
	45-25 ws	5.71	2.7	842	3	16.4	6.2	11.3	5.5	11.1	79.8	1	252	0.8	10.8	4.5	184	1.2	199	31.1	62.7	7.54	28.8	5.57	1.21	5.42	0.82	4.93	29.2	1.08
	<25 ws	71.4	5.59	1369	5	27	8.7	32.5	5.6	15.7	111	3	391	1	14.3	7.3	275	2.4	205	42.7	82.9	10.2	38.2	7.5	1.68	7.21	1.14	6.76	40	1.46
S4 ESP22	>75	4.90	53.9	492	2	9.1	3	11.6	1.9	5.4	39.4	1	147	0.4	5.4	3.4	140	2.3	68.3	16.2	30.7	3.92	14.9	2.82	0.65	2.58	0.41	2.43	14.1	0.54
	75-45	10.0	20.78	970	5	18.7	5.7	23.2	3.6	10.6	75.3	3	270	0.7	10.2	5.7	252	2.8	139	32	61.6	7.45	28.5	5.62	1.19	5	0.8	4.74	27.1	1
	45-25	28.5	5.17	1265	7	25.2	7.4	32.5	4.9	14	95.2	4	356	0.9	13.8	7.2	316	3.4	178	39.5	76.6	9.42	36	7.21	1.62	6.83	1.06	6.7	37.5	1.27
	<25	55.0	1.57	1490	8	29.6	9	39.9	5.1	15.4	109	5	413	1.1	14.9	8	340	4	187	45.3	86.9	10.9	41.8	7.89	1.84	7.76	1.18	7.39	43.8	1.44
S4 ESP32	>75	3.61	41.71	1020	5	18.4	4.4	27.9	2.9	8.6	56.5	4	276	0.6	8.6	5.5	241	4	103	26	49.6	6.16	23.8	4.59	1.03	4.38	0.67	3.99	23.4	0.88
	75-45	19.0	18.54	1342	2	25.2	6.6	38.6	4.2	12.5	84.9	5	361	0.8	12.5	8.1	346	4.7	151	38.3	72.2	8.93	34.3	6.51	1.44	6.27	0.96	5.78	32.7	1.19
	45-25	32.8	3.4	1611	5	30.4	8.4	44.2	4.9	15	101	6	430	1	15.1	9.3	378	6.1	183	45.5	86.1	10.7	41.3	7.97	1.83	7.69	1.18	7.24	42.6	1.48
	<25	46.3	1.25	1663	6	32.4	8.7	46.8	4.9	15.6	107	6	440	1	15.6	9	388	4.7	182	46.7	90.2	11.2	41.4	8.19	1.95	7.87	1.24	7.51	44.3	1.57
Minimum				410	1	8.8	3.0	6.5	1.9	5.4	39.4	1	147	0.4	5.4	2.3	111	0.8	68.3	16.2	30.7	3.92	14.9	2.82	0.65	2.58	0.41	2.43	14.1	0.54
Average				875	4	17.9	6.3	18.3	5.0	11.7	84.2	2	260	0.8	11.2	4.9	216	2.0	184.1	33.2	64.3	7.83	29.8	5.84	1.29	5.48	0.86	5.16	30.1	1.07
Maximum				1663	8	32.4	9.0	46.8	7.8	15.7	115.7	9	440	1.1	15.6	9.3	388	6.1	295.6	46.7	90.2	11.22	41.8	8.19	1.95	7.87	1.24	7.51	44.3	1.57
CV (%)				27.7	39.3	26.7	22.9	48.4	22.6	20.7	20.1	62.2	25.1	21.2	20.1	27.7	25.6	53.2	22.6	19.3	19.5	19.8	19.9	19.8	20.6	20.7	20.3	21.1	21.3	20.5

Table A6 – Continuation.

Sample	Fraction	Er	Tm	Yb	Lu	∑REE	REO	L/H	Critical	Uncritical	Excessive	EF	Recovery	La_N/ Lu_N	La_N/ Sm_N	Gd_N/ Lu_N	Y_N/ Ho_N	Eu_N/ Eu*	Ce_N/ Ce_N*	Gd_N/ Gd_N*	REYdef, rel%	C_{outl}
S1 ESP 35/45	>75	2.62	0.37	2.27	0.36	155.5	186.84	7.66	54.98	43.52	56.97	0.75	8.05	0.79	0.91	0.91	1.03	1.07	0.94	1.08	35.36	0.97
	75-45	2.86	0.42	2.76	0.41	175.5	210.96	7.32	64.85	48.40	62.26	0.85	11.55	0.76	0.91	0.92	1.12	1.07	0.91	1.10	36.95	1.04
	45-25	3.31	0.48	3.04	0.46	196.7	236.53	7.16	72.10	53.41	71.18	0.95	22.35	0.73	0.84	0.96	1.12	1.00	0.95	1.12	36.66	1.01
	<25	3.9	0.55	3.54	0.57	235.4	282.95	7.30	86.23	64.94	84.26	1.14	58.05	0.72	0.85	0.93	1.09	1.05	0.92	1.14	36.63	1.02
S4 BA (mm)	>4	3.52	0.49	3.31	0.52	211.2	254.08	7.33	75.94	57.49	77.75	1.01	39.36	0.71	0.90	0.86	1.18	1.03	0.97	1.08	35.96	0.98
	4-2	3.67	0.55	3.54	0.57	218.9	263.28	7.08	79.98	59.37	79.59	1.05	20.32	0.66	0.86	0.87	1.11	1.01	0.96	1.12	36.53	1.00
	2-1	3.84	0.55	3.58	0.57	218.3	262.67	6.85	82.14	58.33	77.86	1.05	11.22	0.65	0.86	0.85	1.15	1.05	0.95	1.08	37.62	1.05
	1-0.5	3.56	0.5	3.26	0.52	206.3	248.05	7.10	75.89	56.48	73.94	0.99	5.03	0.69	0.87	0.89	1.11	1.02	0.93	1.12	36.78	1.03
	0.5-0.25	3.42	0.51	3.27	0.49	200.1	240.68	7.00	73.52	54.16	72.41	0.96	4.38	0.70	0.88	0.93	1.12	1.06	0.94	1.14	36.74	1.02
	0.25-0.125	3.28	0.48	3.11	0.47	191.4	230.09	7.00	69.49	52.23	69.68	0.92	5.77	0.70	0.85	0.92	1.04	1.02	0.94	1.10	36.31	1.00
	0.125-0.090	3.14	0.45	2.98	0.46	184	221.23	6.98	67.78	49.86	66.37	0.88	2.98	0.69	0.89	0.90	1.06	1.06	0.94	1.12	36.83	1.02
	0.090-0.063	3.34	0.51	3.2	0.47	198.2	238.41	7.02	73.67	52.60	71.97	0.95	3.74	0.70	0.85	0.93	1.05	1.03	0.96	1.10	37.16	1.02
	<0.063	3.46	0.48	3.26	0.5	197.9	237.96	6.93	72.79	53.48	71.66	0.95	7.20	0.67	0.84	0.90	1.09	1.05	0.95	1.14	36.78	1.02
S4 ECO (µm)	> 150	3.1	0.47	3.08	0.46	186.9	224.66	6.93	69.02	50.74	67.09	1.08	14.61	0.70	0.90	0.91	1.09	1.09	0.93	1.12	36.94	1.03
	150-75	2.29	0.33	2.28	0.34	144.3	173.45	7.41	51.68	39.34	53.26	0.84	22.81	0.74	0.88	0.91	1.05	1.04	0.95	1.08	35.82	0.97
	75-45	2.83	0.41	2.65	0.42	172	206.76	7.32	61.23	46.93	63.83	1.00	26.61	0.71	0.90	0.92	1.06	1.04	0.96	1.13	35.60	0.96
	45-25	3.17	0.47	3.19	0.48	188.3	226.39	7.04	68.78	51.07	68.45	1.09	19.41	0.68	0.89	0.86	1.05	1.02	0.94	1.11	36.53	1.00
	<25	4.07	0.6	3.97	0.6	228.4	274.77	6.58	86.81	60.14	81.48	1.32	16.56	0.62	0.83	0.87	1.07	1.06	0.95	1.13	38.00	1.07
S4 ESP12	>75	1.69	0.25	1.6	0.25	106.2	127.70	7.47	37.55	29.39	39.29	0.51	4.11	0.74	0.84	0.95	1.05	1.04	0.96	1.14	35.35	0.96
	75-45	2.56	0.38	2.38	0.39	168.2	202.14	7.98	60.62	45.93	61.64	0.81	11.66	0.75	0.90	0.91	1.09	1.08	0.95	1.12	36.04	0.98
	45-25	3.5	0.52	3.24	0.51	203.3	244.41	7.12	74.92	54.80	73.55	0.98	25.56	0.68	0.86	0.88	1.07	1.05	0.95	1.11	36.86	1.02
	<25	4.27	0.61	3.91	0.62	245.4	295.05	6.93	91.79	65.76	87.81	1.18	58.67	0.67	0.84	0.88	1.06	1.08	0.95	1.11	37.41	1.05
	45-25 ws	3.08	0.46	2.9	0.44	185.3	222.79	7.16	68.04	49.63	67.58	0.84	4.78	0.71	0.85	0.95	1.07	1.02	0.96	1.15	36.73	1.01
	<25 ws	4.19	0.62	3.87	0.59	249	299.46	7.09	91.97	67.60	89.44	1.13	80.44	0.72	0.86	0.95	1.08	1.05	0.94	1.11	36.93	1.03
S4 ESP22	>75	1.51	0.22	1.46	0.22	92.66	111.35	7.38	34.00	25.52	33.14	0.39	1.93	0.74	0.87	0.91	1.03	1.09	0.91	1.09	36.69	1.03
	75-45	2.89	0.42	2.83	0.41	181.6	218.21	7.54	65.22	50.07	66.26	0.77	7.76	0.78	0.86	0.95	1.07	1.01	0.94	1.08	35.92	0.98
	45-25	3.9	0.56	3.6	0.56	232.3	279.37	6.96	86.78	62.96	82.59	0.99	28.14	0.71	0.83	0.95	1.17	1.06	0.93	1.12	37.35	1.05
	<25	4.41	0.64	3.96	0.62	265.8	319.71	7.10	100.42	71.85	93.56	1.13	62.17	0.73	0.87	0.97	1.20	1.09	0.92	1.15	37.78	1.07
S4 ESP32	>75	2.44	0.35	2.26	0.34	149.9	180.18	7.26	55.33	41.13	53.43	0.58	2.09	0.76	0.86	1.00	1.05	1.06	0.92	1.14	36.91	1.04
	75-45	3.45	0.51	3.2	0.5	216.2	259.88	7.40	78.63	60.01	77.60	0.83	15.87	0.77	0.89	0.97	1.09	1.04	0.92	1.14	36.36	1.01
	45-25	4.35	0.62	3.99	0.61	263.2	316.45	7.12	98.50	71.88	92.80	1.02	33.34	0.75	0.87	0.98	1.14	1.08	0.92	1.14	37.43	1.06
	<25	4.69	0.64	4.16	0.65	272.3	327.49	7.05	101.09	73.98	97.22	1.05	48.70	0.72	0.86	0.94	1.12	1.11	0.93	1.12	37.13	1.04
Minimum		1.51	0.22	1.46	0.22	92.66	111.35	6.58	34.00	25.52	33.14	0.39	1.93	0.62	0.81	0.85	1.03	0.98	0.91	1.06	34.79	0.93
Average		3.17	0.46	2.97	0.46	192.01	230.87	7.27	70.40	52.33	69.28	0.95	22.16	0.73	0.86	0.92	1.11	1.04	0.94	1.11	36.61	1.01
Maximum		4.69	0.64	4.16	0.65	272.29	327.49	7.98	101.09	73.98	97.22	1.34	80.44	0.81	0.91	1.00	1.20	1.11	0.97	1.16	38.17	1.09
CV (%)		21.0	21.2	20.4	20.6	19.9	19.9	3.5	20.5	19.5	19.5	19.6	87.3	5.1	2.8	3.5	4.1	2.6	1.6	2.0	1.7	2.9

BA, bottom ash; ECO, economizer; ESP, Electrostatic precipitator; CV, coefficient of variation; REO, rare earth elements as oxides; L/H, ratio between light REE and heavy REE; REYdef, rel%, (Y+Nd+Eu+Tb+Dy+Er)/∑REE; C_{outl}, ((Nd+Eu+Tb+Dy+Er+Y)/∑REE)/((Ce+Ho+Tm+Yb+Lu)/∑REE))

Table A7 - Trace elements (ppm), enrichment patterns, anomalies for individual REE for coal combustion ashes magnetic and non-magnetic fractions.

	S1 BA		S1 ECO		S1 ESP		S4 BA		S4 ECO		S4 ESP12		Min	Avg	Max	CV (%)
	Mag	Non-mag	Mag	Non-mag	Mag	Non-mag	Mag	Non-mag	Mag	Non-mag	Mag	Non-mag				
wt.%	5.44	94.24	11.58	87.73	4.49	94.09	5.54	94.13	13.06	85.74	5.94	93.24				
Ba	821	858	686	756	641	958	859	928	704	823	679	1112	641	819	1112	16.0
Be	4	3	4	6	5	3	2	5	3	3	5	4	2	4	6	28.5
Co	19.8	17.1	21.7	13.1	43.7	18.1	23.4	18.5	34.1	14	44.1	19.7	13.1	23.9	44.1	42.9
Cs	6.3	6.9	3.8	5.2	3.6	8.1	5.3	6.6	3.8	5.7	3.2	7.80	3.2	5.5	8.1	29.0
Ga	15.6	13.7	13.8	12	27.8	23.2	12.7	12.8	13.5	11.1	24.1	22.4	11.1	16.9	27.8	32.7
Hf	5.4	5.9	3.4	6.2	3	5.4	5.1	5.8	3.6	5	3	5.4	3.0	4.8	6.2	23.6
Nb	12.1	12.5	8.4	10.5	8.7	13.5	11.7	12.9	9.4	11.3	8.7	13.2	8.4	11.1	13.5	16.2
Rb	86.7	93.3	51.6	76.3	48.1	104.5	73.4	84	54.5	76.7	45.8	98.1	45.8	74.4	104.5	26.0
Sn	1	<1	1	1	4	4	1	<1	1	<1	3	2	<1	2	4	77.6
Sr	248.6	242.1	214.1	211.5	216.3	257.6	269.9	282.5	245.3	250.6	229.8	320.0	211.5	249.0	320.0	12.0
Ta	0.8	0.8	0.7	0.8	0.6	1	0.8	0.9	0.7	0.7	0.6	0.90	0.6	0.8	1.0	15.0
Th	12.5	11.7	8.8	10	9.4	12.7	11.5	11.9	9.3	10.4	8.6	12.60	8.6	10.8	12.7	13.7
U	4.8	4.7	4.9	3.9	8.5	5.6	4.7	4.8	5	3.9	7.6	6.1	3.9	5.4	8.5	25.0
V	228	204	236	159	420	229	205	192	229	166	372	239	159	240	420	31.2
W	2.9	1.2	1.8	1.5	5.1	1.7	1.7	1.1	1.9	1	2.7	1.6	1	2.0	5.1	53.6
Zr	195.5	215.4	128.3	227	111.3	190.7	183.8	208.6	135.9	184.5	113.5	192.2	111.3	173.9	227	22.4
La	34.7	34.7	27.9	29.4	27.9	37	32.5	35.6	28.3	30.5	26.9	37.6	26.9	31.9	37.6	11.7
Ce	68.2	69.5	54.8	57.3	54.8	72.9	64.2	68.5	55.4	60.7	51.7	72.7	51.7	62.6	72.9	11.8
Pr	8.24	8.25	6.76	7	6.68	8.79	7.83	8.38	6.7	7.32	6.37	8.83	6.37	7.60	8.83	11.2
Nd	31.1	32	26	26.1	26.1	33.5	31	31.4	26	27.9	25.3	34	25.3	29.2	34	10.7
Sm	6.2	6.09	5.28	5.16	5.24	6.67	5.8	6.15	5.37	5.37	5.12	6.65	5.12	5.76	6.67	9.6
Eu	1.4	1.33	1.23	1.14	1.28	1.4	1.32	1.38	1.2	1.16	1.23	1.43	1.14	1.29	1.43	7.4
Gd	5.78	5.86	5.39	4.86	5.35	6.07	5.65	5.83	5.37	5.03	5.15	6.2	4.86	5.55	6.20	7.2
Tb	0.94	0.89	0.87	0.78	0.83	0.94	0.91	0.94	0.83	0.79	0.82	0.98	0.78	0.88	0.98	7.2
Dy	5.55	5.38	5.15	4.76	4.92	5.52	5.45	5.63	5.13	4.8	4.97	5.8	4.76	5.26	5.8	6.3
Y	31.7	29.9	28.6	25.8	27.2	30.6	30.9	33.1	29.5	28	28.3	34	25.8	29.8	34	7.7
Ho	1.14	1.14	1.05	0.94	1.02	1.12	1.13	1.18	1.03	1.05	1.04	1.19	0.94	1.09	1.19	6.6
Er	3.44	3.36	3.05	2.81	2.84	3.32	3.3	3.44	2.96	2.98	3.09	3.7	2.81	3.19	3.70	8.3
Tm	0.51	0.48	0.43	0.43	0.42	0.5	0.5	0.51	0.45	0.44	0.44	0.53	0.42	0.47	0.53	7.9
Yb	3.26	3.09	2.81	2.7	2.68	3.28	3.16	3.38	2.82	2.81	2.67	3.33	2.67	3.00	3.38	8.8
Lu	0.52	0.48	0.42	0.43	0.42	0.5	0.48	0.51	0.44	0.45	0.41	0.53	0.41	0.47	0.53	8.8
^{d}∑REE	202.7	202.5	169.7	169.6	167.7	212.1	194.1	205.9	171.5	179.3	163.5	217.5	163.5	188.0	217.5	10.0
REO	243.7	243.3	204.1	203.9	201.6	254.9	233.4	247.7	206.3	215.6	196.6	261.5	196.6	226.0	261.5	10.0
L/H	7.09	7.34	6.36	7.12	6.60	7.54	6.93	7.07	6.46	7.25	6.27	7.24	6.27	6.94	7.54	5.7
EF	1.00	1.00	1.01	1.01	0.81	1.02	0.95	1.01	0.97	1.02	0.77	1.02	0.77	0.97	1.02	8.5
Recovery	5.47	94.53	11.67	88.33	3.63	96.37	5.26	94.74	12.72	87.28	4.57	95.43	3.63	50.00	96.37	85.9
Critical	74.13	72.86	64.9	61.39	63.17	75.28	72.88	75.89	65.62	65.63	63.71	79.91	61.39	69.61	79.91	8.5
Uncritical	54.92	54.9	45.33	46.42	45.17	58.53	51.78	55.96	45.74	48.22	43.54	59.28	43.54	50.82	59.28	10.8
Excessive	73.63	74.69	59.51	61.8	59.34	78.3	69.47	74.08	60.14	65.45	56.26	78.28	56.26	67.58	78.30	11.4
La_N/ Lu_N	0.67	0.72	0.66	0.68	0.66	0.74	0.68	0.70	0.64	0.68	0.66	0.71	0.64	0.68	0.74	4.0
La_N/ Sm_N	0.85	0.86	0.80	0.86	0.81	0.84	0.85	0.88	0.80	0.86	0.80	0.86	0.80	0.84	0.88	3.4
Gd_N/Lu_N	0.86	0.95	0.99	0.88	0.99	0.94	0.91	0.89	0.95	0.87	0.97	0.91	0.86	0.92	0.99	4.8
Y_N/ Ho_N	1.10	1.04	1.08	1.08	1.05	1.08	1.08	1.11	1.13	1.05	1.08	1.13	1.04	1.08	1.13	2.6
Eu_N/ Eu*	1.06	1.03	1.06	1.03	1.12	1.00	1.05	1.05	1.04	1.02	1.10	1.01	1.00	1.05	1.12	3.2
Ce_N/Ce_N*	0.95	0.97	0.94	0.94	0.95	0.95	0.95	0.93	0.95	0.96	0.93	0.94	0.93	0.95	0.97	1.0
Gd_N/ Gd_N*	1.08	1.15	1.12	1.10	1.15	1.11	1.11	1.09	1.15	1.11	1.13	1.10	1.08	1.12	1.15	1.9
REYdef, rel%	36.57	35.99	38.23	36.19	37.67	35.49	37.54	36.85	38.26	36.60	38.96	36.75	35.49	37.09	38.96	2.7
C_{outl}	1.01	0.98	1.09	0.99	1.06	0.96	1.05	1.02	1.09	1.00	1.13	1.02	0.96	1.03	1.13	4.8

BA, bottom ash; ECO, economizer; ESP, Electrostatic precipitator; Mag, magnetic fraction; non-mag, non-magnetic fraction; CV, coefficient of variation; REO, rare earth elements as oxides; L/H, ratio between light REE and heavy REE; REYdef, rel%, (Y+Nd+Eu+Tb+Dy+Er)/∑REE; C_{outl}, ((Nd+Eu+Tb+Dy+Er+Y)/∑REE)/((Ce+Ho+Tm+Yb+Lu)/∑REE))

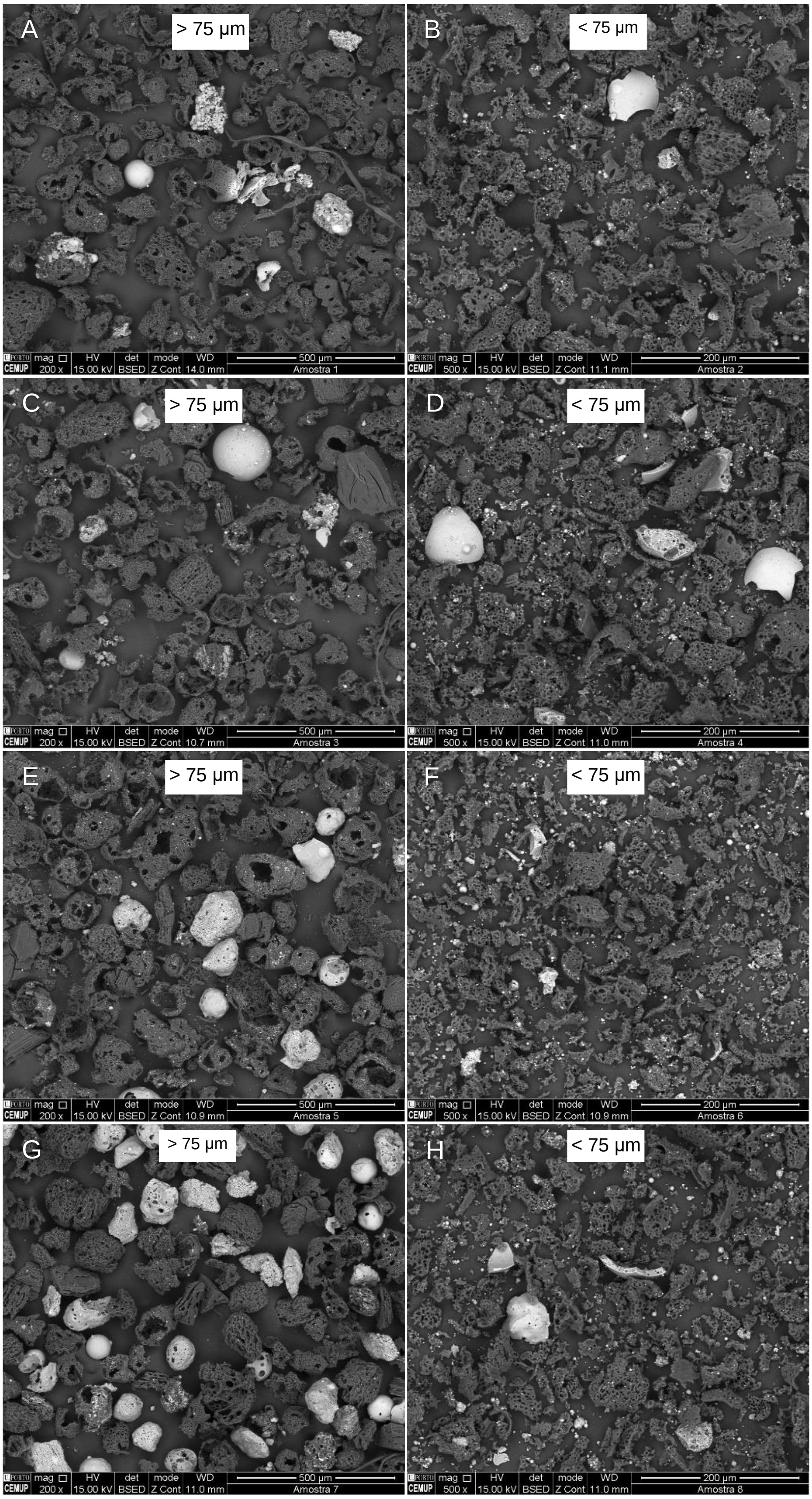

Figure A1 - Comparison of the size-fractions obtained after sonication trials (SEM/EDS, BSE mode): (1) 10 min – 50 %; 20 min – 50 %; (3) 20 min – 50 % and (4) 10 min – 70 % .

Table A8 - Trace elements results regarding magnetic concentrates and respective size-fractions. World coal ash (WCA; Ketris and Yudovich, 2009) added for comparison.

				PPB	%									PPM									
			C_{tot}	Ag	Al	Ca	Fe	K	Mg	Na	P	S	Ti	As	Ba	Be	Bi	Cd	Co	Cr	Cu	Hf	In
	WCA		n.a.	0.6	n.a.	n.a.	n.a.	n.a.	n.a.	n.a.	n.a	n.a	n.a	51	1040	13	7.9	1.5	39	125	115	9.3	0.39
S1-BA	Bulk		0.35	0.1	7.42	0.79	5.14	1.6	0.96	0.76	0.054	<0.04	0.478	2.1	764	4	0.13	0.27	17.7	91	56.6	3.87	0.03
	Fe	MC	0.07	0.1	8.52	1.26	9.05	1.49	1.45	0.634	0.059	<0.1	0.414	3	750	3	0.1	0.3	19.9	97	53.2	3.4	<0.05
		>500	0.04	0.1	8.65	0.98	5.43	1.87	1.16	0.71	0.067	<0.1	0.497	3	986	4	<0.1	0.5	20.2	86	54.7	4.1	<0.05
		500-150	0.08	0.1	9.11	1.25	6.32	1.78	1.28	0.692	0.074	<0.1	0.492	4	916	4	0.1	0.5	20.4	87	59.6	4	0.06
		150-75	0.08	0.1	8.49	1.2	8.21	1.68	1.46	0.644	0.074	<0.1	0.474	5	822	4	<0.1	0.6	20.5	91	56.3	3.6	<0.05
		75-45	0.1	0.1	8.55	1.17	10.2	1.52	1.58	0.634	0.065	<0.1	0.441	5	807	3	<0.1	0.6	22.9	100	56.9	3.5	<0.05
		<45	0.24	0.2	9.13	1.13	13.5	1.56	1.74	0.632	0.072	<0.1	0.463	7	844	4	0.1	0.7	30.6	169	66.8	3.7	0.06
		TL	0.24	0.1	8.43	0.82	4.45	1.62	0.96	0.719	0.053	<0.1	0.449	1	767	3	<0.1	0.2	16.7	77	47.4	3.9	<0.05
	Nd	MC	0.21	0.1	8.98	0.9	4.58	1.88	1.06	0.759	0.066	<0.1	0.497	3	914	3	0.1	0.5	19.3	85	63.3	4	0.05
		> 2000	0.05	0.1	9.07	0.93	4.94	1.93	1.09	0.686	0.06	<0.1	0.508	3	965	4	<0.1	0.4	21.1	104	67.6	4.3	0.05
		2000-500	0.05	0.2	9.36	0.96	4.96	1.9	1.12	0.681	0.069	<0.1	0.509	2	988	3	0.1	0.8	22.4	93	61.7	4.3	0.06
		500-150	0.28	0.1	8.78	1.05	4.87	1.77	1.11	0.737	0.069	<0.1	0.492	4	911	4	<0.1	0.6	24.5	85	54.7	3.9	0.06
		150-75	0.23	0.1	7.9	0.87	3.9	1.74	0.95	0.698	0.063	<0.1	0.459	4	831	3	<0.1	0.4	18.1	71	50.1	3.7	<0.05
		75-45	0.27	0.1	8.9	0.74	3.63	1.93	0.91	0.79	0.068	<0.1	0.481	4	894	3	0.3	0.6	18.6	71	51.3	3.8	0.05
		<45	0.51	0.1	9.18	0.6	3.8	2.02	0.94	0.844	0.063	<0.1	0.534	4	958	4	0.2	0.9	22.6	90	57.8	4.3	0.05
		TL	0.22	<0.1	8.22	0.84	4.98	1.64	1.02	0.751	0.062	0.1	0.479	12	803	4	<0.1	<0.1	17.4	108	44.8	4	<0.05
S1-ECO	Bulk		1.69	0.1	6.67	1.12	5.42	1.33	1.01	0.839	0.054	0.05	0.376	6.5	696	3	0.16	0.7	15.2	76	48.1	3.05	0.04
	Fe	MC	0.41	<0.1	6.43	2.09	23.8	0.96	2.48	0.443	0.066	<0.1	0.312	10	634	3	0.1	0.5	23	120	53	2.6	<0.05
		>150	2.52	0.2	8.84	1.45	7.04	1.73	1.43	0.777	0.085	<0.1	0.475	14	902	4	0.2	1.4	20.4	117	58.2	3.7	0.08
		150-75	1.15	0.1	7.28	2.25	17.6	1.15	2.26	0.583	0.08	<0.1	0.362	9	782	4	<0.1	0.9	20.2	103	49.5	3.1	<0.05
		75-45	0.27	0.1	6.75	1.99	22.3	0.95	2.45	0.408	0.066	<0.1	0.35	8	700	3	<0.1	0.6	25.8	105	54.1	2.9	<0.05
		<45	0.23	0.2	7.78	1.9	23.4	1.06	2.54	0.398	0.091	<0.1	0.395	16	814	4	0.2	1.2	34.5	174	74.6	3.5	0.07
		TL	1.76	0.1	7.12	0.92	2.67	1.42	0.82	0.781	0.052	<0.1	0.403	5	688	3	0.1	0.7	13.2	66	40	3	<0.05
	Nd	MC	0.53	0.2	8.44	1.17	3.86	1.7	1.1	0.744	0.063	<0.1	0.465	8	961	3	0.2	1.3	20	74	54.8	4.1	<0.05
		>150	0.68	0.2	9.2	1.05	4.62	1.8	1.15	0.767	0.069	<0.1	0.52	9	961	4	0.3	1.4	22.6	101	63.6	4.3	0.06
		150-75	0.46	0.1	6.52	1.28	3.22	1.3	0.96	0.824	0.06	<0.1	0.337	6	709	3	<0.1	0.7	13.7	55	39.5	2.7	0.05
		75-45	0.25	0.1	8.83	1.28	3.58	1.65	1.06	0.885	0.069	<0.1	0.445	6	844	3	0.2	0.7	16	59	48.4	3.5	<0.05
		<45	0.35	0.3	9.81	1.09	4.18	1.92	1.21	0.951	0.075	<0.1	0.57	10	1101	4	0.3	1.5	22.8	94	65	5	0.07
		TL	3.49	<0.1	6.68	0.84	1.45	1.22	0.59	0.94	0.049	<0.1	0.314	3	614	2	0.2	0.6	9.6	44	31.5	2.8	<0.05

BA - bottom ash; ECO, economizer fly ash; ESP, electrostatic; MC, magnetic concentrate; TL, tailings;

Table A8 – Continuation.

PPM																					
Li	Mn	Mo	Nb	Ni	Pb	Re	Rb	Sb	Se	Sn	Sr	Ta	Te	Th	Tl	U	V	W	Zn	Zr	Sc
87	460	15	23	105	61	n.a.	120	8.1	10.7	8.4	780	2.1	n.a.	24	5	16	180	8.4	180	240	25
80.7	593	4.6	12.03	60.7	11.17	<0.002	36	2.67	0.6	1.1	200	0.8	<0.05	5.6	0.48	3.9	217	1	89.8	142.6	14.2
70.3	1082	4.3	10.6	66.6	10.8	<0.005	73	3.2	<1	1.4	225	0.7	<0.5	9.3	<0.5	4.1	231	1.3	95	125.9	21
75.1	589	3.7	13.3	62.9	15.3	<0.005	101.1	4.1	<1	1.5	271	1	<0.5	12.1	0.6	4.9	231	4.2	114	148.1	19
72.7	749	4	12.5	65.2	14	<0.005	100.1	3.8	<1	1.4	272	0.9	<0.5	12.5	<0.5	4.9	225	4.2	109	144.2	20
68.1	1046	4.1	11.2	63.6	12.4	<0.005	80.1	3.5	<1	1.4	243	0.8	<0.5	10.4	<0.5	4.2	238	3	100	131.3	21
72	1173	4.6	10.9	68.2	12.5	<0.005	70.5	3.4	<1	1.5	231	0.8	<0.5	10.3	0.5	4.5	250	2.4	99	130	22
70.4	1319	6.7	11.4	96.2	14.5	<0.005	81.4	4.9	<1	2.2	241	0.7	<0.5	11	0.6	5.3	297	4.3	143	130.2	25
75.2	470	2.3	11.7	55	9.7	<0.005	84.4	2.4	<1	0.9	214	0.8	<0.5	9.5	<0.5	3.9	202	1	74	146	17
73.5	491	3.1	12.9	61.5	14.5	<0.005	97.6	3.6	<1	1.4	262	0.9	<0.5	11.8	0.6	4.6	224	2.5	110	148.3	19
75.2	535	2.9	13.3	77.8	14.7	<0.005	102.4	3.6	<1	1.3	274	0.9	<0.5	11.8	0.5	4.9	225	1.9	112	154	20
76.2	534	3.7	14	70.4	16.7	<0.005	104.6	4.5	<1	2.1	285	1	<0.5	12	0.7	5	236	2.4	132	160.8	20
80	540	3.4	12.9	66.1	13.3	<0.005	95.5	3.5	<1	1.3	262	0.9	<0.5	10.7	0.5	1.1	222	2.7	104	143.1	19
70.2	427	2.9	11.6	54.8	12.1	<0.005	89.2	3	<1	1.2	230	0.8	<0.5	10.6	0.5	4	199	3	88	131.2	17
79	383	3.1	12.9	56.4	14	<0.005	95.4	3.4	<1	1.2	238	0.9	<0.5	11.2	0.6	3.9	203	3.1	92	149.6	18
87	367	3	13.9	67.5	16.8	<0.005	105	3.9	<1	1.5	248	1	<0.5	12	0.7	4	219	4.6	116	165.7	20
72.5	512	3	11.5	63.2	8.2	<0.005	85.9	2.2	<1	0.8	216	0.8	<0.5	10.3	<0.5	4	197	1.8	67	151.9	18
64.2	626	5.4	8.79	50.1	11.52	0.008	31.9	3.42	0.9	1.3	194	0.6	0.07	5.5	0.56	3.3	184	1	82.9	108	12.6
43.8	2592	8.5	7.9	79.4	7.9	<0.005	51.3	4.5	<1	1.3	209	0.5	<0.5	7.9	<0.5	4.2	242	1.5	85	98.8	26
74.5	939	6.9	11.5	67	15.3	<0.005	82.9	6.3	<1	1.8	261	0.8	<0.5	10.8	0.6	4.8	252	1.7	120	132.4	22
56.1	2385	7.6	8.8	66	9.7	<0.005	66.8	4.1	<1	1.2	231	0.6	<0.5	10.2	<0.5	4.2	222	1.5	85	104	25
41.7	2546	7.6	8.3	79.5	9.1	<0.005	59.4	4.6	<1	1.4	220	0.6	<0.5	9.8	<0.5	4.6	244	1.4	88	104.5	27
49.1	2187	11	10.5	112.2	13.3	<0.005	72.6	7.8	<1	2.5	267	0.7	<0.5	11.8	0.6	7	346	2.7	146	122.9	29
62.1	304	3.3	9.3	44.3	10.3	<0.005	73.4	3	<1	1	196	0.6	<0.5	8	0.6	3.2	156	0.9	73	114.8	14
69.8	451	4.5	12.6	62	16	<0.005	101.9	5.1	<1	1.6	276	0.9	<0.5	12.6	0.7	5	204	1.7	116	147.2	17
76	508	5.3	13.2	70.2	18.5	<0.005	96.7	6.1	<1	2	282	0.9	<0.5	11.7	0.8	5.5	250	1.8	132	151.8	20
55.8	404	3.2	8.1	40.9	9.9	<0.005	69.9	2.9	<1	0.9	197	0.6	<0.5	8.9	<0.5	3.3	146	1.2	74	97.5	14
76.5	438	3.5	11.1	52.7	11.9	<0.005	80.8	3.7	<1	1.1	240	0.8	<0.5	11.3	0.5	4.2	196	1.1	80	137.5	18
98.5	478	5.3	14.2	70.8	19.4	<0.005	104.6	6	<1	1.8	322	1	<0.5	14.4	0.8	5.8	260	1.8	116	176.1	23
61.2	167	2	7.7	29.2	7.9	0.007	62.3	2	<1	0.6	176	0.5	<0.5	7.2	<0.5	2.6	114	0.7	52	94.4	11

Table A8 -Continuation.

				PPB	%									PPM									
			C_{tot}	Ag	Al	Ca	Fe	K	Mg	Na	P	S	Ti	As	Ba	Be	Bi	Cd	Co	Cr	Cu	Hf	In
S1-ESP12	Bulk		5.51	0.3	7.5	0.65	4.37	1.81	0.9	0.794	0.066	0.11	0.507	18	813	4	0.39	1.91	20.3	107	68.9	3.8	0.08
	Fe	MC	1.72	0.1	6.5	1.68	26.8	0.88	2.3	0.329	0.085	<0.1	0.293	24	565	4	0.2	1	40.2	242	59.1	2.4	0.07
		> 75	9.95	0.1	7.49	1.88	14.3	1.32	1.76	0.566	0.068	0.2	0.344	13	682	4	0.2	0.9	17.4	100	46.2	2.8	0.07
		75-45	3.58	0.1	7.72	1.99	25.4	1.09	2.43	0.498	0.07	<0.1	0.351	14	652	3	0.2	0.8	32.6	126	53.7	2.6	0.09
		45-25	1.32	0.1	6.93	1.72	26.3	0.88	2.3	0.408	0.076	<0.1	0.332	21	645	3	0.2	1.2	40	186	59.7	2.8	0.11
		<25	0.66	0.3	8.37	1.69	27.7	1.18	2.57	0.443	0.132	<0.1	0.4	53	827	6	0.6	2.5	47.9	374	83.1	3	0.15
		TL	5.69	0.3	8.61	0.58	3.15	1.96	0.92	0.784	0.065	<0.1	0.521	17	944	4	0.4	1.9	20.9	114	69	4.3	0.07
	Nd	MC	7.54	0.2	9.18	0.95	5.25	1.76	1.31	0.646	0.084	<0.1	0.497	24	899	4	0.4	2.1	24.7	155	67.5	3.7	0.08
		>75	16.79	0.2	7.82	0.87	4.5	1.64	1.04	0.717	0.068	<0.1	0.438	18	840	4	0.7	2.3	17.3	115	62.1	3.4	0.09
		75-45	10.32	0.2	9.16	0.97	4.45	1.84	1.1	0.813	0.07	<0.1	0.474	20	957	4	0.3	2.1	20.5	122	66.3	3.6	<0.05
		45-25	5.9	0.2	9.53	1.1	4.84	1.77	1.23	0.693	0.077	<0.1	0.494	24	881	4	0.3	1.8	23	144	66	3.8	<0.05
		<25	1.81	0.3	10.7	0.95	6.63	2.08	1.59	0.749	0.099	<0.1	0.596	32	1061	5	0.5	2.7	30.6	185	78.9	4.4	0.12
		TL	6.13	0.3	9.12	0.6	2.64	2.04	0.89	0.682	0.068	<0.1	0.529	18	1025	4	0.6	2.4	21.3	97	68.2	4.5	0.08
S4-BA	Bulk		0.22	0.1	7.43	0.83	5.99	1.44	0.87	0.692	0.043	<0.04	0.476	3.8	894	4	0.09	0.33	20.3	88	73.5	4.5	0.04
	Fe	MC	0.05	0.1	8.31	1.33	10.4	1.37	1.3	0.595	0.048	<0.1	0.408	5	811	4	0.1	0.4	24	98	49.3	3.4	<0.05
		TL	0.13	0.1	8.44	0.93	5.5	1.52	0.92	0.683	0.042	<0.1	0.466	4	907	4	<0.1	0.2	20.3	73	45.2	4.3	<0.05
S4-ECO	Bulk		5.32	0.1	8.77	1.31	6.32	1.42	0.97	0.684	0.049	0.07	0.422	11	854	4	0.11	0.76	18.3	85	47.2	3.75	0.04
	Fe	MC	2.73	0.1	7.35	1.73	24.3	1.06	1.72	0.437	0.055	<0.1	0.342	15	698	4	0.1	0.6	36.7	111	51	3	<0.05
		TL	5.97	0.1	7.89	0.97	2.94	1.46	0.8	0.663	0.043	<0.1	0.418	10	818	4	0.1	0.6	15.4	71	40.4	3.7	<0.05
S4-ESP	Bulk		6.32	0.3	10.9	1.22	5.53	1.73	1.08	0.862	0.06	0.15	0.511	28	1151	5	0.4	2.25	24.9	108	70.1	4.24	0.09
	Fe	MC	1.78	0.1	6.52	1.56	29.8	0.8	1.82	0.333	0.067	<0.1	0.289	27	652	5	0.2	1	49	212	59.3	2.4	0.06
		TL	7.1	0.3	9.11	0.82	3.28	1.83	0.95	0.799	0.055	<0.1	0.503	24	1156	5	0.4	1.9	23.3	103	66.3	4.3	0.07

BA - bottom ash; ECO, economizer fly ash; ESP, eletrostatic; MC, magnetic concentrate; TL, tailings;

Table A8 – Continuation.

Li	Mn	Mo	Nb	Ni	Pb	Re	Rb	Sb	Se	Sn	Sr	Ta	Te	Th	Tl	U	V	W	Zn	Zr	Sc
89.6	451	13	12.26	70	25.25	0.03	36.3	7.64	5	3	203	0.8	0.17	4.7	1.73	4.6	275	2.1	169.2	137.9	14.3
41.5	2315	15	7.9	111	13.2	<0.005	37.9	9.1	6	3.3	201	0.5	<0.5	7.5	0.7	7	419	4.1	164	89.4	25
64.4	1898	15	8.5	56.9	11.5	0.035	48.8	4.6	13	1.5	222	0.6	<0.5	7.9	0.7	3.9	225	2.2	88	99.1	22
58.7	2534	11	8.4	94.6	11.1	0.014	57.5	5.1	7	1.7	222	0.6	<0.5	10	0.5	5.4	290	2	98	102.9	26
54.2	2202	13	9	109.7	13.3	0.009	36.9	8	7	2.6	228	0.6	<0.5	8.9	0.6	7.2	376	3.4	149	95.8	26
60.1	2236	26	10.7	138	25.1	0.015	64.7	18.7	10	6.5	278	0.7	<0.5	12.2	1.3	13.3	664	8.5	301	112.3	33
88.6	338	5.8	13.9	73	27	0.015	95.1	7.5	7	3.7	239	0.9	<0.5	9.9	1.9	5.2	249	1.7	171	158.7	19
77.1	601	6.8	12.4	76.2	25.4	0.021	93.7	9.8	9	4.1	267	0.9	<0.5	12.3	1.7	6.4	314	2.3	184	139.5	22
75.5	524	7.5	11	61.2	22.2	0.031	84.6	8	8	2.8	242	0.7	<0.5	10.2	1.4	5.8	237	1.9	154	120.1	20
81.8	520	6.6	12	64.5	22.2	0.034	92.1	7.6	7	3	262	0.8	<0.5	11.9	1.4	6	260	2.2	146	132.9	20
80.4	579	6.8	12.1	71.4	22	0.026	86.3	8.8	11	3.3	278	0.8	<0.5	11.9	1.4	6.4	311	2.4	156	138	22
93	738	7.5	15.4	93.5	32.5	0.012	97.2	13	10	5.2	308	1	<0.5	12.7	1.9	8.3	404	2.7	237	158.5	26
82.1	295	4.3	14.3	68.7	29.1	0.022	112.9	8	8	3.5	261	1	<0.5	11.7	2	5.4	237	1.5	180	161	19
84.1	566	4.7	12.91	69.9	11.43	<0.002	35.2	3.47	<0.3	1.1	249	0.9	0.06	6.1	0.59	4.1	214	1	99.5	169.8	16.3
73.9	1111	5.8	11.1	77.2	10.6	<0.005	66.9	3.6	<1	1.2	267	0.7	<0.5	9.6	0.5	4.3	223	1.3	91	130.5	21
81.4	497	3	12.7	62.8	10.5	<0.005	78.4	3.2	<1	1	276	0.9	<0.5	10.3	0.5	4.2	210	1	84	167.8	20
83.6	626	11	11.29	61.1	11.43	0.015	43.2	3.89	1.1	1.2	262	0.8	0.07	7.5	0.81	3.9	201	1.3	74.3	138.4	17.2
56.6	2052	11	9.4	108	9	<0.005	60.1	4.6	<1	1.3	260	0.6	<0.5	8.6	0.6	4.7	251	1.9	90	114.4	24
79	297	4.6	11.3	50.3	10.6	0.01	78.7	3.3	<1	0.9	259	0.8	<0.5	9.6	0.8	3.8	174	1.1	71	138	18
96.5	538	21	13.18	84.4	26.23	0.048	53.7	10.1	18.9	3	323	0.9	0.15	7.8	2.02	5.7	283	2.6	159.4	158.5	20.9
45.3	2122	16	8.5	134.6	11.8	<0.005	43.4	8.7	9	2.7	224	0.5	<0.5	7.6	0.8	7.3	408	3.2	154	97.4	25
91.3	340	8.2	14.1	78.7	26.1	0.022	97.7	9.1	13	2.6	329	0.9	<0.5	11.2	2.1	5.7	253	1.8	170	164.4	23

Table A9 - Pearson´s correlation coefficients for bulk Fe-MC.

	C_{tot}	Al	Ca	Fe	K	Mg	Na	P	Ti	As	Ba	Be	Bi	Cd	Co	Cr	Cu	Hf	Li	Mn	Mo	Nb	Ni	Pb	Rb	Sb	Sn	Sr	Ta	Th	U	V	W	Zn	Zr	Sc
C_{tot}	1.00																																			
Al	-0.50	1.00																																		
Ca	0.32	-0.80	1.00																																	
Fe	0.75	**-0.94**	0.67	1.00																																
K	-0.65	**0.97**	-0.68	**-0.99**	1.00																															
Mg	0.23	**-0.88**	**0.88**	0.70	-0.74	1.00																														
Na	-0.72	**0.93**	-0.58	**-0.98**	**0.98**	-0.69	1.00																													
P	0.30	-0.72	0.39	0.63	-0.66	0.76	-0.73	1.00																												
Ti	-0.61	**0.98**	-0.70	**-0.98**	**0.99**	-0.80	**0.98**	-0.75	1.00																											
As	0.73	-0.79	0.31	**0.90**	**-0.90**	0.47	**-0.95**	0.68	**-0.88**	1.00																										
Ba	-0.49	**0.90**	-0.67	**-0.83**	**0.84**	**-0.89**	**0.87**	**-0.93**	**0.90**	-0.75	1.00																									
Be	0.58	-0.32	-0.16	0.53	-0.53	-0.15	-0.58	0.11	-0.45	0.75	-0.14	1.00																								
Bi	0.44	-0.62	0.03	0.67	-0.71	0.36	-0.79	0.77	-0.72	**0.90**	-0.68	0.69	1.00																							
Cd	0.66	-0.77	0.27	**0.86**	**-0.87**	0.48	**-0.94**	0.74	**-0.86**	**0.99**	-0.76	0.74	**0.94**	1.00																						
Co	0.80	-0.63	0.14	**0.82**	-0.79	0.23	**-0.86**	0.48	-0.75	**0.96**	-0.56	**0.88**	**0.83**	**0.93**	1.00																					
Cr	0.47	-0.71	0.18	0.73	-0.77	0.51	**-0.85**	**0.86**	-0.79	**0.91**	-0.79	0.59	**0.98**	**0.96**	0.80	1.00																				
Cu	0.36	-0.67	0.14	0.68	-0.70	0.50	-0.76	**0.86**	-0.75	**0.84**	-0.78	0.46	**0.94**	**0.86**	0.72	**0.93**	1.00																			
Hf	-0.51	**0.97**	-0.65	**-0.93**	**0.97**	**-0.82**	**0.95**	-0.81	**0.99**	**-0.87**	**0.92**	-0.42	-0.77	**-0.87**	-0.72	**-0.84**	**-0.81**	1.00																		
Li	-0.52	**0.98**	-0.77	**-0.93**	**0.94**	**-0.90**	**0.92**	-0.81	**0.98**	-0.79	**0.96**	-0.26	-0.65	-0.78	-0.62	-0.75	-0.73	**0.98**	1.00																	
Mn	0.53	**-0.96**	**0.92**	**0.90**	**-0.90**	**0.92**	**-0.85**	0.64	**-0.92**	0.65	**-0.87**	0.14	0.41	0.62	0.49	0.54	0.49	**-0.89**	**-0.95**	1.00																
Mo	0.74	**-0.82**	0.36	**0.92**	**-0.91**	0.51	**-0.97**	0.70	**-0.90**	**1.00**	-0.78	0.73	**0.89**	**0.99**	**0.95**	**0.91**	**0.82**	**-0.89**	**-0.82**	0.69	1.00															
Nb	-0.46	**0.97**	-0.81	**-0.89**	**0.91**	**-0.94**	**0.88**	-0.81	**0.95**	-0.72	**0.96**	-0.15	-0.58	-0.71	-0.53	-0.70	-0.69	**0.95**	**0.99**	**-0.96**	-0.75	1.00														
Ni	**0.81**	-0.67	0.21	**0.85**	**-0.82**	0.26	**-0.87**	0.45	-0.78	**0.96**	-0.56	**0.87**	0.80	**0.91**	**1.00**	0.77	0.69	-0.74	-0.64	0.54	**0.94**	-0.56	1.00													
Pb	0.14	-0.06	-0.50	0.12	-0.16	-0.10	-0.31	0.54	-0.18	0.52	-0.27	0.51	0.79	0.61	0.51	0.74	0.68	-0.26	-0.12	-0.16	0.50	-0.06	0.43	1.00												
Rb	-0.51	**0.93**	-0.56	**-0.89**	**0.94**	-0.76	**0.96**	**-0.83**	**0.95**	**-0.90**	**0.90**	-0.50	**-0.84**	**-0.92**	-0.75	**-0.91**	**-0.81**	**0.97**	**0.93**	**-0.82**	**-0.92**	**0.89**	-0.76	-0.41	1.00											
Sb	0.55	-0.75	0.22	0.80	**-0.83**	0.49	**-0.90**	0.81	**-0.84**	**0.96**	-0.78	0.68	**0.98**	**0.99**	**0.87**	**0.99**	**0.92**	**-0.87**	-0.77	0.58	**0.96**	-0.71	**0.85**	0.68	**-0.92**	1.00										
Sn	0.42	-0.60	0.05	0.63	-0.66	0.43	-0.76	**0.86**	-0.69	**0.85**	-0.74	0.55	**0.98**	**0.91**	0.76	**0.99**	**0.93**	-0.75	-0.66	0.42	**0.85**	-0.60	0.71	**0.83**	**-0.84**	**0.96**	1.00									
Sr	0.05	0.62	-0.42	-0.44	0.48	-0.77	0.48	**-0.88**	0.59	-0.40	0.81	0.21	-0.53	-0.45	-0.16	-0.61	-0.75	0.68	0.71	-0.57	-0.41	0.75	-0.15	-0.29	0.62	-0.54	-0.61	1.00								
Ta	-0.49	**1.00**	-0.76	**-0.93**	**0.96**	**-0.88**	**0.93**	-0.76	**0.99**	-0.80	**0.92**	-0.32	-0.66	-0.79	-0.64	-0.74	-0.72	**0.99**	**0.99**	**-0.95**	**-0.82**	**0.98**	-0.67	-0.10	**0.94**	-0.77	-0.64	0.67	1.00							
Th	-0.53	**0.97**	-0.66	**-0.93**	**0.95**	**-0.84**	**0.94**	**-0.84**	**0.98**	**-0.86**	**0.95**	-0.35	-0.75	**-0.85**	-0.70	**-0.83**	**-0.82**	**0.99**	**0.99**	**-0.90**	**-0.87**	**0.97**	-0.72	-0.25	**0.95**	**-0.85**	-0.75	0.73	**0.98**	1.00						
U	0.55	-0.64	0.05	0.73	-0.75	0.33	**-0.83**	0.71	-0.75	**0.95**	-0.66	0.77	**0.99**	**0.97**	**0.91**	**0.96**	**0.91**	-0.78	-0.66	0.44	**0.93**	-0.58	**0.88**	0.75	**-0.84**	**0.98**	**0.95**	-0.44	-0.67	-0.76	1.00					
V	0.51	-0.67	0.11	0.73	-0.76	0.42	**-0.84**	0.80	-0.77	**0.93**	-0.74	0.67	**0.99**	**0.97**	**0.86**	**0.99**	**0.94**	**-0.81**	-0.71	0.49	**0.93**	-0.64	**0.82**	0.75	**-0.87**	**0.99**	**0.98**	-0.55	-0.71	-0.80	**0.99**	1.00				
W	0.58	-0.67	0.16	0.73	-0.74	0.47	**-0.85**	**0.85**	-0.76	**0.91**	-0.78	0.60	**0.95**	**0.95**	**0.82**	**0.98**	**0.89**	-0.79	-0.71	0.52	**0.92**	-0.66	0.78	0.75	**-0.88**	**0.97**	**0.98**	-0.54	-0.69	-0.79	**0.95**	**0.97**	1.00			
Zn	0.42	-0.55	-0.04	0.61	-0.64	0.32	-0.74	0.78	-0.66	**0.86**	-0.66	0.65	**0.99**	**0.92**	0.80	**0.97**	**0.93**	-0.72	-0.59	0.35	**0.85**	-0.53	0.75	**0.85**	-0.80	**0.96**	**0.99**	-0.53	-0.59	-0.70	**0.97**	**0.99**	**0.96**	1.00		
Zr	-0.48	**0.96**	-0.67	**-0.89**	**0.92**	**-0.88**	**0.92**	**-0.88**	**0.97**	**-0.82**	**0.97**	-0.28	-0.74	**-0.83**	-0.64	**-0.83**	-0.81	**0.98**	**0.99**	**-0.90**	**-0.84**	**0.98**	-0.65	-0.27	**0.96**	**-0.84**	-0.76	0.77	**0.98**	**0.99**	-0.73	-0.79	-0.80	-0.70	1.00	
Sc	0.52	**-0.98**	**0.88**	**0.92**	**-0.93**	**0.90**	**-0.88**	0.65	**-0.95**	0.70	**-0.88**	0.20	0.48	0.67	0.54	0.59	0.56	**-0.92**	**-0.97**	**0.99**	0.73	**-0.97**	0.59	-0.11	**-0.85**	0.63	0.47	-0.59	**-0.97**	**-0.93**	0.50	0.54	0.55	0.40	**-0.92**	1.00

Table A10 - Pearson´s correlation coefficients for size-fractions of Fe-MC.

	Ctot	Ag	Al	Ca	Fe	K	Mg	Na	P	Ti	As	Ba	Be	Cd	Co	Cr	Cu	Hf	Li	Mn	Mo	Nb	Ni	Pb	Rb	Sb	Sn	Sr	Ta	Th	U	V	W	Zn	Zr	Sc
Ctot	1.00																																			
Ag	-0.16	1.00																																		
Al	-0.28	0.33	1.00																																	
Ca	0.37	-0.02	**-0.81**	1.00																																
Fe	0.07	0.30	**-0.68**	**0.72**	1.00																															
K	-0.14	-0.05	**0.86**	**-0.83**	**-0.93**	1.00																														
Mg	0.02	0.31	**-0.70**	**0.81**	**0.97**	**-0.94**	1.00																													
Na	-0.02	-0.15	**0.75**	**-0.66**	**-0.93**	**0.93**	**-0.91**	1.00																												
P	-0.15	**0.86**	0.10	0.19	0.45	-0.21	0.44	-0.30	1.00																											
Ti	-0.45	0.13	**0.91**	**-0.87**	**-0.82**	**0.93**	**-0.81**	**0.80**	-0.05	1.00																										
As	0.07	**0.75**	-0.13	0.31	**0.66**	-0.43	**0.59**	-0.50	**0.91**	-0.33	1.00																									
Ba	-0.47	0.27	**0.80**	**-0.69**	**-0.71**	**0.83**	**-0.67**	**0.70**	0.14	**0.91**	-0.18	1.00																								
Be	-0.03	**0.76**	0.38	-0.08	0.04	0.20	0.04	0.06	**0.84**	0.26	**0.67**	0.44	1.00																							
Cd	0.06	**0.83**	-0.05	0.29	0.54	-0.34	0.51	-0.36	**0.94**	-0.24	**0.96**	-0.06	**0.71**	1.00																						
Co	-0.24	**0.63**	-0.19	0.23	**0.81**	**-0.59**	**0.71**	**-0.70**	**0.69**	-0.37	**0.81**	-0.30	0.32	**0.72**	1.00																					
Cr	-0.13	**0.83**	0.00	0.16	**0.64**	-0.38	**0.57**	-0.50	**0.90**	-0.21	**0.95**	-0.08	**0.68**	**0.90**	**0.89**	1.00																				
Cu	-0.45	**0.87**	0.29	-0.12	0.39	-0.13	0.37	-0.34	**0.81**	0.15	**0.69**	0.25	**0.63**	**0.70**	**0.78**	**0.84**	1.00																			
Hf	-0.50	0.06	**0.80**	**-0.79**	**-0.80**	**0.85**	**-0.77**	**0.72**	-0.12	**0.94**	-0.44	**0.93**	0.18	-0.32	-0.41	-0.29	0.13	1.00																		
Li	0.01	0.00	**0.86**	**-0.80**	**-0.82**	**0.91**	**-0.88**	**0.90**	-0.15	**0.80**	-0.27	**0.67**	0.19	-0.19	-0.43	-0.24	-0.12	**0.68**	1.00																	
Mn	0.22	0.09	**-0.82**	**0.90**	**0.92**	**-0.96**	**0.96**	**-0.87**	0.26	**-0.93**	0.45	**-0.80**	-0.09	0.36	0.53	0.38	0.09	**-0.89**	**-0.89**	1.00																
Mo	0.31	**0.62**	-0.29	0.45	**0.73**	-0.55	**0.65**	**-0.60**	**0.78**	-0.53	**0.95**	-0.38	**0.58**	**0.88**	**0.76**	**0.87**	0.54	**-0.61**	-0.37	**0.59**	1.00															
Nb	-0.49	0.22	**0.87**	**-0.86**	**-0.70**	**0.85**	**-0.73**	**0.67**	0.08	**0.95**	-0.18	**0.94**	0.35	-0.10	-0.19	-0.05	0.31	**0.94**	**0.75**	**-0.89**	-0.38	1.00														
Ni	-0.25	**0.70**	-0.15	0.25	**0.80**	**-0.57**	**0.73**	**-0.70**	**0.72**	-0.34	**0.80**	-0.24	0.38	**0.73**	**0.99**	**0.90**	**0.84**	-0.36	-0.45	0.53	**0.74**	-0.16	1.00													
Pb	-0.19	**0.82**	0.46	-0.30	0.13	0.18	0.04	0.01	**0.84**	0.30	**0.78**	0.41	**0.83**	**0.78**	**0.59**	**0.82**	**0.78**	0.18	0.28	-0.16	**0.63**	0.45	**0.60**	1.00												
Rb	-0.47	0.08	**0.80**	**-0.68**	**-0.75**	**0.85**	**-0.70**	**0.72**	-0.06	**0.92**	-0.39	**0.94**	0.26	-0.31	-0.42	-0.28	0.11	**0.93**	**0.64**	**-0.80**	**-0.56**	**0.89**	-0.36	0.19	1.00											
Sb	-0.07	**0.82**	-0.03	0.20	**0.60**	-0.35	0.53	-0.46	**0.94**	-0.20	**0.98**	-0.03	**0.73**	**0.95**	**0.83**	**0.97**	**0.80**	-0.29	-0.23	0.36	**0.90**	-0.03	**0.83**	**0.85**	-0.25	1.00										
Sn	-0.12	**0.83**	0.07	0.08	0.55	-0.27	0.47	-0.42	**0.92**	-0.12	**0.96**	0.01	**0.74**	**0.91**	**0.83**	**0.98**	**0.83**	-0.22	-0.15	0.28	**0.87**	0.04	**0.84**	**0.89**	-0.20	**0.98**	1.00									
Sr	-0.41	**0.59**	**0.63**	-0.43	-0.26	0.49	-0.27	0.28	**0.59**	**0.65**	0.32	**0.81**	**0.70**	0.40	0.18	0.38	**0.65**	**0.66**	0.38	-0.49	0.12	**0.79**	0.25	**0.73**	**0.68**	0.45	0.47	1.00								
Ta	-0.42	-0.02	**0.76**	**-0.83**	**-0.77**	**0.87**	**-0.80**	**0.70**	-0.08	**0.91**	-0.31	**0.89**	0.20	-0.25	-0.36	-0.25	0.08	**0.90**	**0.74**	**-0.90**	-0.49	**0.95**	-0.35	0.30	**0.88**	-0.18	-0.12	**0.69**	1.00							
Th	**-0.68**	0.47	**0.65**	-0.44	-0.23	0.45	-0.20	0.25	0.44	**0.68**	0.14	**0.80**	0.51	0.17	0.18	0.27	**0.62**	**0.69**	0.30	-0.42	-0.09	**0.77**	0.24	**0.56**	**0.79**	0.29	0.34	**0.88**	**0.68**	1.00						
U	-0.20	**0.78**	0.01	0.12	**0.60**	-0.33	0.52	-0.49	**0.91**	-0.15	**0.94**	0.00	**0.68**	**0.88**	**0.88**	**0.97**	**0.85**	-0.23	-0.22	0.32	**0.85**	0.04	**0.88**	**0.86**	-0.20	**0.98**	**0.98**	0.49	-0.11	0.38	1.00					
V	-0.15	**0.79**	-0.01	0.14	**0.64**	-0.37	**0.55**	-0.51	**0.90**	-0.20	**0.96**	-0.08	**0.66**	**0.89**	**0.90**	**0.99**	**0.83**	-0.30	-0.24	0.37	**0.87**	-0.03	**0.89**	**0.84**	-0.28	**0.98**	**0.99**	0.40	-0.19	0.29	**0.99**	1.00				
W	-0.26	**0.66**	0.40	-0.33	0.18	0.12	0.06	-0.11	**0.73**	0.25	**0.70**	0.33	**0.78**	**0.61**	**0.62**	**0.80**	**0.75**	0.16	0.20	-0.12	**0.59**	0.43	**0.61**	**0.92**	0.18	**0.77**	**0.85**	**0.64**	0.27	**0.55**	**0.83**	**0.81**	1.00			
Zn	-0.22	**0.85**	0.18	-0.04	0.46	-0.17	0.38	-0.34	**0.91**	0.00	**0.91**	0.14	**0.77**	**0.88**	**0.82**	**0.97**	**0.88**	-0.08	-0.06	0.17	**0.79**	0.18	**0.83**	**0.93**	-0.08	**0.96**	**0.99**	**0.56**	-0.01	0.44	**0.98**	**0.97**	**0.89**	1.00		
Zr	-0.49	0.08	**0.86**	**-0.84**	**-0.79**	**0.89**	**-0.77**	**0.73**	-0.10	**0.97**	-0.39	**0.92**	0.18	-0.31	-0.37	-0.26	0.16	**0.97**	**0.73**	**-0.90**	**-0.57**	**0.96**	-0.33	0.24	**0.95**	-0.25	-0.17	**0.67**	**0.95**	**0.73**	-0.18	-0.24	0.21	-0.04	1.00	
Sc	-0.11	**0.65**	-0.40	**0.57**	**0.89**	**-0.75**	**0.91**	**-0.80**	**0.72**	**-0.56**	**0.79**	-0.40	0.36	**0.74**	**0.86**	**0.83**	**0.68**	**-0.57**	**-0.69**	**0.78**	**0.79**	-0.45	**0.89**	0.41	-0.51	**0.79**	**0.76**	0.04	**-0.61**	0.07	**0.78**	**0.81**	0.40	**0.70**	**-0.56**	1.00